

Clemson University

**TigerPrints**

---

All Dissertations

Dissertations

---

December 2020

## The Role of Low Carbon Alcohol Fuels in Advanced Combustion

Brian Gainey

*Clemson University*, [briangainey22@gmail.com](mailto:briangainey22@gmail.com)

Follow this and additional works at: [https://tigerprints.clemson.edu/all\\_dissertations](https://tigerprints.clemson.edu/all_dissertations)

---

### Recommended Citation

Gainey, Brian, "The Role of Low Carbon Alcohol Fuels in Advanced Combustion" (2020). *All Dissertations*. 2728.

[https://tigerprints.clemson.edu/all\\_dissertations/2728](https://tigerprints.clemson.edu/all_dissertations/2728)

This Dissertation is brought to you for free and open access by the Dissertations at TigerPrints. It has been accepted for inclusion in All Dissertations by an authorized administrator of TigerPrints. For more information, please contact [kokeefe@clemson.edu](mailto:kokeefe@clemson.edu).

THE ROLE OF LOW CARBON ALCOHOL FUELS  
IN ADVANCED COMBUSTION

---

A Dissertation  
Presented to  
the Graduate School of  
Clemson University

---

In Partial Fulfillment  
of the Requirements for the Degree  
Doctor of Philosophy  
Automotive Engineering

---

by  
Brian Gainey  
December 2020

---

Accepted by:  
Dr. Benjamin Lawler, Committee Chair  
Dr. Zoran Filipi  
Dr. Robert Prucka  
Dr. Jiangfeng Zhang

## **Abstract**

The production of alcohol fuels from bioderived feedstocks and the performance of next generation stratified low temperature combustion (LTC) modes for internal combustion engines are two research areas that have recently undergone rapid growth independently. Now, there is a need to bridge these two fields and identify the optimal combustion strategy for these low-carbon and carbon-neutral alcohol fuels as well as potential synergies. The large set of next generation stratified LTC modes are generalized into two groups based on how the heat release process proceeds in the compositionally stratified combustion chamber: lean- to-rich or rich-to-lean burn stratified combustion. It was found that the C1-C4 alcohol fuels are prime candidates to enable lean-to-rich burn stratified combustion based on their high cooling potentials and lack of cool flame reactivity (pre-ignition reactions). Previous experimental work by the author showed that a lean-to-rich burn stratified combustion mode, thermally stratified compression ignition (TSCI), can be enabled using a split injection of wet ethanol to gain control over the heat release process. The current work further investigates TSCI with wet ethanol experimentally on a diesel engine architecture, finding that the effectiveness of TSCI's heat release control strategy is not affected by the use of external, cooled exhaust gas recirculation or intake boost. Further, it was shown that the effectiveness of TSCI's heat release control strategy is highly coupled to the hardware used. Specifically, an injector whose spray targets high local heat transfer regions in the cylinder during the compression stroke is more effective at controlling the heat release process than an injector whose spray targets the adiabatic core. Additionally, a piston whose geometry allows regions with high

compression stroke heat transfer to be distinct from the adiabatic core, such as a re-entrant bowl piston, will also increase the effectiveness of TSCI's heat release control strategy. Using a split injection strategy to enable TSCI is not the only way to increase natural thermal stratification and control the heat release process. In this work, high-load LTC is experimentally enabled with wet ethanol on a light-duty gasoline engine architecture by employing a side-mounted, single hole injector with a relatively low injection pressure in a fairly quiescent combustion chamber. The low mixing propensity of this architecture results in a self-sustaining increase of thermal stratification that allows the high-load limit of LTC to be oxygen limited rather than noise limited.

Following the experimental work with TSCI with wet ethanol, the LTC performance of seven bio-synthesizable C1-C4 alcohol fuels (methanol, ethanol, n-propanol, isopropanol, n-butanol, isobutanol, and sec-butanol) is experimentally characterized, showing that with the exception of n-butanol, the LTC performance of these fuels are similar, implying the remaining six fuels could form an equivalence class of fuels for LTC. To further explore this possibility, two previously proposed LTC fuel metrics are considered: critical compression ratio, a metric that describes the ignition propensity of a fuel in LTC, and normalized  $\phi$ -sensitivity, a metric that describes how the local ignition delay time responds to a change in  $\phi$ . The critical compression ratio, experimentally measured on a cooperative fuel research (CFR) engine, was shown to accurately predict the HCCI ignition propensity of the alcohol fuels near the critical compression ratio operating conditions. Similarly, the normalized  $\phi$ -sensitivity showed the potential to predict the effectiveness of a fuel to control the heat release process of LTC using small

amounts of in-cylinder stratification. The normalized  $\phi$ -sensitivity could then serve as a blending benchmark for multi-alcohol water fuel blends.

*For the octopus.*

## **Acknowledgments**

I am greatly indebted to my advisor, Dr. Benjamin Lawler, both as a mentor and as a friend. The amount of time you invested in me during my first few years in the lab is the reason for my current and future success. Thank you to my committee members, Dr. Zoran Filipi, Dr. Robert Prucka, and Dr. Jiangfeng Zhang, for their time and feedback. I would also like to thank Dr. Jon Longtin, who served as a mentor during my time at Stony Brook and was the first to recognize my potential as a researcher and recommend graduate school. Special thanks to Dr. Christopher Kolodziej at Argonne National Laboratory for inviting me as a visiting researcher in his lab, where I learned a lot and collected valuable data for this thesis.

Thank you to all my current and former lab mates. Experimental work is a team effort and all of our success is shared. In particular, I would like to thank Dr. Deivanayagam Hariharan and future Dr. Ziming Yan – we made a great team and did a lot of great work together. Finally, I would like to thank my family for their support. Thank you to my wife, Sandy, who knows when to take my mind off of work and when to help me work through a technical problem. I would also like to acknowledge Remy, who was surprisingly interested in hearing about the role of carbon neutral alcohol fuels in advanced combustion.

## Table of Contents

	Page
Title Page .....	i
Abstract .....	ii
Dedication .....	iv
Acknowledgments .....	v
List of Figures .....	x
List of Tables .....	xxii
List of Abbreviations .....	xxiv
Chapter 1. Introduction .....	1
<b>3.1</b> Stratified Advanced Combustion .....	2
<b>3.2</b> Overview of bio-alcohol production .....	9
1.1.1    Bioethanol .....	10
1.1.2    Biomethanol production .....	12
1.1.3    Biopropanol production .....	12
1.1.4    Biobutanol production .....	13
1.1.5    Higher Alcohols .....	14
<b>3.3</b> Alcohol Fuel Candidates .....	14
1.1.6    C1-C4 Alcohols .....	14
1.1.7    C5+ Alcohols .....	16
<b>3.4</b> TSCI with Wet Ethanol .....	17
<b>3.5</b> LTC Fuel Ratings .....	19
1.1.8    Ignition Propensity – Critical Compression Ratio .....	19
1.1.9    Stratification Response – Normalized $\phi$ -Sensitivity .....	20
<b>3.6</b> Objectives .....	23



Chapter 2. Experimental Setup and Methodology .....	26
<b>2.1</b> Light Duty Diesel Engine Architecture Experimental Test Cell .....	26
<b>2.2</b> Light-Duty Gasoline Engine Architecture Experimental Test Cell .....	32
<b>2.3</b> CFR Engine Experimental Test Cell.....	34
<b>2.4</b> Heat Release Analysis.....	35
<b>2.5</b> Uncertainty Analysis.....	36
2.5.1    Statistical Background .....	38
2.5.2    Error Classification .....	40
2.5.3    Uncertainty Propagation .....	41
<b>2.6</b> Open Cycle Engine Thermodynamic Model .....	49
2.6.1    Open Cycle Methodology .....	49
2.6.2    Model Validation .....	50
Chapter 3. Design Parameters for LTC with Wet Ethanol .....	53
<b>3.7</b> HCCI with Wet Ethanol – Light-Duty Diesel Engine Architecture .....	53
3.7.1    Injection timing sweep.....	54
3.7.2    Evaporation Fraction .....	60
<b>3.8</b> TSCI with Wet Ethanol – Light Duty Diesel Engine Architecture.....	62
3.8.1    Injection Strategy .....	62
3.8.2    External, Cooled Exhaust Gas Recirculation.....	67
3.8.3    Intake Boost .....	72
3.8.4    Injector Spray Angle – Re-entrant Bowl Piston .....	76
3.8.5    Injector Spray Angle – Shallow Bowl Piston .....	81
3.8.6    Comparison of Piston Geometries - 150° Injector.....	84
<b>3.9</b> High Load LTC with Wet Ethanol – Light-Duty Gasoline Engine Architecture.....	90
3.9.1    Load range characterization of intake stroke injections .....	90
3.9.2    Using swirl to reduce in-cylinder stratification .....	96
3.9.3    Controlling in-cylinder stratification with a premixed/direct injection split .....	99
3.9.4    Controlling in-cylinder stratification with a split injection strategy.....	101

Chapter 4. Autoignition Characterization of C1-C4 Alcohols in LTC .....	107
<b>4.1</b> Load Sweep.....	108
<b>4.2</b> Combustion Phasing (Intake Temperature) Sweep.....	116
<b>4.3</b> Residual Rate Sweep.....	120
<b>4.4</b> Intake Pressure Sweep .....	123
4.4.1    Load Sweep at Elevated Pressure .....	126
4.4.2    Combustion Phasing Sweep at Elevated Pressure .....	128
<b>4.5</b> Engine Speed.....	130
Chapter 5: LTC Fuel Rating Metrics .....	136
<b>3.10</b> “Beyond-MON” Critical Compression Ratio of C1-C4 Alcohols.....	136
5.1.1    Cetane Number .....	140
5.1.2    Octane Number .....	141
5.1.3    Evaluation of HT HCCI Critical Compression Ratio .....	146
<b>3.11</b> Normalized $\phi$ -sensitivity.....	153
5.1.4    Evaluation of Normalized $\phi$ -sensitivity.....	162
Chapter 6. Conclusions and Scientific Contributions .....	166
<b>6.1</b> Summary and Conclusions .....	166
<b>6.2</b> Scientific Contributions .....	171
<b>6.3</b> Future Work .....	172
Publications.....	174
<b>3.12</b> Thesis Publications .....	174
<b>3.13</b> Other Publications.....	175
References.....	177

## List of Figures

	Page
Figure 1: PLIF images showing thermal stratification during a motored engine cycle [3] .....	3
Figure 2: Diagram illustrating evolution from conventional combustion modes to next generation LTC combustion modes .....	5
Figure 3: A qualitative illustration of the difference between HCCI (top), lean-to-rich burn stratified combustion (middle), and rich-to-lean burn stratified combustion (bottom) using $\phi$ -T distributions of the cylinder evolving from CA0 to CA10. Note that in both lean-to-rich and rich-to-lean burn stratified combustion, $\phi$ should be maintained below stoichiometric (1.0) in each region to avoid soot and NO <sub>x</sub> formation .....	8
Figure 4: Maximum pressure rise rate (MPRR) normalized by intake pressure vs. gross indicated mean effective pressure (IMEPg) for the load range extension of HCCI using a split injection to enable TSCI. Adapted from Ref. [13], the additional extension shows that using an intake boost level of 1.8 bar, the high- load limit of TSCI increases to 11 bar, the maximum rated load of the engine .....	18
Figure 5: 3D CAD model (top) and 2D sketch (bottom) of production re-entrant bowl piston.....	28
Figure 6: 3D CAD model (top) and 2D sketch (bottom) of custom-made shallow bowl piston.....	29
Figure 7: Experimental test cell schematic of the light-duty diesel engine architecture engine at the Advanced Combustion Laboratory at Stony Brook University.....	30
Figure 8: Illustration of the definition of spray included angle .....	31
Figure 9: Experimental test cell schematic of the light-duty gasoline engine architecture at Clemson University International Center for Automotive Research (CU-ICAR).....	34

Figure 10: The resulting standard deviation of 25 individual Monte Carlo simulations are performed with 10, 100, 1,000, 10,000, 100,000 and 1,000,000 trials. The spread of standard deviations is compared with a reference line, at $y=2.89$ , that depicts the standard deviation derived from a statistical approach .....	38
Figure 11: Ensemble averaged cylinder pressure trace superimposed over 300 individual cycles with a measurement uncertainty trace in cylinder pressure (scaled x5) showing high uncertainty in cylinder pressure near ignition due to cycle-to-cycle variations .....	42
Figure 12: Cylinder pressure uncertainty tree .....	43
Figure 13: Bulk temperature uncertainty tree .....	43
Figure 14: Square of sensitivity of bulk temperature to pressure, volume, and in-cylinder mass .....	44
Figure 15: Comparison of bulk temperature standard uncertainty including or excluding pressure and volume terms. From this, it is clear that for most of the cycle, including during heat release, there is no significant loss of information by ignoring pressure and volume uncertainty .....	44
Figure 16: Bulk temperature uncertainty tree after trimming unnecessary branches.....	45
Figure 17: Mass fraction burned (MFB) curve with curves showing uncertainty added/subtracted .....	48
Figure 18: Validation of a motored cycle. Experimental Trapped Mass: $372 \pm 11$ mg. Simulation Trapped mass: 364 mg .....	51
Figure 19: Validation of a fired cycle with premixed fuel and air. Experimental Trapped Mass: $384 \pm 14$ mg. Simulation Trapped mass: 384 mg .....	51
Figure 20: Validation of a fired cycle with a direct injection event at -300 deg aTDC. Experimental Trapped Mass: $384 \pm 15$ mg. Simulation Trapped mass: 383 mg .....	52

Figure 21: The cooling potential (units of $\Delta K$ ) of ethanol, WE80 (80% ethanol 20% water by mass), methanol, butanol, and gasoline as a function of equivalence ratio. This figure assumes all of the heat needed to evaporate the fuel comes from the air .....	53
Figure 22: Intake temperature required to maintain a CA50 of 7.0 deg aTDC vs. injection timing for two coolant/oil temperatures (368K/358K and 353K/343K) with two different injector spray included angles (60° and 150°). Error bars show the expanded uncertainty with a confidence interval of 95% .....	56
Figure 23: Combustion efficiency ( $\eta_c$ ) vs. injection timing for two coolant/oil temperatures (368K/358K and 353K/343K) with two different injector spray included angles (60° and 150°). Error bars show the expanded uncertainty with a confidence interval of 95% .....	57
Figure 24: Emission index (EI) of unburned hydrocarbons (uHC) vs. injection timing for two coolant/oil temperatures (368K/358K and 353K/343K) with two different injector spray included angles (60° and 150°). Error bars show the expanded uncertainty with a confidence interval of 95% .....	58
Figure 25: Emission index (EI) of CO vs. injection timing for two coolant/oil temperatures (368K/358K and 353K/343K) with two different injector spray included angles (60° and 150°). Error bars show the expanded uncertainty with a confidence interval of 95% .....	58
Figure 26: CA25to75 burn duration vs. injection timing for two coolant/oil temperatures (368K/358K and 353K/343K) with two different injector spray included angles (60° and 150°). Error bars show the expanded uncertainty with a confidence interval of 95% .....	60
Figure 27: Intake temperature requirement to maintain CA50 at $7.5 \pm 0.5$ deg aTDC vs. split fraction (split fraction is defined as the percent of the total fuel that is injected during the intake stroke) with a “mid” compression stroke injection (-60 deg aTDC) or an “early” compression stroke injection (-120 deg aTDC). An HCCI case with the same fueling rate is plotted as a reference line.....	64

Figure 28: The start of combustion (SOC) at a constant CA50 of $7.5 \pm 0.5$ deg aTDC vs. split fraction (split fraction is defined as the percent of the total fuel that is injected during the intake stroke) with a “mid” compression stroke injection (-60 deg aTDC) or an “early” compression stroke injection (-120 deg aTDC). An HCCI case with the same fueling rate is plotted as a reference line.....	65
Figure 29: The burn duration (CA25 to CA75) at a constant CA50 of $7.5 \pm 0.5$ deg aTDC vs. split fraction (split fraction is defined as the percent of the total fuel that is injected during the intake stroke) with a “mid” compression stroke injection (-60 deg aTDC) or an “early” compression stroke injection (-120 deg aTDC). An HCCI case with the same fueling rate is plotted as a reference line.....	65
Figure 30: Mass fraction burned vs. crank angle degree for the reference HCCI case and the “mid” compression stroke injection (-60 deg aTDC), 70% split fraction TSCI case, depicting TSCI’s earlier SOC and elongated late stages of combustion.....	66
Figure 31: The combustion efficiency at a constant CA50 of $7.5 \pm 0.5$ deg aTDC vs. split fraction (split fraction is defined as the percent of the total fuel that is injected during the intake stroke) with a “mid” compression stroke injection (-60 deg aTDC) or an “early” compression stroke injection (-120 deg aTDC). An HCCI case with the same fueling rate is plotted as a reference line.....	67
Figure 32: Molar concentration of oxygen, $[O_2]$ , in the cylinder and global equivalence ratio ( $\phi$ ) vs. external, cooled EGR percentage. There are also ~5% hot, internal residuals.....	69
Figure 33: Intake temperature requirement to maintain CA50 at $7.5 \pm 0.5$ deg aTDC vs. external, cooled EGR percentage .....	70
Figure 34: Cylinder pressure and apparent gross heat release rate (AGHRR) vs. crank angle for both a case with no external, cooled exhaust gas recirculation (EGR) and a case with 30% external, cooled EGR. The heat release process of both cases is nearly identical, showing external, cooled EGR does not significantly affect the combustion process of TSCI with wet ethanol.....	70

Figure 35: The start of combustion (SOC) and the burn duration (CA25 to CA75) at a constant CA50 of $7.5 \pm 0.5$ deg aTDC vs. external, cooled EGR percentage .....	71
Figure 36: Both the single cycle combustion efficiency and the overall tailpipe combustion efficiency at a constant CA50 of $7.5 \pm 0.5$ deg aTDC vs. external, cooled EGR percentage .....	72
Figure 37: Global equivalence ratio ( $\phi$ ) and intake temperature requirement to maintain CA50 at $7.5 \pm 0.5$ deg aTDC vs. intake boost level.....	74
Figure 38: The start of combustion (SOC) and the burn duration (CA25 to CA75) at a constant CA50 of $7.5 \pm 0.5$ deg aTDC vs. intake boost level.....	75
Figure 39: The combustion efficiency and gross thermal efficiency (GTE) at a constant CA50 of $7.5 \pm 0.5$ deg aTDC vs. intake boost level.....	75
Figure 40: The emissions index (EI) of NO <sub>x</sub> and ringing intensity vs. combustion efficiency, showing the NO <sub>x</sub> -combustion efficiency tradeoff between boosting while maintain a constant load .....	76
Figure 41: Combustion efficiency ( $\eta_c$ ) vs. start of injection (SOI) timing for all three injectors with the re-entrant bowl piston geometry. The injection timing with the highest combustion efficiency is considered the optimal injection timing for delivering fuel during the intake stroke .....	78
Figure 42: Intake temperature requirement to maintain CA50 at a constant value of $7.0 \pm 0.5$ deg aTDC vs. start of injection (SOI) timing for all three injectors with the re-entrant bowl piston.....	78
Figure 43: CA25-75 burn duration vs. average compression stroke start of injection (SOI) timing for a split fraction of 80% for all three injectors with the re-entrant bowl piston geometry. There are two compression stroke injections, spaced 20 degrees apart from each other and each injecting an equal amount of fuel. -140 deg aTDC on the x-axis corresponds to a set of compression stroke injections at -150 and -130 deg aTDC .....	80

Figure 44: Combustion efficiency ( $\eta_c$ ) vs. start of injection (SOI) timing for all three injectors with the shallow bowl piston geometry. The injection timing with the highest combustion efficiency is considered the optimal injection timing for delivering fuel during the intake stroke .....83

Figure 45: CA25-75 burn duration vs. average compression stroke start of injection (SOI) timing for a split fraction of 80% for all three injectors with the shallow bowl piston geometry. There are two compression stroke injections, spaced 20 degrees apart from each other, each injecting an equal amount of fuel. -140 deg aTDC on the x-axis corresponds to a set of compression stroke injections at -150 and -130 deg aTDC 84

Figure 46: Cylinder pressure and gross heat release rate plotted vs. crank angle for both piston geometries: re-entrant and shallow bowl. The 150° injector is used to deliver fuel at the optimal injection timing determined in Section 3.1.1 for the re-entrant bowl piston (-350 deg aTDC) and in Section 3.2.1 for the shallow bowl piston (-330 deg aTDC) .....85

Figure 47: CA25-75 burn duration vs. average compression stroke start of injection (SOI) timing for a split fraction of 80% for both the re-entrant bowl and the shallow bowl piston geometry with the 150° injector. There are two compression stroke injections, spaced 20 degrees apart from each other, each one injecting an equal amount of fuel. -140 deg aTDC on the x-axis corresponds to a set of compression stroke injections at -150 and -130 deg aTDC.....88

Figure 48: Emissions index of both CO and unburned hydrocarbons (uHC) vs. average compression stroke start of injection (SOI) timing for a split fraction of 80% for both the re-entrant bowl and the shallow bowl piston geometry with the 150° injector. There are two compression stroke injections, spaced 20 degrees apart from each other, each one injecting an equal amount of fuel. -140 deg aTDC on the x-axis corresponds to a set of compression stroke injections at -150 and -130 deg aTDC .....89

Figure 49: Combustion efficiency and intake temperature vs. start of injection (SOI) timing during the intake stroke to characterize the optimal injection timing for the introduction of fuel during the intake stroke and showing a large range of effective intake valve closing temperature control .....91



Figure 50: Ringing intensity (RI) vs. IMEP <sub>g</sub> for both fueling methods at 1200 rpm and 2400 rpm. A reference line a 2.2 MW/m <sup>2</sup> represents the high-load ringing intensity limit .....	93
Figure 51: 25-75% burn duration vs. IMEP <sub>g</sub> for both fueling methods at 1200 rpm and 2400 rpm .....	94
Figure 52: a) Combustion efficiency, b) indicated specific emissions (IS) of CO/uHC, and c) is NO <sub>x</sub> vs. IMEP <sub>g</sub> for both fueling methods at 1200 rpm. Trends are identical at 2400 rpm (not shown for conciseness) .....	95
Figure 53: φ (solid) and φ-prime (dashed) vs. IMEP <sub>g</sub> for both fueling methods at 1200 rpm (trends are identical at 2400 rpm).....	96
Figure 54: Cylinder pressure and gross heat release rate (GHRR) traces vs. crank angle degrees for vaporizer-fueled combustion with low swirl, early (-320 deg aTDC SOI) direct injection-fueled combustion with low swirl, and early direct injection fueled combustion with a swirl ratio of 2.5. CA50 is maintained at 7.0 ± 0.5 deg aTDC by adjusting intake temperature and fueling rate is maintained at ~36.0 ± 0.5 mg/cycle.....	98
Figure 55: Ringing intensity (RI) vs. premixed (vaporized) fraction. Due to high uncertainties in ringing intensity from cyclic variability, the coefficient of variation (COV) of RI is plotted. With the exception of a premixed fraction of 0% (full early DI) and 100% (full vaporizer), the uncertainty in premixed fraction is ~5% .....	101
Figure 56: Indicated specific (IS) emissions of NO <sub>x</sub> and CO vs. premixed (vaporized) fraction. With the exception of a premixed fraction of 0% (full early DI) and 100% (full vaporizer), the uncertainty in premixed fraction is ~5% .....	101
Figure 57: Ringing intensity (RI) vs. SOI for compression stroke injection timing sweep, where 20% of the total fuel is injected during the compression stroke and 80% is vaporized. Due to high uncertainties in ringing intensity from cyclic variability, coefficient of variation (COV) of RI is plotted. A reference line with the RI and COV of RI of a fully vaporized case is shown .....	103

Figure 58: 25-75% burn duration and coefficient of variation (COV) of gross indicated mean effective pressure (IMEP <sub>g</sub> ) of CA50 vs. SOI for the compression stroke injection timing sweep, where 20% of the total fuel is injected during the compression stroke and 80% is injected during the intake stroke .....	103
Figure 59: Combustion efficiency vs. SOI for the compression stroke injection timing sweep where 20% of the total fuel is injected during the compression stroke and 80% is vaporized. A reference line is shown for the combustion efficiency (with a 95% confidence interval) of a fully vaporized case .....	104
Figure 60: Cylinder pressure and gross heat release rate (GHRR) traces vs. crank angle degrees for three cases: Case 1, early direct injection (-320 deg aTDC SOI) fueled combustion, Case 2, split injection strategy (80% of fuel at -320 deg aTDC, 20% of fuel at -60 deg aTDC), and Case 3, vaporizer/early DI split strategy (80% of fuel at -320 deg aTDC, 20% of fuel premixed in vaporizer). CA50 is maintained at $7.0 \pm 0.5$ deg aTDC by adjusting intake temperature and fueling rate is maintained at $\sim 36.0 \pm 0.5$ mg/cycle .....	105
Figure 61: Intake temperature vs. charge-mass equivalence ratio ( $\phi'$ ) for each load case with a constant CA50 of $7.0 \pm 0.5$ deg aTDC. The average uncertainty in $\phi'$ is $\pm 0.02$ .....	109
Figure 62: Exhaust temperature vs. charge-mass equivalence ratio ( $\phi'$ ) for each load case with a constant CA50 of $7.0 \pm 0.5$ deg aTDC. The average uncertainty in $\phi'$ is $\pm 0.02$ .....	109
Figure 63: Intake valve closing (IVC) temperature vs. charge-mass equivalence ratio ( $\phi'$ ) for each load case with a constant CA50 of $7.0 \pm 0.5$ deg aTDC. The average uncertainty in $\phi'$ is $\pm 0.02$ .....	110
Figure 64: Cylinder pressure and gross heat release rate (GHRR) vs. crank angle for three of the seven fuels considered (ethanol, isopropanol, and n-butanol) at a low load condition ( $\phi' = 0.33$ ) and a high load condition ( $\phi' = 0.5$ ).....	113
Figure 65: Indicated specific (IS) emissions of NO <sub>x</sub> vs. charge-mass equivalence ratio ( $\phi'$ ) for each load case with a constant CA50 of $7.0 \pm 0.5$ deg aTDC. The average uncertainty in $\phi'$ is $\pm 0.02$ .....	114

Figure 66: Overall combustion efficiency vs. charge-mass equivalence ratio ( $\phi'$ ) for each load case with a constant CA50 of $7.0 \pm 0.5$ deg aTDC .....	115
Figure 67: Indicated specific (IS) emissions of CO vs. charge-mass equivalence ratio ( $\phi'$ ) for each load case with a constant CA50 of $7.0 \pm 0.5$ deg aTDC .....	115
Figure 68: Indicated specific (IS) emissions of uHC vs. charge-mass equivalence ratio ( $\phi'$ ) for each load case with a constant CA50 of $7.0 \pm 0.5$ deg aTDC .....	116
Figure 69: Intake temperature vs. combustion phasing (CA50) with a $\phi'$ of 0.25 .....	117
Figure 70: Intake temperature vs. combustion phasing (CA50) with a $\phi'$ of 0.33 .....	117
Figure 71: Intake temperature vs. combustion phasing (CA50) with a $\phi'$ of 0.40 .....	118
Figure 72: Intake temperature vs. residual rate with a constant CA50 of $7.0 \pm 0.5$ deg aTDC and constant a $\phi'$ of 0.33. The relative uncertainty of the residual rate is $\sim 10\%$ .....	121
Figure 73: Intake valve closing (IVC) temperature vs. residual rate with a constant CA50 of $7.0 \pm 0.5$ deg aTDC and constant a $\phi'$ of 0.33. The relative uncertainty in the residual rate is $\sim 10\%$ .....	121
Figure 74: CA10 vs. residual rate with a constant CA50 of $7.0 \pm 0.5$ deg aTDC and constant a $\phi'$ of 0.33. The relative uncertainty in the residual rate is $\sim 10\%$ .....	123
Figure 75: Residual rate vs. intake pressure for the intake pressure sweep. The relative uncertainty in the residual rate is $\sim 10\%$ .....	124
Figure 76: Intake valve closing (IVC) temperature vs. intake pressure with a constant CA50 of $7.0 \pm 0.5$ deg aTDC and constant a $\phi'$ of 0.33. The residual rate for each case is given in Figure 75 .....	125
Figure 77: Normalized gross heat release rate (GHRR) vs. crank angle for the three butanol isomers (n- butanol, isobutanol, and sec-butanol) under minimum and maximum boost conditions .....	126
Figure 78: Intake temperature vs. charge-mass equivalence ratio ( $\phi'$ ). The intake pressure $\sim 1.95$ bar with a constant CA50 of $7.0 \pm 0.5$ deg aTDC. The average uncertainty in $\phi'$ is $\pm 0.02$ .....	128

Figure 79: Intake valve closing (IVC) temperature vs. charge-mass equivalence ratio ( $\phi'$ ). The intake pressure $\sim 1.95$ bar with a constant CA50 of $7.0 \pm 0.5$ deg aTDC. The average uncertainty in $\phi'$ is $\pm 0.02$ .....	128
Figure 80: Intake temperature vs. CA50 with a $\phi'$ of 0.33. The intake pressure is $\sim 1.95$ bar .....	129
Figure 81: Intake valve closing (IVC) temperature vs. CA50 with a $\phi'$ of 0.33. The intake pressure is $\sim 1.95$ bar .....	130
Figure 82: Intake temperature vs. engine speed with a constant CA50 of $7.0 \pm 0.5$ deg aTDC and constant $\phi'$ of 0.33 .....	131
Figure 83: Exhaust temperature vs. engine speed with a constant CA50 of $7.0 \pm 0.5$ deg aTDC and constant $\phi'$ of 0.33 .....	131
Figure 84: Combustion efficiency vs. engine speed with a constant CA50 of $7.0 \pm 0.5$ deg aTDC and constant $\phi'$ of 0.33 .....	132
Figure 85: Intake valve closing (IVC) temperature vs. engine speed with a constant CA50 of $7.0 \pm 0.5$ deg aTDC and constant $\phi'$ of 0.33 .....	133
Figure 86: CA10 and CA10 vs. engine speed with a constant CA50 of $7.0 \pm 0.5$ deg aTDC, denoted with a reference line, and constant $\phi'$ of 0.33. The single cycle uncertainty of CA10 and CA90 is $\sim 0.2$ deg while the 300-cycle ensemble average uncertainty is $\sim 1.0$ deg .....	133
Figure 87: Design of experiments for determining the sensitivity of the critical compression ratio of each fuel to CA50 and equivalence ratio ( $1/\lambda$ ) .....	137
Figure 88: High temperature HCCI critical compression ratio vs. cetane number (CN) for the seven alcohol fuels considered. Vertical error bars display the uncertainty in the critical compression ratio. Horizontal error bars on methanol, ethanol, and n-butanol display the range of CN values found for these fuels in Ref. [118] .....	141
Figure 89: High temperature HCCI critical compression ratio vs. motor octane number (MON) for the seven alcohol fuels considered. Vertical error bars display the uncertainty in the critical compression ratio .....	142

Figure 90: High temperature HCCI critical compression ratio vs. research octane number (RON) for the seven alcohol fuels considered. Vertical error bars display the uncertainty in the critical compression ratio .....	143
Figure 91: Data from Ref. [119] showing standard RON and modified RON vs. ethanol content of ethanol- gasoline blends showing the impact of the heightened cooling potential of ethanol on the determined RON values. Modified RON is defined as the RON test with a constant charge inlet temperature designed to compensate for the differences in cooling potentials of the fuel blends .....	144
Figure 92: High temperature HCCI critical compression ratio vs. modified research octane number (RON) for the seven alcohol fuels considered. The modified RON is a metric that is a calculated adjustment to the RON value of a fuel based on its cooling potential. Vertical error bars display the uncertainty in the critical compression ratio .....	146
Figure 93: Intake temperature requirement of gasoline engine architecture vs. high temperature (HT) HCCI critical compression ratio (cCR) measured in this work under five different operating conditions: a) 1200 rpm, 20% internal exhaust gas recirculation (iEGR), b) 1200 rpm, 20% iEGR, c) 1200 rpm, 40% iEGR, d) 900 rpm, 30% iEGR, and e) 2400 rpm, 30% iEGR .....	148
Figure 94: Intake valve closing (IVC) temperature requirement of gasoline engine architecture vs. high temperature (HT) HCCI critical compression ratio (cCR) under six different operating conditions: a) $\phi = 0.33$ , Intake pressure = 1.15 bar b) $\phi = 0.25$ , Intake pressure = 1.15 bar, c) $\phi = 0.45$ , Intake pressure = 1.15 bar 4) $\phi = 0.33$ , Intake pressure = 1.35 bar, e) $\phi = 0.33$ , Intake pressure = 1.65 bar f) $\phi = 0.33$ , Intake pressure = 1.95 bar. *At an intake pressure of 1.95 bar, methanol and n-butanol are not included.....	151
Figure 95: Normalized $\phi$ -sensitivity (Equation 8) for methanol mapped to the $\phi$ -T plane using the ignition delay correlation developed in Ref. [121] .....	154
Figure 96: Normalized $\phi$ -sensitivity (Equation 8) for ethanol mapped to the $\phi$ -T plane using the ignition delay correlation developed in Ref [122].....	155
Figure 97: Normalized $\phi$ -sensitivity (Equation 8) for n-butanol mapped to the $\phi$ -T plane using the ignition delay correlation developed in Ref [61] .....	155

Figure 98: The cooling potential ( $dTd\phi$ ) of wet ethanol blends, wet propanol blends, and wet butanol blends vs. water mass percentage in the wet-alcohol blend. A constant reference line displays the cooling potential of neat methanol. The cooling potential of wet ethanol equals that of neat methanol at a water mass percentage of ~24% (76% ethanol by mass). The cooling potential of wet propanol equals that of neat methanol at a water mass percentage of ~33% (67% propanol by mass). The cooling potential of wet butanol equals that of neat methanol at a water mass percentage of 37% (63% butanol by mass). These values are reported for  $\phi=0.6$  and  $T=700$  K..... 159

Figure 99: Normalized  $\phi$ -sensitivity (Equation 8) for wet ethanol 76 (76% ethanol, 24% water by mass) mapped to the  $\phi$ -T plane using the ignition delay correlation developed in Ref [122]..... 159

Figure 100: Ringing intensity for ethanol and n-butanol for two fueling methods: vaporizer (fully premixed) and early direct injection (stratified). Error bars represent the standard deviation of ringing intensity across 300 consecutive cycles..... 164

## List of Tables

	Page
Table 1: Key fuel properties of select alcohol fuels.....	9
Table 2: Engine geometry and valve timings for the light-duty diesel engine architecture engine at the Advanced Combustion Laboratory at Stony Brook University.....	30
Table 3: Model, range, and instrument uncertainty for each instrument used.....	32
Table 4: Engine geometry and valve timings for the light-duty gasoline architecture engine at Clemson University International Center for Automotive Research.....	33
Table 5: The intake valve closing temperature without any evaporative cooling of the fuel, and evaporation fraction of the fuel in the air required to obtain an intake valve temperature that matches the intake valve temperature of the PFI case for each injection timing/intake air temperature combination.....	61
Table 6: Operating parameters and combustion results for two DI HCCI cases comparing piston geometry: re-entrant vs. shallow. The 150° injector is used for both cases .....	85
Table 7: Operating conditions and results for low vs. high swirl comparison.....	98
Table 8: Relevant operating conditions and combustion results for three cases: Case 1, early direct injection (-320 deg aTDC SOI) fueled combustion, Case 2, split injection strategy (80% of fuel at -320 deg aTDC, 20% of fuel at -60 deg aTDC), and Case 3, vaporizer/early DI split strategy (80% of fuel at -320 deg aTDC, 20% of fuel premixed in vaporizer) .....	106
Table 9: Standard operating conditions for experimentally determining the critical compression ratio .....	136
Table 10: Critical compression ratios for each fuel under each operating condition defined by the design of experiments, shown in Figure 87. Highlighted in blue is the critical compression ratio obtained under the standard operating conditions outlined in Table 9.....	138

Table 11: The sensitivity coefficients of the critical compression ratio with respect to CA50 ( $\partial cCR_{CA50}$ ) and to equivalence ratio ( $\partial cCR_{\phi}$ ), the uncertainty in CA50 ( $\Delta CA50$ ) and equivalence ratio ( $\Delta \phi$ ), and the uncertainty in critical compression ratio ( $\Delta cCR$ ), calculated with equation 2. Additionally, the critical compression ratio (cCR) for each fuel is shown as a reference .....138

Table 12: The Cetane number (CN), motor octane number (MON), research octane number (RON), and the octane sensitivity (S) of the seven alcohol fuels considered. CNs are from Ref. [118]. Note that the reported CN of methanol, ethanol, and n-butanol in this table is the average of several values found in Ref. [118].  
\*The RON of isopropanol reported here was experimentally measured on the CFR used in this study to rectify conflicting reports in the literature ..... 139

Table 13: The modified RON of each alcohol fuel considered, which is a function of the fuel's RON and the fuel's cooling potential, given by equation 1.  $h_{fg}$ , fuel is the latent heat of vaporization of the fuel and  $AFR_{stoich}$  is the stoichiometric air-fuel ratio of the fuel .....145

Table 14: RON, MON, HT HCCI cCR, and chemical composition of the two RON98 gasoline blends. 149 Table 15: Values of  $\beta$ ,  $Ea'$ , and  $\gamma$  from the ignition delay correlations of methanol, ethanol, and n-butanol .....155



## **List of Abbreviations**

**aTDC** – after Top Dead Center

**CAD** – Crank Angle Degrees

**CDC** – Conventional Diesel Combustion

**CFD** – Computational Fluid Dynamics

**COV** – Coefficient of Variance

**DI** – Direct Injection

**DWI** – Direct Water Injection

**EGR** – Exhaust Gas Recirculation

**EI** – Emissions Index

**EVC** – Exhaust Valve Closing

**EVO** – Exhaust Valve Opening

**GHRR** – Gross Heat Release Rate

**HCCI** – Homogeneous Charge Compression Ignition

**IMEP<sub>g</sub>** – Gross Indicated Mean Effective Pressure

**IVC** – Intake Valve Closing

**IVO** – Intake Valve Opening

**LTC** – Low Temperature Combustion

**MPRR** – Maximum Pressure Rise Rate

**NO<sub>x</sub>** – Oxides of Nitrogen (NO or NO<sub>2</sub>)

**NVO** – Negative Valve Overlap

**PFI** – Port Fuel Injection

**PFS** – Partial Fuel Stratification

**PM** – Particulate Matter

**PLIF** – Planar Laser-Induced Fluorescence

**RCCI** – Reactivity Controlled Compression Ignition

**RI** – Ringing Intensity

**SACI** – Spark Assisted Compression Ignition

**SI** – Spark Ignition

**TSA** – Thermal Stratification Analysis

**TSCI** – Thermally Stratified Compression Ignition

**uHC** – Unburned Hydrocarbons

**WE** – Wet ethanol

**WI** – Water Injection

**VCR** – Variable Compression Ratio

## Chapter 1. Introduction

Alcohol has many uses. As the use of fossil fuels becomes increasingly detrimental to the environment, one such critical use is as a biofuel. A biofuel is a fuel that is produced by the use of biomass, and the use of a biofuel can be considered part of the *fast carbon cycle*, meaning carbon dioxide produced during the combustion of a biofuel does not contribute to rising atmospheric carbon dioxide levels. Rather, the carbon source of biofuels, biomass, is derivative of atmospheric carbon. Therefore, biofuels are considered carbon neutral fuels. On the other hand, combustion of fossil fuels directly contributes to rising atmospheric carbon dioxide levels by releasing carbon dioxide that has been stored over millions of years as a part of the *slow carbon cycle*. Ethanol is currently the most widely used bio-alcohol fuel due to its relatively mature production infrastructure. However, metabolic engineering of microorganisms and advancement in catalytic gas fermentation have enabled many avenues of biosynthesizing other alcohols. In parallel with advancement in bio-alcohol synthesis, a considerable amount of research on a number of advanced combustion concepts aims to provide internal combustion engines with high thermal efficiencies and low emissions. Although biofuels such as the alcohol fuels can be used in alternative power generation devices, like fuel cells, it is paramount that their use in internal combustion engines is expanded. The internal combustion engine is a power generation device that is low-cost, highly load-flexible, and highly power dense. These features make the internal combustion engine effectively irreplaceable. The intermittency of renewable energy requires a way to store and retrieve energy that is efficient, cost effective, and power dense. While battery technology is advancing, the volume- and energy- density of liquid fuels is unparalleled. Similarly, the liquid fuel distribution infrastructure is well developed and widely available. Liquid fuels, like biofuels, can therefore be synthesized using renewable energy, serving as an effective energy storage device, with the internal combustion engine serving as an energy retrieving device. Therefore, rather than abandoning the internal combustion engine, the technology should be improved to maximize the efficiency and minimize the emissions of combustion with biofuels.

Due to their chemical structure, alcohols have unique fuel properties. While alcohol fuels can be used effectively in the conventional combustion modes, spark ignition (SI) and conventional diesel combustion (CDC), their unique fuel properties give them potential to enable an advanced combustion concept that has an a wide operating range. With both fields rapidly maturing, there is a strong need for the two fields to intersect. In light of this, this work aims to study the potential of biosynthesized alcohol fuels in advanced combustion, considering advanced combustion concepts that control the heat release process via small-to-medium amounts of in-cylinder stratification introduced via the direct injection of fuel, simultaneously providing cycle-to-cycle control over the heat release process and enabling full load operation. The full scope of work and objectives of this thesis is described in Section 1.6.

## **1.1 Stratified Advanced Combustion**

Advanced combustion concepts aim to break the efficiency-emissions tradeoff of the conventional combustion modes. Low temperature combustion (LTC) is a subset of these advanced combustion concepts that aims to provide high thermal efficiency and low emissions of PM and NO<sub>x</sub> via lean, near-homogeneous, un-throttled operation. Homogeneous charge compression ignition (HCCI), the first LTC concept, achieves this goal [1]. Like spark ignition (SI), HCCI introduces a homogeneous mixture of air and fuel into the cylinder; however, unlike SI, HCCI uses a lean fuel-air mixture and achieves combustion through autoignition rather than a spark discharge and flame propagation. Soot production, which plagues Conventional Diesel Combustion (CDC), is eliminated in HCCI due to the use of a homogeneous mixture of air and fuel. The excess air manages the in-cylinder temperatures, maintaining the peak temperature below the NO<sub>x</sub> production threshold, thus producing virtually zero NO<sub>x</sub> emissions. The thermal efficiency in HCCI is generally diesel-like due to the use of lean fuel-air mixtures, mid-range compression ratios, unthrottled operation, and low peak temperatures, which generally lowers heat transfer losses.

Although HCCI has demonstrated favorable characteristics, it is limited to low load operation due to its lack of a heat release control mechanism. At high loads, engine damaging energy release and pressure

rise rates will occur. Additionally, transient operation is difficult due to this lack of a heat release control mechanism. The heat release process in HCCI is governed by natural thermal stratification that forms in the cylinder via heat transfer during the compression stroke [2, 3]. This is illustrated by optical chemiluminescence and planar laser-induced fluorescence (PLIF) images, shown in Figure 1, which have experimentally measured this temperature distribution. The hottest regions in the cylinder ignite first, further compressing and heating colder regions in the cylinder until they ultimately ignite too in a process known as *sequential autoignition*. Since this natural thermal stratification governs the heat release process, researchers have labored to understand the mechanisms that control the formation of natural thermal stratification in order to attempt to control it. In particular, the Thermal Stratification Analysis (TSA) was developed to quantify natural thermal stratification in HCCI experiments to understand how changes to HCCI operating conditions would affect thermal stratification [4, 5]. The TSA has shown that wall conditions, contrary to intuition, have a small effect on thermal stratification [6], while the top dead center (TDC) average temperature and swirl have a significant effect [7].

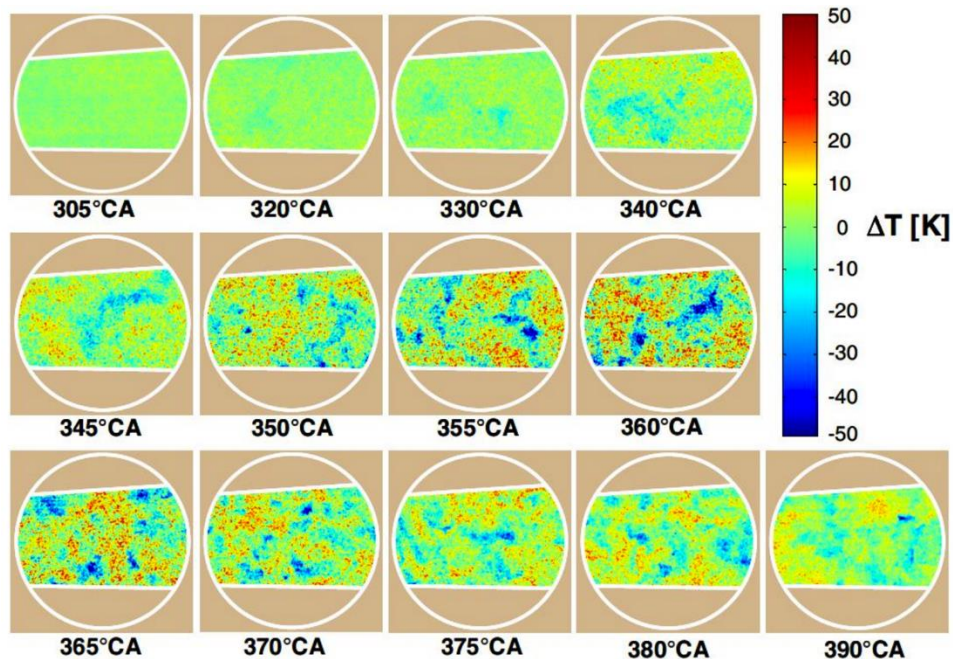


Figure 1: PLIF images showing thermal stratification during a motored engine cycle [3].

While the TSA method is able to shed light on the formation of natural thermal stratification, control over the formation of natural thermal stratification did not seem to be a viable pathway to controlling HCCI. However, there are numerous next generation LTC concepts that aim to provide an alternative control mechanism over the heat release process. These next generation LTC concepts all use a similar control strategy: the direct injection of fuel during the compression stroke. By inducing some compositional stratification into the cylinder, these combustion strategies can achieve cycle-to-cycle control over the heat release process and full load operation. The naming convention of these LTC concepts can be vague, with significant amounts of overlap among most of them. For example, partially premixed combustion (PPC) describes an advanced compression ignition combustion mode that has some degree of fuel inhomogeneity in the combustion chamber that controls the heat release process [8]. Gasoline compression ignition (GCI) describes a PPC-like combustion mode utilizing gasoline [9]. Partial fuel stratification (PFS) is another PPC-like combustion mode that employs a split injection strategy, where a portion of the fuel is injected during the intake stroke to fully premix with air and the remainder of the fuel is injected during the compression stroke to induce stratification [10]. Thus, the difference between PFS, GCI, and PPC largely lays with the injection strategy. Reactivity-controlled compression ignition (RCCI), which uses two distinct fuels with vastly different reactivities, is a PPC-like combustion mode that creates a reactivity gradient in the cylinder by direct injecting a high reactivity fuel during the compression stroke into premixed air and a low-reactivity fuel [11]. Thermally stratified compression ignition (TSCI) was originally proposed as an advanced combustion strategy that used the direct injection of water during the compression stroke to control the heat release process by the advisor of the author of this thesis [12]. The author of this thesis subsequently showed that TSCI could be enabled a single fuel using a split injection strategy similar to PFS in work towards a master's thesis [13]. The difference between TSCI and PFS is subtle and highlights what should be the primary distinction between stratified advanced LTC concepts – the sequence of autoignition within the stratified charge in the combustion chamber. Figure 2 depicts the evolution from the conventional combustion modes to next generation LTC combustion modes.

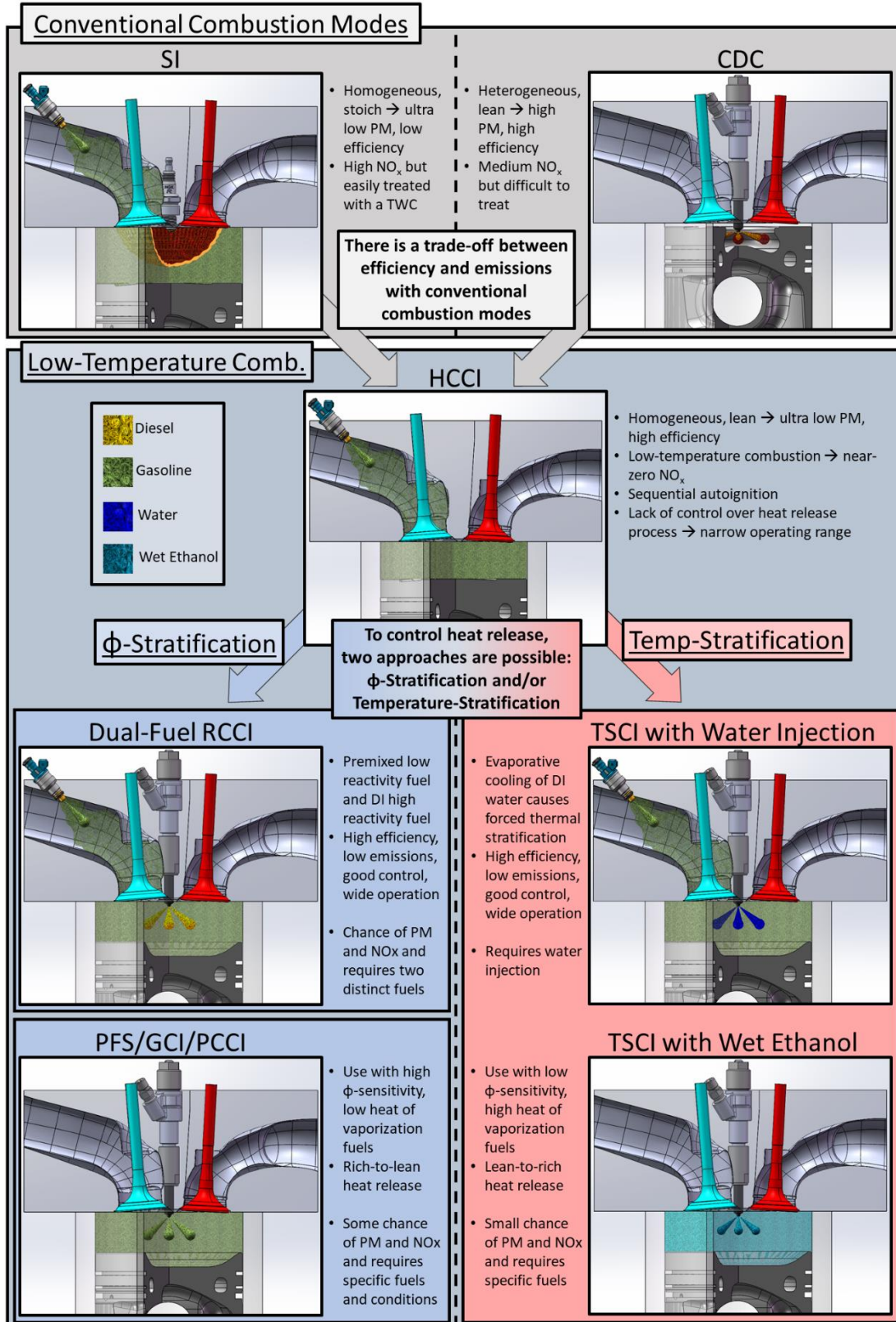


Figure 2: Diagram illustrating evolution from conventional combustion modes to next generation LTC combustion modes

What all of these combustion modes have in common is that the direct injection of fuel during the compression stroke superimposes a coupled equivalence ratio ( $\phi$ )-temperature field on the naturally formed temperature distribution that is a function of the injection timing, geometry of the engine, and bulk motion of the charge, among other factors. Regions targeted by the spray will have their local  $\phi$  increase and their local temperature decrease, due to evaporative cooling. These regions will therefore be richer and lower in temperature than regions not targeted by the spray. Depending on the nature of the fuel, the heat release process will proceed from rich-to-lean, like PFS, or from lean-to-rich, like TSCI. In other words, either the rich regions or the lean regions in the stratified combustion chamber will be the first to autoignite, with sequential autoignition proceeding in either a rich-to-lean or lean-to-rich fashion. The two key fuel properties that determines how the heat release process will proceed are  $\phi$ -sensitivity and cooling potential.  $\phi$ -sensitivity describes how the ignition delay of a fuel changes with  $\phi$ . A fuel is considered highly  $\phi$ -sensitive if its' ignition delay rapidly decreases with an increase in  $\phi$ . This is strongly correlated with the negative temperature coefficient (NTC) behavior of fuels that exhibit low temperature heat release (LTHR) and/or intermediate temperature heat release (ITHR) [14, 15]. NTC behavior is characterized an increase in the ignition delay of a fuel with an increase in the temperature of the charge. This occurs due to an increase in temperature causing a decrease in LTHR and ITHR that both form radicals and release heat that advances hot ignition. The cooling potential of a fuel describes the potential change in temperature a fuel can induce via evaporation, given by the following equation:

$$\text{Cooling Potential} = \frac{\phi * h_{fg, fuel}}{AFR_{stoich} * C_{p, air}} \quad (1)$$

Where  $h_{fg, fuel}$  is the latent heat of vaporization of fuel,  $\phi$  is the equivalence ratio,  $AFR_{stoich}$  is the stoichiometric air-fuel ratio, and  $c_{p, air}$  is the specific heat of air. Note that the cooling potential is not only a function of  $h_{fg, fuel}$ , but of  $AFR_{stoich}$  as well, since a fuel with a lower  $AFR_{stoich}$  will require a larger amount of fuel for a given  $\phi$ . Generalizing, to maximize the control authority of a stratified advanced combustion concept, there are two fuel options to choose from: one with little-to-no  $\phi$ -sensitivity and a high cooling



potential, which will burn lean-to-rich, or one with a high  $\phi$ -sensitivity and a low cooling potential, which will burn rich-to-lean. Therefore, a more intuitive way to describe next generation LTC concepts would be as either “lean-to-rich burn stratified combustion” or “rich-to-lean burn stratified combustion.” A schematic illustrating the difference between lean-to-rich and rich-to-lean burn stratified combustion is shown in Figure 1. Based on the nature of the fuel requirement for each strategy, they have unique drawbacks. Lean-to-rich burn stratified combustion is more prone to poor combustion efficiency, i.e. high CO and uHC emissions, due to the relatively high autoignition resistance of the single-stage ignition fuels employed. On the other hand, rich-to-lean burn stratified combustion is more prone to particulate matter emissions due to the longer molecular structure and low oxygen content associated with the gasoline-like fuels that exhibit NTC behavior. However, both lean-to-rich and rich-to-lean burn stratified combustion are equally effective at controlling the heat release, enabling cycle-to-cycle control over combustion and full load operation, provided the correct fuel and engine hardware are used to maximize the effectiveness of the control strategy used while minimizing their respective drawbacks.

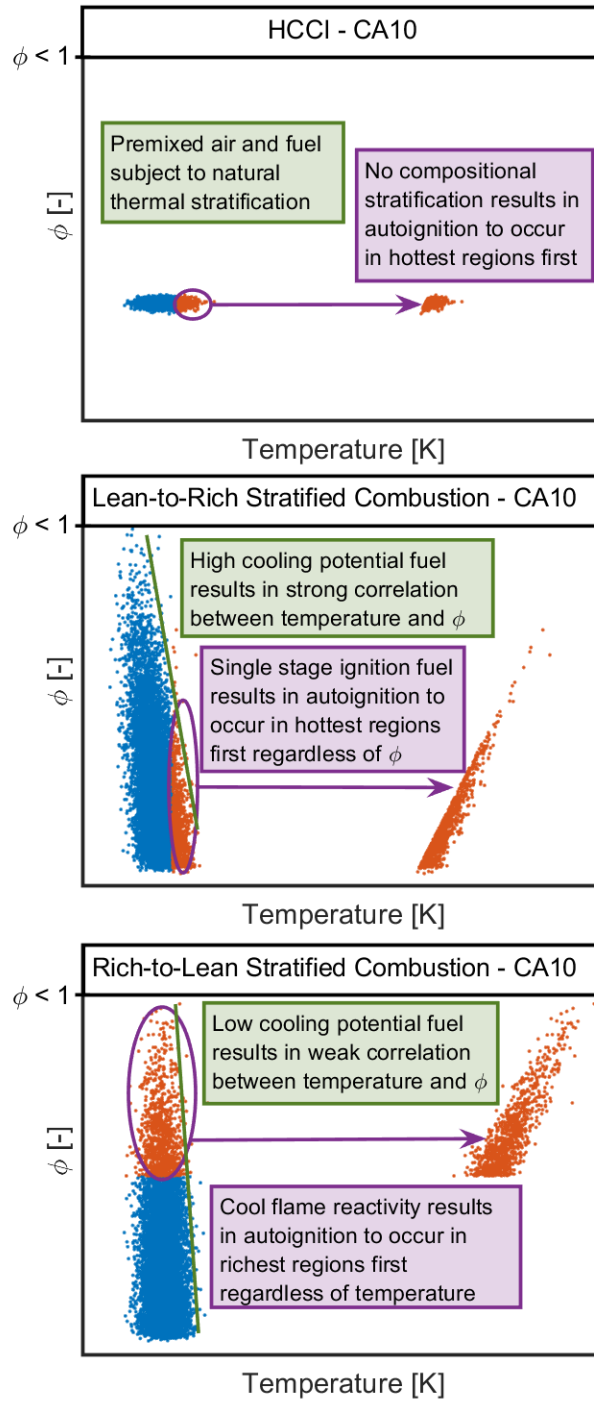
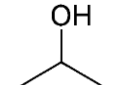
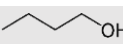


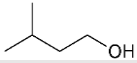
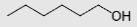

Figure 3: A qualitative illustration of the difference between HCCI (top), lean-to-rich burn stratified combustion (middle), and rich-to-lean burn stratified combustion (bottom) using  $\phi$ -T distributions of the cylinder evolving from CA0 to CA10. Note that in both lean-to-rich and rich-to-lean burn stratified combustion,  $\phi$  should be maintained below stoichiometric (1.0) in each region to avoid soot and  $NO_x$  formation.

## 1.2 Overview of bio-alcohol production

Alcohols are oxygenated hydrocarbons categorized by having a single hydroxyl group ( $-OH$ ) bonded to a carbon atom. The location of this hydroxyl group plays a role in the physical and chemical properties of the molecule. Therefore, alcohols can be grouped into three categories based on the number of carbons bonded to the carbon atom that is bonded to the hydroxyl group: *primary*, *secondary*, and *tertiary alcohols* have one, two, and three carbon-carbon bonds on the hydroxyl group carbon, respectively. This hydroxyl group polarizes the molecule, with the degree of polarization inversely related to the spatial distance between the hydroxyl group and the other atoms of the molecule. As a result, the degree of polarization decreases with an increasing number of carbon atoms and, in general, increases when the molecule branches. Polarization of the molecule causes strong intermolecular bonds, resulting in the unique properties of alcohols, such as a low melting point, a high latent heat of vaporization, and a degree of water solubility. Some key fuel properties of various alcohols are displayed in Table 1.

Table 1: Key fuel properties of select alcohol fuels

IUPAC Name	Molecular Structure	MW [kg/kmol]	Specific Gravity @ 20 C	H.O.V. @ 25°C [kJ/kg]	LHV [MJ/kg]	Stoich AFR	Melting/Boiling Point [°C]	Solubility in Water @ 20°C [%]	Water in Azeotrope [%]	RON/MON
Methanol		32.04	0.792	1168	19.95	6.46	-97.8/64.7	Miscible	0.0	109/89
Ethanol		46.06	0.794	920	26.95	9.00	-114.5/78.3	Miscible	4.0	108/90
1-propanol		60.09	0.804	792	30.72	10.33	-126.2/97.2	Miscible	28.3	104/89
2-propanol		60.09	0.789	757	30.54	10.33	-87.8/2.4	Miscible	12.6	113/99
1-butanol		74.11	0.81	708	33.21	11.17	-89.3/117.7	7.7	37.0	98/85
2-butanol		74.11	0.808	671	32.92	11.17	-114.7/99.4	12.5	27.3	108/93
2-methyl-1-propanol		74.11	0.802	686	33.29	11.17	-107.9/108	8.7	33.2	105/90
2-methyl-2-propanol		74.11	0.789	630	32.57	11.17	25.6/82.5	Miscible	11.8	107/94
1-pentanol		88.15	0.816	647.1	34.93	11.76	-78.5/137.8	2.2	54.4	80/74

3-methyl-1-butanol		88.15	0.812	617.1	34.24	11.76	-117.2/131	2.7	49.5	94/84
1-hexanol		102.17	0.814	603	36.00	12.18	-44.6/157.6	0.6	75.0	56/46
1-Octanol		130.23	0.827	545	37.61	12.74	-16.3/195.1	0.05	90.0	28/27

### 1.2.1 Bioethanol

Ethanol is primarily produced through the fermentation of starch-based crops, like corn or sugarcane. Although more research needs to be conducted, this method of production raises valid concerns over potential competition with food sources if the production of ethanol through this method is scaled up to meet a significant fraction of global energy needs [16]. However, bioethanol can be produced, instead, from lignocellulose, the material that makes up most biomass. Lignocellulose primarily consists of three components: lignin, cellulose and hemicellulose. While lignin cannot be used to produce ethanol, cellulosic ethanol can be produced by fermenting hydrolyzed sugars from cellulose and hemicellulose.

Before being hydrolyzed, a pretreatment process must first break down *lignin-cellulose-hemicellulose* complexes. The specific pretreatment method is generally chosen based on the nature of the biomass in question [17]. After pretreatment, either chemical hydrolysis or enzymatic hydrolysis produces fermentable sugars. Chemical hydrolysis entails steeping the cellulose and hemicellulose in an acidic solution. Sulfuric acid is the most common acid used for chemical hydrolysis, though other acids have been proposed to reduce the production of toxic byproducts and ease the burden of neutralization after hydrolysis [18]. Dilute acidic chemical hydrolysis first converts hemicellulose to both pentose (five-carbon sugar, such as xylose), and hexose (six-carbon sugar, such as glucose). Once the hemicellulose is hydrolyzed, the temperature of the solution is heated to  $\sim 230^{\circ}\text{C}$  to convert the cellulose to glucose [19]. Alternatively, concentrated acid ( $\sim 70\%$ ) may be employed at low temperatures and pressures to produce higher sugar yields than dilute acid. However, this increases the complexity of the solution neutralization and the subsequent removal of salts and fermentation inhibitors [20].

Enzymatic hydrolysis hydrolyzes cellulose and hemicellulose by steeping them in a solution containing enzyme producing micro-organisms, or the enzymes themselves. Enzymatic hydrolysis is

theoretically more efficient than chemical hydrolysis and requires significantly less aftertreatment before fermentation. However, its high cost and technological immaturity are currently limiting factors to its production-scale implementation. Current research is exploring “*designer enzymes*” that improve hydrolysis efficiency while decreasing cost [21]. There is even the potential for bio-engineered yeast strains to both hydrolyze and ferment simultaneously, greatly reducing the complexity and cost of cellulosic ethanol production [22].

Finally, the fermentation process converts sugars to ethanol and carbon dioxide. Fermentation of hexoses using the naturally occurring yeast *Saccharomyces Cerevisiae* is up to 95% efficient [23]. Fermenting pentose sugars, on the other hand, requires metabolic engineering of certain strains of yeast/bacteria. Further complicating the fermentation of pentoses is the requirement of oxygen during the fermentation process, which is currently a limiting factor in ethanol yield. Despite these challenges and although there is more work to be done, researchers have made significant strides in developing yeast strains for the co-fermentation of pentoses and hexoses [24].

Additionally, cellulosic ethanol can be produced via gas fermentation by fermenting syngas produced from biomass. This is distinct from the Fischer Tropsch process, which generates hydrocarbons from syngas using high temperatures and pressures as well as costly catalysts. Instead, gas fermentation employs microorganisms, such as *Clostridium Ljungdahlii*, undergoing autotrophy with CO as a feedstock [25]. One key advantage of gas fermentation over traditional fermentation is that gas fermentation of biomass can produce alcohol from lignin, which can account for a significant amount of the total biomass [26].

Lignocellulose can come from dedicated energy crops, such as switchgrass, or agricultural waste, such as corn stover. For example, the crop residue/crop ratio of corn, i.e. the ratio of corn stover/corn grain yield, is ~1. Considering the theoretical ethanol yield of corn stover is slightly lower than that of corn grain due to the production of xylose and other five-carbon sugars during the hydrolysis process, the theoretical ethanol yield of the entire crop can increase by nearly 70% [27]. However, roughly half of the corn stover

produced must be retained to prevent soil erosion and carbon depletion, leaving a net theoretical ethanol yield increase of ~35% [28]. The production of *second-generation bioethanol* can therefore increase the yield from each hectare of crop. Additionally, lignocellulose can come from forest or municipal waste [28]. There is ~100 million dry tons of forest biomass and waste resource potential currently unused, ranging from forest trimmings to wood chips [30, 31]. With potential ethanol yields ranging from of 40-80 gallons/ton of biomass [28], 4-8 billion gallons of ethanol can be created from the underutilized resources alone, a significant fraction of the 16.1 billion gallons of ethanol produced in the US in 2018 [32].

### **1.2.2 Biomethanol production**

Unlike ethanol, methanol is traditionally synthesized from non-renewable sources. Fossil fuels are typically used to create syngas, which is then used to produce methanol via catalytic reactions at elevated temperatures and pressures. However, the syngas used to synthesize methanol can easily be created by gasifying any biomass, with little change to the actual production process. As a polar molecule, methanol is miscible with water and will absorb water during the production process. Unlike ethanol, methanol does not form an azeotrope with water, meaning no energy intensive dehydration process is required to fully dry the fuel [33].

In addition to the production of biomethanol from syngas derived from biomass, methanol can be produced as an *e-fuel*, from H<sub>2</sub> and CO<sub>2</sub> with the input of electricity [34]. Synthesizing methanol using renewable electricity is not only an energy dense way to store electricity, but also a more efficient means of storing hydrogen fuel [32, 34].

### **1.2.3 Biopropanol production**

1-propanol is generally produced via catalytic hydrogenation propionaldehyde, which itself is produced from ethylene sourced from fossil fuels [35]. Therefore, bio-1-propanol could be produced through biosynthesized ethylene. However, currently, the most economically viable pathway of ethylene biosynthesis is through catalytic conversion of bioethanol [36, 37]. Syngas fermentation can coproduce the C<sub>2</sub>-C<sub>4</sub> primary alcohols (ethanol, 1-propanol, and 1-butanol) in a mass ratio of 8:6:1 [38]. Metabolic

engineering of *Propionibacterium freudenreichii* has produced strains that produce 1-propanol from glycerol [38], while metabolic engineering of *Escherichia Coli* bacteria has produced strains that coproduce 1-propanol and 1-butanol in nearly equal quantities from glucose, via 2-ketoacid pathways [39]. In essence, this metabolic engineering allows a process, either fermentative or non-fermentative, to primarily produce alcohols other than ethanol from similar feedstocks. Therefore, the same arguments of feedstock generation discussed in Section 3.1 will apply here, and for all metabolically engineered micro-organisms.

2-propanol, the simplest *secondary (sec) alcohol*, has two main production methods: hydration of propylene and hydrogenation of acetone. Biosynthesis of 2-propanol currently has lower yields than that of other bio alcohols, since as a secondary alcohol, 2-propanol biosynthesis from micro-organisms use different chemical pathways than biosynthesis of primary alcohols. However, recent progress in metabolic engineering of *E. Coli* bacteria has shown promise in achieving high yields [40]. Alternatively, hydrogenation of biosynthesized acetone or coproduction with butanol and ethanol are viable bioproduction methods; for example, the conversion of acetone produced in acetone-butanol-ethanol fermentation (ABE, detailed in Section 1.2.4 to isopropanol via metabolic engineering of *Clostridium acetobutylicum* [42].

#### **1.2.4 Biobutanol production**

n-butanol and isobutanol are both primarily produced in large quantities by carbonylation of fossil fuel sourced propylene. 2-butanol, less commonly used, is currently produced by the hydration of fossil fuel sourced butene. n-butanol was first biosynthesized in the early 1900s via ABE fermentation of glucose by various strains of the bacteria family *Clostridium*. The ABE process effectively produces acetone, n-butanol, and ethanol in a 3:6:1 ratio from a variety of feedstocks. However, one of the largest challenges to overcome is the low butanol tolerance of *Clostridium*. To address this, continuous recovery of butanol during the fermentation process must occur [42].

Non-fermentative processes of biobutanol production exist using metabolically engineering bacteria, such as *E. Coli* [43, 44]. However, using yeast for biobutanol production has practical advantages over using bacteria [45]. As butanol is a natural byproduct of the fermentation of glucose by *Saccharomyces*

*cerevisiae* yeast, metabolic engineering can enhance these pathways and suppress ethanol production pathways to biosynthesize n-butanol, isobutanol, and 2-butanol [46]. Although this is promising, bacteria can synthesize biobutanol with yields near the theoretical limit, which cannot be said for yeast; therefore, a considerable amount of research is dedicated to increasing the yield of biobutanol from yeast [47, 48], including the utilization of xylose [49, 50]. Like 2-propanol, 2-butanol is a secondary alcohol, and therefore biosynthesis via micro-organisms requires more metabolic engineering than its' primary alcohol to maximize yields. Progress in both metabolic engineering of bacteria [46] and yeast [52] have yielded promising results in the biosynthesis of 2-butanol.

### **1.2.5 Higher Alcohols**

Effective biosynthesis of higher alcohols is achieved through a recursive elongation process, where the carbon chain length of a 2-ketoacid, the precursor to alcohol synthesized via the Ehrlich pathway [52, 54], is enzymatically increased with each iteration within a metabolically engineered micro-organism [55]. This method has been shown to biosynthesize most higher alcohols, including pentanol and its isomers [39, 56, 57], and straight chained primary alcohols [58], among others, using bioderived glucose as a feedstock.

All of the metabolically engineered microorganisms discussed for the biosynthesis of alcohols are currently at the research stage, having yet to be demonstrated on large scales. While both the technical and economic hurdles to overcome are significant, progress to this point has been made at an encouragingly high rate. Therefore, it is important for combustion research using a variety of alcohol fuels to continue in parallel so that when large-scale production is available, there is a use for the biofuel.

## **1.3 Alcohol Fuel Candidates**

### **1.3.1 C1-C4 Alcohols**

There are eight C1-C4 alcohols. Of them, seven are liquid at room temperature and are thus viable fuels. Tert-butanol is not liquid at room temperature and will therefore not be considered as a potential fuel for advanced combustion in this work. Going forward, the phrase C1-C4 alcohols refers to other seven alcohols. Since the RON and MON scales are created with respect to primary reference fuels with strong NTC



behavior, a high, positive octane sensitivity (RON – MON) implies that a fuel has little-to-no NTC behavior. The C1-C4 alcohols do not exhibit any NTC behavior. With the exception of n-butanol, they are single stage ignition fuels, primarily because cool flame reaction pathways essentially require at least a four-carbon chain alkyl group in the molecule [59]. Under high boost conditions, n-butanol displays some intermediate temperature heat release [60]; however, the ignition delay of n-butanol does not experience an NTC region [61]. The hydroxyl group of the alcohol acts as a radical chain terminating group following H-abstraction, which inhibits cool flame reactivity [62, 63]. This not only supports their lack of NTC behavior, but also results in their ability to suppress the NTC behavior of other fuels. As a result, the C1-C4 alcohols are often used as a blend stock in gasoline to improve anti-knock index (AKI) [64]. The high latent heat of vaporization of the C1-C4 alcohols also serves to both lower knock propensity and increase volumetric efficiency in production engines.

Having a fuel bound oxygen on a short-chained hydrocarbon results in a fuel with a lower energy density, a lower stoichiometric air fuel ratio, which further increases its' cooling potential (Eq. 1), and a lower sooting potential. The high cooling potential, low sooting potential, and lack of NTC behavior of the C1-C4 alcohols make them good candidates for lean-to-rich burn stratified combustion. In HCCI, the start of combustion of both methanol and ethanol showed little-to-no sensitivity to changes in equivalence ratio and high sensitivity to changes in intake temperature [65, 66]. Methanol has been shown to enable lean-to-rich burn stratified combustion in a heavy-duty engine, with all of the fuel injected during the compression stroke [67, 68] while ethanol has been shown to enable lean-to-rich burn stratified combustion in a light-duty engine using a split injection strategy [13, 69]. In an HCCI autoignition study with n-butanol and isobutanol, n-butanol showed similar  $\phi$ - and temperature-sensitivity to gasoline, including ITHR under boosted conditions, while isobutanol showed similar  $\phi$ - and temperature-sensitivity to ethanol [60]. This means that isobutanol is likely a better candidate to enable lean-to-rich burn combustion than n-butanol. Another factor to consider for the C1-C4 alcohols is water solubility. All of the C2-C4 (methanol excluded) alcohols form azeotropes during production. Since ethanol and both propanol isomers are completely

miscible with water, there are potential energy savings during production of these fuels if some amount of water is tolerable [70]. With lean-to-rich burn stratified combustion, this water in the fuel is actually advantageous, since the cooling potential of the fuel will increase, and the  $\phi$ -sensitivity of the fuel will be largely unchanged, an effect explored in a following section. This is with the caveat that the fuel will have a lower energy density and combustion efficiency can decrease if the water content in the fuel is too high; therefore, a balance must be found. For the three bio-synthesizable butanol isomers, their miscibility with water is lower than the water content found in their azeotrope – they only form a homogeneous azeotrope up to their miscibility limit, beyond which a heterogeneous azeotrope forms. This means that potential energy savings and cooling potential increases are limited for the pure butanol isomers.

### 1.3.2 C5+ Alcohols

As carbon number increases, the number of isomers increases exponentially, as chain branching occurs, e.g. octanol (C8) has 89 isomers. As a result, not all of the higher alcohols have well characterized fuel properties. The difference in fuel properties, such as heat of vaporization, between alcohols and alkanes with the same structure decreases as carbon number increases, as the effect of the hydroxyl group decreases. As the carbon chain increases, the ability of the hydroxyl group to suppress low-temperature alkyl-peroxyl radical isomerization reaction pathways and NTC behavior appears. This NTC behavior is seen with all of the C5+ alcohols with the exception of some pentanol isomers [70, 72]. For example, isopentanol, like n-butanol, showed some ITHR under boosted conditions but not enough to create significant NTC behavior that would result in the  $\phi$ -sensitivity needed to enable rich-to-lean burn stratified combustion [73]. Although at low boost levels, isopentanol could enable a lean-to-rich burn stratified combustion, its inability to control the heat release process at high boost levels makes isopentanol a poor candidate.

For the other higher alcohols, NTC behavior, and with it,  $\phi$ -sensitivity, increases as carbon number increases. Additionally, the cooling potential of alcohols decrease as carbon number increases, since the effect of the hydroxyl group weakens as the molecule grows. Therefore, higher alcohols become good candidates to enable rich-to-lean burn stratified combustion. However, as indicated by their octane

numbers, the autoignition resistance of the higher alcohols decreases significantly as carbon number is increased, which limits the compression ratio, and subsequently the efficiency, of the engine.

#### **1.4 TSCI with Wet Ethanol**

As a domestically source biofuel, finding a synergetic pairing with wet ethanol and an advanced combustion concept mode is highly desirable. Based on its fuel properties, wet ethanol is an excellent candidate to enable lean-to-rich stratified combustion. TSCI can be enabled by either the injection of a non-combustible liquid, like water [12], into a homogeneous mixture of fuel and air, or an injection of a high latent heat of vaporization fuel, like wet ethanol, using a split injection strategy (i.e., 70-90% of the total injected mass is injected during the intake stroke, while 10-30% of the total injected mass is injected during the compression stroke) [13]. The advantage of using a non-combustible liquid is that no equivalence ratio stratification is induced, which is important since locally rich and stoichiometric regions can produce soot and NO<sub>x</sub>, respectively. While TSCI with direct water injection has shown many promising results, including a high load limit of at least 8.4 bar compared to 3.6 bar in HCCI [12], this approach requires two injection systems and onboard water storage, which may be a potential drawback in certain applications.

Employing a water-fuel mixture in a split injection strategy allows TSCI to be enabled using a single injection system on completely production hardware. However, equivalence ratio stratification will be induced, coupled with increased thermal stratification. Therefore, it is important that the water-fuel mixture used has a high latent heat of vaporization and a low sensitivity to equivalence ratio. In previous work by the author using wet ethanol 80 in TSCI, a load range extension of over 300% was achieved compared to naturally aspirated HCCI [13]. When 1.8 bar of intake boost is used, the high-load limit of TSCI increased to the maximum rated load of the engine, 11 bar, while maintaining a healthy constraint on the maximum pressure rise rate in the cylinder IMEP<sub>g</sub>. This is illustrated in Figure 4.

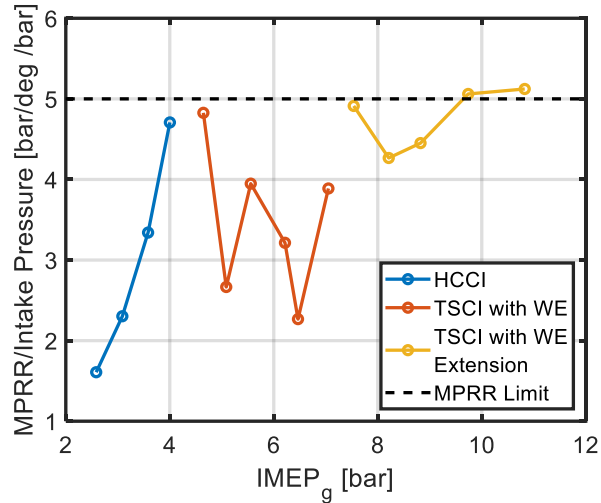


Figure 4: Maximum pressure rise rate (MPRR) normalized by intake pressure vs. gross indicated mean effective pressure (IMEP<sub>g</sub>) for the load range extension of HCCI using a split injection to enable TSCI. Adapted from Ref. [13], the additional extension shows that using an intake boost level of 1.8 bar, the high-load limit of TSCI increases to 11 bar, the maximum rated load of the engine

Compression stroke injections were found to fall into three categories: “early” (IVC to -100 deg aTDC), “mid” (-90 to -30 deg aTDC), and “late” (-20 deg aTDC and later) [74]. Early compression stroke injections do not significantly affect the level of thermal stratification in the cylinder; rather, the evaporative cooling they induce tends to simply lower the average in-cylinder temperature, providing a means to control the start of combustion. Mid-compression stroke injections can tailor the level of thermal stratification, thereby elongating the combustion process. It has been shown that multiple mid-compression stroke injections may be the most effective way to deliver fuel without excessively cooling regions targeted by the spray, which would negatively affect combustion efficiency [13]. Late compression stroke injections were found to be ineffective at retarding or elongating the combustion process.

Currently, all experimental data for TSCI with wet ethanol 80 has been collected on a light-duty, production geometry, diesel engine, with a re-entrant bowl piston and a solenoid-style direct injector whose included spray angle is 150°. A significant amount of the scope of work of this thesis, described in a following section, focuses on expanding on these promising preliminary results to gain a fuller understanding of TSCI with wet ethanol.

## 1.5 LTC Fuel Ratings

With next generation advanced LTC concepts showing promise as the future combustion strategy for internal combustion engines, there is a glaring need for a metric that describes the ignition propensity of fuels in LTC. The conventional combustion modes, SI and CDC, use octane number and cetane number, respectively, to describe the ignition propensity of fuels in their respective combustion modes. Next generation advanced LTC concepts would likely need at least two fuel metrics: one which describes the ignition propensity of the fuel and a second which describes how the heat release process would respond to induced stratification.

### 1.5.1 Ignition Propensity – Critical Compression Ratio

Octane index (OI), a metric designed to address the shortcomings of the traditional SI ignition propensity metrics, was amended and proposed as an ignition propensity metric for HCCI combustion research octane number (RON) and motor octane number (MON) [75, 76]. This HCCI OI is a function of the RON, MON, and octane sensitivity ( $S = \text{RON} - \text{MON}$ ) of a fuel, as well as an additional engine specific parameter,  $K$ . While the HCCI OI had some limited success, it was shown that this metric did not work well for all fuels [77]. Additionally, the requirement of an engine specific parameter is seen as a drawback.

To improve the HCCI OI, Shibata and Urushihara proposed a new metric, the absolute HCCI Index, which is a function of fuel composition (iso-paraffins, n-paraffins, olefins, aromatics, and oxygenates) in addition to either RON or MON [78]. Although this metric considered fuel composition, it still could not predict the HCCI ignition propensity of a wide array of fuels [79]. One critical shortcoming of these proposed HCCI fuel metrics is that they try to describe a fuel's HCCI behavior using an SI fuel quality metric. Knocking SI has vastly different operating conditions than HCCI, namely equivalence ratio and, in general, P-T trajectory. Further, the octane rating of a fuel is determined by the reading of a D1 knockmeter during knocking SI relative to the reading of a primary reference fuel (PRF), which is a blend of iso-octane and n-heptane. It has been shown that this knockmeter reading does not correlate well with any autoignition

based phenomena [79]. As a result, it is no surprise that an HCCI metric fuels based on octane number would have limited success.

Considering the need for an HCCI ignition propensity metric to be based on HCCI combustion data, Truedsson et al. proposed the Lund-Chevron HCCI number [79]. This metric is derived by measuring the *critical compression ratio* (cCR) of a fuel. The critical compression is defined as the compression ratio of an engine that results in a particular HCCI combustion phasing for a well-defined set of operating conditions. Specifically, in the first proposed work, the compression ratio that resulted in a CA50 (crank angle location of 50% mass fraction burned) of 3.0 deg aTDC with an equivalence ratio of 0.33 ( $\lambda = 3$ ) and an intake pressure of 1.0 bar (naturally aspirated). The critical compression ratio was found for multiple engine speeds, 600 rpm and 900 rpm, and multiple intake temperatures between 323 K and 423 K (50-150°C), meaning multiple critical compression ratios were found for each fuel. Once the critical compression ratio is found, the Lund-Chevron HCCI number can be determined by either bracketing or performing a regression analysis using a set of reference fuels.

If a set (or multiple sets) of operating conditions and reference fuels are standardized, the Lund-Chevron number has the potential to serve as an ignition propensity standard for LTC. Without reference fuels, the critical compression ratio still provides useful insight into the HCCI ignition propensity of fuels relative to each other. For example, for a set of gasolines of differing composition, the critical compression ratio correlated well with the intake temperature required to achieve a CA50 of 3.0 deg aTDC on a modern multimode engine [81].

### **1.5.2 Stratification Response – Normalized $\phi$ -Sensitivity**

To determine which fuels are the best candidates to enable either lean-to-rich or rich-to-lean burn stratified combustion, there needs to be some metric that different fuels can be compared with, like RON and MON is for spark ignition. Lopez-Pintor et al. first proposed normalized  $\phi$ -sensitivity as a metric to compare the  $\phi$ -sensitivity of different fuels [14], given by Equation 2:

$$\text{Normalized } \varphi - \text{sensitivity} = -\frac{1}{\tau} \frac{d\tau}{d\varphi} \quad (2)$$

where the partial derivative of ignition delay,  $\tau$ , with respect to  $\varphi$  is normalized by the negative of  $\tau$ . The minus sign is included so that the normalized  $\varphi$ -sensitivity will be positive, since ignition delay tends to decrease with increasing  $\varphi$ . As pointed out by Messerly et al., this definition depends inversely on  $\varphi$  [15]. To amend this, Messerly suggested a new definition of  $\varphi$ -sensitivity that is truly normalized, i.e. unitless, by multiplying Equation 2 by  $\varphi$ . This definition will be henceforth called the  $\varphi$ -normalized  $\varphi$ -sensitivity:

$$\varphi - \text{Normalized } \varphi - \text{sensitivity} = -\frac{\varphi}{\tau} \frac{\partial \tau}{\partial \varphi} = -\frac{\partial \log(\tau)}{\partial \log(\varphi)} \quad (3)$$

The work conducted in Ref. [14], which analyzed the  $\varphi$ -sensitivity of fuels using chemical kinetics in a constant volume reactor, did account for how changes in  $\varphi$  would result in changes in temperature due to evaporative cooling. Contrarily, Ref. [15] did not, justified by considered the low cooling potential of the fuels studied. Without considering evaporative cooling-driven changes in temperature, these metrics are useful to understand how staged the combustion process will be in a fuel inhomogeneous cylinder that is thermally isotropic. If the evaporative cooling driven changes in temperature are considered, the metric provides a more realistic prediction of  $\varphi$ -sensitivity of fuels employed in a rich-to-lean burn combustion mode. This is illustrated by the authors choice to use a total derivative in Equation 2 and a partial derivative in Equation 3. Using a total derivative, changes in temperature that result from changes in  $\varphi$  are accounted for and are functionally represented by the cooling potential equation (Equation 1). For a compression stroke injection of fuel that is injected into a combustion chamber that may have a non-zero  $\varphi$  at the time of injection, the coupled relationship between changes in temperature and changes in  $\varphi$  can be expressed by modifying Eq. 1 to produce the following equation:

$$\frac{dT}{d\varphi} = -\frac{h_{fg}}{(AFR_{stoich} + \varphi_{bg})C_p} \quad (4)$$

where  $\varphi_{bg}$  is the background equivalence ratio, i.e. the equivalence ratio of the charge before the compression stroke injection, and  $c_p$  is now the specific heat of the background fuel-air mixture. Note the minus sign in Equation 4, since the temperature will decrease from evaporative cooling. Either  $\varphi$ -sensitivity metric can be used with either a partial or a total derivative based on whether evaporative cooling is being considered. When evaporative cooling is considered, the total derivative of  $\tau(\varphi, T(\varphi))$ , with respect to  $\varphi$  is:

$$\frac{d\tau}{d\varphi} = \frac{\partial\tau}{\partial\varphi} + \frac{\partial\tau}{\partial T} \frac{dT}{d\varphi} \quad (5)$$

The total derivative is the sum of how the ignition delay changes with  $\varphi$  and how the ignition delay changes with the coupled change in temperature. If  $\frac{dT}{d\varphi}$  is negative, the ignition delay in rich regions will shorten and the charge will burn rich-to-lean. If  $\frac{dT}{d\varphi}$  is positive, the ignition delay in rich regions will lengthen and the charge will burn lean-to-rich.

When Messerly et al. proposed the  $\varphi$ -normalization of Equation 2 in Ref. [15], a primary motivation was to simplify the analytical solution of Equation 3 when  $\tau$  is given as an ignition delay correlation in the Arrhenius form:

$$\tau = Ap^\alpha \varphi^\beta \chi_{O_2}^\gamma \exp \frac{E'_a}{T} \quad (6)$$

where  $A$  is the pre-exponential coefficient,  $p$  and  $\alpha$  are pressure and its exponential coefficient, respectively,  $\varphi$  and  $\beta$  are equivalence ratio and its exponential coefficient, respectively,  $\chi_{O_2}$  and  $\gamma$  are the mole fraction of oxygen and its exponential coefficient, respectively,  $E'_a$  is the activation energy divided by the universal gas constant, and  $T$  is the temperature. If Eq. 3 is then evaluated using Eq. 6, the resulting normalized  $\varphi$ -sensitivity is simply  $-\beta$ , which is in principle a function of temperature and pressure that varies insignificantly over engine relevant conditions near ignition [15], meaning  $\varphi$ -normalized  $\varphi$ -sensitivity is not a function of  $\varphi$ . However, if Equation 3 is evaluated analytically using the total derivative  $\frac{d\tau}{d\varphi}$  instead of the partial derivative  $\frac{\partial\tau}{\partial T}$  to account for charge cooling,  $\varphi$ -normalized  $\varphi$ -sensitivity is now:



$$\varphi - \text{normalized } \varphi - \text{sensitivity} = -\frac{\varphi}{\tau} \frac{d\tau}{d\varphi} = -\beta + \frac{\varphi E'_a}{T^2} \frac{dT}{d\varphi} - \frac{\varphi \gamma}{\chi_{O_2}} \frac{d\chi_{O_2}}{d\varphi} \quad (7)$$

Note that in Equation 7, the term  $\frac{d\chi_{O_2}}{d\varphi}$  considers how  $\chi_{O_2}$  changes with changes in  $\varphi$ . There is no analogous pressure term since there is no cylinder pressure gradient induced, i.e. cylinder pressure remains uniform. Equation 7 illustrates that while normalizing  $\varphi$ -sensitivity by  $\varphi$  produces a unitless value, it does not remove the functional dependence of  $\varphi$ -sensitivity on  $\varphi$ . This equation also has a term with  $T^{-2}$  dependence, and within the term  $\frac{dT}{d\varphi}$  is  $c_p$ , which is a function of both  $\varphi$  and temperature. Equation 6 can also be used in Equation 2 to calculate a normalized  $\varphi$ -sensitivity:

$$N \varphi - \text{sen} = -\frac{1}{\tau} \frac{d\tau}{d\varphi} = \frac{-\beta}{\varphi} + \frac{E'_a}{T^2} \frac{dT}{d\varphi} - \frac{\gamma}{\chi_{O_2}} \frac{d\chi_{O_2}}{d\varphi} \quad (8)$$

Both normalized  $\varphi$ -sensitivity and  $\varphi$ -normalized  $\varphi$ -sensitivity are valuable tools to evaluate a fuel's ability to enable a stratified advanced combustion mode. In this work, the authors choose to use the metric normalized  $\varphi$ -sensitivity because this metric can directly provide information relative changes in ignition delay for a given cylinder condition, expressed as a fractional change. Normalized  $\varphi$ -sensitivity could then instead be multiplied by  $\Delta\varphi$ , producing a unitless value that describes how the ignition delay distribution in the combustion chamber changes with a level of stratification characterize by  $\Delta\varphi$  (a measure of the level  $\varphi$  stratification that exists in the cylinder). In principle, a fuel with a normalized  $\varphi$ -sensitivity double that of another fuel would require half the amount of stratification to achieve the same effect on the burn duration, thereby serving as a useful metric for describing a fuel's response to stratification in stratified LTC.

## 1.6 Objectives

The bio-synthesizability of alcohol fuels make them ideal candidates as an alternative fuel for the future. Their unique fuel properties may allow them to enable high-efficiency advanced combustion concepts with low engine-out emissions while minimizing life-cycle CO<sub>2</sub> emissions. The first set of objectives of this thesis include:

- Demonstrate that the high cooling potential of the alcohol fuels can be used to control the combustion phasing of HCCI, and by extension, advanced, stratified LTC modes by performing injection timing sweeps of wet ethanol during the intake stroke, using multiple injector spray angles.
- Further develop TSCI enabled by a split injection strategy with wet ethanol building upon my previous master's thesis work. Specifically, this PhD thesis will experimentally study the effects of various operating conditions and strategies on the effectiveness of a split injection of wet ethanol to provide cycle-to-cycle control over the heat release process, including:
  - Injection strategy
  - External exhaust gas recirculation (EGR)
  - Intake boost level
  - Injector included angle
  - Piston geometry

This is done on the light-duty diesel engine architecture with a centrally mounted injector on which TSCI with wet ethanol was first experimentally demonstrated.

- Experimentally demonstrate high-load LTC and control over thermal stratification on a light-duty gasoline engine architecture with a side-mounted gasoline direct injector (GDI) using wet ethanol.

Finally, the general use of biosynthesized alcohol fuels in advanced LTC is considered. The following set of objectives are considered:

- Experimentally characterize the LTC performance of the seven C1-C4 bio-synthesizable fuels in HCCI. Specifically, study the sensitivity of these fuels to  $\phi$ , intake temperature, intake pressure, residual rate, and engine speed.
- Evaluate two potential LTC fuel rating metrics, the critical compression ratio and the normalized  $\phi$ -sensitivity.

- Experimentally determine the critical compression ratios of the seven C1-C4 alcohol fuels at high temperature HCCI conditions using a cooperative fuel research (CFR) and correlate the critical compression ratios to traditional ignition propensity metrics (RON, MON, and cetane number (CN) ) and to HCCI data from the gasoline-engine architecture.
- Use ignition delay data from the literature to examine the normalized  $\phi$ -sensitivity of the candidate fuels and compare the results to data from the gasoline-engine architecture.

## **Chapter 2. Experimental Setup and Methodology**

The experimental work conducted for this thesis occurred on three different engines at three laboratories:

1. A light duty diesel engine architecture at Stony Brook University
2. A light-duty gasoline engine architecture at Clemson University
3. A CFR engine at Argonne National Laboratory

Experiments studying the role of injection system design, combustion chamber design, and in-cylinder charge conditions on TSCI and the effectiveness of compression stroke injections of wet ethanol as a heat release control mechanism were conducted on the diesel engine architecture at Stony Brook University. This experimental work was complimented through thermodynamic modeling. Experimental work characterizing the autoignition characteristics of the seven C1-C4 alcohol fuels were performed on the gasoline engine architecture at Clemson University. Additionally, lean-to-rich stratified combustion was experimentally studied on the gasoline engine architecture at Clemson University using wet ethanol and the seven C1-C4 alcohol fuels in their neat form. Finally, the critical compression ratio was measured on the CFR engine at Argonne National Laboratory.

### **2.1 Light Duty Diesel Engine Architecture Experimental Test Cell**

Experiments conducted on a light-duty diesel engine architecture took place conducted in the Advanced Combustion Laboratory at Stony Brook University. The engine consisted of a 4-cylinder production, diesel 1.7L General Motors/Isuzu engine head with one cylinder fully instrumented and mounted to a Ricardo Hydra engine block. The other three cylinders deactivated. Two pistons are used in this study: 1) a re-entrant bowl piston geometry found in production for light-duty diesel engines, and 2) a custom-made open shallow bowl piston. CAD models of the re-entrant bowl piston and shallow bowl piston are shown in Figure 5 and Figure 6, respectively . The custom-made piston was designed to have the same compression ratio as the production re-entrant bowl piston,  $16.0 \pm 0.5$ . The geometry of the piston was designed based on results from other researchers that found that the combustion efficiency and emissions characteristics of low temperature combustion improved with the employment of an open, shallow bowl piston geometry.

Intake and exhaust manifolds are custom made to seal against the single cylinder. The engine is coupled to an active GE dynamometer and has an oversized flywheel to help maintain engine speed. The production camshafts are designed with 12 degrees of positive valve overlap and were not modified. There are two intake and two exhaust valves. Valve timings are shown in Table 1, along with engine geometry. The Stony Brook experimental test cell is shown in Figure 5.

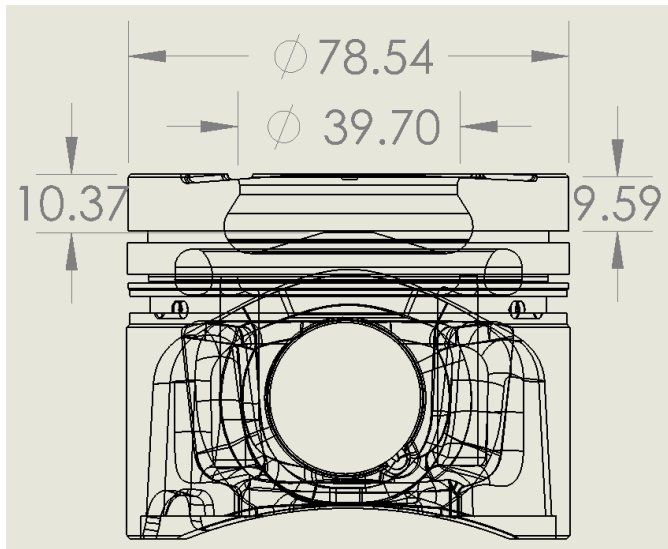
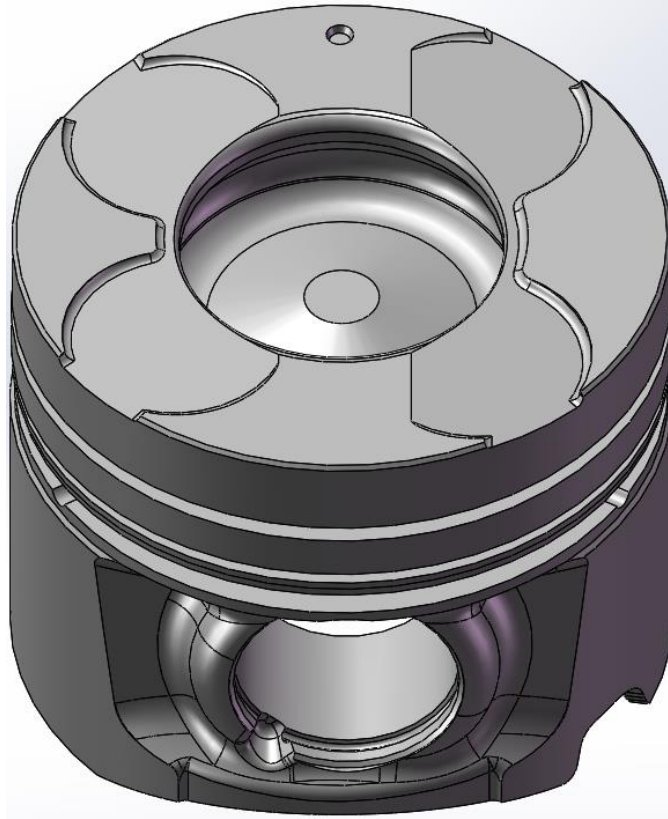


Figure 5: 3D CAD model (top) and 2D sketch (bottom) of production re-entrant bowl piston.

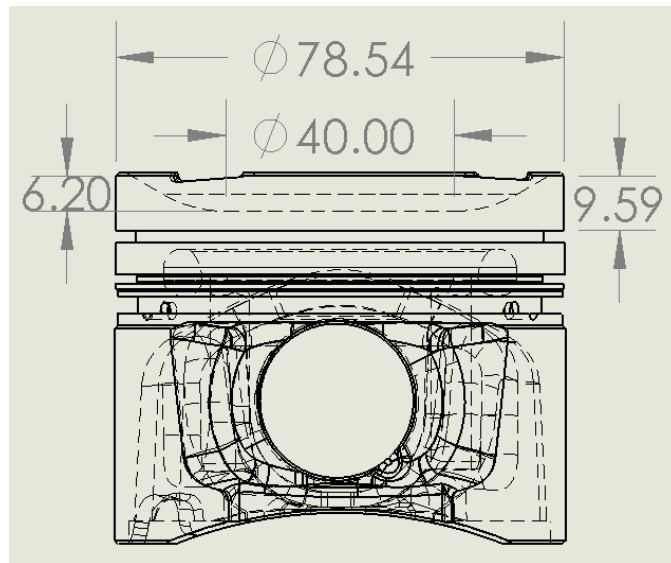
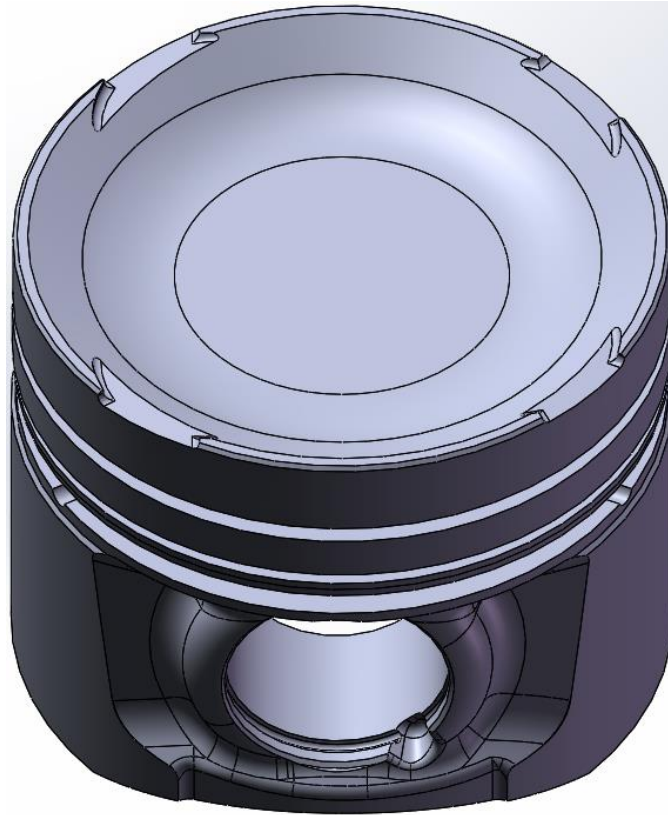


Figure 6: 3D CAD model (top) and 2D sketch (bottom) of custom-made shallow bowl piston.

Table 2: Engine geometry and valve timings for the light-duty diesel engine architecture engine at the Advanced Combustion

Laboratory at Stony Brook University

Engine Displacement	[cc]	421.5
Compression Ratio	[-]	16.0
Stroke	[mm]	86
Bore	[mm]	79
IVO	[deg bTDC]	366
IVC	[deg bTDC]	146
EVO	[deg aTDC]	122
EVC	[deg aTDC]	366

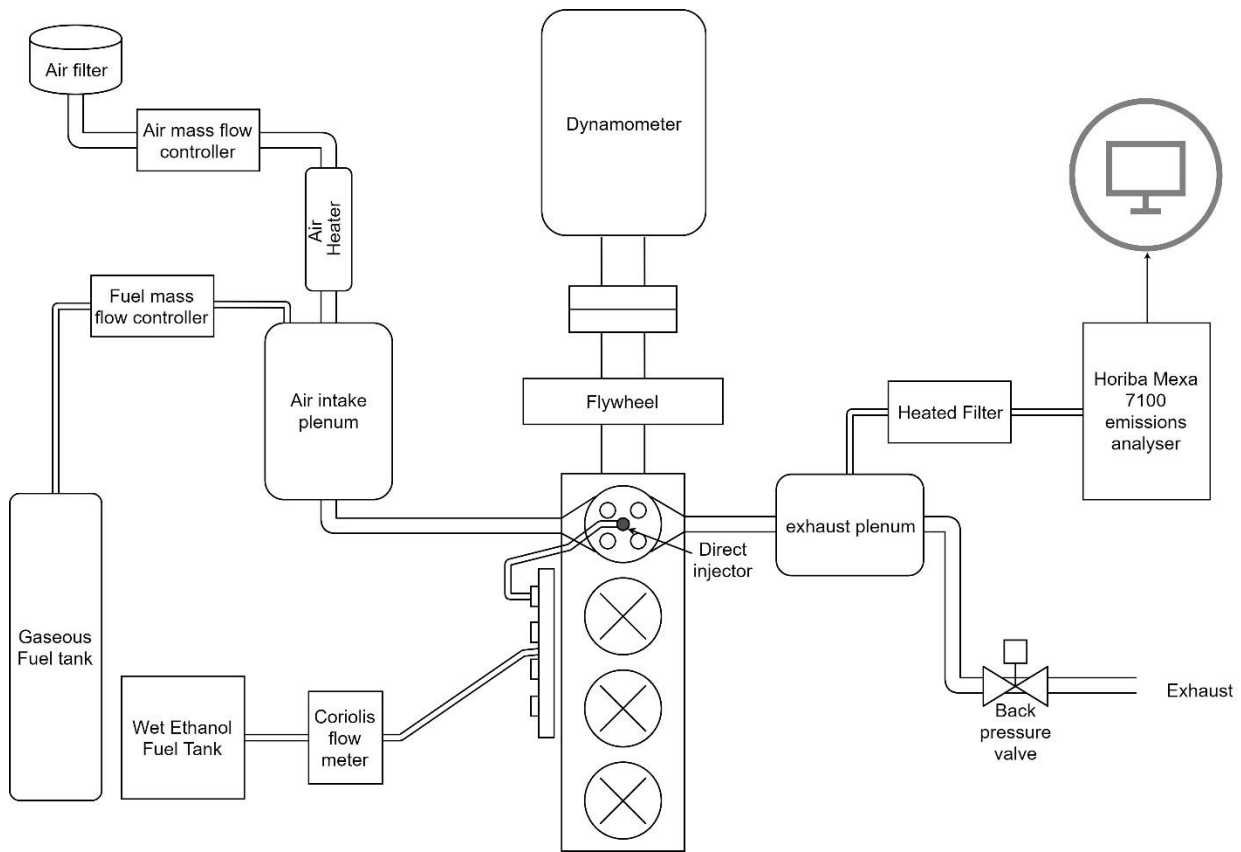


Figure 7: Experimental test cell schematic of the light-duty diesel engine architecture engine at the Advanced Combustion

Laboratory at Stony Brook University

Wet ethanol 80, 80% ethanol and 20% water by mass, is the fuel considered on this engine. The fuel system is a production high pressure diesel common rail system, employing a Bosch CP3 pump and a Bosch solenoid style injector. Three injector tips are considered: Bosch part number DLLA150P (150° included



spray angle), DLLA118P (118° included spray angle), and DLLA60P (60° included spray angle). An illustration of the definition of spray included angle is given in Figure 8. Normally, the diesel fuel in the fuel system serves as the lubricant for the fuel pump and injector. To ensure the longevity of the fuel system components, a lubricity additive (Infineum R655) is blended into the wet ethanol 80 at a concentration <500ppm. The combustion characteristics of wet ethanol 80 with and without the lubricity additive were found to be effectively identical in a previous study, meaning the lubricity additive does not appreciably affect the fuel properties of wet ethanol 80 at the concentrations used in this study.

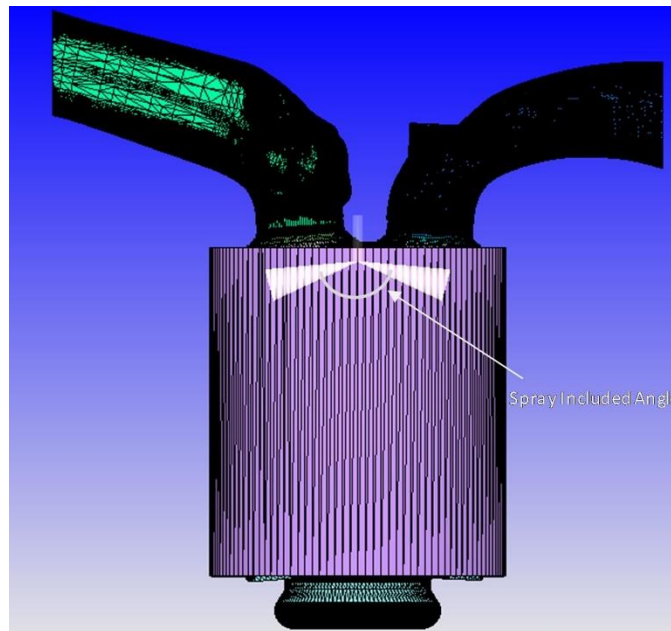


*Figure 8: Illustration of the definition of spray included angle.*

Data acquisition and engine control are provided by a custom-built LabView code. Four high-speed pressure transducers are instrumented on this engine: 1) in-cylinder, 2) intake manifold, 3) exhaust manifold, and 4) fuel rail. Fuel flow is measured through a Coriolis flow meter while air flow is measured through a laminar flow element. Low-speed measurements, such as thermocouples, are recorded at a rate of 0.5 Hz while high-speed measurements like in-cylinder pressure, are coupled to an encoder which measures crank angle every 0.1°. A Horiba MEXA 7100-DEGR measures engine exhaust composition, including CO, CO<sub>2</sub>, O<sub>2</sub>, NO<sub>x</sub>, and unburned hydrocarbons (uHC). It has been shown that a flame ionization

detector (FID) has a lower response ratio to measuring unburned, oxygenated organic species, like ethanol. Therefore, a correction factor of 1.2 must be applied to uHC measurements for wet ethanol 80, i.e. uHC measurements are multiplied by 1.2 [82]. Table 3 displays the model, range, and instrument uncertainty for each instrument used.

Constant operating conditions that were used in this study include fuel injection pressure, which is held at 500 bar, engine speed, which is held at 1200 RPM using a GE 30 hp active dynamometer, and intake pressure, which is naturally aspirated. At each operating condition, 300 consecutive cycles are recorded under steady state operation and a custom MATLAB code performs heat release and uncertainty analysis, following the procedures outlined in a following section.

*Table 3: Model, range, and instrument uncertainty for each instrument used.*

Model	Used For	Range	Uncertainty
Alicat MCRWH-1000	Air Flow Control and Measurement	0 - 1000 SLPM	$\pm(0.4\%$ of reading + 2 SLPM)
Micrometer CMFS007	Fuel Flow Rate	0 - 11.36 g/s	$\pm 0.05\%$ of reading
K-type Thermocouple	Temperature	75 - 1200 K	$\pm 0.4\%$ of reading
Ohaus CL 2000	Blending Fuel	0 - 2000 g	$\pm 1.0$ g
Kistler 6041A	Cylinder Pressure	0 - 250 bar	$\pm 1.25$ bar
Kistler 4011A	Intake Pressure	0 - 5 bar	$\pm 0.025$ bar
Kistler 4049B	Exhaust Pressure	0 - 5 bar	$\pm 0.015$ bar
Horiba MEXA 7100 uHC	uHC Emissions Analyzer	0 – 10000 ppm	$\pm 100$ ppm
Horiba MEXA 7100 CO	CO Emissions Analyzer	0 – 5000 ppm	$\pm 50$ ppm
Horiba MEXA 7100 NO <sub>x</sub>	NO <sub>x</sub> Emissions Analyzer	0 – 200 ppm	$\pm 2$ ppm
Horiba MEXA 7100 O <sub>2</sub>	O <sub>2</sub> Emissions Analyzer	0 – 18%	$\pm 0.18\%$
Horiba MEXA 7100 CO <sub>2</sub>	CO <sub>2</sub> Emissions Analyzer	0 – 5%	$\pm 0.05\%$

## 2.2 Light-Duty Gasoline Engine Architecture Experimental Test Cell

Experiments performed on a light-duty gasoline architecture were conducted on a single-cylinder research engine consisting of a Ricardo Hydra engine block with a pent-roof head and a centrally mounted spark

plug and dual overhead camshafts at the Clemson University International Center for Automotive Research. The cam profiles were custom-made to enable exhaust rebreath, i.e., opening the exhaust valve during the intake stroke to allow large amount of hot exhaust gases to re-enter the cylinder. The engine is maintained at 1200 RPM or 2400 RPM in this work. Engine geometry and valve timings of this engine are displayed on Table 4.

*Table 4: Engine geometry and valve timings for the light-duty gasoline architecture engine at Clemson University International Center for Automotive Research.*

Engine Displacement	[cc]	549.5
Compression Ratio	[-]	13
Stroke	[mm]	94
Bore	[mm]	86
Connecting Rod Length	[mm]	152.2
Engine Speed	[RPM]	1200/2400
IVO	[deg aTDC]	-374
IVC	[deg aTDC]	-150
EVO	[deg aTDC]	130
EVC	[deg aTDC]	368
EVO rebreath	[deg aTDC]	-340
EVC rebreath	[deg aTDC]	-171

The fuel system consists of a hydraulic accumulator, which uses pressurized nitrogen to maintain a constant fuel pressure, and two gasoline direct injectors. One of the injectors is side-mounted in the cylinder while the other is mounted in a fuel vaporizer upstream of the intake plenum, which is used to fully premix the fuel and air before entering the cylinder, eliminating any thermal or compositional stratification induced by the direct injection of fuel. The injectors used are single-hole, hollow-cone injectors with a spray angle of 70 degrees. The fuel injection pressure was maintained at a constant pressure of 100 bar.

A custom-built LabView code serves as both the data acquisition and engine control unit for this test cell. As a data acquisition system, this code measures in-cylinder pressure, intake manifold pressure, and exhaust manifold pressure triggered by a crank-angle encoder with a resolution of 0.1° and records all low-speed measurements at a rate of 1.0 Hz. A five-gas emissions analyzer (Horiba MEXA 7100-DEGR) is used to measure exhaust composition, including CO, CO<sub>2</sub>, O<sub>2</sub>, NO<sub>x</sub>, and unburned hydrocarbons. The

uHC output of the emissions bench is scaled to account for the lower response ratio of a flame ionization detector (FID) to unburned, oxygenated organic species like ethanol [82]. As an engine control unit, this code actuates the injectors and the spark plug. In addition, electronic valves are controlled in the intake, exhaust, and EGR line to precisely control the boost level and residual gas fraction in the cylinder. A schematic of the experimental test cell can be found in Figure 9.

Three hundred consecutive cycles are recorded under steady-state operation at each operating condition. These cycles are individually processed with a custom MATLAB heat release and uncertainty analysis script described in a following section.

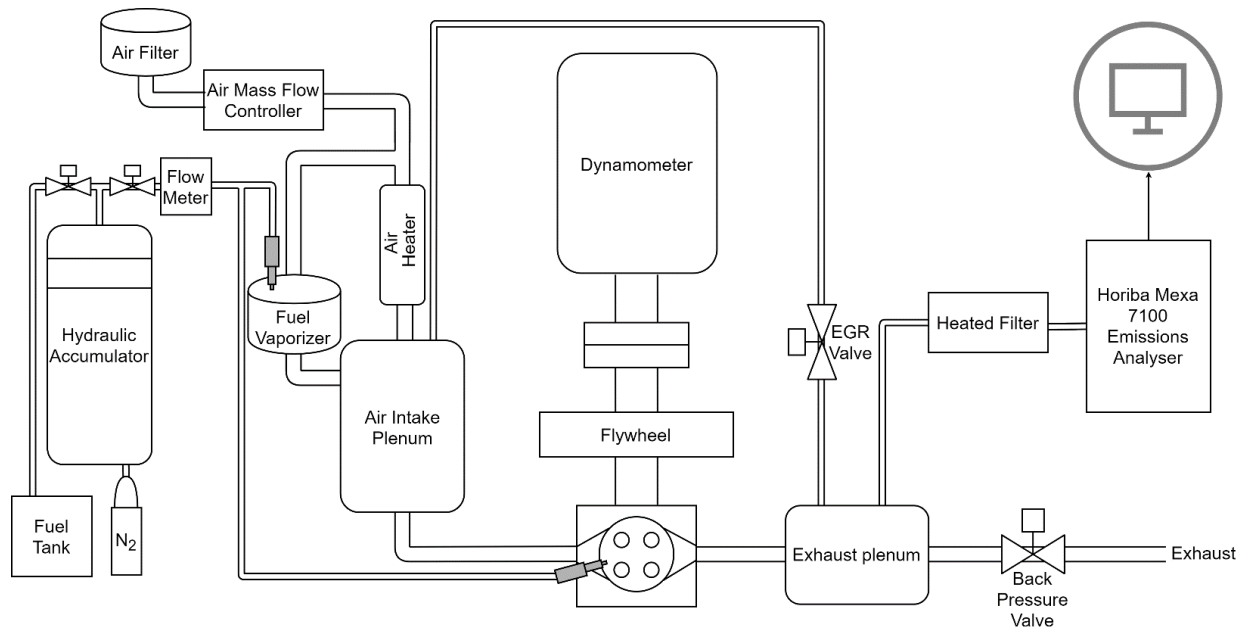


*Figure 9: Experimental test cell schematic of the light-duty gasoline engine architecture at Clemson University International Center for Automotive Research (CU-ICAR).*

### 2.3 CFR Engine Experimental Test Cell

A fully instrumented Waukesha CFR F1/F2 octane rating engine at Argonne National Laboratory is used to experimentally measure the critical compression ratio. The engine is equipped with two cylinder pressure transducers, an intake pressure transducer, and an exhaust pressure transducer that are coupled to a crank

angle encoder to provide crank-angle resolved pressure measurements. The engine is carbureted, with fuel flow manually controlled via the height of the carburetor bowl. Downstream of the carburetor, a MON mixture air heater is mounted to maintain a constant charge temperature entering the cylinder. The exhaust is equipped with an oxygen sensor and an AVL five-gas emission bench that are used to determine the operating equivalence ratio of the engine. The compression ratio is varied using the CFR engine's compression ratio motor, which drives a worm gear that moves the cylinder head up and down, varying the clearance volume of the engine, thereby changing the compression ratio. The correlation between cylinder head height and compression ratio was calibrated using both in-house measurements and ASTM standards.

## **2.4 Heat Release Analysis**

When performing a heat release analysis on experimental data, each cycle is processed individually. The results are then ensemble averaged. While this is more computationally expensive than ensemble averaging the data before processing, it provides a more realistic depiction of the uncertainty, which will be discussed in the following section. During the processing of each cycle, any value that measured on a low-speed basis is taken as the average of the low-speed data.

The measured pressure traces are passed through a low-pass filter to filter out signal noise. The piezoelectric high-speed cylinder pressure transducer does not measure pressure on an absolute scale – it must be pegged to a known value. The cylinder pressure transducer is pegged to the average piezoresistive intake pressure read by the pressure transducer between -190 and -170 deg aTDC. The internal residual trapped mass is calculated by using the ideal gas equation of state, knowing the pressure in the cylinder at intake valve closing (IVC), the intake and exhaust temperatures, and the total amount of fresh charge that has entered the cylinder, while estimating the fraction of the cylinder volume at IVC by subtracting the fraction of the cylinder volume at IVC from the total IVC cylinder volume. The net heat release rate (NHRR) is calculated during the closed portion of the cycle using the following equation, derived from the first law of thermodynamics employing the ideal gas equation of state:

$$\frac{dQ_i}{d\theta} = \frac{\gamma_i P_i \frac{dV_i}{d\theta} + V_i \frac{dP_i}{d\theta}}{\gamma_i - 1} \quad (9)$$

Where  $\frac{dQ_i}{d\theta}$  is the NHRR,  $\gamma_i$  is the ratio of specific heats,  $P_i$  is the cylinder pressure and  $V_i$  is the cylinder volume. The gross heat release rate (GHRR) is then calculated by adding heat transfer, estimated using the Hohenberg heat transfer correlation [83], and crevice losses, estimated by following the procedure outline in Heywood [84], to the NHRR. Energy closure is used to scale the heat transfer such that the total calculated heat release of the cycle equals the total heat release of the cycle, as calculated by the total fuel in the cylinder multiplied by the combustion efficiency. The combustion efficiency is calculated using the emissions data:

$$\eta_c = 1 - \frac{m_T}{m_f Q_{LHV,f}} \sum_{i=1}^n \Delta x_i Q_{LHV,i} \quad (10)$$

Where the values  $x_i$  and  $Q_{LHV,i}$  are the mass fractions and lower heating values of unburned fuel components such as H<sub>2</sub>, CO, or unburned Hydrocarbons (uHC). The gross heat release rate trace is then integrated and normalized to produce a mass fraction burned curve. The crank angle location of any point,  $x$ , on the mass fraction burned curve is called CA $x$ .

## 2.5 Uncertainty Analysis

Uncertainty analysis is vital to quantifying the uncertainty in measured data. Performing uncertainty analysis for experimental engine research presents unique challenges due to the multiple and varied parameters measured, the signal conditioning performed, and the large number of data points collected. Additionally, it can often be difficult to separate experimental uncertainty from physical phenomena due to cycle-to-cycle variations of the combustion process. Because the potential efficiency or emissions improvements of one technology over another may be small, it is critical to quantify uncertainty when reporting experimental results.

*The Guide to the Expression of Uncertainty in Measurement* (GUM) [85] is the official standard regarding uncertainty analysis. As the title implies, however, the GUM is only a *guide*; it does not provide solutions for all possible situations, and is, in fact, sparse in those aspects of uncertainty measurement specific to experimental engine research. Two popular methods of propagating uncertainty include *statistical* and *Monte Carlo* approaches. The statistical approach, outlined in the GUM, and later in this paper, establishes functional relationships to propagate probabilities, with the end resulting in uncertainty expressed as interval and confidence level. Contrarily, the Monte Carlo approach, outlined in an addendum to the GUM [86], is an empirical approach that uses many random simulated measurements to create a probability density function of the desired measurement variation.

The Monte Carlo approach is preferred in some applications [87, 88], as it provides insight into the nature of the uncertainty via the probability density function. In addition, the functional dependence of the input and output variables is not required. However, a significant disadvantage of the Monte Carlo method is the large number of trials needed to produce accurate results. When applied to experimental engine research, this results in a large number of simulated engine cycles that require post-processing. Figure 10 is an example of the convergence of the standard deviation of the Monte Carlo approach to the standard deviation of the statistical approach with an increase in the number of trials. When sophisticated post-processing methods are employed, including subroutines for determining mixture properties and heat transfer correlations, the computational expense of the Monte Carlo approach may become excessively high.

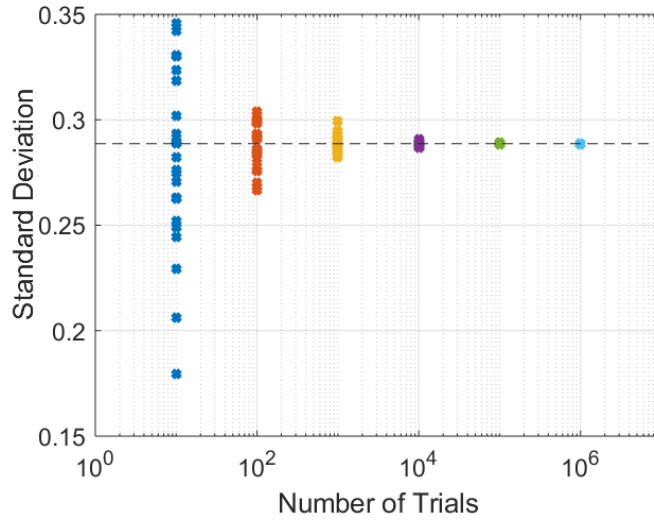


Figure 10: The resulting standard deviation of 25 individual Monte Carlo simulations are performed with 10, 100, 1,000, 10,000, 100,000 and 1,000,000 trials. The spread of standard deviations is compared with a reference line, at  $y=2.89$ , that depicts the standard deviation derived from a statistical approach.

In this work, the traditional statistical approach is applied to experimental combustion post-processing techniques. Throughout the uncertainty propagation, sensitivities to various parameters are examined, and the parameter relationships are reduced in the context of engine research. Based on the knowledge gained and the down-selection of the relevant terms, a set of best practices for post-processing and quantifying the uncertainty in experimental combustion data is obtained and used for the uncertainty analysis of the data in this work.

### 2.5.1 Statistical Background

The variance,  $\sigma_x^2$ , of a set of measurements,  $\{x\}$ , is described by Equation 11, where the brackets “ $\langle \rangle$ ” and the overbar notation denote the mean.

$$\sigma_x^2 = \langle (x - \bar{x})^2 \rangle = \overline{x^2} - \bar{x}^2 \quad (11)$$



The variance is equal to the square of one standard deviation of the set of measurements if the set can be described as gaussian. Another important parameter,  $\sigma_{xy}$ , is the *covariance* between two sets of measurements,  $\{x\}$  and  $\{y\}$ . The covariance describes how changes in one measurement affect changes in the other. If  $x$  and  $y$  are completely independent measurements, their covariance will equal zero. Note that the covariance will only equal zero when the population of a set approaches infinity; thus, covariance may be non-zero for independent measurements of finite set sizes – this should be negligible in size and ignored during uncertainty propagation. Equation 12 describes the covariance of  $\{x\}$  and  $\{y\}$ .

$$\sigma_{xy} = \langle (x - \bar{x})(y - \bar{y}) \rangle = \overline{xy} - \bar{x}\bar{y} \quad (12)$$

A statistical approach is employed to derive the equations for uncertainty propagation. For example, when  $z = ax + by$  and  $a$  and  $b$  are constants (note:  $\langle ax + by \rangle = a\langle x \rangle + b\langle y \rangle$ ), the variance in  $z$ ,  $\sigma_z^2$ , can be related to the variance in  $x$ ,  $\sigma_x^2$ , and the variance in  $y$ ,  $\sigma_y^2$ , by taking Equation 11, and deriving Equation 13:

$$\begin{aligned} \sigma_z^2 &= \langle (z - \bar{z})^2 \rangle = \langle (ax + by - a\bar{x} - b\bar{y})^2 \rangle \\ &= \langle a^2x^2 + b^2y^2 + a^2\bar{x}^2 + b^2\bar{y}^2 + 2ab(xy + \bar{x}\bar{y}) - 2(ax + by)(a\bar{x} + b\bar{y}) \rangle \\ &= a^2(\overline{x^2} - \bar{x}^2) + b^2(\overline{y^2} - \bar{y}^2) + 2ab(\overline{xy} - \bar{x}\bar{y}) \\ &= a^2\sigma_x^2 + b^2\sigma_y^2 + 2ab\sigma_{xy} \end{aligned} \quad (13)$$

A common method of uncertainty propagation is the root sum square method. Equation 3 simplifies to the root sum square method if the covariance between  $x$  and  $y$  is zero.

If  $z = f(x, y)$ , the uncertainty  $\Delta z$  may be related to the uncertainty in  $\Delta x$  and  $\Delta y$  using a first-order Taylor series expansion, provided that the step size is small. In uncertainty propagation, this means that the relative uncertainty in  $x$  is small, resulting in a near-linear functional relationship:  $\Delta z \approx \partial_{z,x}\Delta x +$

$\partial z_y \Delta y$  where  $\partial z_x$  is the partial derivative of  $z$  with respect to  $x$ . The authors found the linearity of all of the functions analyzed in this study were greater than 99% for the range of  $\Delta x$  explored in this work. The partial derivatives are referred to as the *sensitivity coefficient* of  $z$  to changes in  $x$ . Equation 13 can be generalized for a function of  $n$  variables:

$$\sigma_z^2 = \sum_{i=1}^n \partial z_{x_i}^2 \sigma_{x_i}^2 + 2 \sum_{i=1}^{n-1} \sum_{j=i+1}^n \partial z_{x_i} \partial z_{x_j} \sigma_{x_i x_j} \quad (14)$$

In Equation 14, the first summation term corresponds to the root sum square method, while the second double summation term corresponds to the covariance between each input variable. If the input variables are uncorrelated, the second term vanishes, and the equation becomes the root sum square method.

### 2.5.2 Error Classification

Measurement error consists of both *bias* and *random* error. Bias error represents a fixed error while random error averages to zero as the number of samples increases. The uncertainty of a measurement provides an interval about the mean and a confidence level that subsequent measurements will fall within this interval. Error is introduced into measurements by both error in the measurement instruments and from the test environment.

*Instrument error* includes linearity, hysteresis, and repeatability. *Linearity* is associated with instruments whose output is linearly proportional to input and represents the maximum error between the best fit line and the true value. *Hysteresis* is the difference in the measurement of two identical systems, one whose former state had a lower measurement value and one whose former state had a higher measurement value. *Repeatability* is the ability of a measurement device to repeatedly report the same value for an unchanging state, i.e., its precision. This error is captured experimentally through the measurement uncertainty.

Manufacturers may report these uncertainties individually or collectively, sometimes referred to as LHR uncertainty. If reported individually, an overall instrument uncertainty may be obtained using the root

sum square method above, since the covariance for these uncertainties is always zero. Instrument *bias* error, if present, must be eliminated through calibration.

When propagating uncertainty, it is important that all the uncertainties considered have the same level of confidence. As per the GUM [85], the *standard* uncertainty is defined as being the standard deviation of the set of measurements, which is the square root of the variance. The *expanded* uncertainty is the standard uncertainty multiplied by a coverage factor. For example, to provide a level of confidence of 95%, a coverage factor of  $\sim 2$  is used for a large ( $\geq 60$  samples) gaussian dataset. For sample sizes less than 60, the coverage factor is increased slightly to accommodate the additional uncertainty associated with few measurements, with the *student-t* distribution typically used [85]. In this work, all reported uncertainties are expanded uncertainties with a confidence level of 95%, and are denoted with the notation  $\Delta x$ .

The instrument uncertainty reported by a manufacturer may or may not have an associated confidence level. If there is no reported confidence level, one can be assumed. This assumed confidence level should not be exceedingly high – here a confidence level of 95% is assumed when not given by the manufacturer [85].

### **2.5.3 Uncertainty Propagation**

When considering a statistical approach to the uncertainty, however, ensemble-averaging of the cylinder pressure trace should *not* be performed. If an ensemble-averaged pressure trace is created, measurement uncertainty of the cylinder pressure must be accounted for. Due to cyclic variability, the uncertainty in cylinder pressure near ignition will become extremely high. This can be seen in Figure 11, where 300 consecutive cycles, the ensemble-averaged pressure trace, and the measurement uncertainty of the ensemble-averaged cylinder pressure are shown. This uncertainty will affect the uncertainty in heat release and produce unrealistic results.

Instead, each cycle should be post-processed individually, creating an uncertainty profile for each cycle. Then, the uncertainty profiles of each cycle can be combined to create a total uncertainty profile. This results in a more realistic uncertainty profile while also eliminating the covariance terms that would

arise from the propagation of cylinder pressure measurement uncertainty. Although processing each cycle individually incurs a higher computational cost, this method is still significantly less computationally expensive than using a Monte Carlo approach.

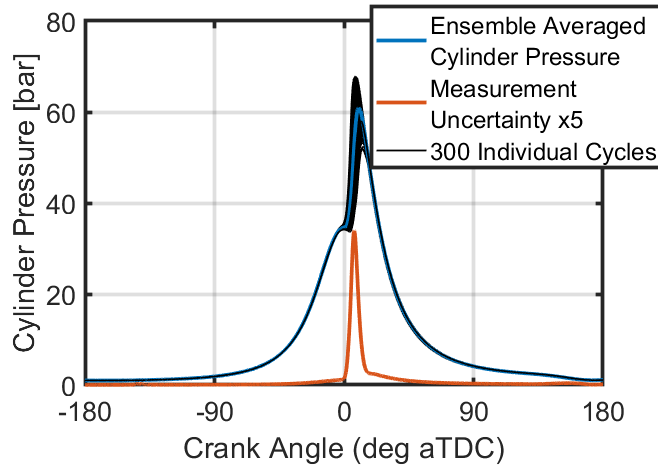


Figure 11: Ensemble averaged cylinder pressure trace superimposed over 300 individual cycles with a measurement uncertainty trace in cylinder pressure (scaled x5) showing high uncertainty in cylinder pressure near ignition due to cycle-to-cycle variations.

Once all uncertainties of measured quantities are accounted for, uncertainty propagation may begin by using the uncertainty tree. Uncertainty trees, proposed by Longtin [88], are used to capture graphically uncertainty propagation in the post-processing of experimental combustion data. A desired uncertainty in a variable  $x$ ,  $\Delta x$ , is found by propagating the precursor uncertainties through the appropriate functional relationships. Each precursor uncertainty is represented as a branch of the uncertainty tree, with  $\Delta x$  at the top of the tree. If an uncertainty is known, such as instrument uncertainty, that branch of the tree is terminated with a double underline. Subscripts *instr* and *meas* represent total instrument uncertainty and measurement uncertainty, respectively. The inverted triangular symbols are links to additional uncertainty trees below on the same branch. Equation 14 is used at each juncture to combine uncertainties. Examples of uncertainty trees are given in Figure 12 and Figure 13.

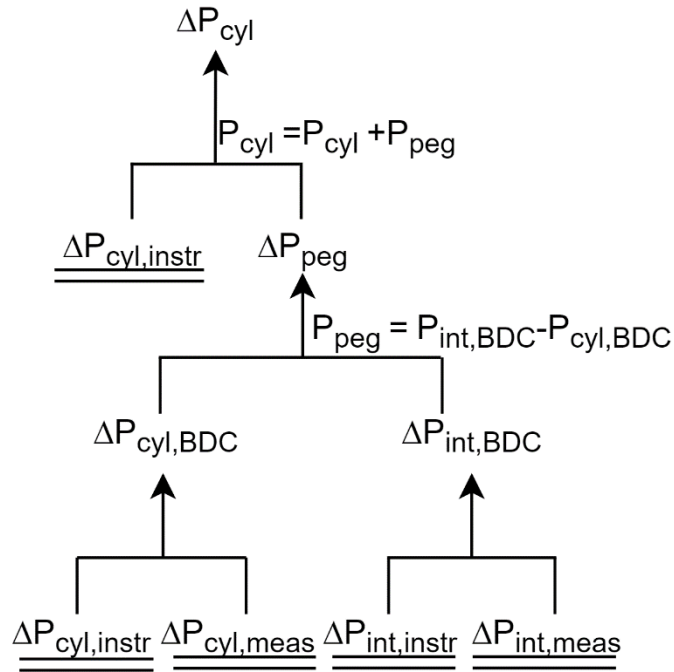


Figure 12: Cylinder pressure uncertainty tree.

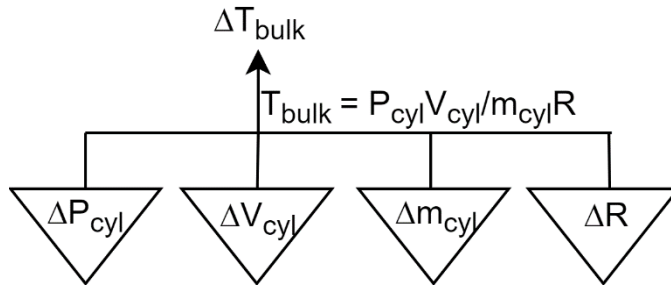


Figure 13: Bulk temperature uncertainty tree.

To determine if any other branches can be trimmed, the square of the sensitivities of each branch must be compared. For example, the square of the sensitivity of  $T_{bulk}$  to pressure, volume, and mass are shown in Figure 14. Determining the uncertainty in mass requires combining the uncertainties of measured air and fuel flow with the uncertainty in internal residual gas fraction.

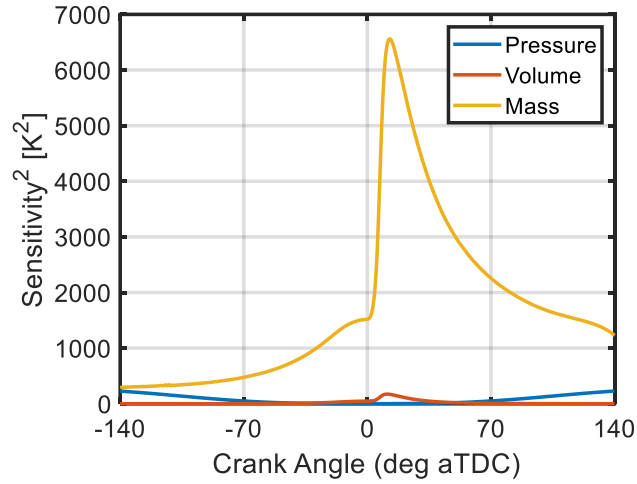


Figure 14: Square of sensitivity of bulk temperature to pressure, volume, and in-cylinder mass.

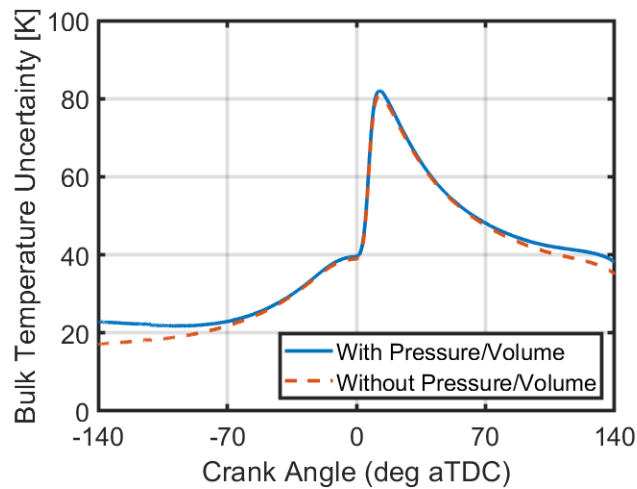


Figure 15: Comparison of bulk temperature standard uncertainty including or excluding pressure and volume terms. From this, it is clear that for most of the cycle, including during heat release, there is no significant loss of information by ignoring pressure and volume uncertainty.

With the exception of the very early period in the compression stroke, the square of the sensitivity of in-cylinder mass dwarfs that of pressure and volume.  $T_{bulk}$  is used for determining mixture properties for accurate heat release calculations and for estimating heat transfer losses, meaning the very early period of the compression stroke is not of interest. The pressure and volume branches may thus be trimmed. To

further demonstrate that pressure and volume are insignificant to the uncertainty in  $T_{bulk}$ , Figure 15 shows a  $T_{bulk}$  standard uncertainty trace with and without including pressure and volume uncertainty during uncertainty propagation.

If two branches are trimmed, then their covariance may also be omitted. If, however, only one of the two branches involved in a covariance term is trimmed, the covariance term may not be immediately eliminated. Rather, another sensitivity analysis must be performed. As mentioned earlier, if an uncertainty analysis is performed on each individual cycle, there will not be a set of measurements at each crank angle increment; thus, there will be no covariance between any term measured or calculated on a high-speed basis. Therefore, no covariance terms need to be accounted for in calculating the uncertainty of  $T_{bulk}$ . The trimmed uncertainty tree is shown in Figure 16. This illustrates how one term can dominate the uncertainty propagation. When that happens,  $\Delta z^2 = (\partial z_x \Delta x)^2$ .

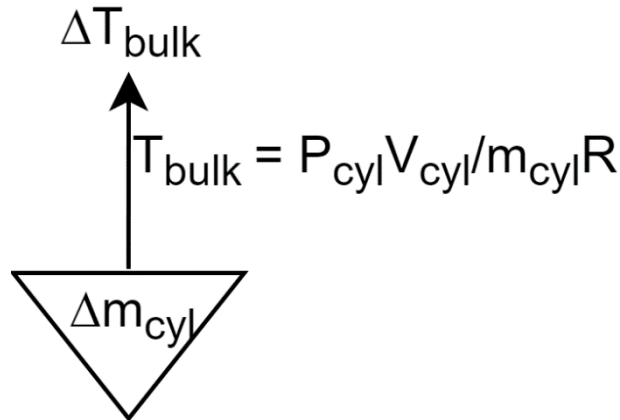


Figure 16: Bulk temperature uncertainty tree after trimming unnecessary branches.

The following set of equations are used propagate the uncertainty throughout the cycle:

$$\Delta P_i^2 = \Delta P_{int,BDC}^2 + \Delta P_{BDC}^2 + \Delta P_{instr}^2 \quad (15)$$

where  $\Delta P_{int,BDC}$ ,  $\Delta P_{cyl,BDC}$ , and  $\Delta P_{instr}$  are the uncertainty in the intake pressure at BDC, the cylinder pressure at BDC, and the instrument uncertainty, respectively, of the cylinder pressure transducer.

$$\Delta V_{cyl,i}^2 = \left( \frac{\partial V_{cyl,i}}{\partial \theta} \Delta \theta_i \right)^2 + \left( \frac{V_d}{(CR-1)^2} \Delta CR \right)^2 \quad (16)$$

where  $V_d$  is the displaced volume,  $\Delta \theta$  is the uncertainty in crank angle, and  $\Delta CR$  is the uncertainty in the compression ratio (here a value of 0.2 was used for  $\Delta CR$ ).

$$\Delta T_{Bulk,i}^2 = T_{Bulk,i}^2 \left( \frac{\Delta m_T}{m_T} \right)^2 \quad (17)$$

where  $\Delta m_T$  is the uncertainty in the *trapped mass*, i.e., the sum of the fuel, air, and residual mass. The residual mass can either be external, cooled exhaust gas recirculation, which can be measured, or internal residuals, which are difficult to quantify. A conservative relative uncertainty of 30% is used in this work.

$$\Delta dP_i^2 = \frac{130 \Delta P_i^2}{(12(\theta_i - \theta_{i-1}))^2} \quad (18)$$

$$\Delta NHRR_i^2 = \frac{(V_i \Delta dP_i)^2 + (dP_i \Delta V_i)^2}{(\gamma_i - 1)^2} \quad (19)$$

$$\Delta HHTR_i^2 = HHTR_i^2 * \frac{\Delta T_{bulk,i}^2 + \Delta T_{wall}^2}{(T_{bulk,i} - T_{wall})^2} \quad (20)$$

$$\Delta \eta_c^2 = (1 - \eta_c)^2 \left( \frac{\Delta m_T}{m_T} \right)^2 + (1 - \eta_c)^2 \left( \frac{\Delta m_f}{m_f} \right)^2 + \frac{2(1 - \eta_c)^2 \sigma_{m_T m_f}}{m_f m_f} + \left( \frac{m_T}{m_f Q_{LHV,f}} \right)^2 \sum_{i=1}^n (\Delta x_i Q_{LHV,i})^2 \quad (21)$$

$$\Delta \alpha^2 = \frac{\Delta Q_{in}^2 + \Delta CNHR_{max}^2}{CHT_{max}^2} \quad (22)$$

$$\Delta dP_i^2 = \frac{130 \Delta P_i^2}{(12(\theta_i - \theta_{i-1}))^2} \quad (23)$$

$$\Delta CGHR_i^2 = \Delta CNHR_i^2 + (CHT_i [\Delta \alpha])^2 \quad (24)$$

The set of equations holds when the following best practices for post-processing experimental engine data are used:

1. The bore, stroke, connecting rod length, piston pin offset, and crank radius are all taken as parameters without uncertainty.
2. 100–1,000 consecutive cycles are recorded in steady state operation.



3. A crank angle encoder with high resolution ( $< 0.5$  CAD) is used and TDC is determined relative to a z-pulse using a TDC probe.
4. A high accuracy, high-speed cylinder pressure transducer is used ( $< 1\%$  relative error).
5. The bulk temperature is found using the ideal gas equation.
6. The net heat release rate is calculated using the ratio of specific heats that is determined by using a temperature correlation based on in-cylinder gas composition which is obtained using the NASA polynomials.
7. The derivative of pressure,  $dP_i$ , should be calculated with a step size of 0.8 crank angle degrees during the early compression and late expansion, with a step size of 0.2 crank angle degrees used during the heat release process. This is done to suppress uncertainty in  $dP_i$  without incurring high numerical error.
8. The Hohenberg heat transfer correlation is used. Any other heat transfer correlation can be used but will produce an uncertainty equation of a slightly different form. Therefore, a sensitivity analysis would need to be performed for the desired heat transfer correlation.
9. The cumulative heat transfer trace is scaled using energy closure to ensure the cumulative gross heat release reaches a value equal to the total heat added to the thermodynamic cycle.

The uncertainty interval in the *MFB* curve is found by normalizing the uncertainty in the *CGHR* curve, shown in Figure 17. With an uncertainty interval in the *MFB* curve, the uncertainty in CA10, CA50, and CA90 may be found graphically.

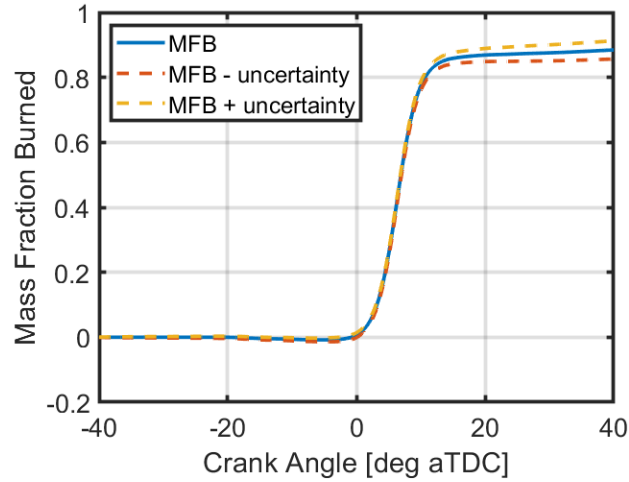


Figure 17: Mass fraction burned (MFB) curve with curves showing uncertainty added/subtracted.

Indicated mean effective pressure (IMEP) is the work of the cycle normalized by the displaced volume. Since the displaced volume is taken as a parameter without uncertainty, the uncertainty in IMEP only depends on the uncertainty of the work of the cycle, which is found through numerical integration. Since a high-resolution crank angle encoder is employed, trapezoidal integration can be used without incurring high integration error. The uncertainty in IMEP is then:

$$\Delta Work^2 = (\Delta PV_d)^2 \quad (25)$$

$$\Delta IMEP^2 = \frac{\Delta Work^2}{V_{disp}^2} \quad (26)$$

The indicated efficiency of the cycle can be found by dividing the work by fuel energy input into the cylinder, i.e.,  $m_f Q_{LHV}$ . The uncertainty in indicated efficiency is then:

$$\Delta \eta_{in}^2 = \eta_{in}^2 \left( \frac{\Delta Work^2}{Work^2} + \frac{\Delta m_f^2}{m_f^2} \right) \quad (27)$$

Finally, emissions are reported either as indicated specific ( $g_{\text{emission}}/kWh_{\text{work}}$ ) or emission index ( $g_{\text{emission}}/kg_{\text{fuel}}$ ). The uncertainty in these parameters are then:

$$\Delta iS_x^2 = iS_x^2 \left( \frac{\Delta m_x^2}{m_x^2} + \frac{\Delta Work^2}{Work^2} \right) \quad (28)$$

$$\Delta EI_x^2 = EI_x^2 \left( \frac{\Delta m_x^2}{m_x^2} + \frac{\Delta m_f^2}{m_f^2} \right) \quad (29)$$

Determining the uncertainty of any parameter,  $x$ , of an ensemble-averaged cycle will equal the average uncertainty of each individual cycle divided by the square root of the number of cycles, the expanded uncertainty of the mean of the ensemble-averaged cycle, and any bias error, added in quadrature, following the equation:

$$\Delta x_{avg\ cyc}^2 = \frac{\Delta \overline{x}_{cyc}^2 + \Delta x_{var}^2}{\sqrt{n_{cycles}}} + \Delta x_{bias}^2 \quad (30)$$

## 2.6 Open Cycle Engine Thermodynamic Model

### 2.6.1 Open Cycle Methodology

In this MATLAB engine cycle simulation, the engine geometry, including valve size and valve lift profile, mimic the engine used in this experiment. Mass flow in and out of control volumes are described using the equations of compressible flow through an orifice described in Heywood [84]:

$$\dot{m} = \frac{C_D A_R p_0}{\sqrt{RT_0}} \left( \frac{p_T}{p_0} \right)^{1/\gamma} \left\{ \frac{2\gamma}{\gamma-1} \left[ 1 - \left( \frac{p_T}{p_0} \right)^{(\gamma-1)/\gamma} \right] \right\}^{1/2} \quad (31)$$

where  $\dot{m}$  is the mass flow,  $C_D$  is the discharge coefficient,  $A_R$  is the area of the orifice,  $P_0$  is the upstream stagnation pressure,  $R$  is the universal gas constant divided by the molecular weight of the gas,  $T_0$  is the upstream stagnation temperature,  $P_T$  is the throat pressure (assumed to be equal to the downstream pressure), and  $\gamma$  is the ratio of specific heats. When the flow is choked, satisfying:

$$\frac{p_T}{p_0} \leq \left( \frac{2}{\gamma+1} \right)^{\gamma/(\gamma-1)} \quad (32)$$

Equation 32 can be simplified to:

$$\dot{m} = \frac{C_D A_R p_0}{\sqrt{RT_0}} \sqrt{\gamma} \left( \frac{2}{\gamma + 1} \right)^{(\gamma+1)/2(\gamma-1)} \quad (33)$$

At each time step, the specific volume and the specific energy are used to define the thermodynamic state in each control volume. With the thermodynamic state defined, a Cantera-style mixture subroutine is then used to determine mixture properties using the NASA polynomials [90]. The specific volume is the total volume of the control volume in question, calculated from the piston motion, divided by the total mass in the control volume in question, calculated by conservation of mass, accounting for flow in and out of the control volume as well as fuel injection, if it applies. The specific energy is calculated using the first law of thermodynamics for an open system, accounting for compression/expansion work, heat transfer, intake/exhaust flow, evaporative cooling from fuel injection if it applies, and heat release from combustion if it applies. Heat transfer in each control volume is calculated using the modified Woshcni heat transfer correlation [91]. The heat release profile is prescribed with a mass fraction burned curve. The average wall temperature is selected to be 400 K.

### 2.6.2 Model Validation

The model is validated in three steps. First, the model is validated against a motored cycle, shown in Figure 18, to validate the open cycle and compression. The pressure trace of the simulated cycle matches well with the experiment. The total trapped mass of the simulated cycle, 364 mg, falls within the experimental trapped mass uncertainty band,  $372 \pm 11$  mg. Next, the model is validated against a fired cycle, where the fuel and air are premixed, shown in Figure 19, to validate the combustion process. Once again, the pressure trace of the simulated cycle matches well with experiment. The total trapped mass of the simulated cycle, 384 mg, matches exactly with the experimental trapped mass,  $384 \pm 14$  mg. Finally, the model is validated against a fired cycle where the fuel is direct injected into the cylinder during the intake stroke. Figure 20 shows this for an injection timing of -300 deg aTDC with an injector angle of 60°. The total trapped mass of the simulated cycle, 384 mg, falls within the experimental trapped mass uncertainty band,  $383 \pm 15$  mg.

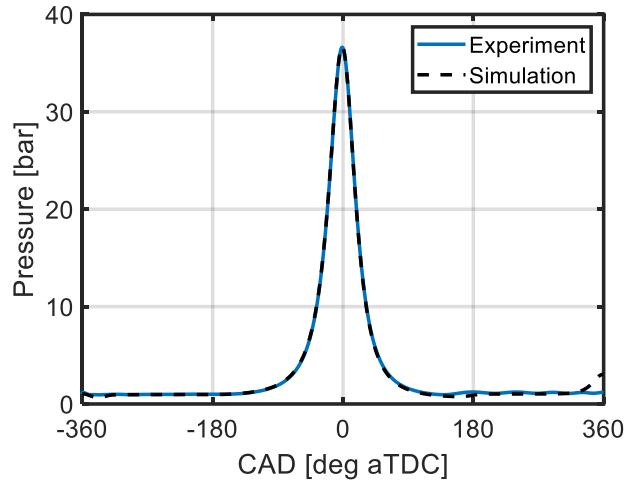


Figure 18: Validation of a motored cycle. Experimental Trapped Mass:  $372 \pm 11$ mg. Simulation Trapped mass: 364 mg

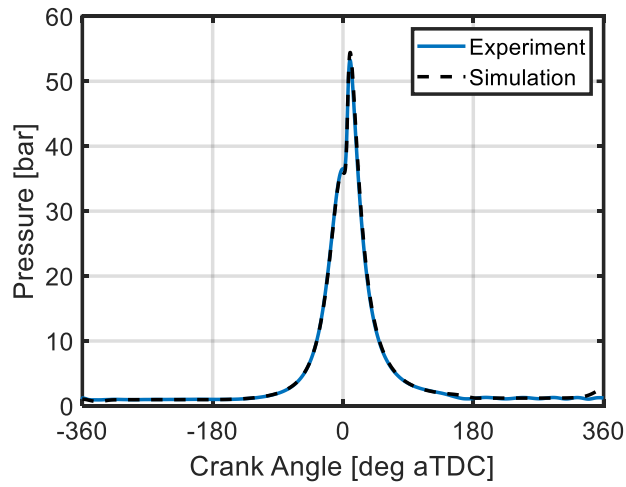


Figure 19: Validation of a fired cycle with premixed fuel and air. Experimental Trapped Mass:  $384 \pm 14$ mg. Simulation Trapped mass: 384 mg.

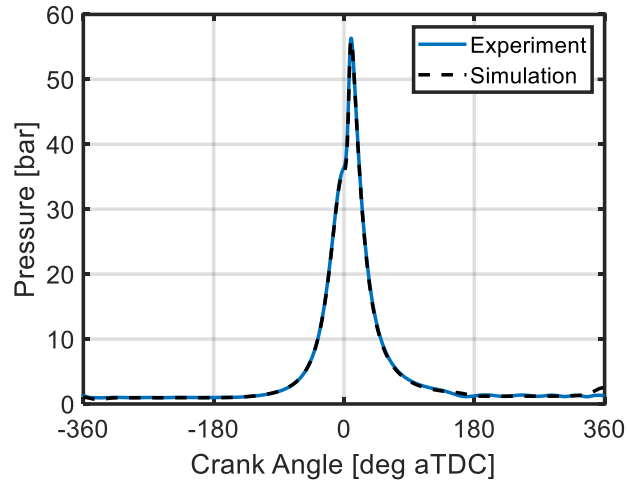


Figure 20: Validation of a fired cycle with a direct injection event at -300 deg aTDC. Experimental Trapped Mass:  $384 \pm 15$ mg. Simulation Trapped mass: 383 mg.

## Chapter 3. Design Parameters for LTC with Wet Ethanol

### 3.1 HCCI with Wet Ethanol – Light-Duty Diesel Engine Architecture

High latent heat of vaporization fuels have a large cooling potential. If the cooling potential of a fuel could be controlled, the temperature of the charge could be controlled. With a blend of 80% ethanol and 20% water by mass (WE80), the effective latent heat of vaporization of wet ethanol is 1130 kJ/kg, slightly higher than methanol (1100 kJ/kg), twice as large as butanol (580 kJ/kg), and greater than 350% higher than gasoline (310 kJ/kg for gasoline). Figure 21 shows the cooling potential of ethanol, WE80, methanol, butanol, and gasoline as a function of equivalence ratio. In the following experiments, WE80 is used with an equivalence ratio of 0.4. This means there is 63K of cooling potential available with WE80, 750% greater than gasoline's cooling potential of 8.4K. However, not all of the available cooling potential can be used to cool the air. Wall wetting will result in heat from the liner and/or piston crown being used to evaporate the fuel. Controlling the fraction of available cooling potential that is used can therefore control the intake temperature on a cycle-to-cycle basis. With 63K of cooling potential, there is the potential for cycle-to-cycle control of a large range of intake temperature.

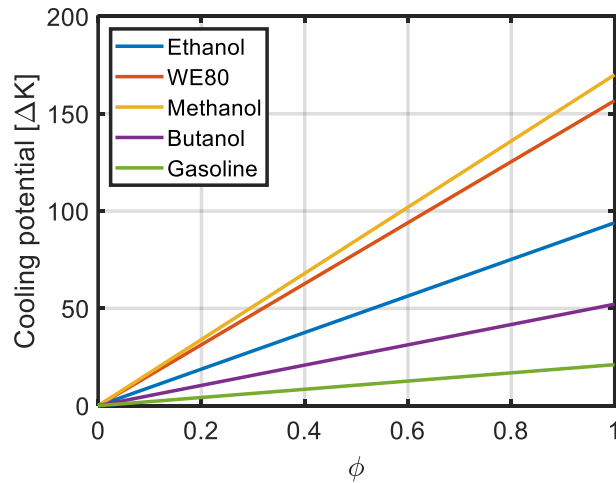


Figure 21: The cooling potential (units of  $\Delta K$ ) of ethanol, WE80 (80% ethanol 20% water by mass), methanol, butanol, and gasoline as a function of equivalence ratio. This figure assumes all of the heat needed to evaporate the fuel comes from the air.

### 3.1.1 Injection timing sweep

To control the fraction of fuel that evaporates in the air vs. on the wall, the amount of fuel that wets the walls must be controlled. With such a high heat of vaporization, the spray penetration length during the intake stroke (low in-cylinder temperature/pressure) will be very large. The location of the piston during injection can therefore control the length a spray can travel before hitting the walls. With this in mind, an experimental injection timing sweep was performed with two different injectors and two different wall temperatures. The effect that injector included angle and wall temperature have on the range of intake temperature control is examined in the sections below. The two injector spray angles used in this study are 60° and 150°. Although the wall temperature is not measured directly, changing the coolant and oil temperature can be used to change the wall temperature. The two coolant/oil temperatures used in this study are 368K/358K (95°C/85°C) and 353K/343K (80°C/70°C).

To determine the effective range of intake temperature control, the injection timing sweeps were performed with a constant fueling rate of WE80 ( $18.75 \pm 0.50$  mg/cycle) and a constant CA50 ( $7.0 \pm 0.5$  deg aTDC). The upstream intake temperature was adjusted at each injection timing to control combustion phasing at the desired CA50. It should be pointed out that although the intake temperature varied largely, the amount of air flowing into the cylinder each cycle did not vary appreciably. This is because the charge is cooled by fuel evaporation (i.e., the fuel's cooling potential), resulting in the same temperature at IVC and therefore the same combustion phasing. The air flowrate does not decrease due to a decrease in air density as intake temperature increases because IVC temperature actually remains constant, and therefore, the equivalence ratio also remains constant ( $0.4 \pm 0.02$ ).

The two injector spray angles used in this study, 150° and 60°, are vastly different, targeting different parts of the combustion chamber. The 150° injector is typically used in CDC, where fuel is injected near TDC into a deep-bowled piston, creating a diffusion flame. When this injector is used to deliver fuel during the intake stroke and into a cylinder whose piston geometry is a wide, shallow bowl, the spray plumes tend to impinge on the liner and the available spray penetration length is always approximately half



of the cylinder bore. Only near TDC do the edges of the piston bowl intercept the spray. This means that once the edge of the bowl moves down past the spray plumes, the ability to extend the spray length by injecting later is lost. This contrasts the 60° injector, whose available spray penetration length increases as the piston recedes to BDC until about -240 deg aTDC, where the spray will begin to impinge on the liner. The maximum available spray penetration length for the 60° injector occurs at -240 deg aTDC and is 2\*the cylinder bore. As a result, the injection timing sweep for the 150° injector is only carried out to -300 deg aTDC. Another reason for this is that the combustion efficiency became excessively low (<80%) and combustion became unstable after -300 deg aTDC due to excessive wall impingement and poor evaporation.

Figure 22 shows the intake temperature required to achieve a CA50 of  $7.0 \pm 0.5$  deg aTDC vs. injection timing for both coolant/oil temperatures with both spray angles. Due to the limitation on spray penetration length imposed by the 150° injector, the range of control over the intake temperature is limited, as seen in Figure 22. On the other hand, the 60° injector's range of control over the intake temperature is very large. The range of intake temperature control of the 150° injector is 9.7K and 8.3K for the high and low coolant/oil temperatures, respectively. The range of intake temperature control of the 60° injector is 57.5K and 47.3K for the high and low coolant/oil temperatures, respectively. The results show that with the 60° injector, there is the potential for cycle-to-cycle control of combustion phasing for advanced combustion strategies using wet ethanol as a fuel.

It is expected that the required intake temperature would increase with retarding injection timings. This trend is seen for the entire limited injection timing sweep with the 150° and up until an injection timing of -240 deg aTDC with the 60° injector. The required intake temperature of -210 deg aTDC is actually lower than that of -240 deg aTDC. The required intake temperature of -180 deg aTDC is then higher than both -210 deg aTDC and -240 deg aTDC. While this brief decrease in required intake temperature may seem like an outlier point, the fact that it occurred with both coolant/oil temperatures, two independent injection timing sweeps, suggests it is a physical result. It is speculated that this result is related to the dynamics of the air flow into the cylinder and the spray dynamics and impingement on the liner rather than

the piston crown. However, to definitively determine the spray interactions and explain the observed phenomena at -210 deg aTDC, further investigation with a future Computational Fluid Dynamics (CFD) study is required.

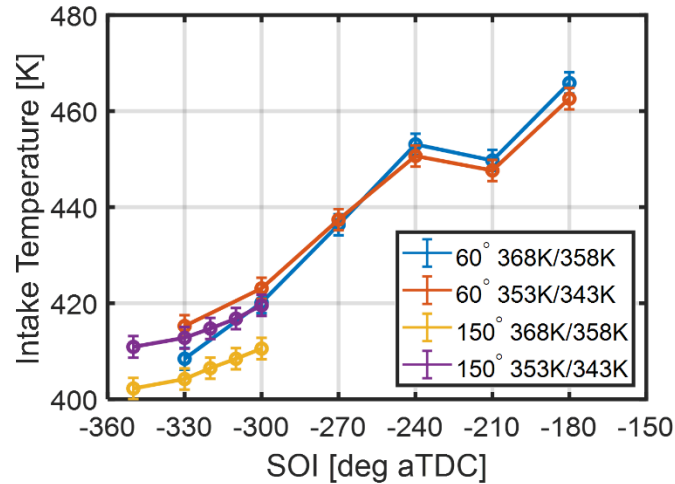


Figure 22: Intake temperature required to maintain a CA50 of 7.0 deg aTDC vs. injection timing for two coolant/oil temperatures (368K/358K and 353K/343K) with two different injector spray included angles (60° and 150°). Error bars show the expanded uncertainty with a confidence interval of 95%.

Figure 23 shows the combustion efficiency ( $\eta_c$ ) vs. injection timing for both coolant/oil temperatures with both spray angles. The combustion efficiency of both injectors increased when the coolant/oil temperature was increased. However, the increase in combustion efficiency due to the increase in coolant/oil temperature was not the same for both injectors. At a coolant/oil temperature of 353K/343K, the 150° injector had a low combustion efficiency at each injection timing. As previously mentioned, the combustion efficiency was extremely low at -270 deg aTDC, combustion became unstable, and the injection timing sweep was truncated. Since the low combustion efficiency is attributed primarily to a large fraction of fuel impinging on the liner and the surface temperature of the cylinder liner is very sensitive to changes in the coolant/oil temperature due to the liner's direct cooling by the water jacket, there is a lot of potential to improve the combustion efficiency of the 150° injector.

Contrarily, the 60° injector tends to wet the piston crown, which lacks direct cooling and is therefore less sensitive than the liner to changes in coolant/oil temperature. As a result, the combustion

efficiency of the 60° injector is higher than that of the 150° injector when the coolant/oil temperature is 353K/343K for similar injection timings. The combustion efficiency of the 60° injector increases less than the 150° injector when the coolant/oil temperature is raised to 368K/358K, resulting in similar combustion efficiencies among the two injectors for similar injection timings.

The emissions index (EI) of unburned hydrocarbons (uHC), and EI CO vs. injection timing for both coolant/oil temperatures with both spray angles are shown in Figure 24 and Figure 25, respectively. The engine-out uHC emissions in these experiments follow the reverse of the trend outlined by the combustion efficiency. On the other hand, the CO emissions, specifically for both injectors with the coolant/oil temperatures of 368K/358K, do not directly follow the reverse of the trend outlined by the combustion efficiency. For both injectors, the CO emissions are generally lower with the higher coolant/oil temperatures. For the 150° injector, the CO emissions remain nearly constant even though the combustion efficiency is decreasing. For the 60° injector, the CO emissions tend to decrease with retarding injection timing. One potential explanation for this is that as the CO emissions are related to the fraction of fuel that evaporates off the walls, since that will result in colder walls with rich regions nearby that might inhibit complete combustion. This would need further exploration in the future.

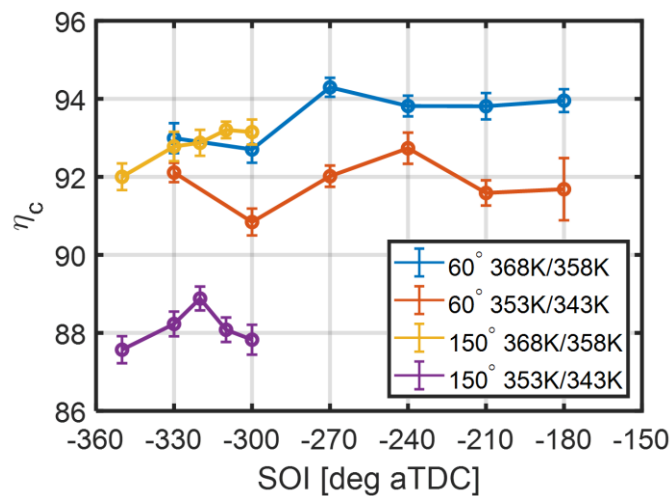


Figure 23: Combustion efficiency ( $\eta_c$ ) vs. injection timing for two coolant/oil temperatures (368K/358K and 353K/343K) with two different injector spray included angles (60° and 150°). Error bars show the expanded uncertainty with a confidence interval of 95%.

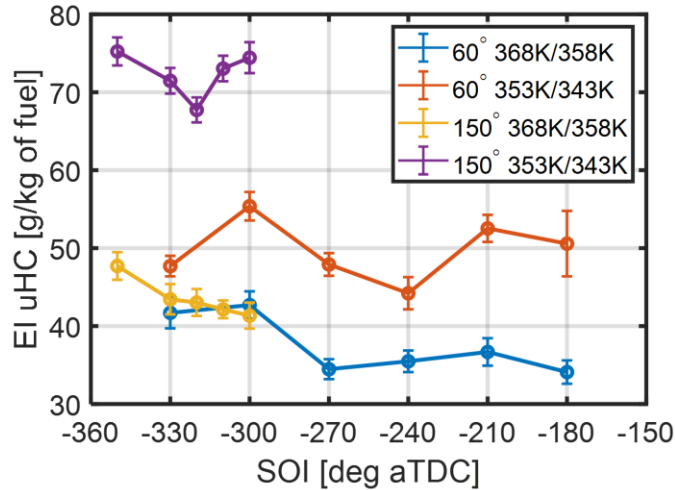


Figure 24: Emission index (EI) of unburned hydrocarbons (uHC) vs. injection timing for two coolant/oil temperatures (368K/358K and 353K/343K) with two different injector spray included angles (60° and 150°). Error bars show the expanded uncertainty with a confidence interval of 95%.

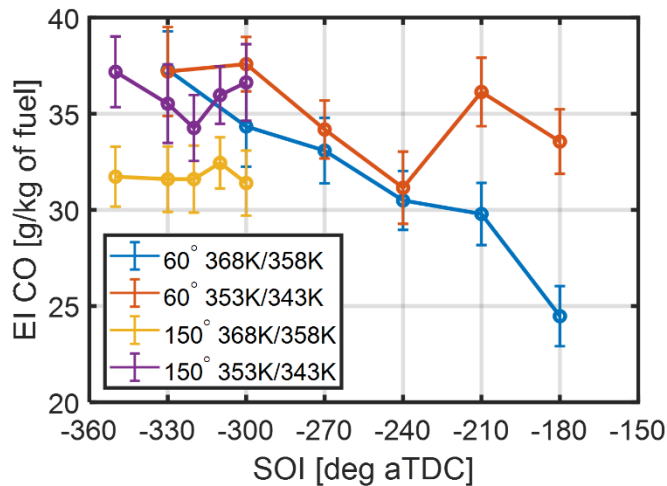


Figure 25: Emission index (EI) of CO vs. injection timing for two coolant/oil temperatures (368K/358K and 353K/343K) with two different injector spray included angles (60° and 150°). Error bars show the expanded uncertainty with a confidence interval of 95%.

Figure 26 shows the CA25 to CA75 burn duration vs. injection timing for both coolant/oil temperatures with both spray angles. The difference in the amount of thermal stratification resulting from a change in wall temperature of ~15K is negligible [35]. Therefore, no significant change in burn duration caused by a change in thermal stratification is expected due to a change in coolant/oil temperature. For a given injection timing with the 60° injector, the burn duration is not highly sensitive to the coolant/oil

temperature, with the difference in burn duration for the two coolant/oil temperatures falling within the bounds of uncertainty. However, with the 150° injector, the burn duration is longer with the lower coolant/oil temperature for a given injection timing. Once again, this can be explained by recalling that the 150° injector targets the cylinder liner, whose surface temperature is more sensitive to changes in coolant/oil temperature than the surface temperature of the piston crown. The resulting low combustion efficiencies are coupled with the longer burn duration.

The length of the error bars in Figure 26 can also provide insight into the cyclic variability (cycle-to-cycle combustion variation) of the operating condition. The variability in the burn duration of the 150° injector is larger with the lower coolant/oil temperatures due to worsening evaporation conditions and poor combustion efficiency. On the other hand, the variability in the burn duration of the 60° injector is not significantly affected by the coolant/oil temperature. However, the cyclic variability in the burn duration does increase as the injection timing is retarded. This could be due to the higher variability in the mixing required to produce a homogeneous mixture of fuel and air. Furthermore, it can be seen that the burn duration begins to trend upward as injection timing is retarded. This may be due to incomplete mixing of the fuel and air, resulting in an increase in thermal stratification. This was seen at injection timings as early as -140 deg aTDC and would not be surprising if it occurred as early as -240 deg aTDC.

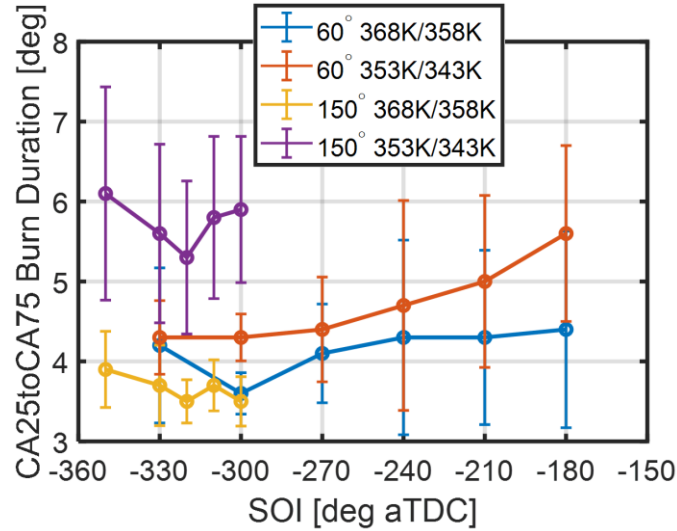


Figure 26: CA25to75 burn duration vs. injection timing for two coolant/oil temperatures (368K/358K and 353K/343K) with two different injector spray included angles (60° and 150°). Error bars show the expanded uncertainty with a confidence interval of 95%.

### 3.1.2 Evaporation Fraction

The injection of a high latent heat of vaporization fuel during the intake stroke has been shown to provide a large range of control over the effective intake temperature via charge cooling. By comparing the difference in experimental intake temperature between a cycle with direct injected fuel and a cycle whose fuel is fully vaporized before entering the cylinder, a rough estimation of the fraction of fuel that is evaporated in the air (i.e. not wetting and evaporating off of the walls) can be obtained. However, this rough estimation does not consider any of the charge heating/cooling effects of heat transfer during the intake stroke. If the walls are hotter than the incoming air, the fraction of fuel evaporating in the air will be underestimated. Similarly, if the walls are colder than the incoming air, then the fraction of fuel evaporating in the air will be overestimated. In order to capture the heat transfer as accurately as possible, a MATLAB engine cycle simulation code is used to simulate the intake portion of the engine cycle to estimate the fraction of fuel that must evaporate in the air at each intake temperature/injection timing pair to achieve an identical temperature at intake valve closing, which will result in identical combustion phasing. It should be noted that for late injection timings, when the burn duration begins to increase, the intake valve closing

temperature should be slightly elevated to advance CA10 in order to maintain a constant CA50. In this study, this effect will be ignored for simplicity, which may result in a slight overestimation of the evaporation fraction.

The MATLAB simulation predicts an intake valve closing temperature of 414 K when premixed fuel and air enter the cylinder at 398 K, which experimentally resulted in a CA50 of 7.0 deg aTDC. For each intake temperature for the injection timing sweep corresponding to the 60° injector with coolant/oil temperatures of 368K/358K, the fraction of fuel evaporated in the air at the respective injection timing is adjusted to achieve an intake valve closing temperature of 414 K. Table 5 shows the intake valve closing temperature when the evaporation fraction is zero, and the evaporation fraction when the intake valve temperature is 414 K for each intake air/injection timing combination.

*Table 5: The intake valve closing temperature without any evaporative cooling of the fuel, and evaporation fraction of the fuel in the air required to obtain an intake valve temperature that matches the intake valve temperature of the PFI case for each injection timing/intake air temperature combination.*

Injection Timing [deg aTDC]	Intake Air Temperature [K]	IVC Temp without evap. cooling [K]	Evap. Fraction in Air
PFI	398	414	--
-330	408	427	0.22
-300	420	432	0.35
-270	436	443	0.55
-240	453	454	0.76
-210	450	455	0.65
-180	466	470	0.82

Since the wall temperature is 400 K, the intake air of all of the direct injected cases is hotter than the walls. Therefore, there is actually a small charge cooling effect that takes place as the intake air rushes over the intake valves and into the cylinder. The heat capacity of wet ethanol is much larger than air. Therefore, the cylinder charge will change temperature more readily due to heat transfer from the walls before the direct injection event. Coupled with the fact that the intake air temperature, in general, increases with retarding injection timing, which increases the heat transfer to the walls, the difference in intake air

temperature and intake valve closing temperature without evaporation decreases with retarding injection timing.

The evaporation fraction ranges from 0.22 at an injection timing of -330 deg aTDC to 0.82 at an injection timing of -180 deg aTDC. The evaporation fraction range shows that wet ethanol is an ideal fuel in this situation. For example, if neat ethanol were used, the maximum range of temperature control would be much smaller, even if the evaporation fraction increased to 1.00. Similarly, if a fuel with a much higher latent heat of vaporization is used, such as wet methanol or wet ethanol with 60% ethanol and 40% water (WE60), the effective evaporation fraction range would be much lower, and the cooling potential will not be fully utilized, since injections even later than -180 deg aTDC will surely result in an inhomogeneous mixture of air and fuel and the combustion mode transitions from HCCI to TSCI.

From an injection timing of -330 deg aTDC to -240 deg aTDC, there is a fairly linear relation between injection timing and evaporation fraction which can be employed to control intake valve closing temperature, and therefore combustion phasing on a cycle-to-cycle basis for varying intake temperature. As seen in the experiment, the injection timing of -210 deg aTDC once again shows outlier behavior, the evaporation fraction is lower than that of -240 deg aTDC, further corroborating the likelihood that there is something physically occurring.

## **3.2 TSCI with Wet Ethanol – Light Duty Diesel Engine Architecture**

### **3.2.1 Injection Strategy**

The injection strategy of TSCI with wet ethanol was studied in depth in Ref. [74], categorizing “early” compression stroke injections (-150 to -100 deg aTDC) as injections that can control the combustion phasing without significantly affecting the thermal stratification, “mid” compression stroke injections (-90 to -30 deg aTDC) as injections that can control the thermal stratification, thereby controlling the heat release process, and “late” compression stroke injections (-20 deg aTDC and later) as injections that cannot affect the already established thermal stratification profile. The study performed in Ref. [74] was done using a constant intake temperature to mimic a production constraint, i.e. intake temperature cannot be changed on



a cycle-to-cycle basis. It is now of interest to take a more fundamental approach and study how the combustion characteristics change when either an “early” or “mid” compression stroke injection is added, changing the intake temperature to maintain constant combustion phasing.

To study how the combustion characteristics are affected by an “early” or “mid” compression stroke injection, six experimentally measured TSCI cases are compared with a reference HCCI case. This is similar to the comparisons of HCCI and TSCI in Ref. [13], except that the intake temperature was used to keep combustion phasing constant so that the features of the heat release process can be studied more fundamentally. In all cases, the fueling rate is maintained at a constant rate of  $25 \pm 0.5$  mg/cycle. This corresponds to an equivalence ratio of  $0.55 \pm 0.01$ . The HCCI case has a single injection at  $-350$  deg aTDC, while the six TSCI cases employ a split injection strategy. Three of the TSCI cases have a single, “early” compression stroke injection at  $-120$  deg aTDC, with a split fraction of 90%, 80%, or 70%. Split fraction is defined as the percent of the total fuel that is injected during the intake stroke, while the remaining fuel is direct injected during the compression stroke. The other three TSCI cases have a single, “mid” compression stroke injection at  $-60$  deg aTDC, also with a split fraction of 90%, 80%, or 70%.

To fairly compare the combustion characteristics of each case, CA50 is held constant at  $7.5 \pm 0.5$  deg aTDC by adjusting the intake temperature. Figure 2 shows the intake temperature vs. split fraction, respectively. In this plot, an HCCI reference line is shown for comparison. The intake temperature of all six TSCI cases are higher than that of the HCCI reference case. This is because the injection and evaporation of wet ethanol during the compression stroke absorbs heat from the gases in the cylinder. Although this heat removal, in general, increases thermal stratification, the overall in-cylinder temperature, and therefore the average in-cylinder temperature, decrease. Therefore, the intake temperature must be increased to compensate and maintain combustion phasing.

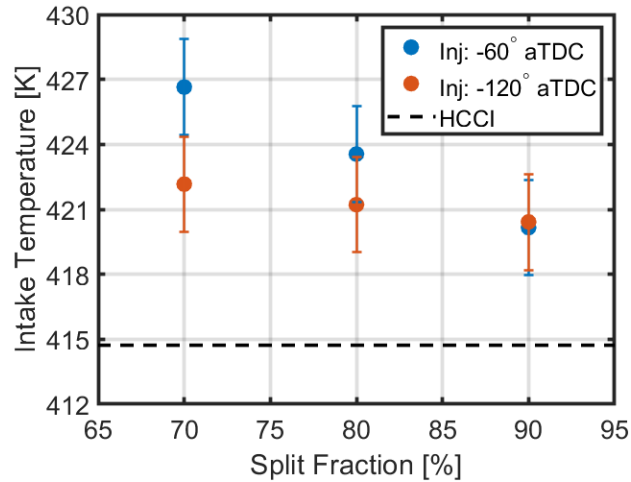


Figure 27: Intake temperature requirement to maintain CA50 at  $7.5 \pm 0.5$  deg aTDC vs. split fraction (split fraction is defined as the percent of the total fuel that is injected during the intake stroke) with a “mid” compression stroke injection (-60 deg aTDC) or an “early” compression stroke injection (-120 deg aTDC). An HCCI case with the same fueling rate is plotted as a reference line.

The required increase in intake temperature to maintain combustion phasing increases as split fraction decreases, i.e. as more fuel is injected during the compression stroke. This can be attributed to more heat removal during compression stroke. However, the required increase in intake temperature for “mid” compression stroke injections is larger than that of “early” compression stroke injections. This can be explained by examining both the start of combustion (SOC) and burn duration. Figure 28 and Figure 29 show the start SOC and burn duration (CA25 to CA75) vs. split fraction, respectively. In these plots, an HCCI reference line is shown for comparison. It has been shown that a “mid” compression stroke injection increases thermal stratification, thereby increasing the burn duration. In order to compensate for the increase in burn duration, SOC must be advanced to maintain combustion phasing, requiring an increase in intake temperature. Considering the 70% split fraction case, a CA10 advancement of  $\sim 1$  degree is needed to maintain a constant CA50, even with burn duration doubling from 4 degrees in HCCI to 8 degrees. This is because the thermal stratification created by evaporative cooling effectively stretches out the end of the heat release process. This can be seen clearly in Figure 30.

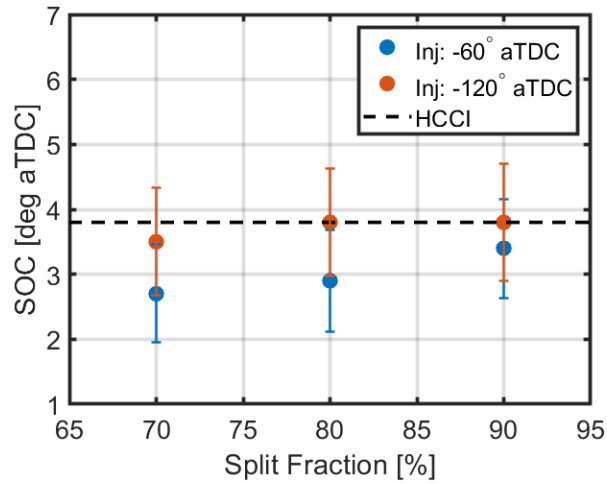


Figure 28: The start of combustion (SOC) at a constant  $CA_{50}$  of  $7.5 \pm 0.5$  deg aTDC vs. split fraction (split fraction is defined as the percent of the total fuel that is injected during the intake stroke) with a “mid” compression stroke injection (-60 deg aTDC) or an “early” compression stroke injection (-120 deg aTDC). An HCCI case with the same fueling rate is plotted as a reference line.

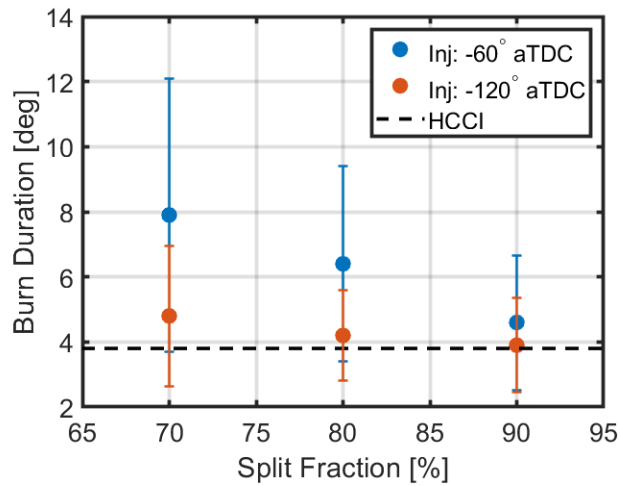


Figure 29: The burn duration ( $CA_{25}$  to  $CA_{75}$ ) at a constant  $CA_{50}$  of  $7.5 \pm 0.5$  deg aTDC vs. split fraction (split fraction is defined as the percent of the total fuel that is injected during the intake stroke) with a “mid” compression stroke injection (-60 deg aTDC) or an “early” compression stroke injection (-120 deg aTDC). An HCCI case with the same fueling rate is plotted as a reference line.

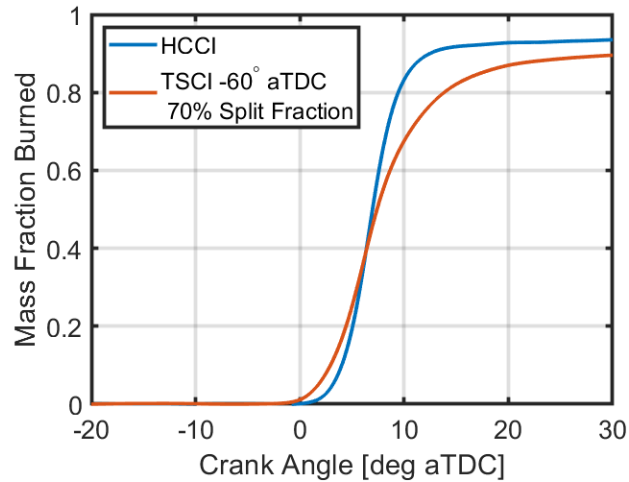


Figure 30: Mass fraction burned vs. crank angle degree for the reference HCCI case and the “mid” compression stroke injection (-60 deg aTDC), 70% split fraction TSCI case, depicting TSCI’s earlier SOC and elongated late stages of combustion.

“Early” compression stroke injections, on the other hand, do not significantly increase thermal stratification and burn duration. Therefore, SOC is left largely unchanged. The burn duration does begin to increase for the “early” compression stroke injection with a split fraction of 70%. However, this can be attributed to excessive wall wetting and poor evaporation.

Combustion efficiency, shown in Figure 31, becomes very low at a split fraction of 70%; to avoid this, multiple injections should be used. The combustion efficiency decreases significantly for “mid” compression stroke injections at a split fraction of 80%, whereas the combustion efficiency for “early” compression stroke injections is still comparable to HCCI at this split fraction. This is because of the shorter burn duration and extra evaporation and mixing time that “early” compression stroke injections have. This implies that a multiple injection strategy is more critical for optimal performance for “mid” compression stroke injections.

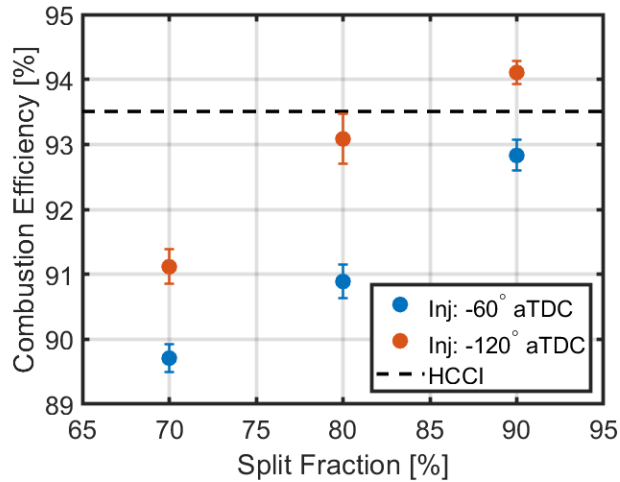


Figure 31: The combustion efficiency at a constant CA50 of  $7.5 \pm 0.5$  deg aTDC vs. split fraction (split fraction is defined as the percent of the total fuel that is injected during the intake stroke) with a “mid” compression stroke injection (-60 deg aTDC) or an “early” compression stroke injection (-120 deg aTDC). An HCCI case with the same fueling rate is plotted as a reference line.

### 3.2.2 External, Cooled Exhaust Gas Recirculation

External, cooled EGR is often used to reduce knock levels, decrease burn rates, and keep in-cylinder temperatures low. EGR, whether hot internal EGR or cooled external EGR, also provides unburned fuel another chance to burn, improving overall tailpipe combustion efficiency. This is important in low temperature combustion, where combustion efficiencies tend to be lower than the conventional combustion modes. Additionally, a diesel engine architecture, which is designed for mixing-controlled combustion in the piston bowl, typically has a large crevice volume and squish region, further reducing the combustion efficiency in homogeneous or partially premixed combustion modes. The low-internal-residuals diesel engine used in this study has shown lower than average combustion efficiencies for combustion modes such as HCCI and RCCI when compared to the literature [13]. Therefore, combustion performance may improve with the inclusion of external, cooled EGR.

While the inclusion of external, cooled EGR in other combustion modes is well documented, it has never been studied in TSCI combustion using wet ethanol. Incomplete combustion products from ethanol include high levels of aldehydes, which may change the reactivity of the charge [92]. In addition, increased in-cylinder H<sub>2</sub>O content from EGR has been shown to lower the hot-ignition temperature of some fuels;

however, this is primarily for two-stage ignition fuels and should not affect ethanol appreciably [93]. Finally, the inclusion of EGR lowers the mole fraction of  $O_2$ ,  $[O_2]$ , in the cylinder during compression, which can affect ignition delay. Dec et al. has shown that ethanol is insensitive to decreases in  $[O_2]$  down to a mole fraction of 17%, when subsequent reduction of  $[O_2]$  results in an increase in the ignition delay [66].

With all of the effects of EGR on the autoignition properties of ethanol in mind, it is of interest to see if the inclusion of external, cooled EGR will increase or hinder the effectiveness of a split injection of wet ethanol to control the heat release process. To answer this question, experiments are conducted, adding external, cooled EGR to the cylinder in increments of 6% from 0% to 30% by mass. This is in addition to the ~5% of mass of internal residuals that reside in the cylinder. Figure 32 relates external, cooled EGR percentage to  $[O_2]$  and global equivalence ratio for convenience. In all cases, the fueling rate is maintained at a constant rate of  $25 \pm 0.5$  mg/cycle. A split fraction of 85% is used. A single injection during the intake stroke at -350 deg aTDC is used to deliver 85% of the fuel, while the remaining 15% of the fuel is split between three “mid” compression stroke injections (-80, -60, and -40 deg aTDC) to increase thermal stratification. Three “mid” compression stroke injections are used to improve combustion efficiency.

It can be seen in Figure 32 that the largest global equivalence, corresponding to the largest fraction of EGR, is ~0.87. While EGR can mimic excess air as a heat sink, maintaining low in-cylinder temperatures during combustion and preventing  $NO_x$ , it cannot prevent soot from locally rich areas. TSCI, being a partially premixed combustion mode, has a distribution of equivalence ratios. Therefore, the EGR sweep was truncated at 30% to ensure local equivalence ratios do not become excessively rich, which would be detrimental to combustion efficiency.

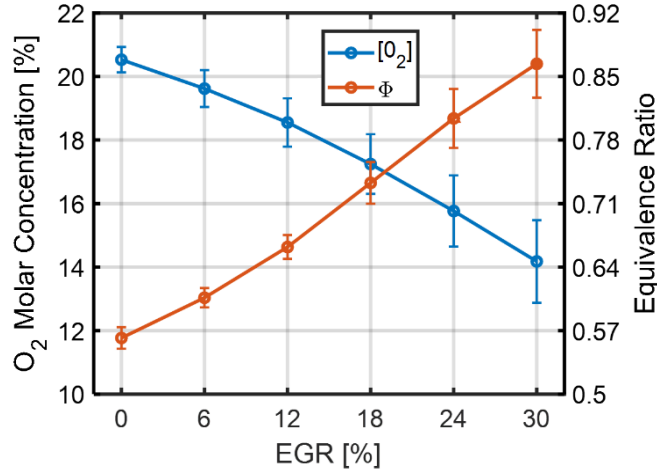


Figure 32: Molar concentration of oxygen,  $[O_2]$ , in the cylinder and global equivalence ratio ( $\phi$ ) vs. external, cooled EGR percentage. There are also  $\sim 5\%$  hot, internal residuals.

To fairly compare the combustion characteristics of each case, CA50 is held constant at  $7.5 \pm 0.5$  deg aTDC by adjusting the intake temperature. The intake temperature for each case is shown in Figure 33. The intake temperature required to maintain combustion phasing increases with increasing EGR. Although the addition of EGR may change the hot ignition temperature, no conclusions can be drawn in this work because the uncertainty in bulk temperature, which is  $\sim \pm 30K$  near ignition for each operating condition, is larger than any difference in the hot ignition temperature observed. Additionally, EGR can change the amount of LTHR or ITHR exhibited by a fuel. However, ethanol does not have a negative temperature coefficient (NTC) region under engine-relevant conditions [66]. Further, ethanol's hydroxyl group promotes chain-terminating reactions, quenching radical-induced cool-flame reaction pathways [94]. As a result, no significant heat release is seen prior to the main heat release event in Figure 34, which displays the cylinder pressure and gross heat release rate (GHRR) vs. crank angle for both a case with no external, cooled EGR and a case with 30% external, cooled EGR. The intake temperature therefore needs to increase to compensate for the decrease in the ratio of specific heats during the compression stroke that occurs when triatomic combustion products like  $CO_2$  and  $H_2O$  are added in place of diatomic  $N_2$  and  $O_2$ .

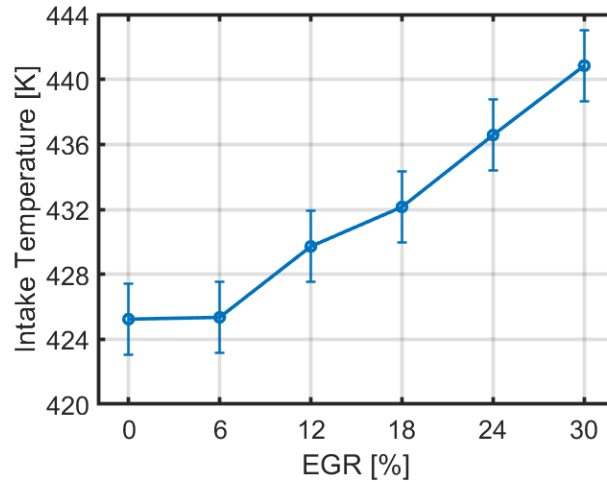


Figure 33: Intake temperature requirement to maintain CA50 at  $7.5 \pm 0.5$  deg aTDC vs. external, cooled EGR percentage.

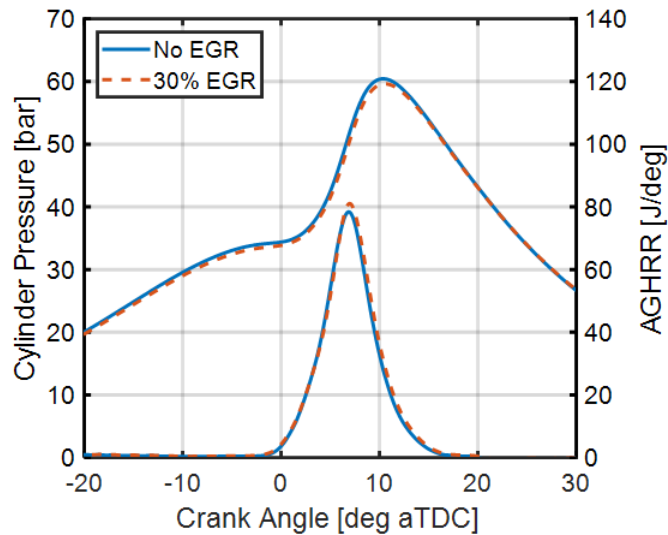


Figure 34: Cylinder pressure and apparent gross heat release rate (AGHRR) vs. crank angle for both a case with no external, cooled exhaust gas recirculation (EGR) and a case with 30% external, cooled EGR. The heat release process of both cases is nearly identical, showing external, cooled EGR does not significantly affect the combustion process of TSCI with wet ethanol.

SOC and burn duration (CA25 to CA75) vs. EGR are shown in Figure 35. Considering the hot-ignition temperature is largely unchanged, it makes sense that the SOC is also unchanged. As previously indicated, with constant combustion phasing, the burn duration provides insight into the thermal stratification. One possible effect of EGR is that the higher specific heat of the charge would require more cooling potential to be introduced in the compression stroke (i.e. a lower split fraction) to obtain the same



increase in thermal stratification. This would manifest as a decrease in burn duration with increasing EGR. Figure 35, however, shows that the burn duration is largely insensitive to increases in EGR. It can therefore be concluded that EGR does not affect the effectiveness of TSCI combustion with wet ethanol. In fact, since EGR only increases the intake temperature requirement, it behaves similar to an “early” compression stroke injection.

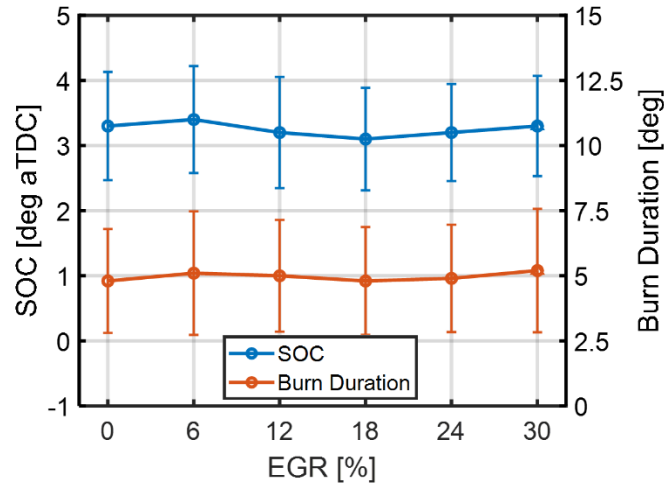


Figure 35: The start of combustion (SOC) and the burn duration (CA25 to CA75) at a constant CA50 of  $7.5 \pm 0.5$  deg aTDC vs. external, cooled EGR percentage.

Now that it is confirmed that moderate levels of external, cooled EGR do not appreciably affect the combustion process of TSCI with wet ethanol, meaning moderate amounts of EGR does not reduce the heat release control authority of a split injection strategy with wet ethanol, it is of interest to examine its effect the combustion efficiency. Figure 36 displays the both the single-cycle combustion efficiency and the overall tailpipe combustion efficiency vs. EGR percentage. The single-cycle efficiency is relatively insensitive to EGR. This is because the EGR serves the same role as excess air. The overall tailpipe combustion efficiency, on the other hand, increases with increasing EGR, since EGR gives some of the unburned fuel a second chance to burn in the cylinder.

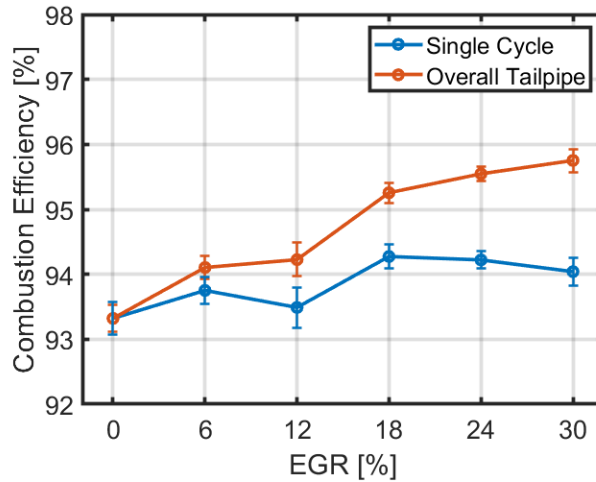


Figure 36: Both the single cycle combustion efficiency and the overall tailpipe combustion efficiency at a constant CA50 of  $7.5 \pm 0.5$  deg aTDC vs. external, cooled EGR percentage.

### 3.2.3 Intake Boost

The load range of HCCI is limited due to excessive energy release rates, therefore HCCI combustion cannot operate at high equivalence ratios. Intake boost has been used in the past to raise the high load limit of HCCI by maintaining low global equivalence ratios [95]. Unlike HCCI, LTC combustion modes that have a mechanism to control the heat release process, like TSCI, can achieve higher loads under naturally aspirated conditions. As these higher loads are approached, more fuel is required, and therefore the global equivalence ratio increases. The efficiency and emissions advantage that LTC has over the conventional combustion modes hinges upon maintaining lean cylinder conditions. Compounding this issue is the fact that combustion modes like TSCI with wet ethanol use fuel inhomogeneity to control the heat release process, meaning locally rich and stoichiometric areas can form even when the global equivalence ratio is lean, leading to soot and NO<sub>x</sub> production, respectively. To maintain low global and local equivalence ratios, intake boost must be used.

If intake boost is to be used to further extend the load range of TSCI with wet ethanol while also improving performance and lowering emissions, it is important to characterize whether intake boost will affect the combustion process. For example, intake boost is required to enable ITHR in gasoline, enabling

PFS. The effectiveness of PFS is therefore very sensitive to the intake boost level. Dec et al. has shown that ethanol maintains its single-stage ignition characteristics at high levels of intake boost [66]. To study the effects of intake boost on TSCI with wet ethanol, an experimental intake boost sweep was performed.

The intake boost sweep was performed by increasing the intake pressure in increments of 0.125 bar from 1.0 bar to 1.5 bar of absolute pressure. In all cases, the fueling rate is maintained at a constant rate of  $30 \pm 0.5$  mg/cycle. A split fraction of 80% is used. A single injection during the intake stroke at -350 deg aTDC is used to deliver 80% of the fuel, while the remaining 20% of the fuel is split between three “mid” compression stroke injections (-80, -60, and -40 deg aTDC) to increase thermal stratification. Three “mid” compression stroke injections are used to improve combustion efficiency.

The global equivalence ratio vs. intake pressure is shown in Figure 37. Naturally, as the intake pressure increases, the global equivalence ratio decreases, since the mass of incoming air increases with a constant fueling rate. To fairly compare the combustion characteristics of each case, CA50 is held constant at  $7.5 \pm 0.5$  deg aTDC by adjusting the intake temperature. The intake temperature for each case is also shown in Figure 37. The intake temperature decreases with increasing intake boost level, which agrees with Ref. [66]. While some of the decrease in intake temperature with increasing boost level can be attributed to 1) an increase in the ratio of specific heats during the compression stroke due to a leaner charge and 2) an increase in heat transfer during the intake and compression strokes due to a denser, colder charge, there is still a clear increase in the autoignition propensity of ethanol. This increase, however, does not make the fuel extremely  $\phi$ -sensitive.

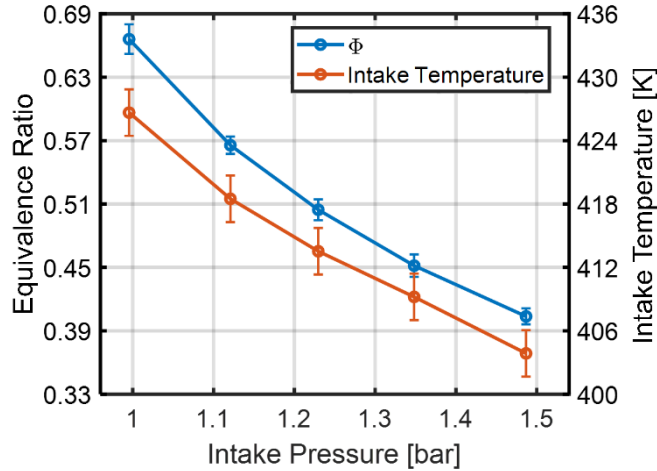


Figure 37: Global equivalence ratio ( $\phi$ ) and intake temperature requirement to maintain CA50 at  $7.5 \pm 0.5$  deg aTDC vs. intake boost level.

The SOC and burn duration (CA25 to CA75) are shown in Figure 38. The SOC tends to advance slightly as intake boost level increases, and a corresponding increase in burn duration occurs, which makes sense considering combustion phasing remains constant. One possible explanation for the increase in burn duration is that the charge is getting leaner as the intake boost level increases, which leads to less effective sequential autoignition due to a reduction in the compression effect from combustion elsewhere in the cylinder. This is why HCCI can achieve higher loads at moderate energy release rates by boosting. Another possible explanation is that the denser charge provided with intake boost will reduce the spray penetration length of the fuel injected during the compression stroke, increasing the evaporation efficiency of the fuel in the air, which is needed to increase thermal stratification. From these results, it is seen that intake boost level does not negatively impact the effectiveness of TSCI with wet ethanol and may slightly improve it. Now that it is confirmed that moderate levels of intake boost do not appreciably affect the combustion process of TSCI with wet ethanol, it is of interest to examine how it affects the combustion efficiency and the thermal efficiency of the cycle. Figure 39 shows the combustion efficiency and gross thermal efficiency (GTE) vs. intake boost level. The combustion efficiency does decrease with increasing boost level. This is because the decrease in the global equivalence ratio leads to a much slower progression of sequential autoignition due to the reduction in the strength of the compression effect from combustion elsewhere in

the cylinder. Figure 40 shows the emissions index (EI) of NO<sub>x</sub> and ringing intensity vs. the combustion efficiency. As combustion efficiency decreases with increasing boost level, the ringing intensity [96] and NO<sub>x</sub> emissions both decrease, which follows trends found in the literature [97]. The increase in excess air with increasing intake boost level decreases in-cylinder temperatures.

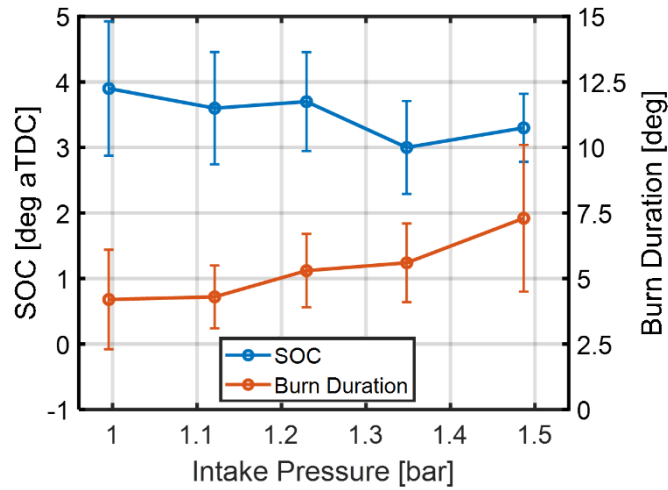


Figure 38: The start of combustion (SOC) and the burn duration (CA25 to CA75) at a constant CA50 of  $7.5 \pm 0.5$  deg aTDC vs. intake boost level.

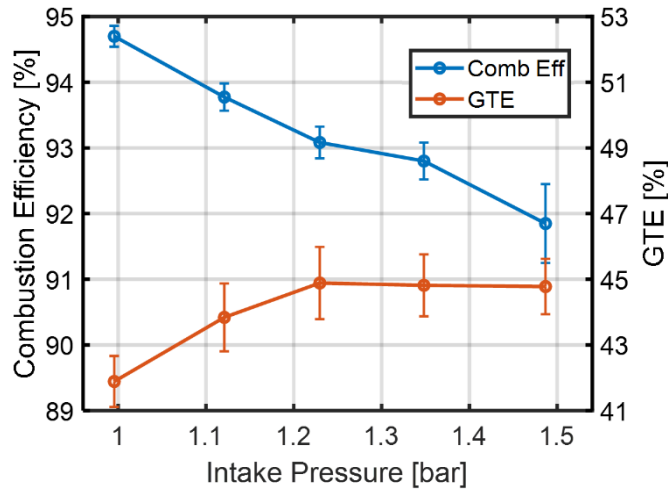


Figure 39: The combustion efficiency and gross thermal efficiency (GTE) at a constant CA50 of  $7.5 \pm 0.5$  deg aTDC vs. intake boost level.

Referring to Figure 39, it is interesting that the thermal efficiency first increases with boost level, but then quickly levels off. The initial increase in thermal efficiency is due to the increase in the ratio of

specific heats and reduced heat transfer that occurs as combustion get leaner and the peak bulk temperature decreases. However, the burn duration also increased with intake boost, which is detrimental to thermal efficiency (but is sometimes required to stay within the hardware constraints of the engine). Overall, these results show that moderate amounts of intake boost do not reduce the heat release control authority of a split injection strategy with wet ethanol.

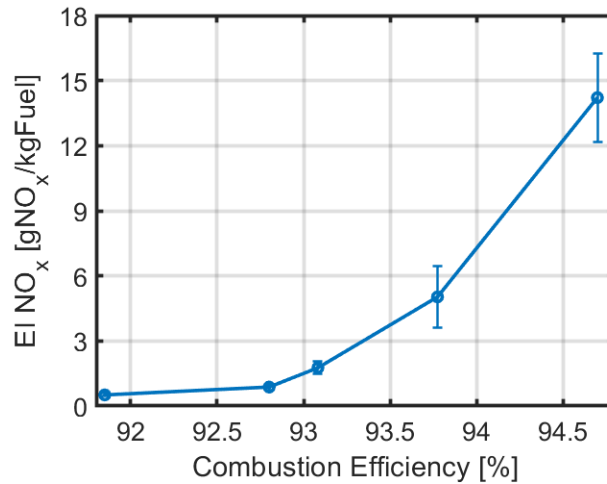


Figure 40: The emissions index (EI) of  $NO_x$  and ringing intensity vs. combustion efficiency, showing the  $NO_x$ -combustion efficiency tradeoff between boosting while maintain a constant load.

### 3.2.4 Injector Spray Angle – Re-entrant Bowl Piston

When employing a split injection strategy to enable TSCI with a single injection system, 70-90% of the total mass of fuel injected during the cycle is injected sometime during the intake stroke. The injector included angle determines what regions in the cylinder are targeted by the spray. This is an important factor both in intake stroke and in compression stroke injections of fuel, since it can impact the effectiveness of heat release control as well as the combustion efficiency. It was found earlier that the optimal way to deliver the fuel during the intake stroke with the 150° injector is with a single injection at -350 deg aTDC. This is because at -350 deg aTDC, the spray is aimed into the bowl, keeping it from impinging on the cylinder liner. It is now of interest to find this optimal timing for both the 118° and the 60° injectors. To do this, an

injection timing sweep was performed for all three injectors experimentally, with equivalence ratio held at  $0.41 \pm 0.01$  and CA50 held at  $7.0 \pm 0.5$  deg aTDC by adjusting the intake temperature.

To identify what injection timing is the optimal injection timing for each injector, the combustion efficiency will be examined and the injection timing with the highest combustion efficiency will be selected. Figure 41 plots the combustion efficiency of each injector vs. the start of injection timing. Agreeing with previous results, the 150° injector's optimal injection timing is -350 deg aTDC; injecting any later than that results in very low combustion efficiencies. The results show that -350 deg aTDC is also the optimal injection timing for the 118° injector. The 60° injector has nearly the same combustion efficiency across the entire injection timing sweep, meaning any injection timing can be selected; -270 deg aTDC will be selected.

Figure 42 shows the intake temperature required to maintain a constant CA50 for each injection timing. As discussed earlier, the injection timing can be used to provide cycle-to-cycle control over the temperature at intake valve closing, creating a mechanism to control combustion phasing. In that study, the custom wide shallow bowl was used. Here, it can be seen that the injection timing can still be used to control the temperature at intake valve closing with the re-entrant bowl piston geometry using the 60° injector. This is evident by the large range of intake temperatures that result in the same CA50. The 150° injector's combustion efficiency becomes excessively low when the injection timing is retarded past -350 deg aTDC, and therefore injection timing cannot be used to provide cycle-to-cycle control over the temperature at intake valve closing. The 118° injector does show a range of equivalent intake temperature control if a moderate decrease in combustion efficiency is willing to be tolerated. None of these operating conditions produced any appreciable level of NO<sub>x</sub>.

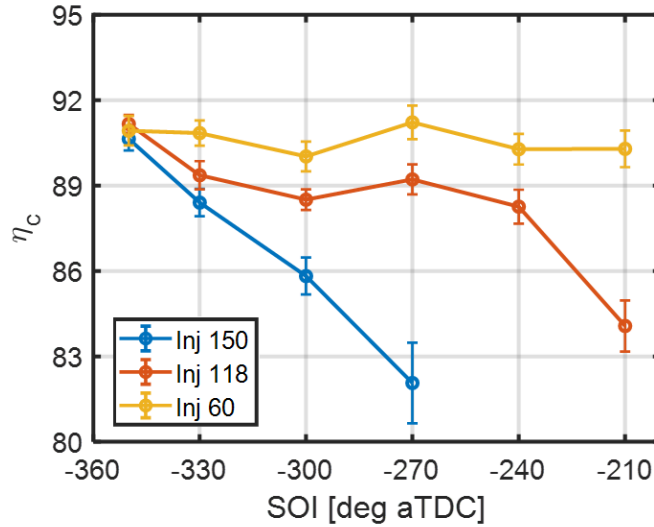


Figure 41: Combustion efficiency ( $\eta_c$ ) vs. start of injection (SOI) timing for all three injectors with the re-entrant bowl piston geometry. The injection timing with the highest combustion efficiency is considered the optimal injection timing for delivering fuel during the intake stroke.

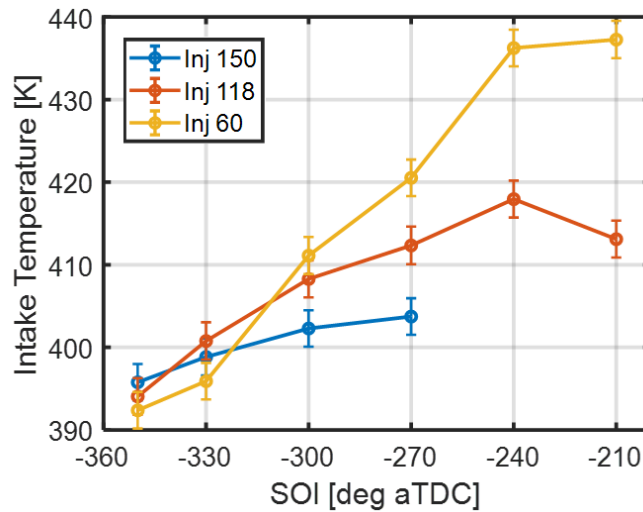


Figure 42: Intake temperature requirement to maintain  $CA_{50}$  at a constant value of  $7.0 \pm 0.5$  deg aTDC vs. start of injection (SOI) timing for all three injectors with the re-entrant bowl piston.

With the optimal injection timing to deliver fuel during the intake stroke identified for each injector, it is now of interest to study how the combustion process is affected by compression stroke injections. To do this, the injection timing of compression stroke injections is swept. Two compression stroke injections will be used to deliver the fuel to avoid overcooling regions targeted by the spray. The split fraction, which



is the percentage of the total fuel that is injected during the intake stroke, is 80%. In this sweep, the global equivalence ratio is held at  $0.5 \pm 0.01$  and CA50 is held at  $7.0 \pm 0.5$  deg aTDC by adjusting the intake temperature. The background equivalence ratio, i.e. the equivalence ratio after the intake stroke injection, was 0.4. The two compression stroke injections are always 20 degrees from each other with a 50/50 fuel mass split between them. Therefore, when referring to a set of compression stroke injection timings, e.g. -130 and -110 deg aTDC, the average of the two injection timings will be used, e.g. -120 deg aTDC. The set of compression stroke injections is swept from -140 to -40 deg aTDC in increments of 20 degrees.

Figure 43 shows the CA25-75 burn duration for each injector across the compression stroke injection timing sweep. Burn duration is a useful metric to assess the increase of thermal stratification in the cylinder since the heat release process is dictated by thermal stratification, i.e., an increase in burn duration implies an increase in thermal stratification. For the 150° injector, as the compression stroke injections are phased later from -140 to -80 deg aTDC, the burn duration steadily increases, reaching a nearly constant value of  $\sim 6^\circ$  for compression stroke injection timings between -80 and -40 deg aTDC. This is a factor of 1.8x larger than the burn duration of the -140 deg aTDC case,  $3.4^\circ$ . Since it has been shown that very early compression stroke injections, like -140 deg aTDC, do not appreciably alter thermal stratification, this is equivalent to saying that the burn duration for compression stroke injection timings between -80 deg and -40 deg aTDC are a factor of 1.8x larger than that of an HCCI case. These results agree with previous compression stroke injection sweep results performed with this injector and piston geometry. As shown in previous CFD results presented in Ref. [98], compression stroke injections with the 150° injector target the squish region, a region with locally high heat transfer losses and lower average temperatures. Therefore, targeting this region will increase the in-cylinder thermal stratification by working with the natural thermal stratification and cooling the regions that would naturally be cooler due to the geometry of the combustion chamber, thereby increasing the burn duration.

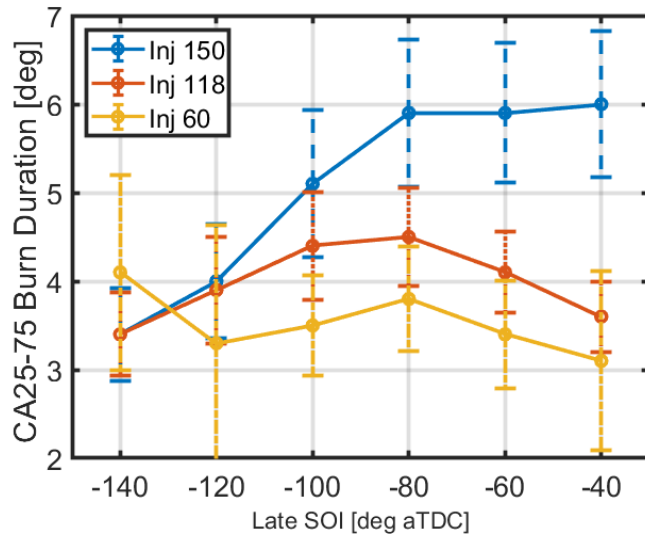


Figure 43: CA25-75 burn duration vs. average compression stroke start of injection (SOI) timing for a split fraction of 80% for all three injectors with the re-entrant bowl piston geometry. There are two compression stroke injections, spaced 20 degrees apart from each other and each injecting an equal amount of fuel. -140 deg aTDC on the x-axis corresponds to a set of compression stroke injections at -150 and -130 deg aTDC.

The 118° injector has a burn duration similar to the 150° injector for compression stroke injection timings of -140 and -120 deg aTDC. However, unlike the 150° injector, the burn duration for the 118° injector does not continue to steadily increase as the compression stroke injection timing is retarded further. Rather, the burn duration plateaus at ~4.5° at -80 deg aTDC, only a factor of 1.3x larger than the burn duration at -140 deg aTDC (3.4°). Then, the burn duration actually decreases as the compression stroke injection timing is further retarded to -40 deg aTDC. Ref. [98] showed that, contrary to targeting the squish region, compression stroke injections that target the inside of the piston bowl, a region with relatively lower heat transfer, can actually reduce in-cylinder thermal stratification, thereby decreasing the burn duration. The negative-inflection parabolic in burn duration displayed by the 118° injector can be attributed to the following: “early” compression stroke injection timings will target the squish region and increase thermal stratification. However, near -100 to -80 deg aTDC, the compression stroke injections will start to shift from targeting the squish region to targeting the bowl region. By -40 deg aTDC, the compression stroke injection is primarily targeting the bowl, resulting in a similar burn duration to the -140 deg aTDC case.

Therefore, the 118° injector can be used to increase thermal stratification slightly, though not as effectively as the 150° injector and without as wide of a region with high controllability.

Finally, considering the uncertainty in the burn duration, the 60° injector shows relative invariance in the burn duration across all compression stroke injection timings. Even at early timings, such as -140 deg aTDC and -120 deg aTDC, the 60° injector primarily targets the inside of the piston bowl. Therefore, the 60° injector is ineffective at controlling the heat release process via increasing natural thermal stratification. In order for the 60° injector to effectively control the heat release process in TSCI, the amount of cooling potential introduced during the compression stroke would have to first overpower natural thermal stratification and then force the level of thermal stratification needed to stage the combustion process as desired. While this is possible with a non-combustible liquid like water, it is difficult to do with a water-fuel mixture, since the amount of fuel needed to overpower natural thermal stratification could create locally rich and stoichiometric regions in the cylinder that will produce soot and NO<sub>x</sub>, respectively.

Alternatively, the 60° injector would actually be an ideal injector to enable a combustion mode like PFS. Similar to how TSCI aims to work with natural thermal stratification, enhancing it as needed to provide control over the combustion process, PFS may have to work against thermal stratification, since the rich areas that are supposed to ignite first in PFS may be colder than the lean regions that are intended to ignite later due to evaporative cooling of the direct injected fuel. For this reason, PFS and TSCI have opposite needs when it comes to injector spray angle. Using the 60° injector in PFS could potentially be optimal since this injector targets the hottest regions in the cylinder during the compression stroke.

### **3.2.5 Injector Spray Angle – Shallow Bowl Piston**

Switching focus to the shallow bowl piston, it is first of interest to determine if the optimal intake stroke injection timing for each injector is the same as it is for the re-entrant bowl piston geometry. To do this, an injection timing sweep, identical to Section 3.1.1, is performed for all three injectors experimentally. Once again, equivalence ratio is held at  $0.41 \pm 0.01$  and CA50 is held at  $7.0 \pm 0.5$  deg aTDC by adjusting the

intake temperature. The injection timing with the highest combustion efficiency will be selected as the optimal point.

Figure 44 shows the combustion efficiency for each injector vs. the start of injection timing, similar to Figure 41. First, it should be noted that an injection timing of -350 deg aTDC was not included – this is because for all three injectors, the combustion efficiency was near 80% or less. The 150° injector shows the same trend with this piston as it did with the re-entrant bowl piston: the combustion efficiency monotonically decreases as injection timing is retarded. Therefore, for the 150° injector, -330 deg aTDC is selected as the optimal injection timing.

For both the 118° and the 60° injector, -330 deg aTDC does not provide the highest combustion efficiency. The highest combustion efficiency for the 60° injector comes at -270 deg aTDC, the same as with the re-entrant bowl geometry. The 118° injector has a nearly constant peak in combustion efficiency at -300 deg aTDC and -270 deg aTDC. -270 deg aTDC is selected as the optimal injection timing for the 118° injector so that it is the same as the 60° injector. It should be noted that the peak combustion efficiency for the 118° injector is lower than that of the 150° and 60° injectors. This was not the case with the re-entrant bowl geometry, which had a nearly identical peak combustion efficiency across all three injectors.

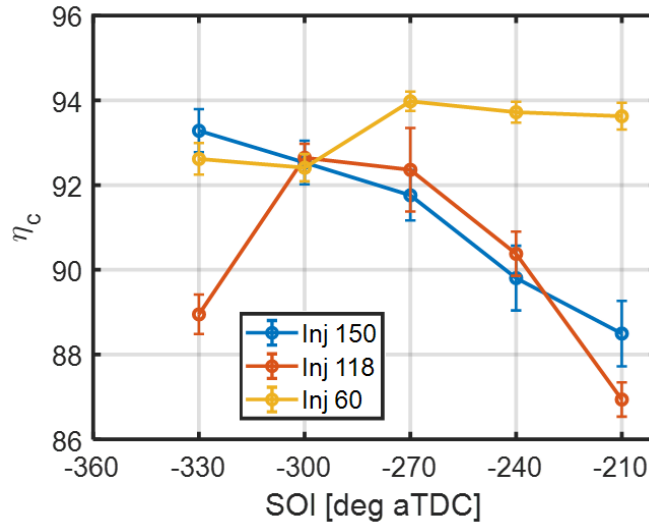


Figure 44: Combustion efficiency ( $\eta_c$ ) vs. start of injection (SOI) timing for all three injectors with the shallow bowl piston geometry. The injection timing with the highest combustion efficiency is considered the optimal injection timing for delivering fuel during the intake stroke.

Now that the optimal injection timing to deliver fuel during the intake stroke has been identified for each injector with the shallow bowl piston, it is again of interest to study how the combustion process is affected by compression stroke injections for each injector. Like Section 3.1.2, the injection timing of two compression stroke injections are swept. The two injections are spaced 20 degrees apart and split the total fuel injected during the compression stroke 50/50. The split fraction chosen is 80%, with 80% of the fuel injected during the intake stroke with a single injection at the optimal injection timing found in Section 3.2.1: -330 deg aTDC for the 150° injector and -270 deg aTDC for the 118° and the 60° injector. Throughout the sweep, the equivalence ratio is held at  $0.5 \pm 0.01$  and CA50 is held at  $7.0 \pm 0.5$  deg aTDC by adjusting the intake temperature.

Figure 45 displays the CA25-75 burn duration vs. compression stroke average start of injection timing for each injector. The 150° and 60° injectors have a similar trend with the shallow bowl piston as they do with the re-entrant bowl piston. The compression stroke average start of injection timing provides controllability over the burn duration with the 150° injector and does not with the 60° injector. With the re-entrant bowl piston, the 118° injector had the ability to slightly control the combustion process by enhancing

natural thermal stratification between -140 and -100 deg aTDC. Now, with the shallow bowl piston, it appears that the 118° injector is no longer capable of doing so. Instead, the burn duration remains nearly constant throughout the injection timing sweep, meaning the 118° injector cannot provide any control over the heat release process with compression stroke injections that have this amount of cooling potential. This may be due to the lack of bulk motion induced by piston geometry which would lead to poor mixing characteristics, as suggested by Ref. [99].

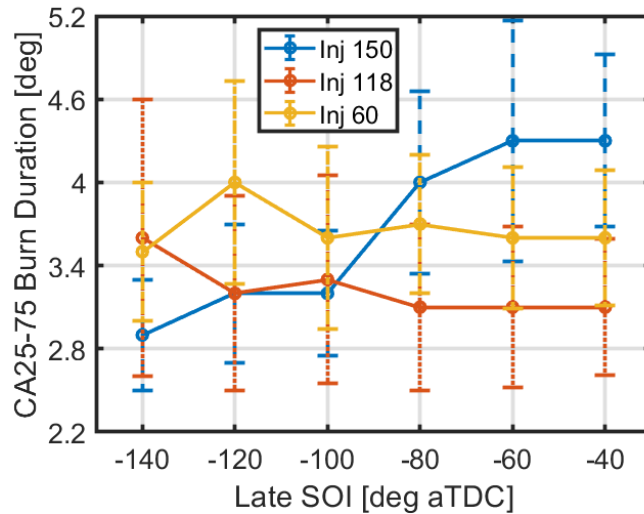


Figure 45: CA25-75 burn duration vs. average compression stroke start of injection (SOI) timing for a split fraction of 80% for all three injectors with the shallow bowl piston geometry. There are two compression stroke injections, spaced 20 degrees apart from each other, each injecting an equal amount of fuel. -140 deg aTDC on the x-axis corresponds to a set of compression stroke injections at -150 and -130 deg aTDC.

### 3.2.6 Comparison of Piston Geometries - 150° Injector

Considering the combustion efficiency values during the intake stroke injection timing sweeps, the shallow bowl piston generally had higher values than that of the re-entrant bowl piston for all three injectors. Similarly, the values for burn duration for all three injectors are generally lower with the shallow bowl piston than the re-entrant bowl piston. To further investigate this, identical operating conditions across both piston geometries are compared in this section. The 150° injector is selected since it was the only injector that could enable TSCI with a split injection strategy for both piston geometries. First, DI HCCI is compared

by considering the optimal injection timing case from Sections 3.1.1 and 3.2.1. The in-cylinder pressure trace and gross heat release rate (GHRR) trace for each case are shown in Figure 46. Table 6 displays operating conditions and combustion results for the two cases.

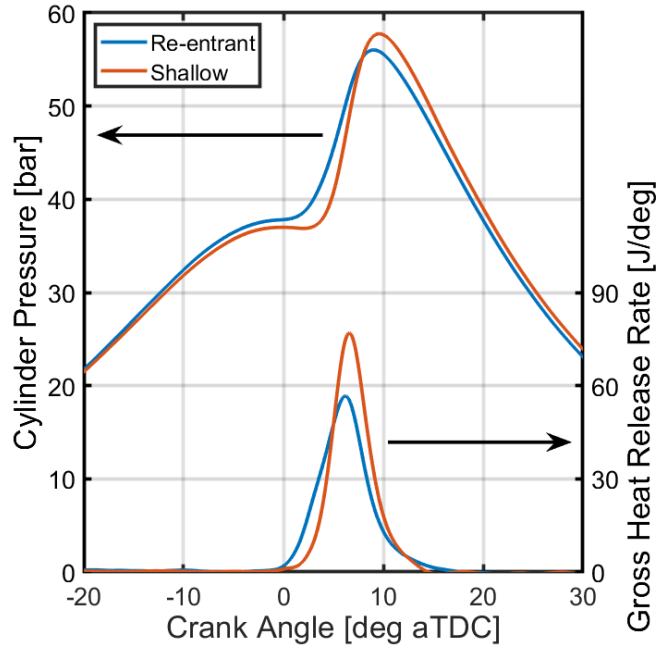


Figure 46: Cylinder pressure and gross heat release rate plotted vs. crank angle for both piston geometries: re-entrant and shallow bowl. The 150° injector is used to deliver fuel at the optimal injection timing determined in Section 3.1.1 for the re-entrant bowl piston (-350 deg aTDC) and in Section 3.2.1 for the shallow bowl piston (-330 deg aTDC).

Table 6: Operating parameters and combustion results for two DI HCCI cases comparing piston geometry: re-entrant vs. shallow. The 150° injector is used for both cases.

		Re-entrant	Shallow
SOI	[deg aTDC]	-350	-330
Inj. Duration	[ms]	0.86	0.86
$\phi$	--	$0.410 \pm 0.01$	$0.416 \pm 0.01$
IMEP <sub>g</sub>	[bar]	$3.56 \pm 0.04$	$3.80 \pm 0.04$
CA50	[deg]	$6.7 \pm 0.5$	$7.1 \pm 0.5$
CA25-75 Burn Dur.	[deg]	$3.1 \pm 0.5$	$4.5 \pm 0.5$
Intake Temp.	[K]	$395.8 \pm 2.2$	$397.7 \pm 2.2$
Exhaust Temp	[K]	$534.6 \pm 2.2$	$557.4 \pm 2.2$
Comb Eff.	[%]	$90.6 \pm 0.5$	$93.3 \pm 0.5$
Thermal Eff.	[%]	$42.6 \pm 1.1$	$43.3 \pm 0.8$
Fuel Conv. Eff.	[%]	$38.3 \pm 1.1$	$40.2 \pm 0.8$

MPRR	[bar/deg]	$4.0 \pm 0.7$	$5.8 \pm 0.7$
------	-----------	---------------	---------------

Examining Figure 46, it can immediately be seen that the shallow bowl piston has a sharper, narrower heat release rate shape than the re-entrant bowl piston, which manifests as a later ignition timing, a higher peak pressure, and a higher pressure throughout the expansion stroke. It is true that with near identical CA50s, the burn duration of the shallow bowl piston is ~70% that of the re-entrant bowl piston. This means that there is less natural thermal stratification produced with the shallow bowl piston geometry. Intuitively, this is because the shallow bowl piston's design is well suited for low temperature combustion by reducing the surface-to-volume ratio, thereby reducing heat transfer. However, since heat transfer is the mechanism with which natural thermal stratification forms during the compression stroke, this reduction in heat transfer will reduce natural thermal stratification, making the HCCI combustion process occur more quickly and violently. While this can have advantages, such as yielding a higher combustion efficiency (93.3% vs. 90.6%), which agrees with results from Ref. [100, 101], higher thermal efficiency (43.3% vs. 42.6%), and therefore a significantly higher fuel conversion efficiency (40.2% vs. 38.3%), as seen in Table 6, it can also be detrimental to the engine, given that a quicker combustion process will result in damaging energy release rates. For example, the maximum pressure rise rate (MPRR) for the shallow bowl piston case is 5.8 bar/deg, which is outside of the acceptable MPRR limit of 5 bar/deg outlined in Ref. [13]. If the intake temperature is reduced to retard combustion phasing to 8.9 deg aTDC to obtain an MPRR of 4.1 bar/deg, which is nearly the same value as the re-entrant bowl piston case (4.0 bar/deg), the efficiency benefits diminish, with combustion, thermal, and fuel conversion efficiency now being 91.2%, 42.5%, and 38.7%, respectively. Fuel conversion efficiency is now only marginally better with the shallow bowl piston, and the expected HCCI load range will be narrower.

Considering now TSCI, the compression stroke injection timing sweeps for the 150° injector for each piston, shown in Section 3.1.2 for the re-entrant bowl piston and Section 3.2.2 for the shallow bowl piston, are replotted together in Figure 47. Both pistons display a similar near-linear controllability range over the burn duration by adjusting the compression stroke injection timing between -140 and -80 deg



aTDC. However, the re-entrant bowl piston displays a higher sensitivity (i.e. larger slope) to compression stroke injection timing than the shallow bowl piston. Further, the re-entrant bowl piston has a larger injection timing window where the burn duration is largest and nearly constant (-80 to -40 deg aTDC) than the shallow bowl piston, which is useful when multiple compression stroke injections are needed to deliver the required mass of fuel while avoiding combustion efficiency penalties. Not only does the shallow bowl piston geometry have a shorter burn duration in HCCI than the re-entrant bowl piston geometry, but the ability of compression stroke injections to extend the burn duration is lower. From a minimum of  $2.9^\circ$  at -140 deg aTDC, equivalent to that of an HCCI case [74], to a maximum of  $4.4^\circ$  at -60 deg aTDC, the burn duration is increased by a factor of 1.5x, less than the factor of 1.8x achieved with the re-entrant bowl piston geometry.

The reason that the re-entrant bowl piston is more effective at elongating the burn duration in TSCI with a wide-angle injector is because of the natural thermal stratification that exists in the cylinder and the difference in heat transfer between the squish and bowl regions of the combustion chamber. It was found in Ref. [98] that with the re-entrant bowl piston, there was a strong divide in bulk properties inside the piston bowl vs. in the squish region. Therefore, using the fuel spray to cool the squish region during the compression stroke will increase the natural thermal stratification that results from this piston geometry. However, targeting the fuel spray into the piston bowl will attempt to cool the region of the cylinder that naturally would have been warmer: the bowl region. Attempting to overpower the natural thermal stratification with the compression stroke injection is not as effective as using the compression stroke injection to work with the natural thermal stratification and further cool the regions that would naturally be cooler. The shallow bowl piston also has regions that are warmer or cooler based on heat transfer differences and the shape of the piston, but the temperature distribution in the shallow bowl piston is not quite segregated into a cool squish region and a warm bowl region like the re-entrant bowl piston. Therefore, it is much more difficult to simply target a specific region in the cylinder to maximize the effectiveness of a

compression stroke injection in enhancing thermal stratification. This explanation agrees well with the CFD simulation results found in Ref. [98].

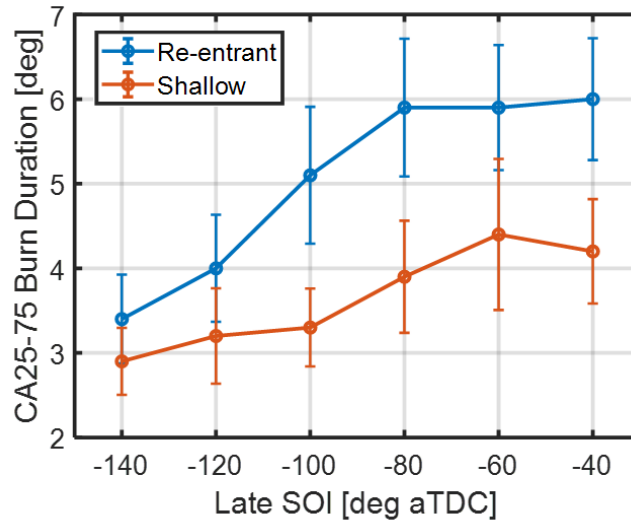


Figure 47: CA25-75 burn duration vs. average compression stroke start of injection (SOI) timing for a split fraction of 80% for both the re-entrant bowl and the shallow bowl piston geometry with the 150° injector. There are two compression stroke injections, spaced 20 degrees apart from each other, each one injecting an equal amount of fuel. -140 deg aTDC on the x-axis corresponds to a set of compression stroke injections at -150 and -130 deg aTDC.

Comparing the emissions characteristics of both piston geometries, Figure 48 displays the emissions index (EI) of CO and uHC vs. the average start of injection timing. The re-entrant bowl piston consistently has higher amounts of uHC and CO than the shallow bowl piston, which agrees with the results shown above that the re-entrant bowl piston has a lower overall combustion efficiency due to its large squish region. When using the re-entrant bowl piston with the 150°, injector the spray targets the squish region at all late injection timings. The fuel in the squish region is more likely to be too cold to fully oxidize. Since a later injection timing implies less time for the fuel to mix and be expelled from the squish region by the squish motion, both uHC and CO emissions tend to increase as the compression stroke injection timing is retarded. There is also possible wall wetting and crevice flow to consider, since the spray is aimed at the walls. This explains why the CO and uHC emissions also tend to increase as the compression stroke injection timing is retarded for the shallow bowl piston, which does not have a large squish region.

Interestingly, as injection timing is further retarded from -80 deg aTDC with the shallow bowl piston, the uHC emissions begin to decrease while the CO continues to increase. This is likely due to higher in-cylinder pressures and temperatures at the time of injection providing more favorable spray breakup and evaporation conditions, reducing the spray penetration length and minimizing wall wetting and fuel flow into the crevices, which is the primary source of uHC emissions. Rich regions are still cold, however, and may still suffer from incomplete oxidation of fuel, hence the CO emissions continuing to rise.

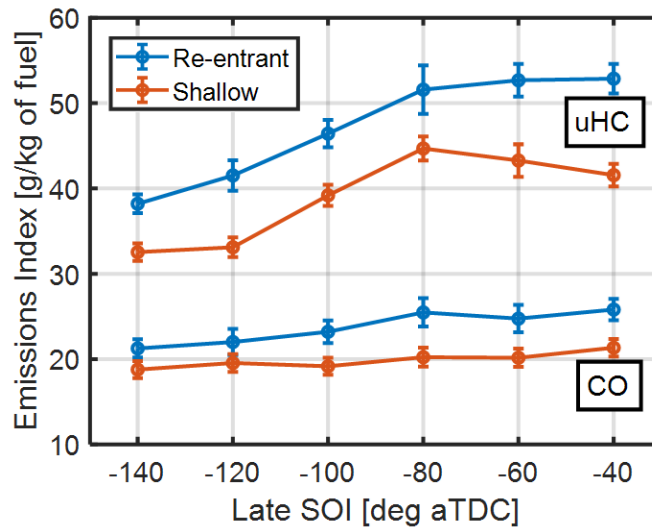


Figure 48: Emissions index of both CO and unburned hydrocarbons (uHC) vs. average compression stroke start of injection (SOI) timing for a split fraction of 80% for both the re-entrant bowl and the shallow bowl piston geometry with the 150° injector. There are two compression stroke injections, spaced 20 degrees apart from each other, each one injecting an equal amount of fuel. -140 deg aTDC on the x-axis corresponds to a set of compression stroke injections at -150 and -130 deg aTDC.

It can be concluded that not only is the natural thermal stratification lower, but the effectiveness of a compression stroke injection to increase thermal stratification is lower with a shallow bowl piston than it is with a re-entrant bowl piston. It is recommended that TSCI with wet ethanol 80 be used with a re-entrant bowl or similar piston geometry and an injector that can target the regions with the lowest local surface-to-volume ratio in the cylinder. If TSCI is desired to be enabled with a shallow bowl or similar piston geometry, a water-fuel mixture with a higher cooling potential could be employed, such as a wet ethanol blend with more water, with an injector that can target the regions with the highest rate of heat transfer in

the cylinder. Alternatively, a non-combustible liquid could be employed with any injector. It is still recommended that an injector that can target the regions with the highest rate of heat transfer in the cylinder when using a non-combustible liquid to avoid a significant drop in thermal efficiency due to heat absorption during the compression stroke.

### **3.3 High Load LTC with Wet Ethanol – Light-Duty Gasoline Engine Architecture**

#### **3.3.1 Load range characterization of intake stroke injections**

TSCI was effectively enabled on a diesel engine architecture using a split injection strategy. It was found that injector spray angle and piston geometry played a significant role in the effectiveness of the split injection strategy to control the heat release process and enable high load LTC. It is of interest to determine whether a split injection strategy could effectively enable TSCI on a gasoline engine architecture. With the gasoline engine architecture, the injector is a single hole, side mounted injector, contrasting the multi-hole, centrally mounted injector used in the diesel engine architecture. Additionally, the injection pressure used in the gasoline engine architecture is 100 bar, much lower than the 500 bar used in the diesel engine architecture. As a result, it is likely that achieving high load LTC using wet ethanol on the gasoline engine architecture considered will require a different strategy than previously used.

In previous work on the diesel engine architecture, the load range of HCCI was characterized experimentally, followed by a demonstration of load range extension using either direct water injection or a split injection strategy of wet ethanol. With direct water injection, the fuel is premixed in the port. However, with a split injection strategy, the premixed fuel is delivered during the intake stroke through one or more direct injection events. Since this work proposes a water-fuel mixture to extend the high-load limit of LTC, the load range of a single intake stroke injection of wet ethanol was characterized first. The optimal injection timing was found via an experimental injection timing sweep at an engine speed of 1200 rpm. In this sweep, CA50 was held constant at  $7.0 \pm 0.5$  deg aTDC by adjusting the intake air temperature, holding the residual rate at a constant 25%. Figure 49 displays the combustion efficiency results over the injection timing sweep. It is seen here that the combustion efficiency is largely unaffected by changes in injection

timing on the GDI engine architecture. In previous work, it was imperative to inject the fuel into the piston bowl to minimize wall impingement; therefore, the combustion efficiency was highly sensitive to the start of injection timing during the intake stroke. In contrast, this GDI engine employs a side-mounted GDI-style injector with a narrow spray included angle and a piston that lacks a deep bowl and squish region. Since combustion efficiency is largely unaffected by injection timing in Figure 49, the injection timing -320 deg aTDC is selected for further studies.

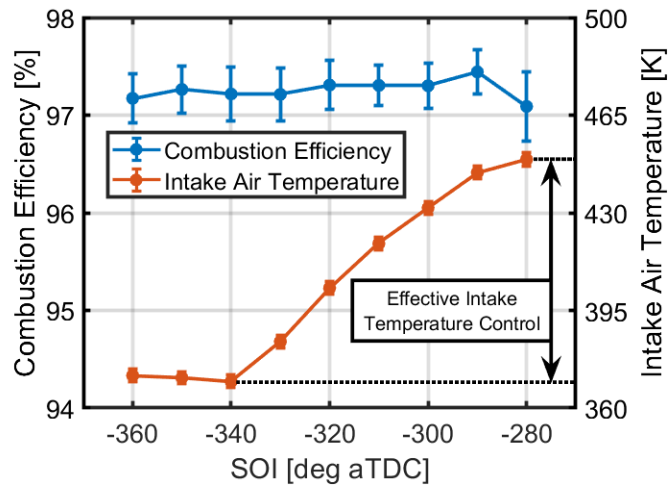


*Figure 49: Combustion efficiency and intake temperature vs. start of injection (SOI) timing during the intake stroke to characterize the optimal injection timing for the introduction of fuel during the intake stroke and showing a large range of effective intake valve closing temperature control*

Another interesting result of this injection timing sweep is the large range of intake air temperature required to maintain a constant combustion phasing, also shown in Figure 49. As detailed above, in HCCI, a constant combustion phasing implies a constant temperature at intake valve closing. Therefore, the large range of intake air temperatures measured upstream of the port is a result of the injection timing modulating the amount of fuel that evaporates off of the cylinder walls and piston crown vs. evaporating in the incoming air and trapped residual gases, i.e., a higher intake temperature is required when more fuel evaporates in the air. With this in mind, the injection timing can be used as a control mechanism, providing cycle-to-cycle control over combustion phasing.

With -320 deg aTDC selected as the intake stroke injection timing, next, a load sweep was performed at an engine speed of 1200 rpm. Combustion phasing was again held constant at  $7.0 \pm 0.5$  deg aTDC by adjusting the intake temperature, while holding the residual rate at 25%. The low-load limit is governed by a coefficient of variation (COV) of indicated mean effective pressure (IMEPg) of 5%. The high-load limit is set at a ringing index (RI) threshold of 2.5 MW/m<sup>2</sup>. RI is used instead of maximum pressure rise rate (MPRR) to give a fairer comparison across different engine speeds and intake pressure levels [96]. While the typical high-load limit of HCCI with wet ethanol would be around 4-4.5 bar, the high-load limit found in this early direct injection load sweep was nearly 7 bar. This result was highly unexpected and unlike the behavior of gasoline HCCI on this engine [101]. It was presumed that the intake stroke injection of wet ethanol was not completely mixing with the incoming air, resulting in a stratified mixture at TDC that staged the combustion process, allowing for higher loads than typical HCCI.

To test this theory, a load sweep of wet ethanol 80 was performed using the upstream fuel vaporizer, eliminating any stratification induced by the direct injection of fuel. The resulting high load limit was ~4.5 bar, in the expected range for pure HCCI operation with wet ethanol. This proved that the direct injection of wet ethanol during the intake stroke did not completely mix with the incoming air and residuals, resulting in inhomogeneities around TDC that staggered ignition timing and extended the high load limit of LTC. This conclusion is distinct from the previous experimental work on the diesel engine architecture which did not show any indications of inhomogeneity around TDC, presumably due to a difference in turbulent mixing during the intake and compression stroke

The ringing intensity vs. load for both the vaporizer and the early direct injection cases are shown in Figure 50. In addition, loads sweeps were performed with both methods of fuel delivery at a higher engine speed of 2400 rpm to ensure that this phenomenon was not an artifact of low engine speed. The load range at 2400 rpm is similarly extended, albeit with higher ringing intensities and an operating range that is correspondingly shifted toward lower loads than seen at 1200 rpm.

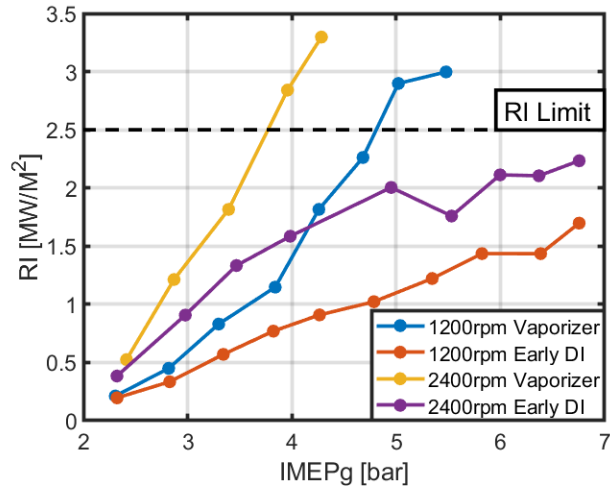


Figure 50: Ringing intensity (RI) vs.  $IMEP_g$  for both fueling methods at 1200 rpm and 2400 rpm. A reference line a  $2.2 \text{ MW/m}^2$  represents the high-load ringing intensity limit.

Upon further examination of Figure 50, it can be seen that at the low-load limit, the ringing intensity is nearly the same for both modes of fuel delivery. However, as load increases, ringing intensity increases more rapidly for the vaporizer-fueled cases than the direct injection cases. This implies an increase in stratification that extends the heat release process as more fuel is injected, as seen by examining the trends in burn duration in Figure 51. Here, the burn duration is defined as the crank angle duration between CA25 and CA75. This definition of burn duration was chosen over the more commonly used CA10 to CA90 definition so that this work can be easily compared to previous wet ethanol TSCI work, which used CA25 to CA75 to capture the bulk of the heat release process rather than the behavior or the tails.

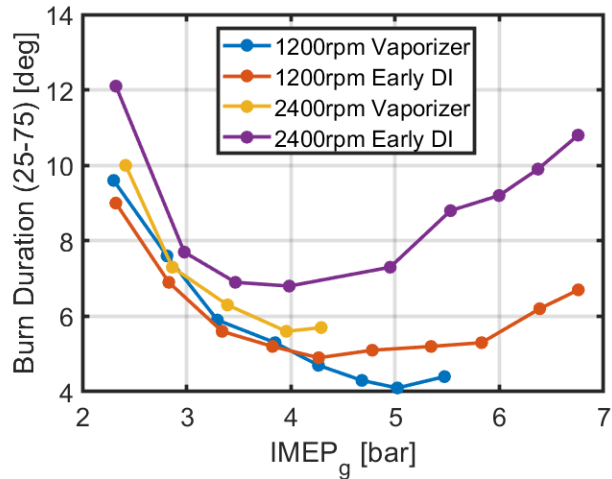


Figure 51: 25-75% burn duration vs.  $IMEP_g$  for both fueling methods at 1200 rpm and 2400 rpm.

Based on the load limits, the RI results, and the burn durations, it is hypothesized that the wet ethanol that is direct injected during the intake stroke is not fully mixing with the incoming air and residuals, resulting in increased thermal stratification around TDC. This could be due to some combination of the high heat of vaporization of wet ethanol (most likely resulting in longer spray penetration lengths), the single-hole injector, rebreath operation, and the relatively low injection pressure. While this is beneficial, the lack of independent control over the level of thermal stratification and the load, which are coupled through the intake stroke injection, is undesirable.

A lack of control authority over the stratification induced from intake stroke injections can have a negative impact on emissions. Injections of fuel that stratify the cylinder create a coupled  $\phi$ -temperature distribution in the cylinder. Since there is evidence of induced thermal stratification from the early direct injection of wet ethanol, there is likely a coupled  $\phi$ -stratification field. The nature of this coupled stratification becomes clearer when the emissions results are examined. Figure 52a), b), and c) display the combustion efficiency, indicated specific (IS) emissions of uHC/CO, and NO<sub>x</sub> for both 1200 rpm load sweeps, respectively. The 2400 rpm load sweeps are omitted for conciseness, but they show the same trends.

As expected, at low loads, large quantities of uHC and CO are produced, resulting in low combustion efficiency. As load increases, combustion efficiency increases. For the vaporizer load sweep,



this trend continues through a load of 5.5 bar, where the load sweep was truncated for engine safety. For the early DI load sweep, as the load is increased past 5.5 bar, the combustion efficiency begins to decrease. This decrease in combustion efficiency is not due to an increase in uHC, but rather a stark increase in CO. The reason this occurs can be seen by considering Figure 53, which plots both fuel-air equivalence ratio ( $\phi$ ) and charge-mass equivalence ratio ( $\phi'$ ) vs. load for both fuel preparation load sweeps at 1200 rpm. Charge-mass equivalence ratio is a metric that considers both air and residual gases in its calculation and is related to fuel-air equivalence ratio by the equation:  $\phi' = \phi \cdot (1 - \text{residual rate})$ . The increase in CO emissions corresponds to the point when the global  $\phi$  increases above 0.8. This implies that there is significant enough  $\phi$ -stratification to produce locally rich regions that cannot support complete fuel oxidation above a global  $\phi$  of 0.8. Note that uHC emissions do not increase when CO emissions increase, as there is still enough oxygen in locally rich regions, including the fuel bound oxygen, for the ethanol to oxidize to CO. Therefore, if the amount of induced stratification could be controlled independently of the load, the onset of CO formation could be delayed.

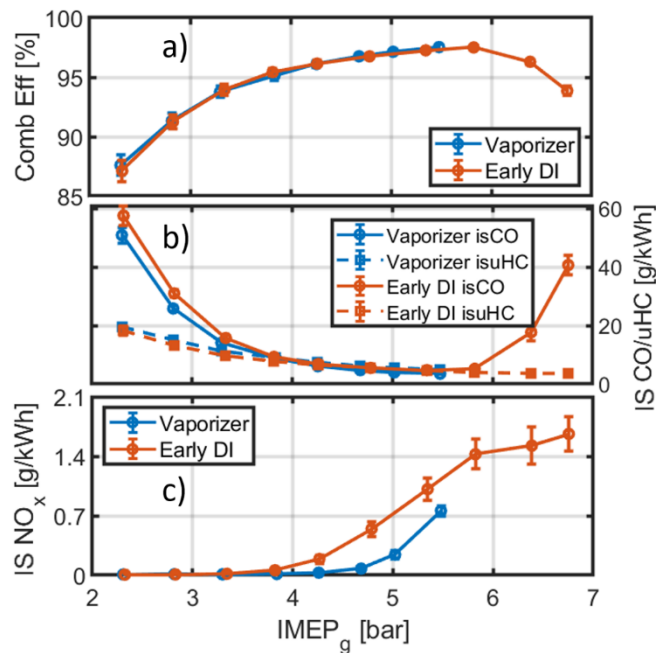


Figure 52: a) Combustion efficiency, b) indicated specific emissions (IS) of CO/uHC, and c) is NO<sub>x</sub> vs. IMEP<sub>g</sub> for both fueling methods at 1200 rpm. Trends are identical at 2400 rpm (not shown for conciseness).

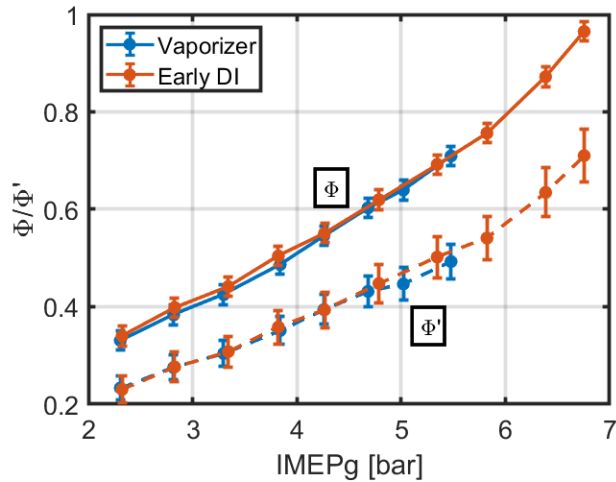


Figure 53:  $\phi$  (solid) and  $\phi$ -prime (dashed) vs. IMEP<sub>g</sub> for both fueling methods at 1200 rpm (trends are identical at 2400 rpm)

Like CO formation, NO<sub>x</sub> formation is governed by local conditions; for NO<sub>x</sub>, it is the local temperature, and therefore, the local charge-mass equivalence ratio is a strong indicator of thermal NO<sub>x</sub>, since residuals can act as a heat sink. NO<sub>x</sub> formation occurs earlier in the load sweep than CO formation, even when considering that  $\phi'$  is lower than  $\phi$ , since NO<sub>x</sub> formation occurs when regions are slightly lean of stoichiometry whereas CO formation occurs when regions are slightly rich of stoichiometry. With the vaporizer, load conditions do not form significant NO<sub>x</sub> lower than 5 bar IMEP<sub>g</sub>; for early DI cases, NO<sub>x</sub> forms as early as 4 bar, providing further evidence that the cylinder contents are somewhat stratified for the early DI cases. As with the onset of CO formation, the onset of NO<sub>x</sub> formation could be delayed by reducing the amount of stratification induced.

### 3.3.2 Using swirl to reduce in-cylinder stratification

In order to identify a mechanism of controlling the in-cylinder stratification induced by an early direct injection of a high latent heat of vaporization fuel into a quiescent combustion chamber, a more fundamental understanding is necessary.

Based on the apparent inhomogeneity around TDC, it was hypothesized that this combustion chamber must be relatively quiescent and does not naturally provide enough bulk motion during the intake

and compression stroke to completely premix the charge. One way to test this hypothesis is to significantly increase bulk motion during the intake process via swirl.

Swirl is defined as the ratio of angular momentum of the incoming charge to its axial momentum [84]. Due to the low viscosity of the charge and the short timescales associated with an engine cycle, the majority of the angular momentum of the incoming charge does not dissipate. Instead, this rotational flow persists throughout gas exchange and into the closed portion of the cycle. Increasing swirl has been shown to reduce the combustion duration in advanced stratified combustion modes by enhancing fuel-air mixing during the compression stroke [103, 104].

To test the hypothesis that a lack of bulk motion results in significant stratification of the early direct injected wet ethanol, early direct injection data is collected with the addition of swirl. The swirl ratio of the engine without modification is 0.5. For this comparison, the swirl ratio is increased to 2.5 using a swirl control valve, which partially closes access to one of the two intake ports. Figure 54 displays the cylinder pressure and gross heat release rate (GHRR) traces for three cases: 1) a vaporizer-fueled case with low swirl, 2) an early DI-fueled case with low swirl, and 3) an early DI-fueled case with high swirl. These three cases have the same combustion phasing and fueling rate, at  $7.0 \pm 0.5$  deg aTDC and  $\sim 36.0 \pm 0.5$  mg/cycle, respectively, holding the residual rate constant at 25%. Detailed operating conditions and results can be found in Table 7.

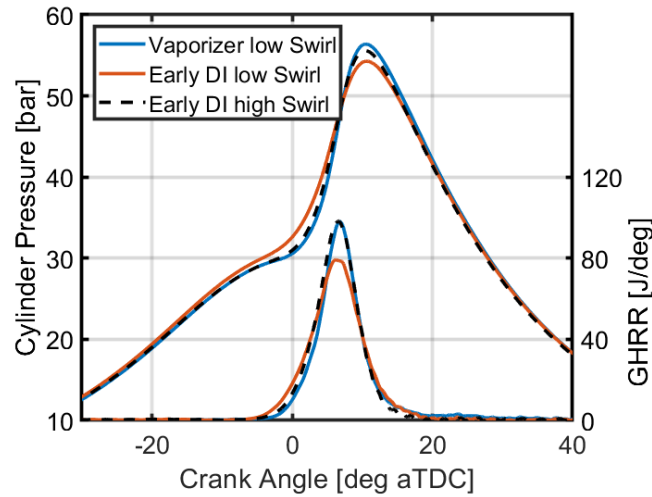


Figure 54: Cylinder pressure and gross heat release rate (GHRR) traces vs. crank angle degrees for vaporizer-fueled combustion with low swirl, early (-320 deg aTDC SOI) direct injection-fueled combustion with low swirl, and early direct injection fueled combustion with a swirl ratio of 2.5. CA50 is maintained at  $7.0 \pm 0.5$  deg aTDC by adjusting intake temperature and fueling rate is maintained at  $\sim 36.0 \pm 0.5$  mg/cycle.

Table 7: Operating conditions and results for low vs. high swirl comparison.

		Vaporizer with low Swirl	Early DI with low swirl	Early DI with high swirl
Swirl Ratio	[-]	0.5	0.5	2.5
IMEPg	[bar]	$5.48 \pm 0.04$	$5.35 \pm 0.04$	$5.32 \pm 0.04$
Phi	[-]	$0.71 \pm 0.01$	$0.71 \pm 0.01$	$0.71 \pm 0.01$
Inj Mass	[mg/cycle]	$35.8 \pm 0.5$	$36.1 \pm 0.5$	$36.2 \pm 0.5$
Thermal Efficiency	[%]	$40.7 \pm 1.2$	$40.1 \pm 1.3$	$38.8 \pm 1.3$
Combustion Efficiency	[%]	$97.5 \pm 0.2$	$97.3 \pm 0.2$	$97.8 \pm 0.2$
Burn Duration (25-75)	[deg]	$4.4 \pm 1.0$	$5.7 \pm 1.4$	$4.3 \pm 1.1$
Burn Duration 10-90)	[deg]	$7.7 \pm 1.9$	$9.3 \pm 2.6$	$7.0 \pm 2.1$
MRR	[bar/deg]	6.1	3.5	5.1
COV of MRR	[%]	24%	21%	20%
RI	[MW/m <sup>2</sup> ]	2.9	1.1	2.1
COV of RI	[%]	35%	34%	29%
is CO	[g/kWh]	$3.5 \pm 0.2$	$4.8 \pm 0.2$	$3.9 \pm 0.2$
is uHC	[g/kWh]	$4.8 \pm 0.5$	$4.6 \pm 0.5$	$3.8 \pm 0.5$
is NOx	[g/kWh]	$0.8 \pm 0.3$	$1.0 \pm 0.2$	$1.6 \pm 0.1$

As explained above, when the fueling method is switched from the vaporizer to early DI, the combustion process elongates, resulting a wider GHRR profile with a lower peak. When the swirl ratio is increased to 2.5, the heat release process of the early DI case appears nearly identical to the low swirl vaporizer case. This implies that the significant increase in swirl provided enough bulk charge motion to premix the fuel and air during the intake stroke. Although there may be some remaining inhomogeneities, the remaining forced thermal stratification is a small fraction of the natural thermal stratification and does not significantly affect the combustion process.

Although the heat release process of the vaporizer-fueled case and the early DI with high swirl case look nearly identical, the peak pressure of the early DI with high swirl case is lower. This lower peak pressure is due to the higher heat transfer that results from increasing swirl. As a result, the thermal efficiency is also lower with swirl. Although swirl could potentially be a mechanism for controlling induced stratification during the intake stroke, the efficiency penalty is significant.

### **3.3.3 Controlling in-cylinder stratification with a premixed/direct injection split**

Although swirl could be used as a control mechanism over the induced stratification from early DI of wet ethanol, its efficiency penalty makes it less than ideal; therefore, another possible candidate must be identified. This Section explores the effects of introducing a portion of the fuel in the port, such that only the required amount of fuel needed to induce the desired stratification is direct injected during the intake stroke. While this would require two separate injectors per cylinder, i.e., a GDI injector and a port fuel injection (PFI) injector, which is a potential drawback, it would not require two separate fuel systems. Modern production GDI engines are beginning to employ both a PFI and a GDI injector, which makes this strategy production-relevant.

To determine whether splitting the total injected fuel between premixed injection and intake stroke direct injection can control the amount of in-cylinder stratification, the premixed fraction, i.e. the fuel that is vaporized, is swept from 0% to 100%. Throughout this sweep, CA50 is maintained at  $7.0 \pm 0.5$  deg aTDC by adjusting the intake temperature, the fueling rate is maintained at  $36.0 \pm 0.5$  mg/cycle (IMEPg of  $\sim 5.4$

$\pm 0.1$ ), and the residual rate is maintained at 25%. Figure 55 displays RI and COV of RI vs. premixed fraction and Figure 56 displays IS NO<sub>x</sub> and IS CO vs. premixed fraction. These parameters are used as an indicator of the level of stratification that exists in the cylinder. RI shows a near linear trend with premixed fraction from 0% to 100%. In other words, as soon as the first amount of direct injected fuel is injected, the in-cylinder stratification increases. The linearity in induced stratification with premixed fraction indicates that this mechanism for varying the level of in-cylinder stratification is highly controllable.

The IS NO<sub>x</sub> data shows relatively insignificant changes between premixed fractions of ~70% to 100% compared to the linear behavior between 0% and 70%. This means that the induced stratification from the direct injection of ~30% of the total fuel amount does not create a significant number of regions in the cylinder with conditions that support NO<sub>x</sub> formation when the global  $\phi'$  is ~0.57. There is an even larger near-constant band of CO emissions – CO emissions only increase at premixed fractions below ~40%. The onset of increasing CO emissions occurs at lower premixed fractions than the onset of increasing NO<sub>x</sub> emissions because as stratification increases, regions must first cross through NO<sub>x</sub> formation conditions before becoming rich enough to form CO, similar to the discussion above surrounding Figure 52 related to the effects of load on CO and NO<sub>x</sub>.

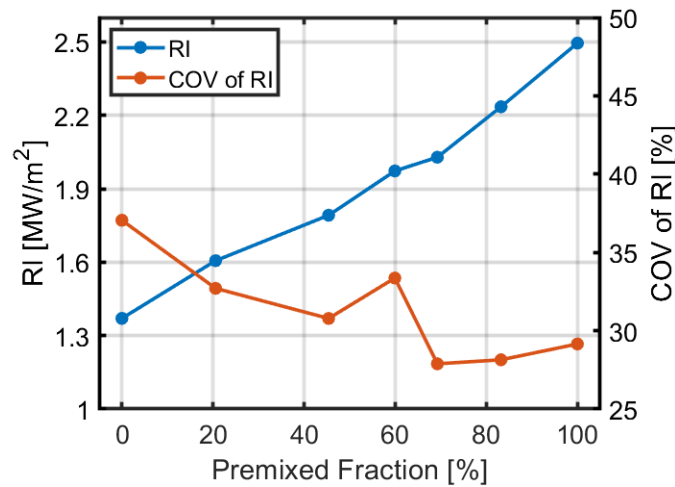


Figure 55: Ringing intensity (RI) vs. premixed (vaporized) fraction. Due to high uncertainties in ringing intensity from cyclic variability, the coefficient of variation (COV) of RI is plotted. With the exception of a premixed fraction of 0% (full early DI) and 100% (full vaporizer), the uncertainty in premixed fraction is ~5%.

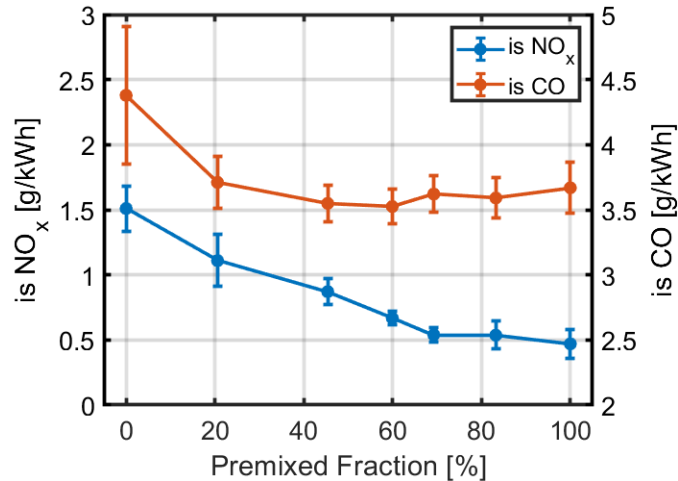


Figure 56: Indicated specific (IS) emissions of NO<sub>x</sub> and CO vs. premixed (vaporized) fraction. With the exception of a premixed fraction of 0% (full early DI) and 100% (full vaporizer), the uncertainty in premixed fraction is ~5%.

### 3.3.4 Controlling in-cylinder stratification with a split injection strategy

Using a two-injector fuel system to deliver a fraction of the fuel in the port to promote homogeneity, and a fraction of the fuel directly into the quiescent combustion chamber to increase thermal stratification shows promise as a highly controllable combustion strategy to enable high-load LTC with a high latent heat of vaporization fuel. However, it is still of interest to determine if a similar effect can be achieved with a single injector. In the previous work on a diesel engine architecture, a split injection strategy was employed, where intake stroke injections largely premixed the fuel with the incoming air and compression stroke injections modulated the thermal stratification to elongate the combustion process. However, recent studies have shown that the compression stroke injection's ability to increase thermal stratification is sensitive to both the combustion chamber geometry and the injector spray angle. More specifically, the compression stroke injection's ability to increase thermal stratification is strongly related to the region in the cylinder that is targeted by the spray. With this in mind, if a split injection strategy is employed on the engine considered in this study, compression stroke injections may actually reduce overall in-cylinder stratification.

To isolate the effects of the compression stroke injection on the heat release process, a compression stroke injection timing sweep is performed, where 20% of the fuel is injected at the indicated injection timing and the remaining 80% of the fuel is injected in the fuel vaporizer. Throughout this sweep, CA50 is maintained at  $7.0 \pm 0.5$  deg aTDC by adjusting intake temperature, the fueling rate is maintained at  $35.5 \pm 0.5$  mg/cycle, and the residual rate is maintained at 25%. Figure 57 plots RI vs. compression stroke SOI for the compression stroke injection timing sweep. A reference line shows the ringing intensity of a fully vaporized case with the same fueling rate and CA50. In addition, the COV of RI is shown in lieu of uncertainty bounds, since cyclic variability produces larger uncertainty values of RI. Here it can be seen that at a compression stroke injection timing of -130 deg aTDC, during the early compression stroke, the ringing intensity is slightly higher than the reference vaporizer case. As the compression stroke injection timing is retarded, ringing intensity increases significantly to a peak of  $\sim 6$  MW/m<sup>2</sup> at an SOI of -110 deg aTDC. Additionally, the COV of RI increases at these operating conditions. During experimental testing, it was clear to the authors that these cases had bimodal behavior, i.e. oscillating between high knocking and low knocking cycles. The COV of IMEPg for these cases also increased significantly, as shown in Figure 58. By examining both Figure 57 and Figure 58 together, it can be seen that the average burn duration of the cycle did not decrease significantly, which is typically seen with an increase in ringing intensity; rather, the source of the high average ringing intensity is a subset of the sampled cycles. This bi-modal behavior, which may be due to a combination of spray variability and high cycle-hysteresis due to the moderately high fraction of internal residuals, is undesirable and eliminates that SOI window as a candidate to reduce overall in-cylinder stratification.



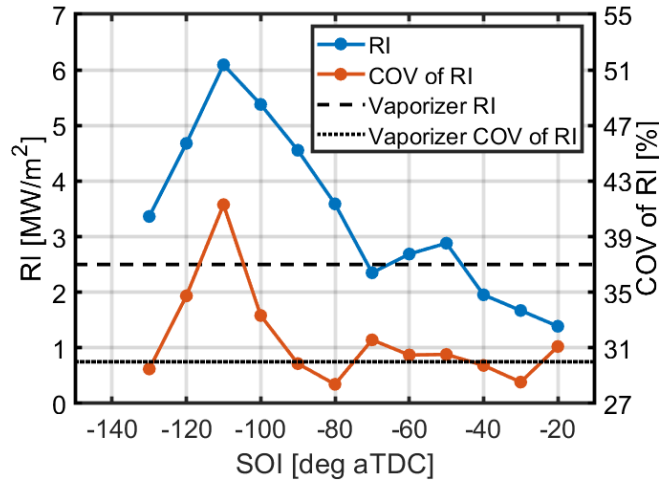


Figure 57: Ringing intensity (RI) vs. SOI for compression stroke injection timing sweep, where 20% of the total fuel is injected during the compression stroke and 80% is vaporized. Due to high uncertainties in ringing intensity from cyclic variability, coefficient of variation (COV) of RI is plotted. A reference line with the RI and COV of RI of a fully vaporized case is shown.

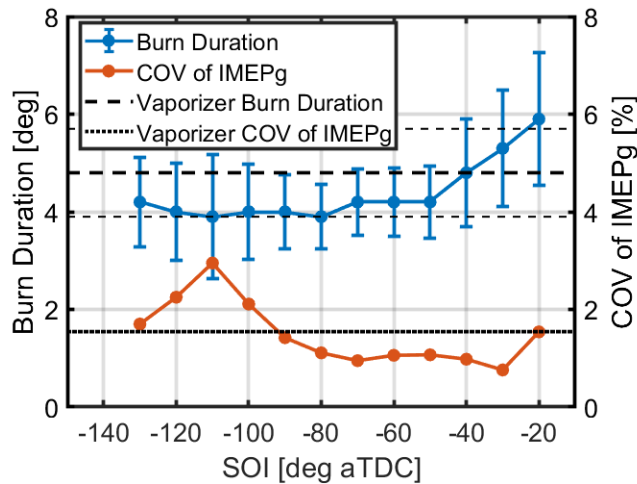
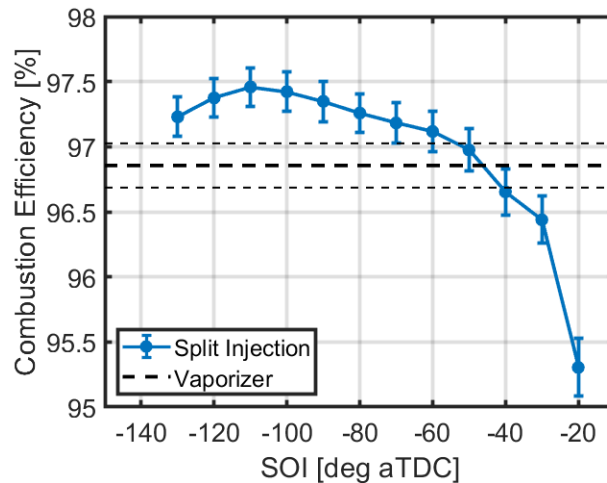


Figure 58: 25-75% burn duration and coefficient of variation (COV) of gross indicated mean effective pressure (IMEPg) of CA50 vs. SOI for the compression stroke injection timing sweep, where 20% of the total fuel is injected during the compression stroke and 80% is injected during the intake stroke.

SOIs of -90 deg aTDC and later return to steady state operation with a low COV of IMEP<sub>g</sub>. As SOI is retarded beyond -40 deg aTDC, RI begins decreasing and burn duration begins to increase. While this may be due in part to an increase in thermal stratification, it is also possibly due to an increase in locally rich areas from the late injection of fuel during the compression stroke. These rich areas elongate the heat

release process by requiring time during the expansion stroke to continue oxidation via mixing. Evidence of this is seen by noting that the combustion efficiency of these late compression stroke SOIs decreases, shown in Figure 59. SOIs between -70 and -50 deg TDC have the same burn duration and very similar RI values compared to the fully vaporized case, implying that these injection timings actually reduce the thermal stratification level in the cylinder compared to the 100% early DI case. Compression stroke injections during this window are the best candidates to enable a split injection strategy which may reduce the overall in-cylinder stratification when compared to a single intake stroke injection. As mentioned above, this behavior is exactly contrary to the behavior seen on the diesel engine architecture where splitting the fuel from purely early DI to a split between the intake and compression strokes resulted in more stratification and longer burn durations.



*Figure 59: Combustion efficiency vs. SOI for the compression stroke injection timing sweep where 20% of the total fuel is injected during the compression stroke and 80% is vaporized. A reference line is shown for the combustion efficiency (with a 95% confidence interval) of a fully vaporized case.*

Figure 60 plots the cylinder pressure and GHRR traces of three cases: Case 1) all of the fuel is introduced as an early DI at -320 deg aTDC; Case 2) a split injection strategy with a split fraction of 80%, with 80% of the fuel injected at -320 deg aTDC and 20% at -60 deg aTDC; and Case 3) 20% of the fuel is premixed via the vaporizer, with the remaining 80% injected at -320 deg aTDC. The relevant operating conditions and combustion results are shown in Table 8. As hypothesized, using a split injection strategy

(Case 2) results in a taller, narrower heat release profiles than the 100% early DI-fueled condition (Case 1), denoting a decrease in thermal stratification. It can also be seen that when 20% of the fuel is vaporized instead of injected during the compression stroke (Case 3), the change in the heat release profile with respect to Case 1 is nearly the same, suggesting that the two approaches to reducing the level of stratification were approximately equally effective.

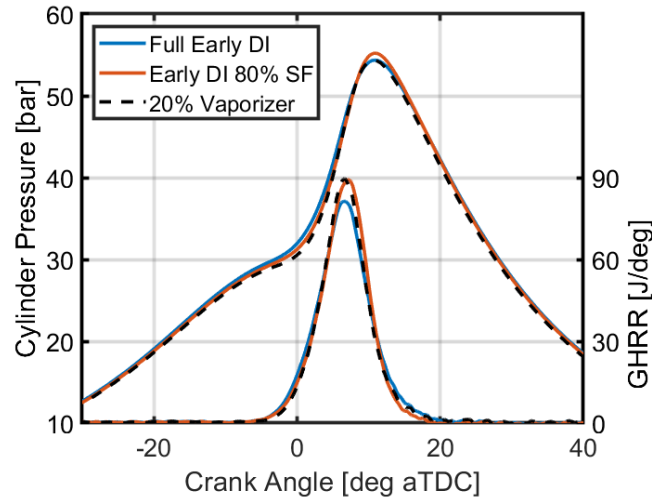


Figure 60: Cylinder pressure and gross heat release rate (GHRR) traces vs. crank angle degrees for three cases: Case 1, early direct injection (-320 deg aTDC SOI) fueled combustion, Case 2, split injection strategy (80% of fuel at -320 deg aTDC, 20% of fuel at -60 deg aTDC), and Case 3, vaporizer/early DI split strategy (80% of fuel at -320 deg aTDC, 20% of fuel premixed in vaporizer). CA50 is maintained at  $7.0 \pm 0.5$  deg aTDC by adjusting intake temperature and fueling rate is maintained at  $\sim 36.0 \pm 0.5$  mg/cycle.

Table 8: Relevant operating conditions and combustion results for three cases: Case 1, early direct injection (-320 deg aTDC SOI) fueled combustion, Case 2, split injection strategy (80% of fuel at -320 deg aTDC, 20% of fuel at -60 deg aTDC), and Case 3, vaporizer/early DI split strategy (80% of fuel at -320 deg aTDC, 20% of fuel premixed in vaporizer).

		100% Early DI	Split Injection	Vaporizer/Early DI Split
Inj. Mass	[mg/cyc]	35.7 ± 0.5	36.1 ± 0.5	35.6 ± 0.5
Phi	[--]	0.71 ± 0.01	0.71 ± 0.01	0.71 ± 0.5
IMEPg	[bar]	5.53 ± 0.04	5.50 ± 0.04	5.42 ± 0.04
DI1 SOI	[deg aTDC]	-320	-320	-320
DI1 Fuel Fraction	[%]	100.0	80 ± 5	80 ± 5
DI2 SOI	[deg aTDC]	--	-60	--
DI2 Fuel Fraction	[%]	--	20 ± 5	--
Vaporizer Fuel Fraction	[%]	--	--	20 ± 5
Thermal Efficiency	[%]	41.3 ± 1.3	41.6 ± 1.3	40.5 ± 1.3
Combustion Efficiency	[%]	97.2 ± 0.2	97.4 ± 0.2	97.1 ± 0.2
Burn Duration (25-75)	[deg]	5.3 ± 1.5	4.6 ± 1.1	4.7 ± 1.3
Burn Duration (10-90)	[deg]	8.7 ± 2.9	7.5 ± 2.2	7.0 ± 2.5
MPRR	[bar/deg]	3.8	4.1	4.6
COV of MPRR	[%]	23%	23%	21%
RI	[MW/m <sup>2</sup> ]	1.2	1.4	1.7
COV of RI	[%]	37%	37%	32%
is CO	[g/kWh]	5.3 ± 0.4	4.1 ± 0.2	3.6 ± 0.2
is uHC	[g/kWh]	4.5 ± 0.4	4.2 ± 0.4	5.1 ± 0.54
is NOx	[g/kWh]	1.3 ± 0.1	1.6 ± 0.2	1.3 ± 0.2

Overall, this chapter provided insight into the operating strategy of TSCI with wet ethanol on both a light-duty diesel engine architecture and a light-duty gasoline engine architecture. Specifically, it was shown that when using wet ethanol, cycle-to-cycle control can be achieved over both the start and rate of combustion by using the fuel's high cooling potential to control the in-cylinder temperature distribution. Further, it was shown that this control is maintained when moderate amounts of EGR and intake boost are included, and that this control is maximized when fuel spray is able to target high local heat transfer regions in the cylinder.

## Chapter 4. Autoignition Characterization of C1-C4 Alcohols in LTC

One of the first steps towards the implementation of alcohol biofuels in LTC is to fully characterize the LTC performance of each fuel experimentally. Other researchers have individually characterized the HCCI performance of some of the fuels considered, including methanol [105], ethanol [66], and n-butanol [107]. Some have compared the HCCI performance characteristics of multiple alcohol fuels, including ethanol/methanol [108, 109], ethanol/n-butanol/isobutanol [60], and ethanol/n-butanol/sec-butanol [110]. However, a significant amount of the LTC characterization of alcohol fuels found in the literature is with respect to alcohols as a bio-blend stock for gasoline. Nowhere in the literature is a direct comparison of all seven fuels considered in their neat form with experimental data collected on the same engine. The primary focus of this chapter is to provide this comparison.

In this chapter, all seven bio-synthesizable C1-C4 alcohol fuels considered are experimentally tested in HCCI under a wide array of operating conditions on a single cylinder light-duty gasoline engine architecture with a rebreathe valvetrain. In particular, the following sweeps were collected and analyzed:

1.  $\phi'$  sweep from 0.25 to 0.5, adjusting the intake temperature to maintain a constant CA50.
2. Combustion phasing sweep from  $\sim 1$  deg aTDC to  $\sim 9$  deg aTDC by adjusting the intake temperature.
3. Residual rate sweep from 20% to 40% by adjusting the exhaust back pressure.
4. Intake pressure sweep from 1.15 bar to 1.95 bar.
  - a.  $\phi'$  and combustion phasing sweeps are performed at 1.95 bar.
5. Engine speed sweep from 900 rpm to 2400 rpm.

## 4.1 Load Sweep

A load sweep for each fuel was conducted, with  $\phi'$  ranging from 0.25 to 0.5 (except methanol, whose highest  $\phi'$  is 0.43 due to limitations on the fuel vaporizer).  $\phi'$  is the charge-mass equivalence ratio, a metric which considers both air and residual gas in its calculation. It is related to the fuel-air equivalence ratio ( $\phi$ ) by the following equation:  $\phi' = \phi * (1 - \text{residual rate})$ . For each load case, the intake temperature was adjusted to maintain a constant CA50 of  $7.0 \pm 0.5$  deg aTDC. The engine speed was maintained at 1200 rpm and the residual rate was maintained at  $\sim 30\%$ . The engine intake pressure is slightly boosted to 1.15 bar and the exhaust pressure is 1.0 bar to facilitate the desired residual rate.

Figure 61 and Figure 62 display the intake and exhaust temperature vs.  $\phi'$ , respectively. As expected, the intake temperature decreases with load while the exhaust temperature increases. The exhaust temperature of methanol is somewhat higher than the other fuels because methanol has a slightly higher in-cylinder energy content than the other six fuels at a given  $\phi'$  based on its LHV and  $\text{AFR}_{\text{stoich}}$ . A significant drop in the intake temperature requirement to maintain a constant CA50 as load increases can be an indicator that a fuel has a significant degree of  $\phi$ -sensitivity due to cool flame reactivity. This is because low temperature heat release (LTHR) and intermediate temperature heat release (ITHR), which increase with  $\phi$ , raise the in-cylinder temperature and radical concentration during the compression stroke, advancing hot ignition. However, in the current study, the primary source of the significant drop in intake temperature with load is the high residual rate. As the exhaust temperature rises with load, the intake temperature must decrease to maintain similar IVC conditions. This is illustrated in Figure 63, which displays IVC temperature vs.  $\phi'$ . Note that the IVC temperature plot shown here does not have error bars. This is because the IVC temperature calculation, using the state equation method [111], results in fairly high uncertainty ( $\sim 35$  K) due to the high relative uncertainty in the residual rate ( $\sim 10\%$ ). While this

makes a statistically significant quantitative argument difficult, it is still qualitatively clear that a large portion of the intake temperature decrease is to offset an increase in the exhaust temperature. Similarly, the high relative uncertainty in the residual rate results in a somewhat high average uncertainty in  $\phi'$  ( $\sim 0.02$ ), although the uncertainty in fueling rate (and  $\phi$ ) is significantly lower.

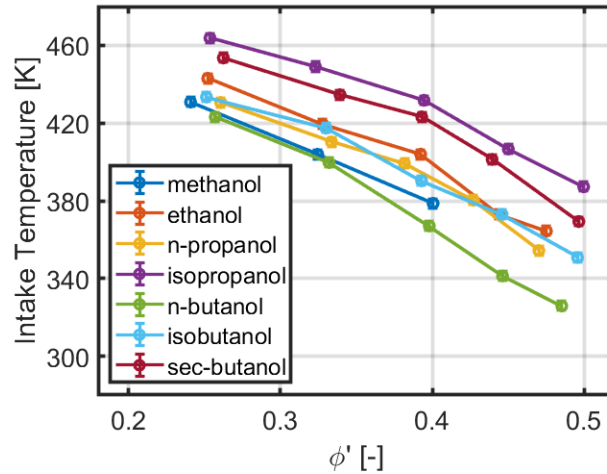


Figure 61: Intake temperature vs. charge-mass equivalence ratio ( $\phi'$ ) for each load case with a constant CA50 of  $7.0 \pm 0.5$  deg aTDC. The average uncertainty in  $\phi'$  is  $\pm 0.02$ .

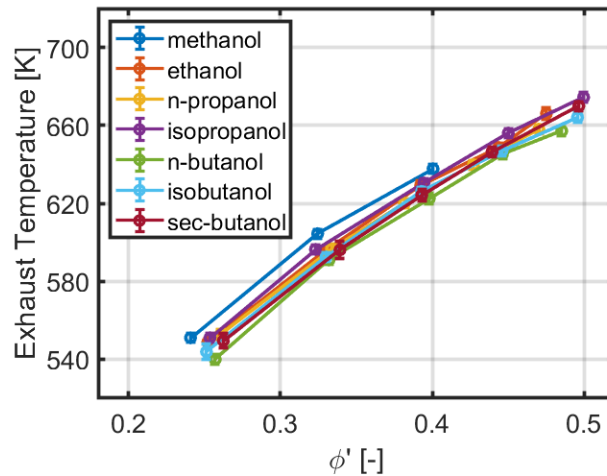


Figure 62: Exhaust temperature vs. charge-mass equivalence ratio ( $\phi'$ ) for each load case with a constant CA50 of  $7.0 \pm 0.5$  deg aTDC. The average uncertainty in  $\phi'$  is  $\pm 0.02$ .

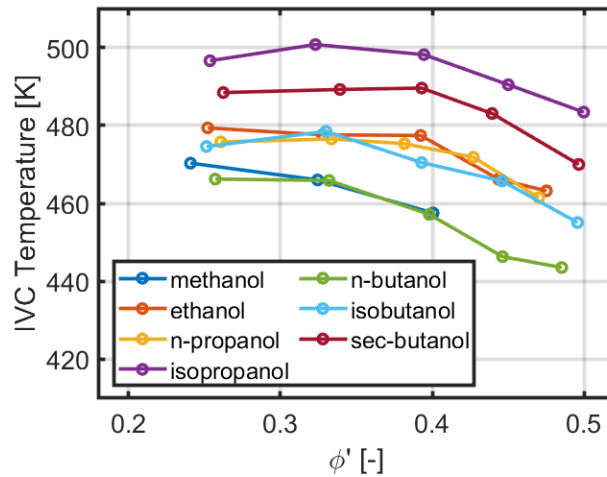


Figure 63: Intake valve closing (IVC) temperature vs. charge-mass equivalence ratio ( $\phi'$ ) for each load case with a constant CA50 of  $7.0 \pm 0.5$  deg aTDC. The average uncertainty in  $\phi'$  is  $\pm 0.02$ .

As  $\phi'$  increases past 0.4, the IVC temperature begins to decrease. In addition to an increase in the exhaust temperature, the wall temperature increases with load as well, both increasing charge heating of the incoming air as well as decreasing heat transfer losses during the compression stroke. This can further lower the IVC temperature requirement. Sjoberg et al. showed that when these effects are removed using a model with chemical kinetics, the IVC temperature requirement of ethanol to maintain a constant CA50 increases with  $\phi'$  due to a thermodynamic cooling effect associated with the increase in the specific heat (decrease in the ratio of specific heats) of the charge as it richens [66]. The intake and IVC temperatures of ethanol, n-propanol, and isobutanol are all nearly the same, indicating similar reactivity. Sec-butanol and isopropanol have higher intake and IVC temperature requirements than the other fuels, showing they have a higher autoignition resistance; the trends of these fuels are identical, implying similar  $\phi$ -sensitivity and single stage ignition behavior. n-butanol and methanol have the lowest intake and IVC temperature requirements, demonstrating their higher reactivity. For n-butanol, these results agree with previous HCCI studies comparing ethanol, n-butanol, and isobutanol [60]. For methanol, this somewhat agrees with the literature in that methanol has a slightly lower autoignition resistance than ethanol



[109]. However, as it will be shown, methanol is less reactive than n-butanol under other operating conditions, which agrees well with results in the literature.

It is well documented that the C1-C4 alcohol fuels lack NTC behavior [59, 112]. The source of a hydrocarbon fuel's NTC behavior is alkyl-peroxyl radical chain branching. These cool flame reactions are generally defined by H-abstraction, followed by O<sub>2</sub> addition to the abstraction site, and finally internal H-transfer to the radical site. Internal H-transfer from another C-H bond creates a new abstraction site for O<sub>2</sub> addition, ergo the term radical chain branching. H-abstraction will occur preferentially at the weakest C-H bonds in the fuel molecule. C-H bond strength in saturated hydrocarbons ordered strongest to weakest is primary (CH<sub>3</sub>), secondary (CH<sub>2</sub>), and tertiary (CH) sites. For alcohols, the weakest C-H bond is next to the hydroxyl group (the  $\alpha$  site) due to strong electron delocalization. Therefore, H-abstraction generally occurs at the  $\alpha$ -site in short-chain alcohols. When H-abstraction occurs at low temperatures at the  $\alpha$  site, internal H-transfer occurs from the hydroxyl group, terminating the radical chain and inhibiting cool flame reactivity. Further, the non-hydroxyl internal H-transfer required for radical chain branching needs a transition state ring that consists of the O<sub>2</sub> radical, the H atom being transferred, and a number of carbon atoms that form a straight chain in the fuel molecule. The more carbon atoms involved in the transition state ring, the lower the ring strain energy (and the higher the likelihood of occurrence). For an alcohol to show non-Arrhenius behavior, a straight chain of four C atoms is required [59]. As a result, the short-chain alcohols do not exhibit cool flame reactivity.

As the carbon chain lengthens, non-hydroxyl group H-transfer becomes possible and cool flame reactivity is enabled. This transition to NTC behavior occurs at n-pentanol, though it was noted that low temperature chemistry was needed in chemical mechanisms of the butanol isomers to accurately model their chemistry [113]. n-butanol has been shown experimentally to show ITHR under boosted conditions, similar to gasoline [60]. This ITHR does not result in NTC behavior,

though it does result in non-Arrhenius ignition delay behavior [114]. Sec-butanol and isobutanol did not display non-Arrhenius behavior in any experimental studies in the literature.

The reaction pathways of the alcohol fuels considered in this work are well summarized in Ref. [112]. The similarity in the reactivity of ethanol, n-propanol, and isobutanol can be attributed to their similar high-temperature combustion chemistries, which are generally described by H-abstraction followed by  $\beta$ -scission reactions, leading to aldehyde formation. Isopropanol forms resonantly stable acetone radicals from  $\alpha$ -site H-abstraction, explaining isopropanol's higher autoignition resistance. Sec-butanol, like isopropanol, is a secondary alcohol and also forms acetone during combustion in addition to aldehyde formation, which explains why sec-butanol's reactivity level is between isobutanol and isopropanol. By naming convention alone, it would appear that isobutanol would have a more similar combustion chemistry to isopropanol than sec-butanol does. However, the prefix *iso* in isopropanol is actually misused; isopropanol should be referred to as sec-propanol since there is no discontinuity in its carbon chain to classify it with the prefix *iso*. Other researchers have noted sec-butanol's reactivity to be equal to or lower than isobutanol under some operating conditions [113]. There is not a significant wealth of experimental studies with sec-butanol, and this discrepancy will be discussed later in this work.

While cool flame chemistry can be relevant for the butanol isomers, particularly n-butanol, there is no evidence of emergent ITHR under the pressure-temperature trajectories considered in this load sweep. To illustrate this, Figure 64 displays the cylinder pressure and gross heat release rate (GHRR) traces for ethanol, isopropanol, and n-butanol under a low load condition ( $\phi' = 0.33$ ) and a high load condition ( $\phi' = 0.5$ ). Only three fuels are shown to avoid crowding the figure; of the seven fuels considered, ethanol and isopropanol are representative of the four fuels omitted. Ethanol and isopropanol have nearly identical heat release profiles. Although n-butanol has a

sharper heat release profile with a larger peak heat release rate, no ITHR characterized by a premature rise in the GHRR before the main combustion event is present.

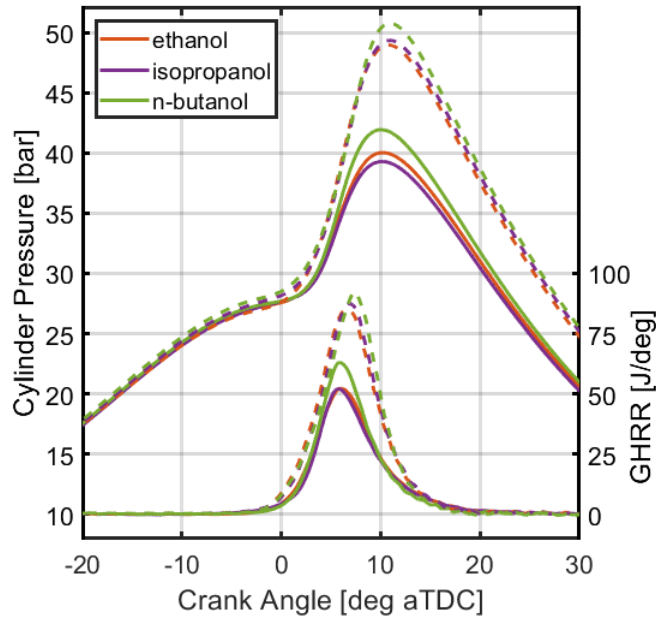


Figure 64: Cylinder pressure and gross heat release rate (GHRR) vs. crank angle for three of the seven fuels considered (ethanol, isopropanol, and n-butanol) at a low load condition ( $\phi' = 0.33$ ) and a high load condition ( $\phi' = 0.5$ ).

Figure 65 displays the indicated specific (IS) emissions of  $\text{NO}_x$  vs.  $\phi'$  for each fuel considered.  $\text{NO}_x$  emissions are negligible below a  $\phi'$  of 0.4. As  $\phi'$  increases past 0.4,  $\text{NO}_x$  emissions begin to increase. In HCCI,  $\text{NO}_x$  emissions are directly correlated with peak bulk temperature. Therefore, isopropanol and sec-butanol, which have a higher autoignition resistance than the other fuels, form more  $\text{NO}_x$  than the other fuels since their higher autoignition resistance requires a higher bulk temperature before combustion to achieve autoignition.

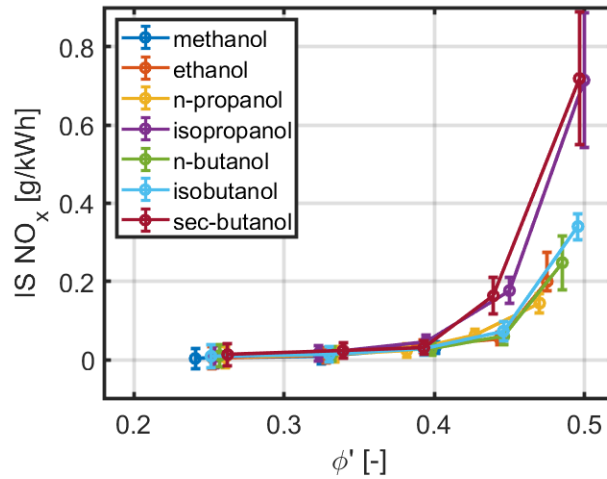


Figure 65: Indicated specific (IS) emissions of  $NO_x$  vs. charge-mass equivalence ratio ( $\phi'$ ) for each load case with a constant CA50 of  $7.0 \pm 0.5$  deg aTDC. The average uncertainty in  $\phi'$  is  $\pm 0.02$ .

Figure 66, Figure 67, and Figure 68 display the overall combustion efficiency, the IS CO emissions, and the IS uHC emissions vs.  $\phi'$  for each fuel considered. As expected, the combustion efficiency increases with load due to a decrease in both CO and uHC emissions as sequential autoignition increases in effectiveness and peak bulk temperature increases. The CO emissions of each fuel are nearly identical above a  $\phi'$  of 0.33. At a  $\phi'$  of  $\sim 0.25$ , differences in CO emissions can be attributed primarily to the slight differences in cylinder energy content for each fuel, which are significant near the low-load combustion stability limit of HCCI. For uHC emissions, some small differences between fuels are present. It appears that isobutanol and sec-butanol have higher uHC emissions than the other fuels. This somewhat agrees with data in the literature related to isobutanol [60] and sec-butanol [110], although those two works conflict when comparing the uHC emissions of ethanol and n-butanol. For the C1-C3 alcohols, no statistically significant difference in uHC emissions is noted, which agrees with the fact that these alcohols have very similar combustion chemistries.

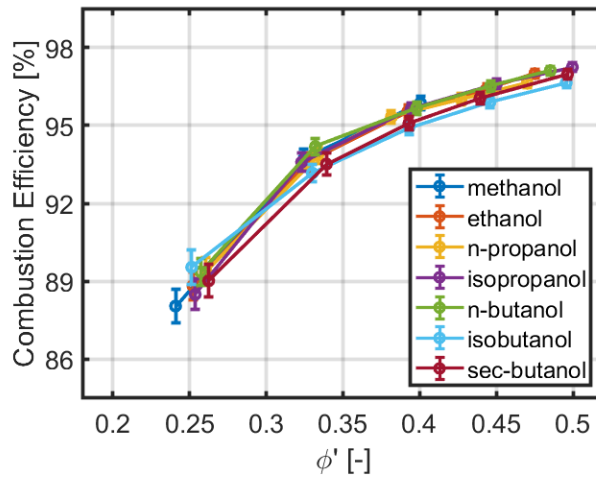


Figure 66: Overall combustion efficiency vs. charge-mass equivalence ratio ( $\phi'$ ) for each load case with a constant CA50 of  $7.0 \pm 0.5$  deg aTDC.

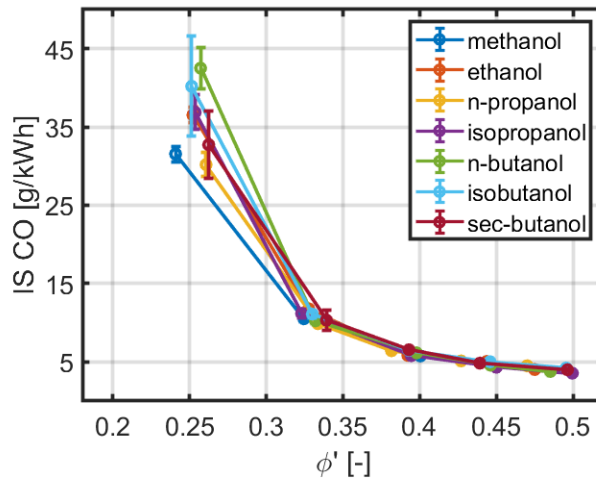


Figure 67: Indicated specific (IS) emissions of CO vs. charge-mass equivalence ratio ( $\phi'$ ) for each load case with a constant CA50 of  $7.0 \pm 0.5$  deg aTDC.

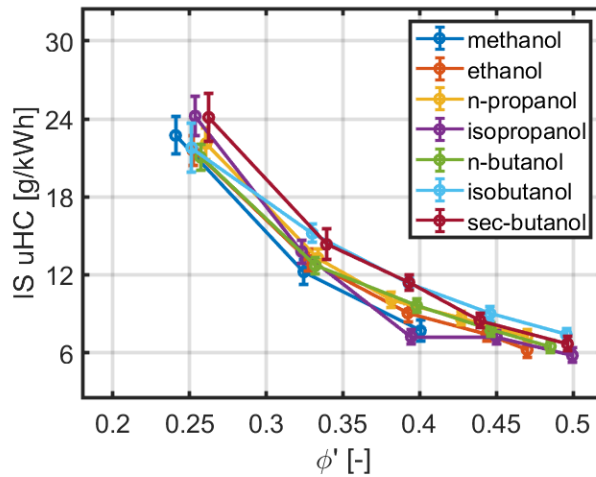


Figure 68: Indicated specific (IS) emissions of uHC vs. charge-mass equivalence ratio ( $\phi'$ ) for each load case with a constant CA50 of  $7.0 \pm 0.5$  deg aTDC.

## 4.2 Combustion Phasing (Intake Temperature) Sweep

To study the autoignition sensitivity of each alcohol fuel to temperature, the combustion phasing is swept via adjusting the intake temperature for each fuel while holding other parameters constant. For all of the following sweeps, the engine speed, intake pressure, and residual rate are maintained at 1200 rpm, 1.15 bar, and 30%, respectively. Combustion phasing sweeps were performed at three values of  $\phi'$ : 0.25, 0.33, 0.40.

Figure 69, Figure 70, and Figure 71 display intake temperature vs. CA50 for a  $\phi'$  of 0.25, 0.33, and 0.40, respectively. In general, the uncertainty in CA50 (or of any CA $x$ ) of any given cycle is low, on the order of 0.2 deg. However, the uncertainty in CA50 for the ensemble average of 300 is on the order 1.0 deg due to cyclic variability. Further, the uncertainty in CA50 due to cyclic variability increases as combustion phasing retards due to the lack of cool flame reactivity exhibited by the fuels considered – this will be expanded on in a following paragraph.

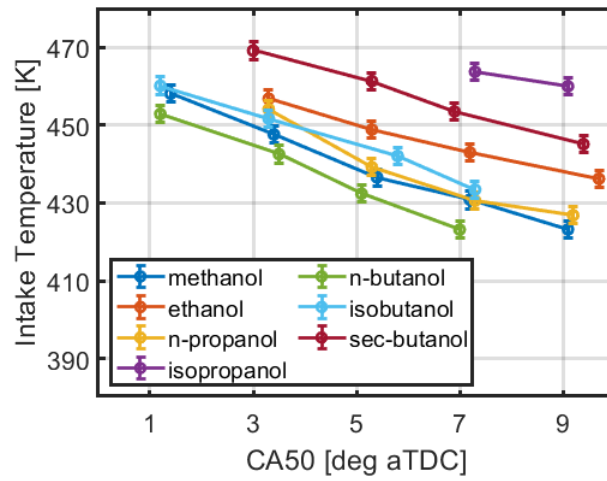


Figure 69: Intake temperature vs. combustion phasing (CA50) with a  $\phi'$  of 0.25.

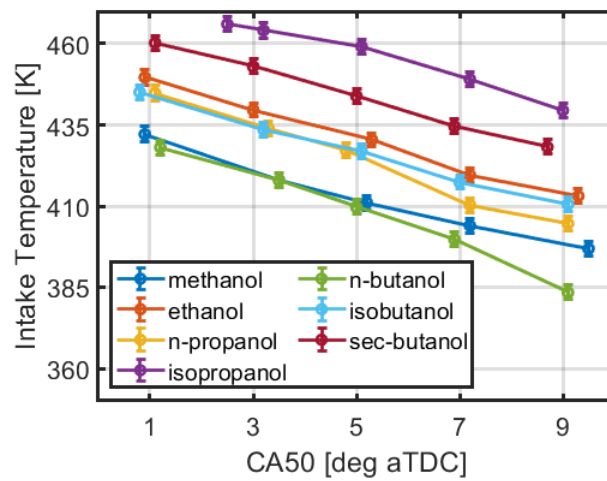


Figure 70: Intake temperature vs. combustion phasing (CA50) with a  $\phi'$  of 0.33.

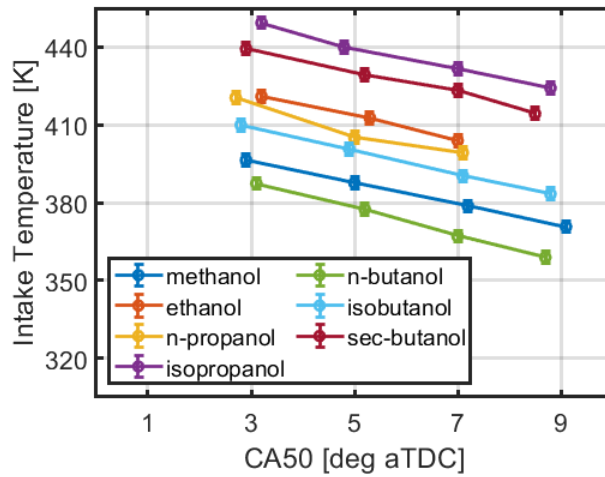


Figure 71: Intake temperature vs. combustion phasing (CA50) with a  $\phi'$  of 0.40.

As intake temperature decreases, combustion phasing retards. The order of reactivity of the seven fuels considered is the same as described in Section 3.1, with isopropanol being the least reactive and n-butanol being the most reactive. The slope of the trend lines in each plot represents the fuels' autoignition sensitivity to temperature. A larger slope implies a lower sensitivity to temperature. Although analyzing this sensitivity via the IVC temperature would be more fundamental, the high uncertainty in the IVC temperature ( $\sim 35$  K, described in Section 3.1) makes this impractical. Within each constant-load intake temperature sweep, the exhaust and wall temperature are nearly constant ( $\Delta T_{ex} < 10$  K across sweep); therefore, using the intake temperature for this sensitivity analysis is still useful.

The sensitivity of methanol, ethanol, isopropanol, isobutanol, and sec-butanol to intake temperature are all similar; their average slope is  $\sim 4.3$  K/deg. n-propanol has a slightly higher average slope of  $\sim 4.8$  K/deg and n-butanol has an even higher average slope of  $\sim 5.3$  K/deg. A larger slope means a lower sensitivity of combustion phasing to temperature. For fuels that exhibit Arrhenius behavior, differences in temperature sensitivity can imply differences in activation



energy. However, this difference is small compared to the effect that non-Arrhenius behavior caused by cool flame reactivity would have.

Although no ITHR is detected in any heat release profiles at this boost level, some small amount of cool flame radical activity can explain the larger slope of n-butanol. Specifically, the increasing slope of n-butanol as CA50 is retarded can be explained by non-detectable but non-negligible amounts of ITHR associated with longer residence time at high temperature and pressure before combustion. No cool flame reactivity has ever been noted with n-propanol experimentally under engine relevant conditions, nor do chemical kinetics imply the need for cool flame reaction pathways to accurately model experimental results [112]. Non- $\alpha$  site H abstraction followed by non-hydroxyl internal H-transfer to enable radical chain branching is highly unlikely in n-propanol due to its short carbon chain, meaning cool flame reactivity is inhibited. However, the propanol isomers have not received nearly as much experimental attention as other low alcohols and there is a lack of reaction rate studies for sophisticated propanol kinetic modeling (n- and sec-butanol analogies were drawn in one modeling study [115]). Therefore, these experimental results highlight the need for more experimental and kinetic modeling studies of the propanol isomers.

Cool flame reactivity can have advantages and disadvantages in LTC. ITHR can enable stable combustion at later CA50s than single-stage ignition can, thereby increasing the energy release rate limited high-load operation of HCCI. Further, ITHR was identified as the primary mechanism of  $\phi$ -sensitivity required to enable next generation LTC concepts that aim to control the heat release process via small-to-medium amounts of  $\phi$ -stratification [14]. However, for the low alcohols specifically, a decreased sensitivity to temperature is not desirable, since their high cooling potential makes them better suited for next generation LTC concepts that aim to control the heat release process via an increase in thermal stratification. A decreased sensitivity to temperature means more evaporative cooling-induced thermal stratification during the compression stroke is

required to control the heat release process, which increases the risk of forming pollutant emissions [74]. Similarly, the high cooling potential of the low alcohols can be used to control the combustion phasing of LTC by varying the injection timing of intake stroke fuel injections, thereby varying the amount of fuel that evaporates in the air vs. off the walls. By varying the amount of fuel that evaporates in the air, the IVC temperature can be controlled on a cycle-to-cycle basis. Therefore, a decrease in temperature sensitivity means the control authority of this mechanism will decrease.

### **4.3 Residual Rate Sweep**

In this section, the residual rate is swept from ~20% to ~40% to characterize the sensitivity of the autoignition process of each fuel to internal, hot residuals. This is done by adjusting the intake and exhaust pressure, respectively, to attain the desired residual rate while maintaining a constant trapped mass in the cylinder. The fueling rate was maintained constant throughout the sweep, with  $\phi'$  at 0.33. The engine speed was maintained at 1200 rpm and the intake temperature was adjusted to maintain CA50 at  $7.0 \pm 0.5$  deg aTDC.

Figure 72 displays the intake temperature vs. residual rate. The order of reactivity of the fuels is constant with changes in residual rate. The intake temperature decreases as residual rate increases to offset for the increasing amount of hot, internal gases heating the incoming charge. However, Figure 73, which displays IVC temperature vs. residual rate, shows that the IVC temperature is approximately constant over the range of residual rates tested.

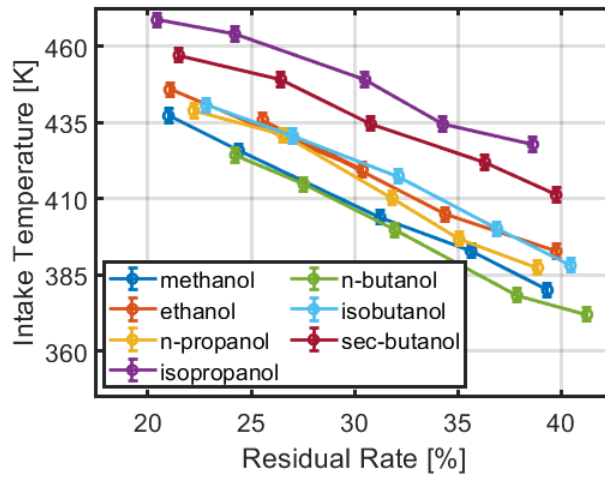


Figure 72: Intake temperature vs. residual rate with a constant  $CA_{50}$  of  $7.0 \pm 0.5$  deg aTDC and constant a  $\phi'$  of 0.33.

The relative uncertainty of the residual rate is ~10%.

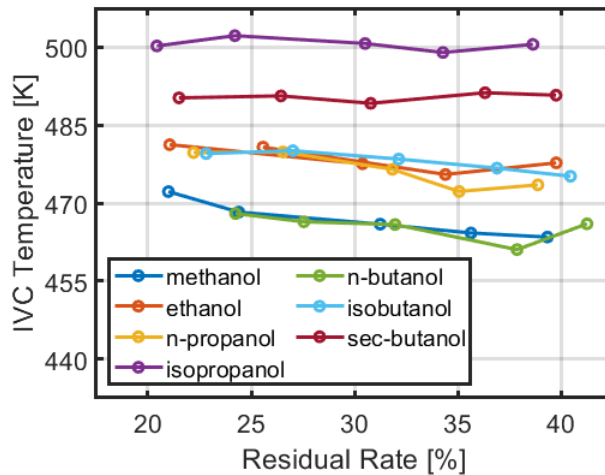


Figure 73: Intake valve closing (IVC) temperature vs. residual rate with a constant  $CA_{50}$  of  $7.0 \pm 0.5$  deg aTDC and

constant a  $\phi'$  of 0.33. The relative uncertainty in the residual rate is ~10%.

While the IVC temperature does not change significantly and the combustion phasing is held constant, the combustion process is affected by an increase in the residual rate.  $CA_{10}$ , an indicator of the start of combustion, advances slightly with an increased residual rate, as seen in Figure 74. Therefore, as the residual rate increases, the start of combustion advances and the burn duration increases for all seven fuels. An increase in burn duration with an increase in residual rate

and a constant fueling rate is well documented in HCCI – residuals have a higher specific heat and therefore slow the sequential autoignition process. To maintain a constant CA50, CA10 must advance.

The advancement of CA10 in the current dataset is a result of competing effects. On one hand, an increase in the residual rate decreases the ratio of specific heats of the charge, resulting in lower compression temperatures/pressures and favoring a delay in the start of combustion. However, from the lowest residual rate (~20%) to the highest (~40%), the difference in the ratio of specific heats is only ~0.005 and will not have a significant thermodynamic influence. On the other hand, there is a chemical effect from increasing the residual rate. Although the in-cylinder oxygen content decreases with residual rate, which can have a diminishing effect on reactivity, it has been shown that the autoignition of single stage ignition fuels like methanol and ethanol are insensitive to changes in oxygen content in the range considered in this work (15-19%) [93, 108]. Cool flame reactions are more sensitive to oxygen content in this range. Further, trace species of partially oxidized hydrocarbons in EGR can have an autoignition enhancing effect, explaining the slight advancement of the start of combustion with an increasing residual rate.

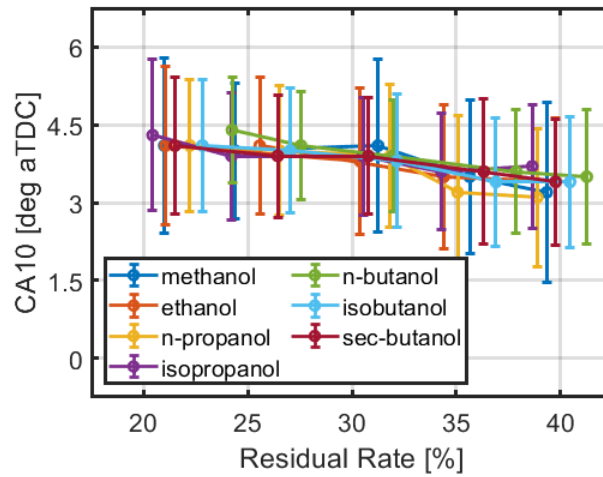


Figure 74: CA10 vs. residual rate with a constant CA50 of  $7.0 \pm 0.5$  deg aTDC and constant a  $\phi'$  of 0.33. The relative uncertainty in the residual rate is  $\sim 10\%$ .

#### 4.4 Intake Pressure Sweep

In this section, an intake pressure sweep is performed from  $\sim 1.15$  bar to  $\sim 1.95$  bar to characterize the sensitivity of each fuel to pressure. For each case,  $\phi'$  was maintained at 0.33. Due to limitations on the fuel vaporizer system, specifically the amount of heat it can provide for evaporation, the boost sweep was truncated at an intake pressure of  $\sim 1.65$  bar for methanol due to its high cooling potential. Similarly, for n-butanol, the boost sweep was truncated at an intake pressure of  $\sim 1.55$  bar due to limitations on the intake conditioning system; specifically, the intake temperature could not be lowered further than 325 K. Unlike previous sweeps, the residual rate was not held constant. Rather, the residual rate was gradually reduced with intake boost to ensure the intake temperature requirement for the remaining five fuels were achievable by the intake system. Figure 75 displays the residual rate vs. intake pressure for the boost sweep. The engine was maintained at 1200 rpm and the intake temperature was adjusted to maintain a constant CA50 of  $7.0 \pm 0.5$  deg aTDC.

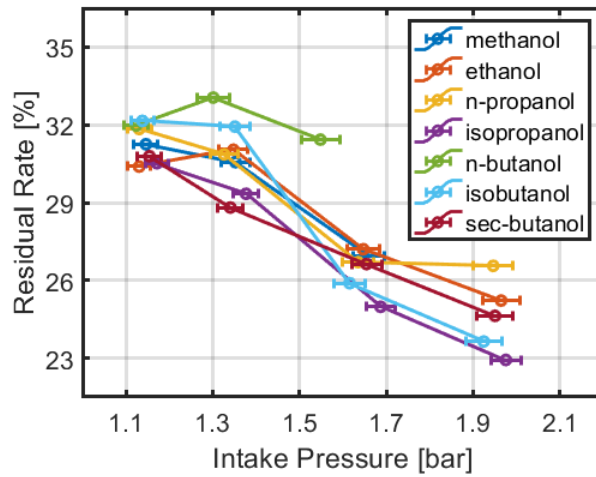


Figure 75: Residual rate vs. intake pressure for the intake pressure sweep. The relative uncertainty in the residual rate is  $\sim 10\%$ .

Figure 76 displays the IVC temperature vs. intake pressure. The order of reactivity of the fuels stays the same for the entirety of the boost sweep. n-butanol requires a significantly higher decrease in its IVC temperature as intake pressure increases. This is due to emergent ITHR as the pressure-temperature history of the boosted n-butanol case shifts towards the non-Arrhenius region. Considering the IVC temperature, which accounts for small differences in the residual rate, the sensitivity of methanol and ethanol to intake pressure are slightly lower than other fuels while that of sec-butanol is slightly higher.

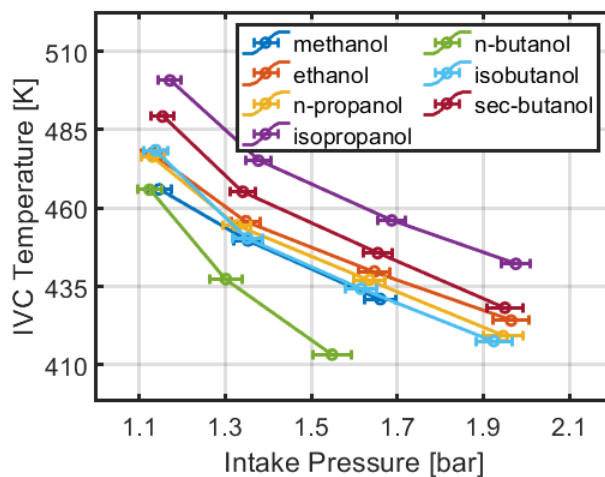


Figure 76: Intake valve closing (IVC) temperature vs. intake pressure with a constant  $CA_{50}$  of  $7.0 \pm 0.5$  deg aTDC and constant a  $\phi'$  of 0.33. The residual rate for each case is given in Figure 75.

Figure 77 displays the normalized GHRR traces for low and high intake pressure cases of the three butanol isomers near ignition. There is ITHR for n-butanol at an intake pressure of  $\sim 1.55$  bar and for sec-butanol at an intake pressure of  $\sim 1.95$  bar. Here, ITHR is indicated by a slight rise in the normalized GHRR before hot ignition representing heat release from alkyl-peroxyl radical isomerization. For n-butanol, this agrees with other experimental data [60, 113]. For sec-butanol, this is somewhat surprising since the limited set of experimental ignition delay data on sec-butanol did not observe non-Arrhenius behavior, although this work did note that the reactivity sensitivity of sec-butanol to pressure was higher than isobutanol [112].

There are currently no experimental boosted LTC studies with neat sec-butanol; therefore, this is the first experimental work to study sec-butanol under this pressure-temperature history. In general, boosting tends to elicit ITHR in fuels because cool flame chain propagating reactions are highly sensitive to oxygen concentration. The amount of ITHR exhibited by sec-butanol at an intake pressure of  $\sim 1.95$  bar is slightly less than n-butanol exhibits at  $\sim 1.55$  bar, meaning sec-butanol displays non-Arrhenius behavior to a lesser degree than n-butanol [60]. This small amount of ITHR could explain why sec-butanol has a slightly steeper slope than the other alcohol fuels.

Considering the discussion of cool flame chemical kinetics from Section 3.1, a straight chain of four C atoms is essentially required for the transition state ring strain energy to be low enough for non-hydroxyl group H-transfer in an alcohol fuel. As seen in Table 1, n-butanol and sec-butanol have a four-carbon straight chain while isobutanol only has a three-carbon straight chain since it is a branched isomer. This would explain why sec-butanol showed some amount of ITHR while isobutanol did not. Sec-butanol displays less ITHR than n-butanol because the hydroxyl group is more centrally located in the molecule, increasing the likelihood of radical chain terminating hydroxyl group H-transfer. This small amount of ITHR did not significantly decrease the autoignition resistance of sec-butanol, likely because the high temperature chemistry of sec-butanol still produced more stable intermediates than the primary alcohols. However, this ITHR could allow later CA50s compared to the other alcohol fuels, thereby enabling higher load HCCI at a lower boost conditions without engine damaging heat release rates.

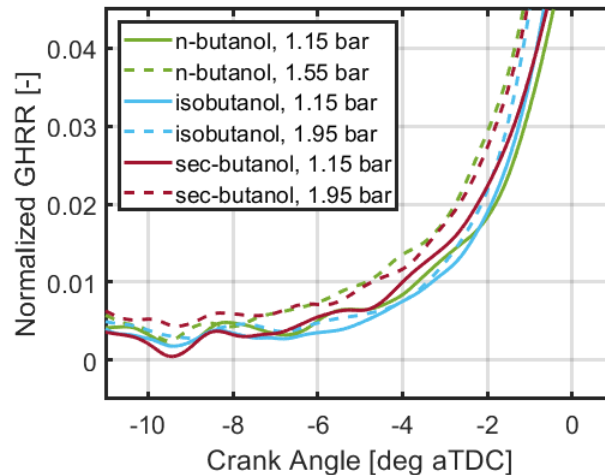


Figure 77: Normalized gross heat release rate (GHRR) vs. crank angle for the three butanol isomers (n-butanol, isobutanol, and sec-butanol) under minimum and maximum boost conditions.

#### 4.4.1 Load Sweep at Elevated Pressure

A load sweep for ethanol, n-propanol, isopropanol, isobutanol, and sec-butanol was performed at an elevated intake pressure of  $\sim 1.95$  bar to compare the load sensitivity of each fuel with boost. n-



butanol and methanol are not considered because of the experimental test cell limitations described above. The intake temperature was adjusted to maintain a constant CA50 of  $7.0 \pm 0.5$  deg aTDC. The engine speed was maintained at 1200 rpm and the residual rate was maintained at the high boost value for each fuel shown in Figure 75. The high  $\phi'$  target was constrained to a value that the intake conditioning system and vaporizer could provide.

Figure 77 and Figure 78 display the intake and IVC temperature vs.  $\phi'$ . At an intake pressure of  $\sim 1.15$  bar, the IVC temperature was nearly constant for the  $\phi'$  range considered in these sweeps (Figure 63). When boosted, there is a slight decrease in IVC temperature as load increases. While it is possible that this implies a slightly higher  $\phi$ -sensitivity with load, it is also possibly a result of an increase in charge heating associated with hotter walls which are not accounted for by the IVC temperature calculation. Overall, if there is an increase in  $\phi$ -sensitivity with boost for the five fuels considered, it is very slight, which is expected for single stage ignition fuels, and detailed chemical kinetics are required to isolate this result. For sec-butanol, which has been shown to have some non-single stage ignition behavior, this  $\phi$ -sensitivity is slightly higher than the other four fuels considered.

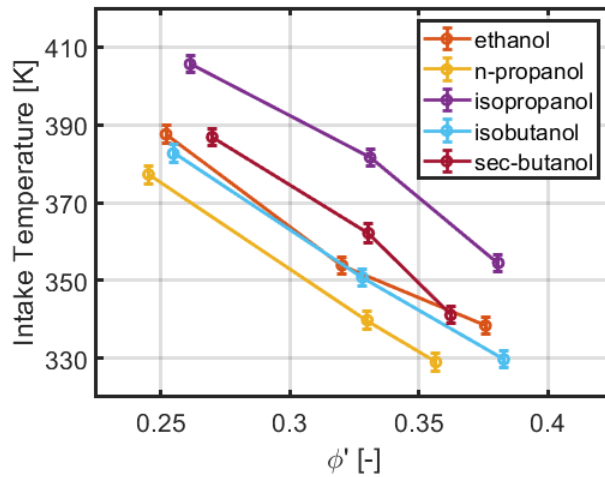


Figure 78: Intake temperature vs. charge-mass equivalence ratio ( $\phi'$ ). The intake pressure  $\sim 1.95$  bar with a constant CA50 of  $7.0 \pm 0.5$  deg aTDC. The average uncertainty in  $\phi'$  is  $\pm 0.02$ .

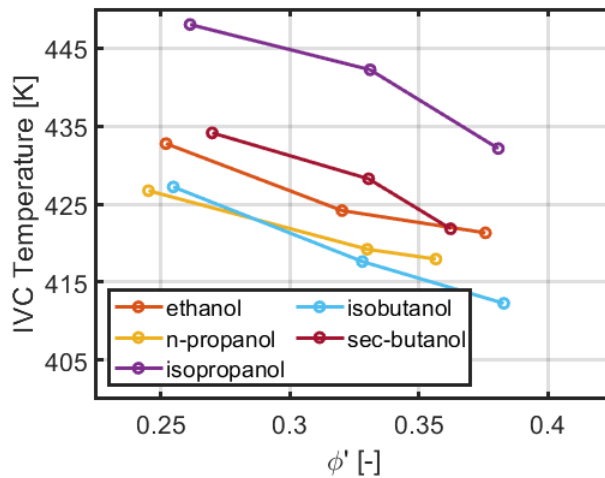


Figure 79: Intake valve closing (IVC) temperature vs. charge-mass equivalence ratio ( $\phi'$ ). The intake pressure  $\sim 1.95$  bar with a constant CA50 of  $7.0 \pm 0.5$  deg aTDC. The average uncertainty in  $\phi'$  is  $\pm 0.02$ .

#### 4.4.2 Combustion Phasing Sweep at Elevated Pressure

Similar to Section 4.4.1, a combustion phasing sweep for ethanol, n-propanol, isopropanol, isobutanol, and sec-butanol was performed at an elevated intake pressure of  $\sim 1.95$  bar to compare the temperature sensitivity of each fuel with boost. n-butanol and methanol are not considered because of the experimental test cell limitations described above.  $\phi'$  was maintained at 0.33, the

engine speed was maintained at 1200 rpm, and the residual rate was maintained at the high boost value for each fuel shown in Figure 75.

Figure 80 and Figure 81 show the intake and IVC temperatures vs. CA50 for each fuel considered. The sensitivity of isopropanol to temperature is higher under high boost conditions, with a slope of  $\sim 2.9$  K/deg, down from  $\sim 4.3$  K/deg under low boost conditions. Ethanol and n-propanol are also slightly more sensitive to temperature while boosted. Sec-butanol is slightly less sensitive to temperature while boosted, which supports the apparent emergence of ITHR. Surprisingly, isobutanol had a significantly lower sensitivity to temperature, with a slope of  $\sim 5.7$  K/deg, comparable to that of n-butanol under low boost conditions. This conflicts with results presented in Ref. [60], which showed isobutanol to have nearly the same temperature sensitivity as ethanol at an intake pressure of 1.8 bar. No ITHR was noted from isobutanol in Figure 77, but this decreased temperature sensitivity implies some increase in cool flame radical activity.

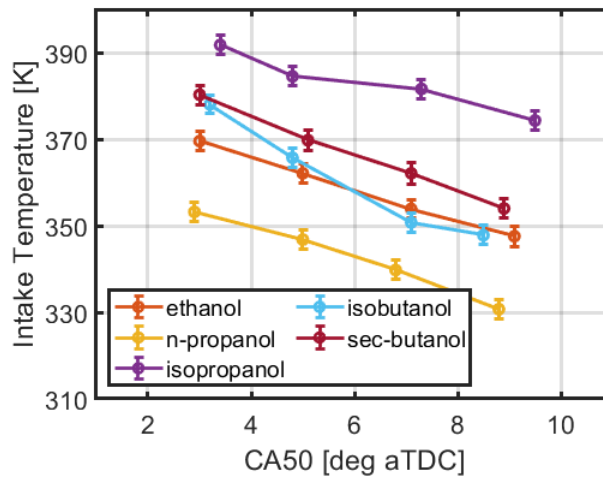


Figure 80: Intake temperature vs. CA50 with a  $\phi'$  of 0.33. The intake pressure is  $\sim 1.95$  bar.

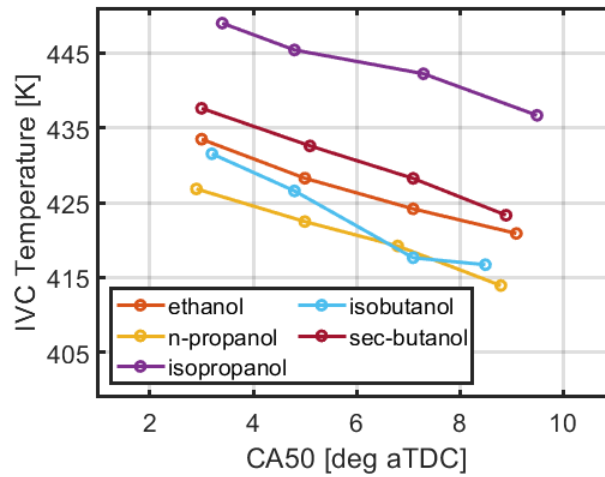


Figure 81: Intake valve closing (IVC) temperature vs. CA50 with a  $\phi'$  of 0.33. The intake pressure is  $\sim 1.95$  bar.

#### 4.5 Engine Speed

In HCCI, an increase in the engine speed can have an impact on fuel reactivity by decreasing the time available for cool flame reactions. In this section, the sensitivity of fuel reactivity to engine speed is examined by performing an engine speed sweep from 900 rpm to 2400 rpm for each fuel. For each speed case, the intake temperature was adjusted to maintain a constant CA50 of  $7.0 \pm 0.5$  deg aTDC,  $\phi'$  is maintained at 0.33, and the residual rate was maintained at  $\sim 30\%$ . The engine intake pressure is slightly boosted to 1.15 bar.

Figure 82 displays intake temperature vs. engine speed for each fuel. The intake temperature generally decreases with engine speed up to 1800 rpm, except for n-butanol, which does not experience a significant change. Coupled with this decrease in intake temperature is an increase in exhaust temperature for each fuel, as shown in Figure 83. The exhaust temperature increases with engine speed for three reasons: a decrease in in-cylinder heat transfer, a decrease in manifold residence time, which decreases heat transfer from the hot exhaust gases before re-entering the cylinder during the rebreathe event, and an increase in combustion efficiency, shown

in Figure 84 and discussed later in this section, which results in more heat release and therefore, more exhaust gas enthalpy.

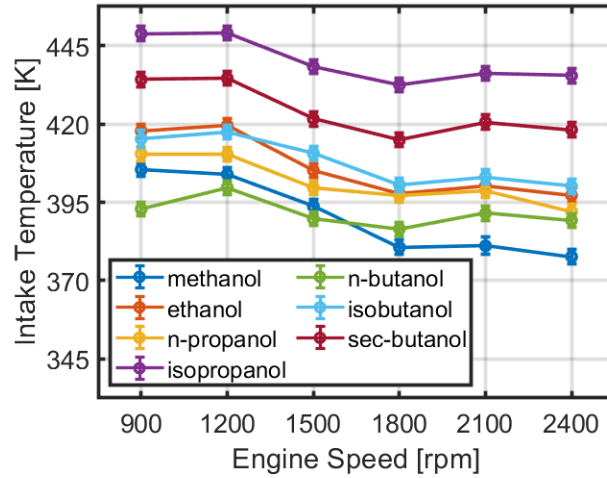


Figure 82: Intake temperature vs. engine speed with a constant CA50 of  $7.0 \pm 0.5$  deg aTDC and constant  $\phi'$  of 0.33.

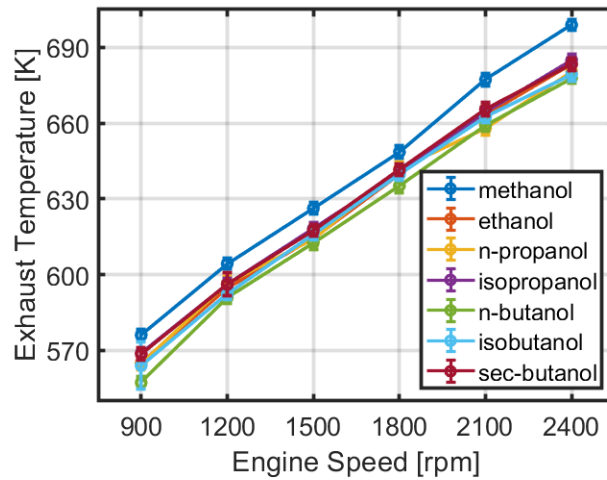


Figure 83: Exhaust temperature vs. engine speed with a constant CA50 of  $7.0 \pm 0.5$  deg aTDC and constant  $\phi'$  of 0.33.

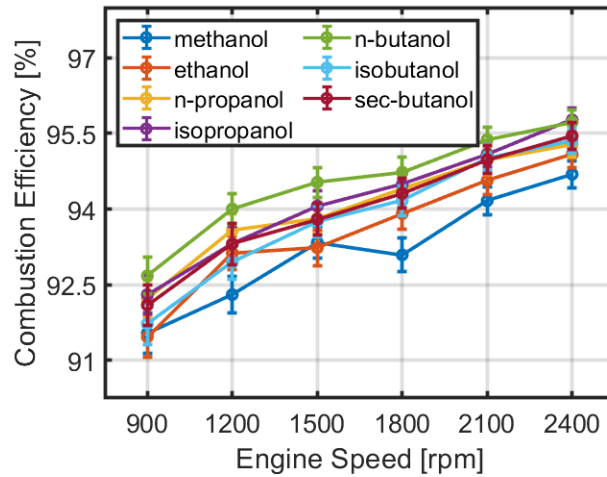


Figure 84: Combustion efficiency vs. engine speed with a constant CA50 of  $7.0 \pm 0.5$  deg aTDC and constant  $\phi'$  of 0.33.

The coupled changes in intake and exhaust temperature result in a net increase in IVC temperature, seen in Figure 85. Methanol appears to have the least change in IVC temperature while n-butanol has the most. An increase in engine speed decreases the amount of time for cool flame reactions to advance hot ignition. As a result, n-butanol requires a larger increase in IVC temperature than the other fuels considered, since n-butanol displays the most cool flame reactivity. Overall, the IVC temperature must increase with engine speed to raise the temperature near TDC to compensate for the lower residence time near TDC and achieve autoignition. This increase in IVC temperature and decrease in compression stroke heat loss, coupled with a shorter residence time near TDC results in a nearly constant ignition time, seen as a constant CA10 in Figure 86.

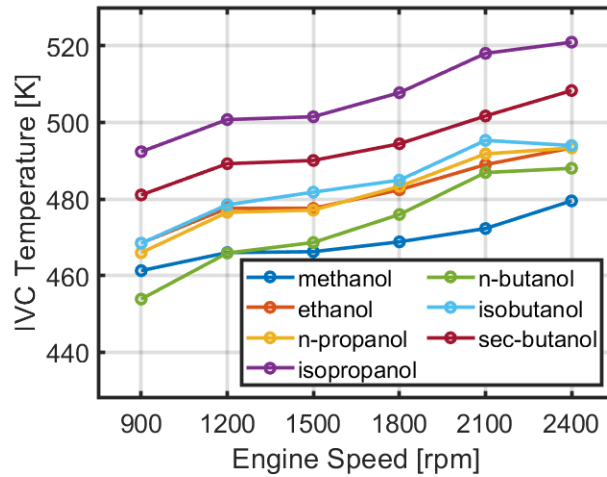


Figure 85: Intake valve closing (IVC) temperature vs. engine speed with a constant CA50 of  $7.0 \pm 0.5$  deg aTDC and constant  $\phi'$  of 0.33.

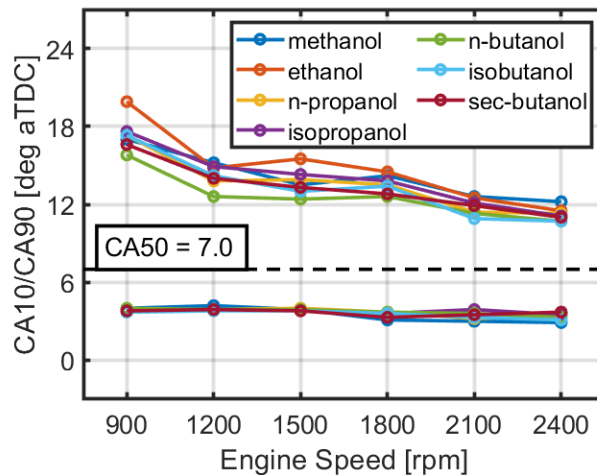


Figure 86: CA10 and CA10 vs. engine speed with a constant CA50 of  $7.0 \pm 0.5$  deg aTDC, denoted with a reference line, and constant  $\phi'$  of 0.33. The single cycle uncertainty of CA10 and CA90 is  $\sim 0.2$  deg while the 300-cycle ensemble average uncertainty is  $\sim 1.0$  deg.

Also shown in Figure 86 is an advance of CA90 with engine speed, i.e., a shortening of the burn duration. This effect and the increase in combustion efficiency with speed are caused by an increase in the positive feedback of sequential autoignition. While it is shown that the heat release profiles of single stage ignition fuels are generally self-similar at different engine speeds [116], this

self-similarity was in the crank-angle domain. A higher engine speed means a faster heat release process in the time domain, reducing heat transfer losses during the heat release process itself, and increasing the effectiveness of sequential autoignition. Specifically, this increase in effectiveness allows some of the colder regions in the cylinder to reach autoignition when they would not have at a lower engine speed. Although the CA10-CA50 burn duration is approximately constant with engine speed, the CA50-CA90 burn duration decreases and the combustion efficiency increases as engine speed increases.

This chapter presents a large array of experimental results characterizing the HCCI behavior of methanol, ethanol, n-propanol, isopropanol, n-butanol, isobutanol, and sec-butanol. Due to its cool flame reactivity, n-butanol behaved differently than the other six alcohols studied. Although some differences in autoignition resistance were found among the other six alcohols, they behaved similarly in response to changes in operating condition, i.e., they had similar sensitivities to operating condition changes. This similarity in LTC performance means these fuels can be used interchangeably with a reasonably sophisticated engine control unit that can adjust parameters like injection timing and NVO cam phasing in response to in-cylinder combustion to optimize performance for a given speed and load.

In the future, it is unlikely that just one fuel will be distributed for widespread use analogous to the way that gasoline or diesel are currently ubiquitous. Rather, it is likely that the specific alcohol fuel used will vary by region and even by season within a region depending on the availability of resources. Having the ability to use multiple carbon-neutral fuels interchangeably greatly increases the likelihood of widespread adoption. In a similar vein, the interchangeability of these fuels also allows for multi-component alcohol fuel blends. This would increase the utilization of alcohols that are produced on smaller scales. Additionally, the radical quenching effect of the



C1-C3 alcohols could be used to suppress the cool flame reactivity of n-butanol and sec-butanol and homogenize their LTC performance with the other low alcohols.

## Chapter 5: LTC Fuel Rating Metrics

### 5.1 “Beyond-MON” Critical Compression Ratio of C1-C4 Alcohols

In this section, the critical compression ratio experiments are conducted using operating conditions shown in Table 9. While the intake pressure, intake temperature, and engine speed all have low relative uncertainties, the relative uncertainty of CA50 can be high due to cyclic variability. Additionally, although the relative uncertainty in the equivalence ratio is not high, HCCI combustion is highly sensitive to equivalence due to factors such as  $\phi$ -sensitivity of the fuel and the difference in temperature of internal residuals. To quantify the uncertainty in critical compression ratio resulting from uncertainty in CA50 and equivalence ratio, a design of experiments is constructed to quantify the sensitivity of critical compression ratio to both CA50 and equivalence ratio. This design of experiments is illustrated in Figure 87.

*Table 9: Standard operating conditions for experimentally determining the critical compression ratio*

Operating Condition	
Intake Pressure	1.0 bar (naturally aspirated)
Intake Temperature	473 K (200°C)
Equivalence Ratio	0.33 ( $\lambda = 3$ )
Engine Speed	600 rpm
CA50	3.0 deg aTDC

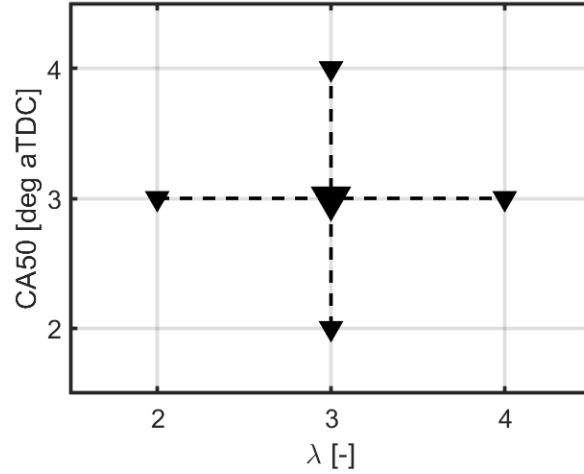


Figure 87: Design of experiments for determining the sensitivity of the critical compression ratio of each fuel to CA50 and equivalence ratio ( $1/\lambda$ )

Once the sensitivity coefficients of the critical compression ratio with respect to CA50 ( $\partial cCR_{CA50}$ ) and to equivalence ratio ( $\partial cCR_{\varphi}$ ) are quantified using the design of experiments, the following equation can be used to quantify the uncertainty in the critical compression ratio:

$$\Delta cCR^2 = (\partial cCR_{CA50} \Delta CA50)^2 + (\partial cCR_{\varphi} \Delta \varphi)^2 + \Delta cCR_{meas}^2 \quad (34)$$

where  $\Delta cCR_{meas}$  is the measurement uncertainty of the compression ratio of the CFR engine. Based on in-house calibration, the measurement uncertainty of the compression ratio is  $\pm 0.02$ .

The high temperature (HT) HCCI critical compression ratios for all seven C1-C4 alcohols considered are shown in Table 10. Highlighted in blue is the critical compression ratio obtained under the standard operating conditions outlined in Table 9. The other four cases correspond to the design of experiments for determining the uncertainty in the critical compression ratio. Due to a limitation on the maximum fuel flow rate imposed by the carburetor horizontal jet, the richest methanol operating condition was not achievable. Using the data in Table 10, the sensitivity coefficients of the critical compression ratio with respect to CA50 and to equivalence ratio are calculated.  $\Delta CA50$  is reported as the uncertainty in the CA50 of the ensemble average, meaning

cycle-to-cycle variation sourced uncertainty is not considered. This is because the HT HCCI critical compression ratio is concerned with the ensemble average CA50, not the “next cycle” CA50. Equation 2 is then used to determine the uncertainty in the critical compression ratio. These results are shown in Table 11.

*Table 10: Critical compression ratios for each fuel under each operating condition defined by the design of experiments, shown in Figure 87. Highlighted in blue is the critical compression ratio obtained under the standard operating conditions outlined in Table 9.*

Fuel	$\phi$ -0.33 CA50-2.0	$\phi$ -0.33 CA50-3.0	$\phi$ -0.33 CA50-4.0	$\phi$ -0.40 CA50-3.0	$\phi$ -0.25 CA50-3.0
methanol	11.77	11.70	11.57	--	12.13
ethanol	12.11	12.02	11.90	11.59	12.75
n-propanol	11.86	11.72	11.64	11.48	12.33
isopropanol	13.26	13.14	13.02	12.89	13.91
n-butanol	11.31	11.20	11.13	10.92	11.96
isobutanol	11.98	11.86	11.77	11.54	12.46
sec-butanol	12.75	12.67	12.56	12.29	13.30

*Table 11: The sensitivity coefficients of the critical compression ratio with respect to CA50 ( $\partial cCR_{CA50}$ ) and to equivalence ratio ( $\partial cCR_{\phi}$ ), the uncertainty in CA50 ( $\Delta CA50$ ) and equivalence ratio ( $\Delta \phi$ ), and the uncertainty in critical compression ratio ( $\Delta cCR$ ), calculated with equation 2. Additionally, the critical compression ratio ( $cCR$ ) for each fuel is shown as a reference.*

Fuel	$\partial cCR_{CA50}$	$\Delta CA50$	$\partial cCR_{\phi}$	$\Delta \phi$	$\Delta cCR$	$cCR$
methanol	0.10	0.3	5.38	0.01	0.06	11.70
ethanol	0.11	0.2	7.73	0.01	0.08	12.02
n-propanol	0.11	0.2	5.67	0.01	0.06	11.72
isopropanol	0.12	0.3	6.80	0.01	0.08	13.14
n-butanol	0.09	0.2	6.93	0.01	0.07	11.20
isobutanol	0.11	0.2	6.13	0.01	0.07	11.86
sec-butanol	0.09	0.2	6.73	0.01	0.07	12.67

In addition to the uncertainty in critical compression ratio, Table 11 also displays the critical compression ratio obtained under the standard operating conditions outlined in Table 9 as

a reference, henceforth referred to as just the critical compression ratio or HT HCCI cCR. Methanol, ethanol, n-propanol, and isobutanol all have very similar critical compression ratio values. Isopropanol has a critical compression ratio much higher than the other C1-C4 alcohols. The critical compression ratio of n-butanol is the lowest of the C1-C4 alcohols. This agrees with the chemical kinetics theory, which states that alcohols with longer alkane groups will have a lower autoignition threshold [59]. Sec-butanol has a higher critical compression ratio than isobutanol.

In the following subsections, the HT HCCI critical compression is compared to the CN, the MON, and the RON rating of each of the seven bio-synthesizable C1-C4 alcohol fuels. The CN, MON, and RON of each fuel considered is shown in Table 12. CNs for the seven alcohol fuels, as reported in Ref. [118], are all below 15. 2,2,4,4,6,8,8-heptamethylnonane, which has a cetane number of 15, is reference fuel used as the lower bound of CN. Additionally, an extremely low CN implies a very long ignition delay, which increases fuel-air mixing, which can affect the behavior of the CN test. As a result, CN measurements below 15 can have high uncertainty.

*Table 12: The Cetane number (CN), motor octane number (MON), research octane number (RON), and the octane sensitivity (S) of the seven alcohol fuels considered. CNs are from Ref. [118]. Note that the reported CN of methanol, ethanol, and n-butanol in this table is the average of several values found in Ref. [118]. \*The RON of isopropanol reported here was experimentally measured on the CFR used in this study to rectify conflicting reports in the literature.*

Fuel	CN	MON	RON	S = RON - MON
methanol	3.3	89	109	20
ethanol	7.0	90	108	19
n-propanol	12.0	89	104	15
isopropanol	10.0	99	113*	14
n-butanol	9.7	85	98	13
isobutanol	8.5	90	105	15
sec-butanol	8.5	93	108	15

### 5.1.1 Cetane Number

CN is an ignition quality metric used to describe a fuel's expected performance in CDC. Specifically, it is a measure of the delay between the injection of a fuel and the start of combustion. Fuels with a high CN will autoignite more readily when injected into the cylinder near the end of the compression stroke whereas fuels with a low CN tend to have a long delay between injection and the start of combustion. This delay allows time for the fuel and air to mix, resulting in a larger amount of heat release in the premixed burn phase of diesel combustion.

Since CN is a metric that measures ignition delay and is the only standard compression ignition fuel reactivity rating by ASTM for fuels, it is of interest to see whether CN correlates well with the HT HCCI cCR. When examining Figure 88, which plots critical compression ratio vs. CN for the seven alcohol fuels considered, there is virtually no correlation. The coefficient of determination ( $R^2$ ) is 0.02.

Comparing the nature of the critical compression test to CN tests helps illuminate why there is no correlation between the two metrics. There are multiple CN tests, including ones performed on a CFR engine and ones performed in a constant volume combustion chamber. What each CN test has in common is the injection of fuel into a high-pressure, high-temperature environment. Since the spray must first break up and evaporate before combustion can begin, the physical properties of the fuel become important; in particular, the viscosity and the cooling potential. Short-chain alcohol fuels have very high heats of vaporization compared to other fuels, and these high heats of vaporization decrease rapidly as carbon chain length increases. Similarly, short-chain alcohol fuels have low  $AFR_{stoich}$  values compared to other fuels, and these low  $AFR_{stoich}$  values increase rapidly as carbon chain length increases. This explains why methanol has the lowest CN of the C1-C4 alcohols. However, it does not explain why isopropanol has a slightly lower CN than n-butanol. Since the HT HCCI cCR test procedure considered in this work premixes fuel and

air in the manifold with a carburetor, with a controlled charge inlet temperature, the effect of liquid physical properties is eliminated. Overall, it is clear that CN and critical compression ratio of alcohol fuels do not correlate.

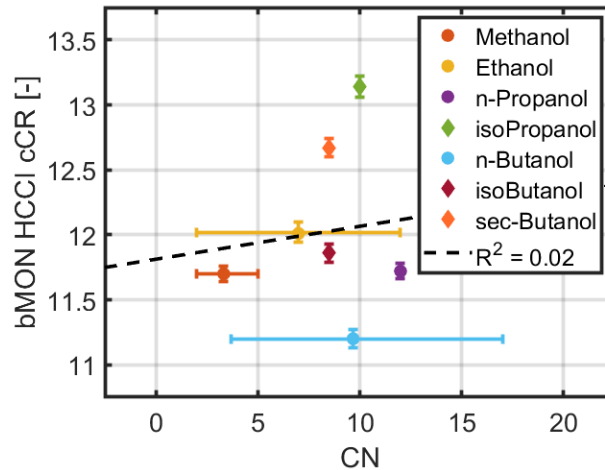


Figure 88: High temperature HCCI critical compression ratio vs. cetane number (CN) for the seven alcohol fuels considered. Vertical error bars display the uncertainty in the critical compression ratio. Horizontal error bars on methanol, ethanol, and n-butanol display the range of CN values found for these fuels in Ref. [118].

### 5.1.2 Octane Number

Octane number is a metric used to describe the knock propensity of a fuel. Fuels with higher octane numbers have a higher resistance to knock than fuels with lower octane numbers. There are two octane number tests: MON and RON. Both octane number tests measure the reading of a knockmeter during knocking SI combustion, where the equivalence ratio is adjusted such that the knockmeter reading is maximized. The difference between the two octane number tests are the operating conditions at which they are conducted. The MON test is run at 900 rpm and has a constant inlet charge temperature of 149°C. The RON test is run at 600 rpm and has a lower inlet temperature than the MON test, 52°C. Additionally, the MON test uses a mixture air heater to ensure the charge temperature entering the cylinder is exactly 149°C. Contrarily, the RON test only

uses an air heater upstream of the carburetor; the actual charge temperature entering the cylinder is a function of the fuel's cooling potential.

Given that the critical compression ratio test conducted in this work was performed at 200°C, using the MON mixture air heater to maintain a constant inlet temperature, it is of interest to determine whether the critical compression ratios of the C1-C4 alcohols correlate with their MON values. Figure 89, which plots critical compression ratio vs. MON, shows that there is a strong correlation between critical compression ratio and MON for the C1-C4 alcohol fuels, with an  $R^2$  of 0.95. While this result may seem to directly contradict the hypothesis that MON is not a good metric for HCCI, it is important to consider that this correlation only considers the C1-C4 alcohol fuels.

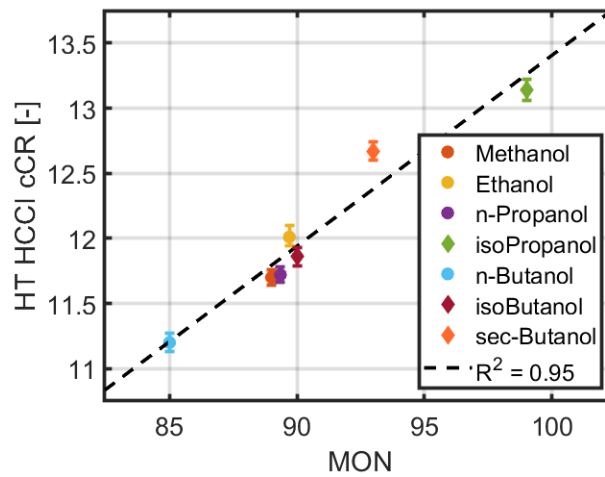


Figure 89: High temperature HCCI critical compression ratio vs. motor octane number (MON) for the seven alcohol fuels considered. Vertical error bars display the uncertainty in the critical compression ratio.

Since the critical compression ratio correlated well with MON, it is of interest to see whether there is also a correlation between the critical compression ratio of the C1-C4 alcohols and their RON values. Figure 90, which plots critical compression ratio vs. RON, shows a moderate correlation, with an  $R^2$  of 0.69. The MON and RON tests subject fuels to different pressure-temperature trajectories; in general, fuels will exhibit more cool flame reactivity in the RON test



than in the MON test. However, the C1-C4 alcohols have little-to-no cool flame reactivity under all engine relevant conditions. Although the operating conditions of the critical compression ratio test could be considered MON-like due to the high intake temperature of that test, it still may be surprising that the critical compression ratio correlates significantly less with RON than it does with MON given the single stage ignition properties of the fuels. To explain this, one subtle difference between the MON and RON tests is highlighted: the mixture air heater. While this difference may not affect most hydrocarbon fuels since they have similar cooling potentials and therefore similar pre- and post-carburetor charge temperatures, the cooling potential looms large for short-chain alcohol fuels.

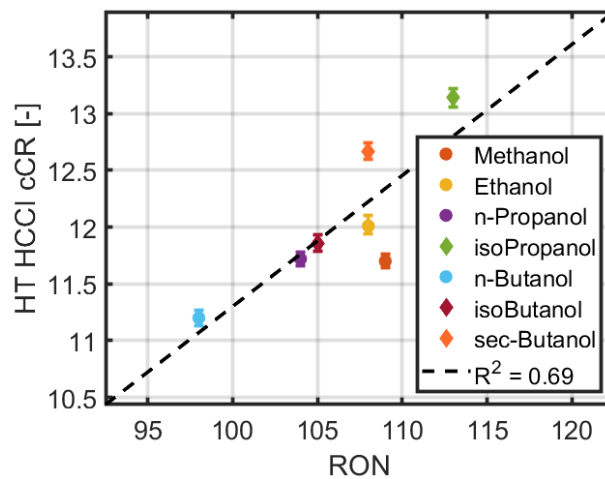


Figure 90: High temperature HCCI critical compression ratio vs. research octane number (RON) for the seven alcohol fuels considered. Vertical error bars display the uncertainty in the critical compression ratio.

Other researchers showed that the RON values of ethanol-gasoline blends would be affected by the high cooling potential of ethanol [119, 120]. To determine how much of an impact the cooling potential of ethanol has on the RON values of ethanol-gasoline blends, Foong et al. measured the RON value of ethanol-gasoline blends ranging from 0% to 100% ethanol under standard RON conditions and under *modified RON* conditions. The modified RON conditions were identical to the RON conditions except that they maintained a constant post-carburetor charge inlet

temperature [120]. Their findings indicated that as the cooling potential of the ethanol-gasoline mixtures increased, the difference between the standard RON value and the modified RON value increased, as indicated in Figure 91.

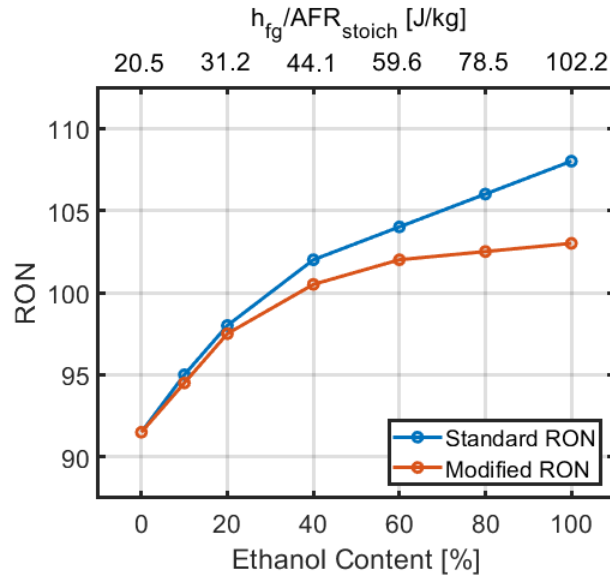


Figure 91: Data from Ref. [119] showing standard RON and modified RON vs. ethanol content of ethanol-gasoline blends showing the impact of the heightened cooling potential of ethanol on the determined RON values. Modified RON is defined as the RON test with a constant charge inlet temperature designed to compensate for the differences in cooling potentials of the fuel blends.

Knowing that the cooling potential of the alcohol fuels studied in this work are significantly higher than that of most hydrocarbons, the RON values of each fuel are modified to account for their high cooling potential. To do this, the cooling potential of each fuel is linearly interpolated between cooling potential of the ethanol-gasoline blends and the difference between the standard RON and the modified RON values in Figure 91 from Ref. [120]. The interpolated difference between the standard RON and modified RON values is then subtracted from the experimentally determined RON values in Figure 90 to correct for the differences in cooling potentials of the various fuels. The results are shown in Table 13. Note that for methanol, the data must be

extrapolated, since the cooling potential of methanol is higher than ethanol. When critical compression ratio is plotted against modified RON, as seen in Figure 92, the  $R^2$  is now 0.95, indicating a strong correlation and indicating that the differences in cooling potential were the main reason for the lower  $R^2$  value in the RON results in Figure 90.

*Table 13: The modified RON of each alcohol fuel considered, which is a function of the fuel's RON and the fuel's cooling potential, given by equation 1.  $h_{fg, fuel}$  is the latent heat of vaporization of the fuel and  $AFR_{stoich}$  is the stoichiometric air-fuel ratio of the fuel.*

Fuel	$h_{fg, fuel}$ [J/kg]	$AFR_{stoich}$ [-]	$\frac{h_{fg, fuel}}{AFR_{stoich}}$ [J/kg]	RON	Modified RON
methanol	1168	6.46	180.80	109	99.0
ethanol	920	9.00	102.22	108	103.0
n-propanol	792	10.33	76.67	104	100.6
isopropanol	757	10.33	73.28	113	109.8
n-butanol	708	11.17	63.38	98	95.7
isobutanol	686	11.17	61.41	105	102.9
sec-butanol	671	11.17	60.07	108	106.0

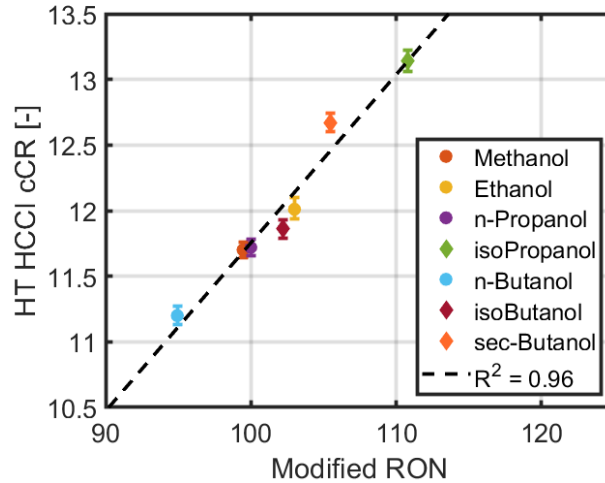


Figure 92 High temperature HCCI critical compression ratio vs. modified research octane number (RON) for the seven alcohol fuels considered. The modified RON is a metric that is a calculated adjustment to the RON value of a fuel based on its cooling potential. Vertical error bars display the uncertainty in the critical compression ratio.

### 5.1.3 Evaluation of HT HCCI Critical Compression Ratio

The predictive capability of the HT HCCI cCR measured on a CFR engine is evaluated by correlating it with the intake temperature requirement to maintain a constant CA50 of 7.0 deg aTDC on the gasoline engine architecture. Figure 93 displays intake temperature vs. HT HCCI cCR for five different operating conditions: a) 1200 rpm, 30% internal exhaust gas recirculation (iEGR), b) 1200 rpm, 20% iEGR, c) 1200 rpm, 40% iEGR, d) 900 rpm, 30% iEGR, and e) 2400 rpm, 30% iEGR. For all five operating conditions, the equivalence ratio is 0.33 and the intake temperature is slightly boosted to 1.15 bar. The  $R^2$  of the first four conditions is very high, indicating a strong correlation. The  $R^2$  of the fifth condition, which is the highest engine speed, is a somewhat lower at 0.84, which indicates a good correlation, but not a great correlation. Specifically, methanol and n-butanol outlay low and high, respectively. The strong correlation between the intake temperature requirement to maintain a CA50 of 7.0 deg aTDC and the HT HCCI cCR measured at a CA50 of 3.0 deg aTDC shows that the specific CA50 chosen for the critical compression ratio test is not of

significant importance as long as stable combustion is achievable. This is supported by observing that  $\partial cCR_{CA50}$  is similar valued for all seven fuels.

The HT HCCI cCR test is performed at a high temperature, achieved by increasing the intake temperature to a 473 K, in order to achieve autoignition at a compression ratio in the mid-range. In a practical setting, negative valve overlap (NVO) or exhaust rebreathe would be used to trap large amounts of iEGR to achieve the high intake valve closing (IVC) temperatures required to achieve autoignition in this compression ratio range. Since the HT HCCI cCR correlated well with the intake temperature reequipment with three rebreathe levels of iEGR, 20%, 30%, and 40%, this means that for the alcohol fuels, the EGR constituents and the subsequent substitution of oxygen in the cylinder do not significantly affect the autoignition process. This agrees well with the analysis performed in Chapter 4, which found that the IVC temperature did not change significantly with the residual rate. As a result, intake charge heating is a sufficient method for the purposes of creating a standardized test on the CFR engine, which cannot achieve high levels of iEGR.

The HT HCCI cCR test is also performed at a relatively low engine speed of 600 rpm, which is on the low end of the speed range of a future LTC engine. Engine speed can be a significant factor in determining the HCCI reactivity of a fuel exhibiting significant cool flame reactivity. However, the C1-C3 alcohols show no cool flame reactivity and under these HT conditions, the butanol isomers show little-to-no cool flame reactivity. At a slightly faster engine speed of 900 rpm and 1200 rpm, there is a strong correlation. At the highest engine speed tested, 2400 rpm, the correlation weakens slightly, but is still good. This means that for single-stage ignition fuels, or under conditions where fuels behave like single-stage ignition fuels, the low speeds of the CFR engine are acceptable for the critical compression ratio test.

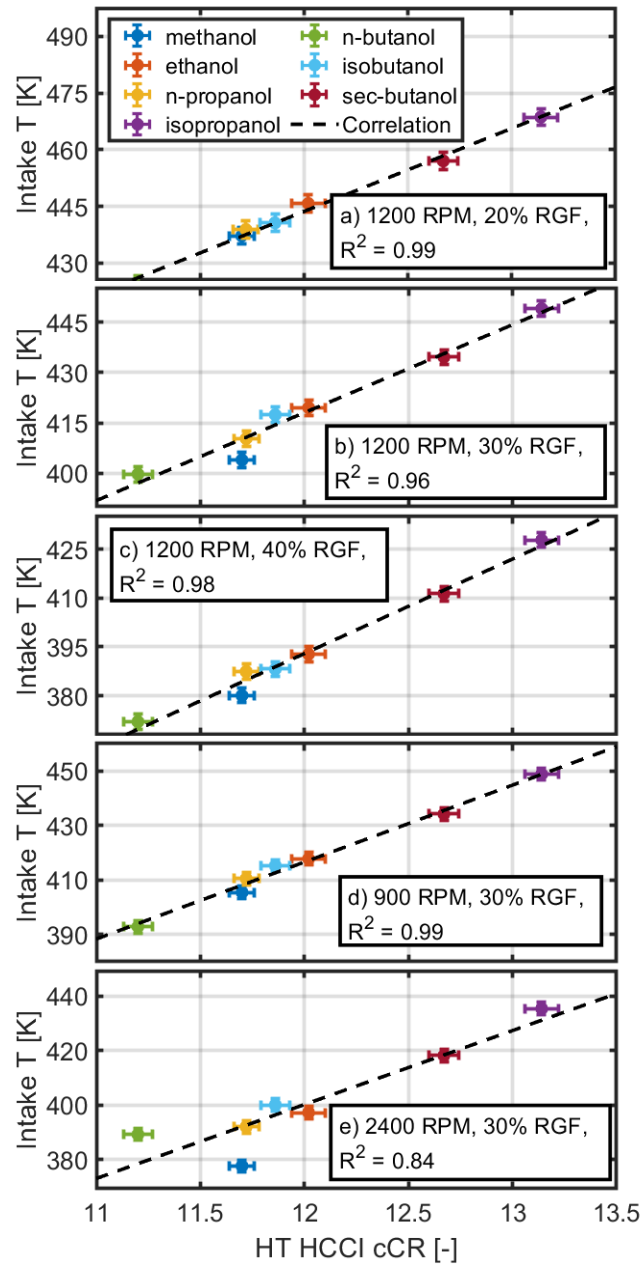


Figure 93: Intake temperature requirement of gasoline engine architecture vs. high temperature (HT) HCCI critical compression ratio (cCR) measured in this work under five different operating conditions: a) 1200 rpm, 20% internal exhaust gas recirculation (iEGR), b) 1200 rpm, 20% iEGR, c) 1200 rpm, 40% iEGR, d) 900 rpm, 30% iEGR, and e) 2400 rpm, 30% iEGR.

In this work, the HT HCCI critical compression ratios of the neat alcohols studied in this work correlated well with their MON (and HOV-modified RON) ratings. In contrast, other researchers have demonstrated that octane number is not adequate for predicting the HCCI reactivity of fuels. To understand this discrepancy, two premium octane (RON 98) gasoline blends from the U.S. Department of Energy’s Co-Optimization of Fuels and Engines program are considered. The RON 98 gasolines had one particular component blended at a high concentration: olefins and cycloalkanes. They are aptly named RON98OLF and RON98CYK, respectively. The measured HT HCCI cCR of RON98OLF and RON98CYK is 12.0 and 13.0 respectively. Table 14 displays the RON, MON, and chemical composition of the two RON98 gasolines as well as their measured HT HCCI cCR. Note that the octane numbers of the two RON98 gasolines are nearly identical while their HT HCCI cCR differs significantly. The IVC temperature requirement to maintain a constant CA50 of 7.0 deg aTDC at an engine speed of 1200 rpm and an iEGR rate of 30% was then correlated with HT HCCI cCR for those two gasolines along with the C1-C4 alcohol fuels, as seen in Figure 94. This is done in under at three values of  $\phi$  (0.25, 0.33, and 0.45) at an intake pressure of 1.15, and under four intake pressures (1.15, 1.35, 1.65, and 1.95 bar) at a  $\phi$  of 0.33. Here, IVC temperature is used in place of intake temperature to account for the difference in exhaust temperatures between the alcohol fuels and the gasolines.

*Table 14: RON, MON, HT HCCI cCR, and chemical composition of the two RON98 gasoline blends.*

	RON98OLF	RON98CYK
RON	98	98
MON	88	87
Sensitivity = RON-MON	10	11
HT HCCI cCR	12.03	13.00
n-paraffin (Vol %)	12	3
Iso-paraffin (Vol %)	44	95
Aromatics (Vol %)	13	0.75
Naphthenes (Vol %)	3	0.01
Olefins (Vol %)	27	0.08
Oxygenates (Vol %)	0	0

[blank page]



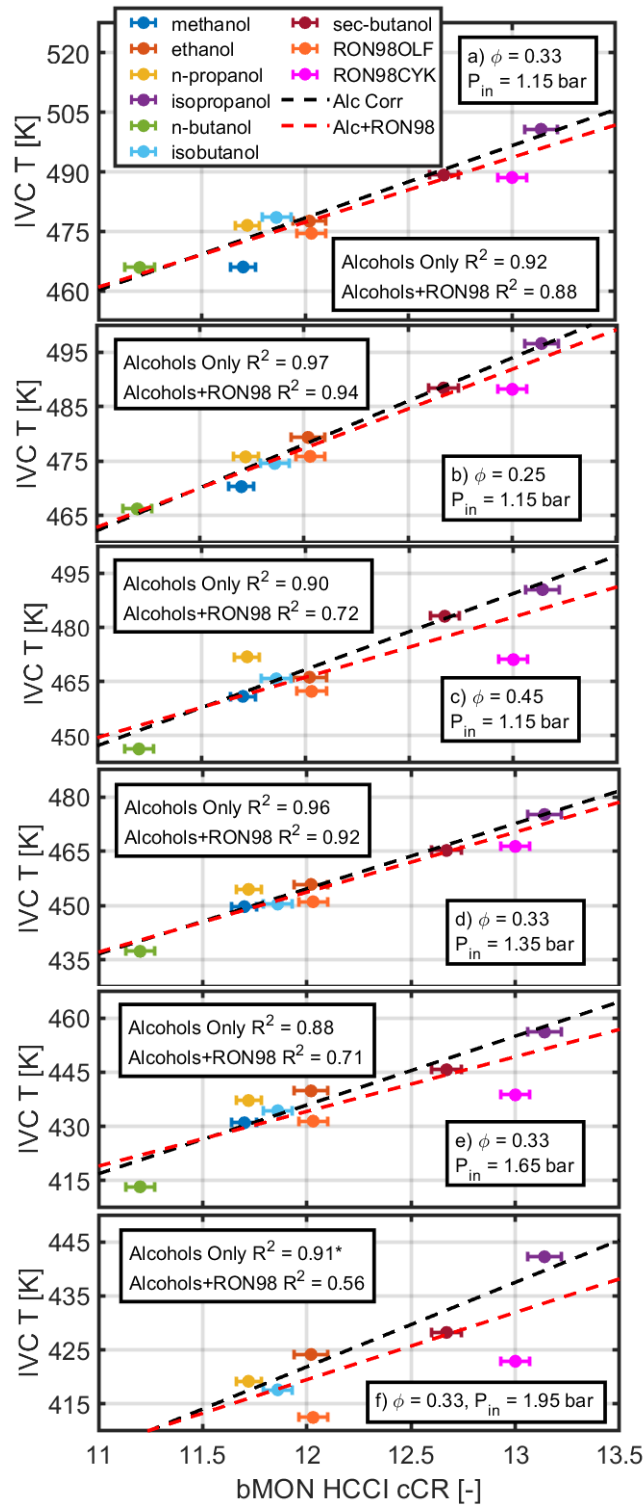


Figure 94: Intake valve closing (IVC) temperature requirement of gasoline engine architecture vs. high temperature (HT) HCCI critical compression ratio (cCR) under six different operating conditions: a)  $\phi = 0.33$ , Intake pressure =

1.15 bar b)  $\phi = 0.25$ , Intake pressure = 1.15 bar, c)  $\phi = 0.45$ , Intake pressure = 1.15 bar 4)  $\phi = 0.33$ , Intake pressure = 1.35 bar, e)  $\phi = 0.33$ , Intake pressure = 1.65 bar f)  $\phi = 0.33$ , Intake pressure = 1.95 bar. \*At an intake pressure of 1.95 bar, methanol and n-butanol are not included.

Under the “standard condition” in Figure 94a, including the two RON98 gasolines in the correlation decreased the  $R^2$  from the alcohol-only correlation from 0.92 to 0.88, which indicates that there is still a good correlation between IVC temperature and HT HCCI cCR for different classes of fuels, which is not true for traditional fuel metrics like octane number. With a reduction of  $\phi$  or a slight increase in intake pressure there is still a strong correlation between IVC temperature and HT HCCI cCR, seen in Figure 94b and Figure 94d, respectively. An increase in  $\phi$  from 0.33 to 0.45 decreases the  $R^2$  of the alcohol-only correlation slightly to 0.9, seen in Figure 94c, but decreases the  $R^2$  significantly to 0.72 when the RON98 gasolines are included. Specifically, it appears that RON98CYK is an outlier, with its required IVC temperature dropping significantly more than other fuels from a  $\phi$  of 0.33 to 0.45. Similarly, n-butanol’s decrease in IVC temperature requirement from a  $\phi$  of 0.33 to 0.45 is more than the other alcohols, implying some larger degree of  $\phi$ -sensitivity.

When the intake pressure is increased further to 1.65 bar and 1.95 bar, Figure 94e and Figure 94f, respectively, both the alcohol-only and the alcohol-plus-RON98 correlations weaken. At 1.65 bar, it is clear that the IVC temperature requirement of n-butanol and RON98CYK more than the other fuels. At 1.95 bar, n-butanol’s IVC temperature requirement drops so much that the intake conditioning system cannot sufficiently cool the incoming air enough to retard combustion to a CA50 of 7.0 deg aTDC due to n-butanol’s emergent ITHR. Similarly, RON98CYK also experiences a large decrease in IVC temperature requirement due to cool flame reactivity. Sec-butanol, which was shown in Chapter 4 to display some small amount of ITHR at an intake pressure of 1.95 bar, and RON98OLF also experience a slightly higher decrease in their required IVC temperature compared to the remaining fuels. These results make it clear that the HT HCCI cCR

cannot capture the ignition behavior of fuels that are highly boosted. Specifically, the change in reactivity undergone by a fuel with cool flame reactivity cannot be captured by the HT HCCI cCR. Therefore, a second critical compression ratio under boosted conditions is likely required to provide a complete description of a fuel's HCCI reactivity.

## 5.2 Normalized $\phi$ -sensitivity

Ignition delay correlations are ineffective at accurately predicting the ignition delay of multi-stage ignition fuels due to their inability to capture NTC behavior. However, for single stage ignition fuels, autoignition phenomena can be accurately modeled with ignition delay correlations. Therefore, while the higher alcohols or any other rich-to-lean burn stratified combustion fuel candidates require chemical kinetics to study their normalized  $\phi$ -sensitivity behavior, the normalized  $\phi$ -sensitivity behavior of the lower alcohols can be studied using ignition delay correlations. Ignition delay correlations are generally computed from datasets collected either on a rapid compression machine (RCM) or a shock-tube. When selecting an ignition delay correlation to study the normalized  $\phi$ -sensitivity behavior of a fuel, it is important that the ignition delay correlation in question was developed under engine relevant conditions. Considering next-generation LTC engines will have medium-to-high compression ratios, this means the ignition delay correlation should be developed under high pressure and intermediate temperature conditions. Additionally, they should be developed with a dataset that includes multiple equivalence ratio points. It has been pointed out that ignition delay predictions of RCMs and shock-tubes differ significantly below 1100 K due to increasing error in shock-tube measurements [105]. For this reason, only ignition delay correlations developed on an RCM should be considered for the study of the normalized  $\phi$ -sensitivity behavior of a fuel. Considering the form of Eq. 8, each term is linearly dependent on one ignition delay correlation parameter. Since the relative uncertainty of the ignition delay parameters considered are on the order of 5% or lower, it follows

that the relative uncertainty of the normalized  $\phi$ -sensitivity would be of the same magnitude, which does not significantly impact the following analysis.

Only three of the seven C1-C4 alcohols have an RCM-developed ignition delay correlation: methanol [121], ethanol [122], and n-butanol [61]. The normalized  $\phi$ -sensitivity, evaluated using Eq. 8, is mapped to the  $\phi$ -T plane for methanol, ethanol, and n-butanol in Figure 95, Figure 96, and Figure 97, respectively. In this map,  $\phi$  can be considered as the background  $\phi$  in the cylinder, or in other words, the lowest  $\phi$  in the cylinder, since changes in the ignition delay are referenced to this background  $\phi$  when quantifying the ignition delay distribution in the cylinder. Because the ignition delay correlations report  $\beta$ ,  $E'_a$ , and  $\gamma$  as constant values rather than functions of operating conditions, the maps developed are independent of in-cylinder pressure. Values of  $\beta$ ,  $E'_a$ , and  $\gamma$  are displayed in Table 15.

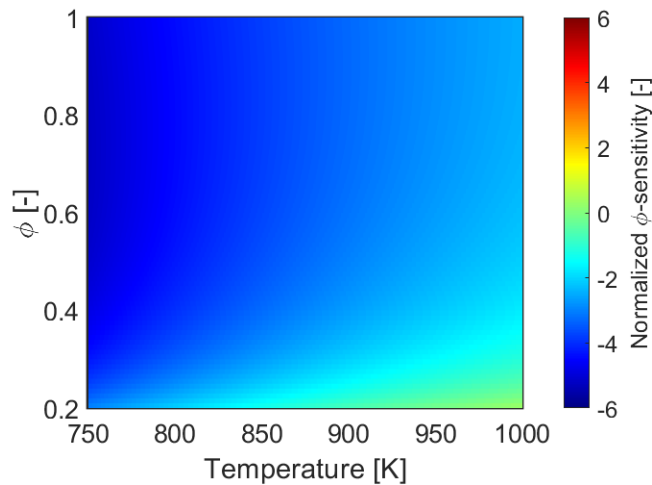


Figure 95: Normalized  $\phi$ -sensitivity (Equation 8) for methanol mapped to the  $\phi$ -T plane using the ignition delay correlation developed in Ref. [121].

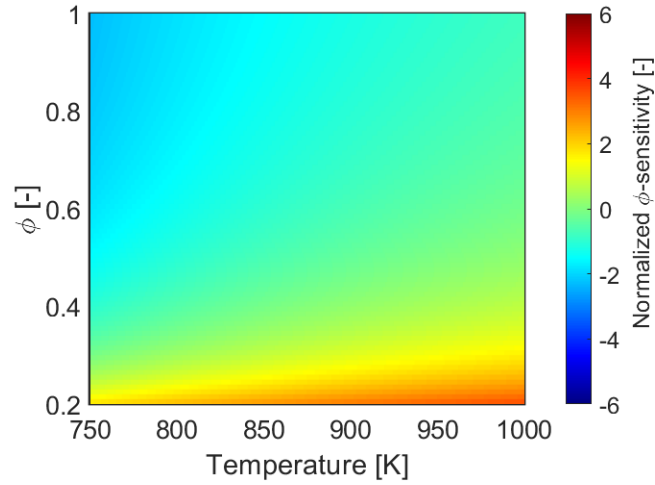


Figure 96: Normalized  $\phi$ -sensitivity (Equation 8) for ethanol mapped to the  $\phi$ -T plane using the ignition delay correlation developed in Ref [122].

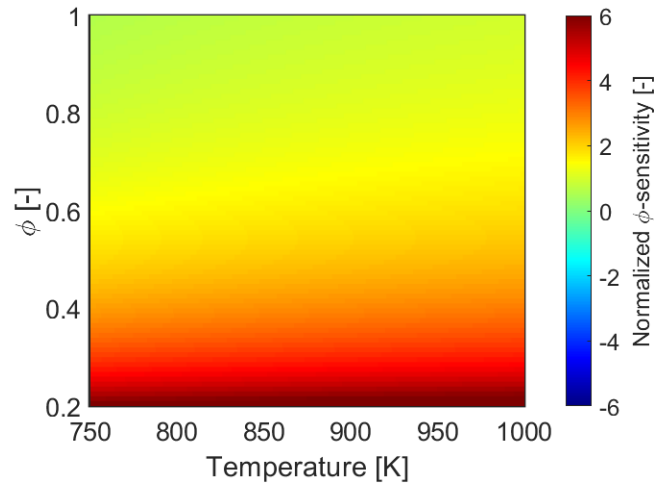


Figure 97: Normalized  $\phi$ -sensitivity (Equation 8) for n-butanol mapped to the  $\phi$ -T plane using the ignition delay correlation developed in Ref [61].

Table 15: Values of  $\beta$ ,  $E'_a$ , and  $\gamma$  from the ignition delay correlations of methanol, ethanol, and n-butanol.

Fuel	Methanol	Ethanol	n-Butanol
$\beta$ [-]	-0.89	-1.16	-1.4
$E'_a$ [K]	26864	25739	9730
$\gamma$ [-]	-0.24	0.00	-1.7
Reference	[121]	[122]	[61]

For a number of the advanced combustion concepts, stratification is used to control the combustion process outside of the operating range of HCCI. With that said, low-temperature, high- $\phi$  regions that correspond to loads that are too high for HCCI combustion are of interest. The temperature and  $\phi$  of the high load regions will depend on two factors: the intake boost level and the required level of stratification to protect the engine from high energy release rates. It is desirable for a fuel to have a large absolute value of normalized  $\phi$ -sensitivity in the high load regime so that only small amounts of stratification need to be induced to control the combustion process, reducing the likelihood of generating rich and near-stoichiometric regions in the cylinder that could produce harmful emissions.

From Figure 95, it can be seen that methanol has highly negative values of normalized  $\phi$ -sensitivity for operating conditions that would correspond to high loads. This makes methanol an ideal fuel candidate to enable lean-to-rich burn stratified combustion. With a normalized  $\phi$ -sensitivity less than -4, the ignition delay of rich regions will be twice the ignition delay of lean regions for a change in  $\phi$  of less than 0.25. The need to induce as little stratification as possible to control the heat release process is not only beneficial for minimizing harmful emissions but is also beneficial for efficiency. There is a potential efficiency detriment from injecting a large quantity of a fuel whose latent heat of vaporization is a non-negligible fraction of its lower heating value during the late compression stroke (e.g., for methanol,  $h_{fg}/Q_{LHV} \sim 6\%$ ). Additionally, minimizing the required stratification is important when exhaust gas recirculation (EGR) is used, since EGR lowers the oxygen content in the cylinder.

Examining Figure 97, n-butanol has, in the high load regime, normalized  $\phi$ -sensitivity values that trend towards zero, implying it would be ineffective at preventing damaging energy release rates and extending the high load limit since stratifying the charge with n-butanol would not significantly impact the ignition delay distribution in the cylinder. This result is not completely

unexpected since there is evidence of ITHR from n-butanol under boosted engine conditions and this ITHR works against the high cooling potential of the fuel. Although when developing the ignition delay correlation of n-butanol, no cool flame reactivity was noted, the low activation energy of n-butanol compared to methanol and ethanol implies that there may be some non-single-stage ignition behavior. More evidence supporting n-butanol's ITHR is found in work comparing the C1-C4 primary alcohols in high temperature shock-tube experiments and simulations. There, the activation energy of n-butanol was found to be close to that of ethanol and larger than methanol [123], meaning that the large difference in activation energy seen in the RCM and the shock tube is likely due to ITHR in the high pressure, intermediate-temperature regime. Overall, n-butanol does not seem to be an ideal fuel candidate to enable either lean-to-rich or rich-to-lean burn stratified combustion on its own. However, the neutral contribution of n-butanol stratification to the ignition delay distribution implies it could serve as a blending additive to increase the biofuel content of a fuel blend for use in either lean-to-rich or rich-to-lean burn stratified combustion. Considering the normalized  $\phi$ -sensitivity of n-butanol, and the autoignition behavior of n-pentanol and n-hexanol compared to n-butanol [124], which show more cool flame reactivity than n-butanol, it is likely n-pentanol or n-hexanol will be good fuel candidates to enable rich-to-lean burn combustion, perhaps blended with some higher octane fuel to increase their autoignition resistance without impacting their cool flame reactivity to allow for high compression ratio operation.

In Figure 96, it can be seen that the normalized  $\phi$ -sensitivity of ethanol has a low absolute value for the entirety of the  $\phi$ -T map. In the high-load regime, ethanol's normalized  $\phi$ -sensitivity is only slightly negative, meaning it can enable lean-to-rich burn stratified combustion, but not very effectively. This was confirmed in experiments that used a split injection of neat ethanol to smoothen heat release rates [69]. Since methanol and ethanol have very similar autoignition properties, the biggest factor resulting in differences in their respective normalized  $\phi$ -sensitivities is their cooling

potential. One way to increase the cooling potential of ethanol is through the addition of water to the fuel. As mentioned earlier, this is dually advantageous, as it reduces the energy requirement during the production of ethanol in addition to increasing its cooling potential. Figure 98 displays the cooling potential ( $\frac{dT}{d\phi}$ ) of wet ethanol vs. the mass percentage of water in the wet ethanol blend. The cooling potential of wet ethanol with a composition of 76% ethanol, 24% water by mass (WE76) is equal to that of neat methanol.

Figure 99 maps the normalized  $\phi$ -sensitivity of WE76 to the  $\phi$ -T plane. WE76 has negative values of normalized  $\phi$ -sensitivity comparable to methanol (Figure 95) in the high load region, meaning wet ethanol blends near WE76 are also ideal fuel candidates to enable lean-to-rich burn stratified combustion. HCCI combustion with various wet ethanol blends showed that combustion did not deteriorate and CO/uHC emissions did not significantly increase with water addition below 35% by mass (WE65) [117]. There will be a balance between how much water is in the water-fuel mixture and how much  $\phi$ -stratification must be induced to control the combustion process. Since methanol is miscible with water, blends of wet methanol could also be used to increase the cooling potential of the fuel for lean-to-rich burn stratified combustion. However, this is unlikely since neat methanol alone shows the potential for effectively enabling lean-to-rich burn stratified combustion, and any further addition of water would only serve to lower the already low energy density of the fuel and possibly produce more harmful emissions.



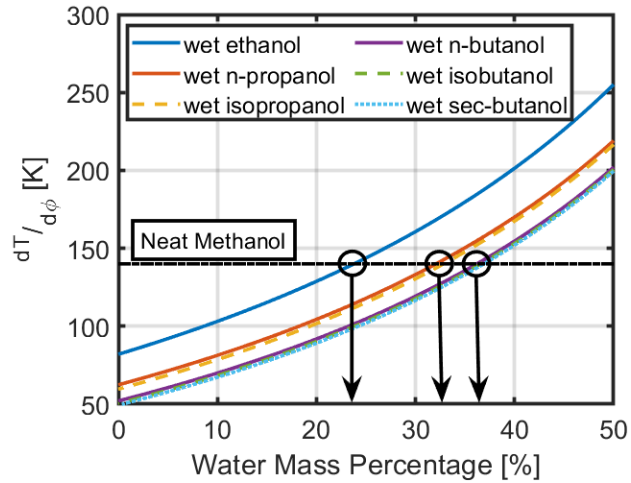


Figure 98: The cooling potential ( $\frac{dT}{d\phi}$ ) of wet ethanol blends, wet propanol blends, and wet butanol blends vs. water mass percentage in the wet-alcohol blend. A constant reference line displays the cooling potential of neat methanol. The cooling potential of wet ethanol equals that of neat methanol at a water mass percentage of ~24% (76% ethanol by mass). The cooling potential of wet propanol equals that of neat methanol at a water mass percentage of ~33% (67% propanol by mass). The cooling potential of wet butanol equals that of neat methanol at a water mass percentage of 37% (63% butanol by mass). These values are reported for  $\phi=0.6$  and  $T=700$  K.

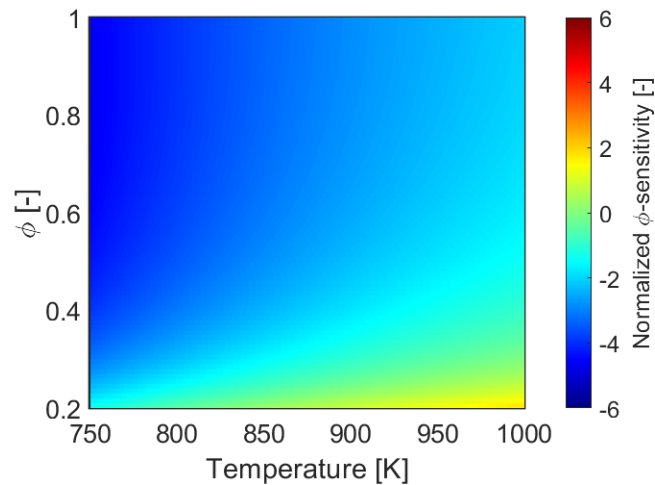


Figure 99: Normalized  $\phi$ -sensitivity (Equation 8) for wet ethanol 76 (76% ethanol, 24% water by mass) mapped to the  $\phi$ - $T$  plane using the ignition delay correlation developed in Ref [122].

Without an ignition delay correlation derived from RCM data, it is not possible to generate a normalized  $\phi$ -sensitivity map for n-propanol, isopropanol, isobutanol, and 2-butanol. However, some conclusions can be drawn about these four low alcohol fuels by comparing their reactivities from data found in the literature. Since all of those fuels do not display NTC behavior, they are candidates for lean-to-rich burn stratified combustion. The autoignition of methanol, ethanol, n-propanol, and n-butanol was compared in shock-tube experiments [123]. Although the lowest temperature tested was  $\sim 1050$  K, it was clear that ethanol and n-propanol had very similar autoignition behavior. A comparative shock-tube study of n-propanol and isopropanol showed that isopropanol had a higher activation energy than n-propanol, though both had similar  $\phi$ -sensitivities [125]. This agrees with the MON ratings of the fuels, with methanol, ethanol, and n-propanol having nearly identical MON ratings and isopropanol having a higher MON rating. The same can be said about RON if the RON rating is modified to account for the high cooling potential of the fuels in question [119, 120]. If n-propanol has similar ignition delay behavior at lower temperature, higher pressure conditions than those studied in Ref. [123], and if isopropanol has a slightly higher activation energy than n-propanol, it can be concluded that isopropanol will be a better candidate fuel than n-propanol. However, neither fuels in their neat form will be great candidates, since they will have a lower cooling potential than ethanol, which in its neat form (Figure 96) is not a great candidate. Fortunately, like ethanol, both propanol isomers are miscible with water, and therefore, their cooling potentials can be increased, as shown in Figure 98. Above water mass percentages of  $\sim 15\%$  (WP85), both propanol isomers have a higher cooling potential than neat ethanol and at  $\sim 33\%$  water content (WP67), the cooling potential of both propanol isomers equals that of neat methanol. To date, there have been no studies on the water tolerability of the propanol isomers in LTC.

In HCCI combustion, isobutanol was shown to behave similarly to ethanol [60]. This is supported by their similar MON and modified RON ratings. All four butanol isomers were studied in an RCM, though no ignition delay correlation was developed [113]. However, it is clear that isobutanol and 2-butanol have very similar ignition delay behavior, with isobutanol being slightly less reactive at higher pressures. With both butanol isomers having a much lower cooling potential than methanol, they will likely struggle to enable lean-to-rich burn stratified combustion. Further compounding this issue is their limited miscibility with water, which limits a potential increase in their cooling potential via water addition.

From the previous analysis, the C1-C4 alcohol fuels' propensities to enable a lean-to-rich burn stratified combustion can be ranked as follows: methanol  $\approx$  wet ethanol  $\approx$  wet isopropanol  $\approx$  wet n-propanol  $>$  ethanol  $>$  isopropanol  $>$  n-propanol  $>$  isobutanol  $\approx$  2-butanol  $>$  n-butanol. To incorporate the less effective C1-C4 alcohol fuels, multi-component alcohol fuel blends can be developed. For example, an ethanol/isobutanol/water blend of 50%/25%/25%, by mass, will have nearly the same cooling potential as methanol. Using multi-component alcohol fuel blends can increase the utilization of biofuels in stratified LTC. In the previous example, ethanol is able to serve as a cosolvent to isobutanol and water, allowing for the use of isobutanol in stratified LTC. For rich-to-lean burn stratified combustion, higher alcohols must be used. Choosing a higher alcohol for rich-to-lean combustion requires a balance between the strength of the NTC behavior and the low autoignition resistance of the fuel. Based on autoignition studies, NTC behavior becomes significant in higher alcohols with at least a five-carbon-long straight chain in the molecule. Alcohols with more than six carbons tend to have autoignition resistance that is too low. Therefore, n-pentanol, n-hexanol, and some hexanol isomers are the best alcohol fuel candidates to enable rich-to-lean stratified combustion.

One final factor to consider that was not mentioned above is the influence of natural thermal stratification on the heat release process of a stratified LTC mode. Since both rich-to-lean and lean-to-rich burn stratified combustion aim to control the distribution of ignition delay times in the combustion chamber through a direct injection event, the distribution of ignition delay times prior to the direct injection event should also be considered. For example, in lean-to-rich stratified combustion, regions targeted by the spray will experience an increase in their local ignition delay time. Therefore, it is advantageous to target the spray to regions in the cylinder that have a longer ignition delay time due to natural thermal stratification. Conversely, in rich-to-lean stratified combustion, regions targeted by the spray will experience a decrease in their local ignition time. In this case, it is advantageous to target the spray to regions in the cylinder that have a longer shorter ignition delay time. Otherwise, the spray may result in a more homogenous distribution of ignition delay times in the combustion chamber. In other words, the stratification process used to control the heat release process should work with natural thermal stratification. Although it is possible to overpower natural thermal stratification with the direct injection event, it is a more efficient use of stratification to work with the natural thermal stratification if possible, which can help minimize the risk of producing harmful emissions. Prior experimental and computational fluid dynamics results have confirmed the importance of injector spray angle on stratified combustion modes [98].

### **5.2.1 Evaluation of Normalized $\phi$ -sensitivity**

To evaluate the predictive capability of normalized  $\phi$ -sensitivity, a quantitative combustion performance metric that the normalized  $\phi$ -sensitivity is correlated to is required, analogous to intake/IVC temperature for the critical compression ratio. Since the critical compression ratio correlates well with intake/IVC temperature, it can be used as a fuel requirement for an engine with a given compression ratio and internal residual control range (e.g., through NVO). This function is somewhat less clear for normalized  $\phi$ -sensitivity. Originally, it was proposed as a metric that should

be maximized when designing gasoline blends to ensure minimum stratification is required to control the heat release process, minimizing potential soot/NO<sub>x</sub> emission formation. By extension, fuels with the same normalized  $\phi$ -sensitivity would behave similarly in stratified LTC in response to a given amount of stratification.

Since the objective of stratifying the cylinder is to elongate the heat release process, it is conceivable that normalized  $\phi$ -sensitivity would correlate with a heat release metric like burn duration or normalized peak heat release rate. However, in HCCI alone, the heat release process varies significantly across different operating conditions and engine platforms. A higher-level combustion performance metric that is important in stratified LTC is RI (or a similar energy release rate/combustion noise metric). Since the objective of stratified LTC is to achieve full load operation while keeping combustion noise below some threshold value, a relationship between normalized  $\phi$ -sensitivity and RI would be useful. In a limited sense, a fuel with a high magnitude normalized  $\phi$ -sensitivity should reduce the RI more than a fuel with a low magnitude. For example, Figure 100 shows a comparison of ringing intensity for ethanol and n-butanol on the gasoline engine architecture under two different fuel preparation techniques: vaporizer (fully premixed) and early direct injection (stratified) described in Section 3.3. These cases are run with a  $\phi'$  of 0.5, an intake pressure of 1.15 bar, a residual rate of 30%, an engine speed of 1200 rpm, and an intake temperature adjusted to maintain a constant CA50 of 7.0 deg aTDC. Ethanol, which has a moderate magnitude of normalized  $\phi$ -sensitivity, shows a 30% reduction in RI with stratification. n-butanol, which has a normalized  $\phi$ -sensitivity of nearly zero actually experienced a slight increase in RI with stratification. Further, the standard deviation of RI of stratified n-butanol is much higher than premixed n-butanol.

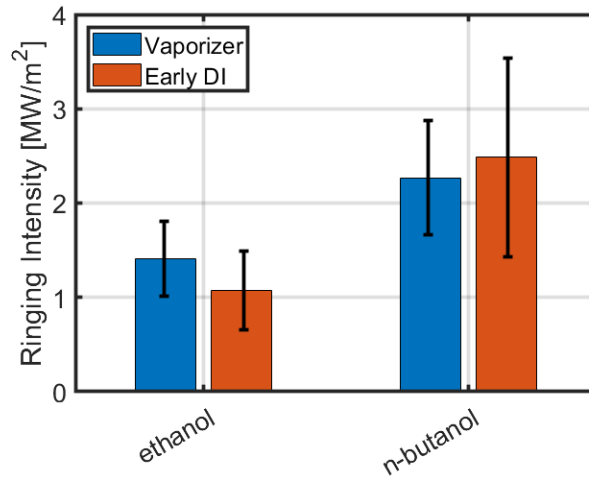


Figure 100: Ringing intensity for ethanol and n-butanol for two fueling methods: vaporizer (fully premixed) and early direct injection (stratified). Error bars represent the standard deviation of ringing intensity across 300 consecutive cycles.

While these limited results lend confidence to normalized  $\phi$ -sensitivity as an indicator of fuel's ability to elongate the heat release process via stratification, it is not comprehensive. It was described in Section 3.3 that it is unclear how much stratification is induced by an early direct injection of fuel on the gasoline engine architecture. The stratification is hypothesized to come from a lack of mixing during the intake and compression stroke. Since the heat-release-elongating stratification is a result of evaporative cooling, it is conceivable that an increase in the cooling potential of the fuel will increase the amount of induced stratification, thereby further reducing the RI. However, for methanol, n-propanol, isopropanol, isobutanol, and sec-butanol, the reduction of RI with an early direct injection of fuel vs. vaporized fuel is ~25-40% consistently, with no clear trend relating to fuel properties. This is likely due to the amount of evaporative cooling that occurs in the air vs. off of the walls, related to the phenomenon described in Section 3.1. If a fuel with a higher cooling potential has a lower evaporation fraction in the air (i.e., more fuel evaporates off of the walls), then the induced stratification can be similar to a fuel with a lower cooling potential and a higher evaporation fraction in the air.

Overall, these limited results indicate that with the exception of n-butanol, the C1-C4 bio-synthesizable alcohol fuels can enable lean-to-rich combustion in some capacity. However, no hierarchal ranking of the effectiveness of the fuels can be obtained from this limited dataset. A more controlled method of evaluating the normalized  $\phi$ -sensitivity would involve inducing a constant amount of stratification and comparing combustion performance. Like the critical compression ratio test, a standardized set of operating conditions would be required. It is possible that multiple sets of operating conditions will be needed to characterize how a fuel's normalized  $\phi$ -sensitivity changes (cooling potential does not change with operating conditions like intake pressure, but cool flame reactivity-based  $\phi$ -sensitivity will). However, in addition to initial operating conditions, other parameters, such as compression stroke injection timing, number of compression stroke injections, or split fraction will begin to play a role. Finally, the difference in required hardware, discussed in Section 5.1, will play a significant role, meaning a priori knowledge of a fuel as an enabler of lean-to-rich or rich-to-lean stratified combustion would be required.

## Chapter 6. Conclusions and Scientific Contributions

### 6.1 Summary and Conclusions

The production of alcohol fuels from bio-derived feedstock is a rapidly improving field. Finding the ideal advanced combustion mode for these alcohol fuels is therefore paramount. Next generation stratified LTC modes that aim to control the heat release process through the compression stroke injection of fuel can be divided into two groups based on how the heat release process proceeds in the combustion chamber: lean-to-rich burn or rich-to-lean burn. This thesis aims to shed light on the role of the bio-synthesized alcohol fuels in advanced LTC where compositional stratification is used to control in-cylinder thermal stratification, simultaneously providing cycle-to-cycle control over the heat release process and increasing the operating range of LTC to the maximum rated load of a light-duty diesel engine. In particular, systemic investigations studying wet ethanol in TSCI, a lean-to-rich burn stratified combustion mode, were conducted. These experiments characterized the role of injection system design, combustion chamber design, and in-cylinder charge conditions on the heat release control effectiveness of compression stroke injections of a high cooling potential, single-stage ignition. The summary of the findings is as follows:

- Using a narrow angle injector, a large range of control over the intake valve closing temperature, and by extension, the combustion phasing, in HCCI can be achieved using a high cooling potential fuel like wet ethanol by varying the injection timing, which varies the fraction of fuel that evaporates in the air vs. off of the walls.
- The use of external, cooled EGR does not significantly affect the hot ignition temperature of ethanol and does not impact the effectiveness of a split injection of wet ethanol to control the heat release process. Using external, cooled EGR offers the potential to increase the overall tailpipe combustion efficiency, which is beneficial for an LTC mode operating on



- a diesel engine architecture with large crevice and squish volumes and low internal residuals.
- Using intake boost to reduce the global equivalence ratio does not impact the effectiveness of a split injection of wet ethanol to control the heat release process. By lowering the global equivalence ratio using intake boost, both NO<sub>x</sub> production and combustion efficiency decrease, demonstrating the tradeoff between NO<sub>x</sub> and combustion efficiency in LTC.
  - Compression stroke injections using wide-angle injectors target the walls and squish regions in the cylinder. These regions are naturally colder during the compression stroke due to heat transfer. Evaporative cooling of the spray in these regions further cools them, thereby working with natural thermal stratification additively to increase overall thermal stratification in the cylinder.
  - Compression stroke injections using narrow-angle injectors target the hotter core of the cylinder. These regions are naturally hotter during the compression stroke due to less heat transfer. Evaporative cooling of the spray in these regions cools them, counteracting and negating natural thermal stratification to create a more uniform temperature distribution in the cylinder.
  - Wide-angle injectors maximize the control authority and effectiveness of lean-to-rich burn stratified combustion while narrow-angle injectors maximize the control authority and effectiveness of rich-to-lean burn stratified combustion.
  - The lower surface-to-volume ratio of a shallow bowl piston geometry is effective at reducing heat transfer, resulting in higher thermal efficiencies than a re-entrant bowl piston geometry. However, this reduces natural thermal stratification, which makes combustion occur quicker and produce more engine-damaging knock than the re-entrant bowl piston geometry would at identical operating conditions.

- The direct injection of wet ethanol into a quiescent, light-duty gasoline architecture combustion chamber during the intake stroke via a side-mounted, single-hole GDI-style injector resulted in a significant amount of stratification that persisted during the compression stroke to elongate the combustion process. This stratification increased as fueling rates were increased, such that the naturally aspirated high-load limit of this LTC combustion strategy was limited by oxygen content rather than RI, which typically limits high-load HCCI operation.
- To introduce a mechanism of control over the induced stratification, and therefore the combustion process, and avoiding the aforementioned drawbacks, two strategies were investigated and were shown to successfully reduce in-cylinder stratification, thereby providing a mechanism of combustion control:
  - Splitting the total fuel mass between early in-cylinder injections and intake system injections (in this work, a fuel vaporizer was used, although a port fuel injector could be used), and,
  - Using a traditional split injection strategy, where a fraction of the fuel is injected during the compression stroke. In this situation, the chosen compression stroke injection timing reduces stratification rather than increases stratification.

With an increased understanding of TSCI with wet ethanol, and in general, lean-to-rich stratified combustion with high cooling potential, low  $\phi$ -sensitivity fuels, the feasibility of a wide array of bio-synthesizable alcohol fuels to effectively enable highly controllable advanced LTC was evaluated. First, the autoignition of methanol, ethanol, n-propanol, isopropanol, n-butanol, isobutanol, and sec-butanol were experimentally characterized over a wide range of operating conditions in HCCI. The following conclusions were drawn from this work:

- For all of the low boost operating conditions (1.15 bar intake pressure), the order of reactivity of the seven fuels considered from low to high is: isopropanol, sec-butanol, ethanol  $\approx$  n-propanol  $\approx$  isobutanol, methanol, n-butanol.
- All seven alcohol fuels exhibit similar sensitivity to  $\phi$ , internal residual rate, and engine speed under low boost conditions.
- Under low boost conditions, the sensitivity of combustion phasing to changes in intake temperature of n-butanol was lower than that of the other six fuels, which were approximately constant, implying cool flame reactivity. n-butanol showed significant ITHR at an intake pressure of 1.55 bar. This emergent ITHR caused a significant decrease in the required IVC temperature to maintain a constant combustion phasing as intake pressure increased.
- Sec-butanol displayed ITHR at an intake pressure of 1.95 bar. This emergent ITHR slightly decreased the intake temperature sensitivity of sec-butanol. The other five fuels considered did not display any ITHR at an intake pressure of 1.95 bar. Although isobutanol displayed no ITHR, a decrease in intake temperature sensitivity was observed.

Following the autoignition characterization of these seven fuels, two potential LTC fuel rating metrics, the critical compression ratio and the normalized  $\phi$ -sensitivity, are evaluated with respect to the alcohol fuels. This analysis yielded the following conclusions:

- Measured on the CFR engine, isopropanol has the highest HT HCCI cCR and n-butanol has the lowest. Methanol, ethanol, n-propanol, and isobutanol have nearly identical critical compression ratios. Sec-butanol has a higher critical compression ratio than isobutanol.
- There is no correlation between critical compression ratio and cetane number for the seven alcohol fuels tested in this study. There is a strong correlation between critical compression ratio and MON and a moderate correlation between critical compression ratio and RON.

When the RON values of the alcohol fuels were modified to remove the effect of cooling potential using data from the literature, the critical compression ratio correlates well with this modified RON metric.

- The CFR measured HT HCCI cCR correlated well with the intake/IVC temperature requirement to maintain a constant CA50 on the gasoline engine architecture near MON conditions when the seven alcohol fuels and two specialty gasoline blends were considered. When the intake pressure or  $\phi$  were increased significantly, this correlation weakened, specifically for the fuels that displayed cool flame reactivity. This suggests the need for a second HCCI cCR that is measured under boosted conditions.
- C1-C4 alcohols have a high cooling potential and lack NTC behavior, making them ideal fuel candidates to enable lean-to-rich burn stratified combustion. With the exception of n-butanol, the reactivity of the C1-C4 alcohols are similar. Therefore, the most important factor determining the potential of the fuel to effectively enable lean-to-rich burn stratified combustion is their cooling potential, specifically their latent heat of vaporization and stoichiometric air-fuel ratio.
- An effective method to increase the cooling potential of a fuel is by blending the fuel with water. The C1-C3 alcohols are completely miscible water, meaning the water-alcohol blend ratio is only limited by potential combustion/emission considerations. The butanols have limited miscibility with water. However, a water-butanol blend can be produced using a C1-C3 alcohol as a cosolvent.
- Ranking the potential of the C1-C4 alcohols to enable lean-to-rich burn stratified combustion: methanol  $\approx$  wet ethanol  $\approx$  wet isopropanol  $\approx$  wet n-propanol > ethanol > isopropanol > n-propanol > isobutanol  $\approx$  2-butanol > n-butanol.

- With the exception of some pentanol isomers, C5+ alcohols show NTC behavior and a cooling potential close to its corresponding alkane, meaning they are good candidates to enable rich-to-lean burn stratified combustion. n-pentanol, n-hexanol, and some hexanol isomers are the best fuel candidates to enable rich-to-lean burn stratified combustion since they have a good balance between normalized  $\phi$ -sensitivity and autoignition resistance.
- n-butanol, which had a near zero normalized  $\phi$ -sensitivity, was unable to elongate the heat release process through stratification on the gasoline-engine architecture. The other six C1-C4 alcohols were able to enable lean-to-rich stratified combustion on the gasoline-engine architecture.

## 6.2 Scientific Contributions

The main scientific contributions of this thesis are twofold: the further development of a new, advanced combustion mode and the identification of fuels that can enable this new, advanced combustion mode. Previous work by the author in a master's thesis showed that this new, advanced combustion mode, thermally stratified compression ignition, can achieve cycle-to-cycle control over the heat release process in LTC with diesel-like efficiencies using a split injection of wet ethanol. In this work, the effect of the unique fuel properties of wet ethanol on the injection strategy and operating conditions of TSCI are studied, providing valuable information towards the implementation of this new combustion mode in a production setting. Additionally, this work provides guidance towards the specific hardware (e.g., injector spray angle, piston geometry) needed to maximize the heat release control authority provided by a compression stroke injection of a high cooling potential, single-stage ignition fuel in a production setting.

In addition to the development of TSCI, the LTC performance of seven carbon-neutral alcohol fuels was characterized and the sensitivities of these fuels to changes in various operating parameters were determined and compared, providing fundamental data to the community. From

this analysis, alcohol fuels with similar LTC performance were identified, meaning these fuels could potentially be used interchangeably in LTC.

Finally, two previously proposed fuel rating metrics were studied: the critical compression ratio as a metric quantifying the LTC ignition propensity of a fuel and the normalized  $\phi$ -sensitivity as a metric quantifying the amount of heat release control authority a fuel can achieve in stratified LTC. The critical compression ratio correlated well with the intake temperature requirement of various alcohol and gasoline fuels in LTC, meaning it shows potential as an LTC fuel rating metric analogous to octane number in SI. In a production setting, the compression ratio and NVO authority of an engine can dictate the acceptable critical compression range of an input fuel. Similarly, fuels with similar values of normalized  $\phi$ -sensitivity would behave similarly in stratified LTC. With this in mind, and with the similarity in LTC performance of many of the low alcohol fuels, equivalent multi-component alcohol fuel blends can be produced based on the local availability of specific alcohol fuels by creating blends that have similar valued critical compression ratios and normalized  $\phi$ -sensitivities. Water can be added to these multi-component alcohol fuel blends to increase the normalized  $\phi$ -sensitivity if needed. These scientific contributions have made significant strides towards enabling a high-efficiency, low-emissions combustion mode with a variety of carbon neutral fuels.

### **6.3 Future Work**

While this thesis has provided a significant amount of guidance towards maximizing the control authority of stratified advanced LTC concepts, there is more work to be done. For example, optimization routines should be performed to determine the optimal combination of injector spray angle and piston geometry to maximize the heat release control authority that results from compression stroke injections while minimizing efficiency penalties associated with the engine hardware. Further, optimization of the injection strategy as a function of operating conditions

should be performed to maximize efficiency and minimize emissions across the entire operating map.

Another area requiring future work is low-load operation of lean-to-rich stratified combustion. Although compression stroke injections of high cooling potential, single-stage ignition fuels are able to elongate natural thermal stratification, controlling the heat release process and enabling high-load operation, the strategy is not effective for enabling low-load operation down to idle. Near idle, HCCI combustion generally misfires. In-cylinder energy content is not high enough to enable effective sequential autoignition. To achieve stable combustion, the IVC temperature would have to increase significantly, which is impractical due to the low exhaust enthalpy of low-load operation. Future work should explore low-load LTC operating strategies with alcohol fuels, including ones with diesel-like injection strategies, where the fuel-bound oxygen would reduce sooting propensity. The use of thick thermal barrier coatings (TBCs) as a means to increase wall temperatures can aid in increasing the LTC low-load combustion stability limit. Therefore, future work would have to characterize the performance of TSCI with thick TBCs to enable low-load operation while also increasing thermal efficiency, combustion efficiency, and exhaust enthalpy for low temperature aftertreatment and turbocharging. Other potential strategies include cylinder deactivation, such that activated cylinders can maintain healthy mid-load operation during overall engine idling conditions, though this strategy would not work on single-cylinder engines. In such cases, mild hybridization that eliminates engine low-load operation altogether may be required.

The HT HCCI critical compression ratio predicted the HCCI ignition propensity of fuels when those fuels did not display significant cool flame reactivity. Future work is thus required to determine whether a second critical compression measurement, one measured under conditions where non single-stage ignition fuels display cool flame reactivity (i.e., boosted conditions), would be able to accurately predict the HCCI ignition propensity of fuels displaying cool flame reactivity.

Additionally, the fuels considered in this work are generally considered high-grade fuels, meaning their autoignition resistance is high. Therefore, while the critical compression results are promising for stratified LTC concepts that employ these high-grade fuels, it is unclear whether the critical compression ratio would be useful for predicting the ignition propensity of lower-grade fuels that are generally desired for rich-to-lean stratified LTC; future work would should examine this.

More experimental TSCI testing with neat and wet alcohol fuels is required to quantify whether the normalized  $\phi$ -sensitivity can accurately predict the performance of a fuel in stratified LTC. Coupled with this is the development of a standardized test that quantifies the heat release control authority of a compression stroke injection of fuel, which determines whether a potential fuel will be able to effectively enable highly controllable stratified LTC over the entire operating range. Finally, future work should quantify specific blends of various alcohols and water (i.e., blending fraction equivalents) that perform nearly identical in stratified LTC over the entire operating range.

## Publications

### Thesis Publications

1. **Gainey B.**, Longtin JP, Lawler B. "A guide to uncertainty quantification for experimental engine research and heat release analysis," SAE Int. J. Engines 12(5):509-523, 2019, <https://doi.org/10.4271/03-12-05-0033>.
2. **Gainey, B.**, Gohn, J., Yan, Z., Rahimi-Boldaji, M., Lawler, B. "HCCI with Wet Ethanol: Investigating the Charge Cooling Effect of a High Latent Heat of Vaporization Fuel In LTC," SAE Technical Paper 2019-24-0024, 2019, <https://doi.org/10.4271/2019-24-0024>.
3. **Gainey, B.**, Yan, Z., Rahimi-Boldaji, M., Lawler, B. "On the Effects of Injection Strategy, EGR, and Intake Boost on TSCI With Wet Ethanol," J. Eng. Gas Turbines Power 142(9): 091013, 2020, <https://doi.org/10.1115/1.4048150>.
4. **Gainey, B.**, Gohn, J., Hariharan, D., Rahimi, M. Lawler, B. "Assessing the impact of injector included angle and piston geometry on thermally stratified compression ignition with wet ethanol," Applied Energy 262:114528, 2020, <https://doi.org/10.1016/j.apenergy.2020.114528>



5. **Gainey, B.**, Yan, Z., Moser, S., Vorwerk, E., Lawler, B. "Tailoring Thermal Stratification to Enable High Load Low Temperature Combustion with Wet Ethanol on a Gasoline Engine Architecture," *Int. J. Eng. Res.* 2020, <https://doi.org/10.1177/1468087420945960>.
6. **Gainey, B.**, Lawler, B. "The role of alcohol biofuels in advanced combustion: an analysis," *Fuel* 283:118915, 2021, <https://doi.org/10.1016/j.fuel.2020.118915>.
7. **Gainey, B.** Yan, Z., Lawler, B. "Autoignition Characterization of Methanol, Ethanol, Propanol, and Butanol Over a Wide Range of Operating Conditions in LTC/HCCI," *Fuel* 119495, 2021, <https://doi.org/10.1016/j.fuel.2020.119495>.
8. **Gainey, B.**, Hoth, A., Waqas, M., Lawler, B., Kolodziej, C. "High Temperature HCCI critical compression ratio of the C1-C4 Alcohol Fuels," *SAE Technical Paper 2021-01-0310*, 2021. *In Review*.

### Other Publications

1. **Gainey, B.**, Hariharan, D., Yan, D., Zilg, S., Boldaji M., Lawler, B. "A split injection of wet ethanol to enable thermally stratified compression ignition". *Int J Engine Res* 21(8):1441-1453, 2018, <https://doi.org/10.1177/1468087418810587>.
2. **Gainey, B.**, Yan, Z., Gohn, J., Rahimi Boldaji, M., Lawler, B. "TSCI with Wet Ethanol: an Investigation of the effects of injection strategy on a diesel engine architecture," *SAE Technical Paper 2019-01-1146*, 2019, <https://doi.org/10.4271/2019-01-1146>.
3. **Gainey, B.**, Lawler, B. "A Fuel Cell Free Piston Gas Turbine Hybrid Architecture for High-Efficiency, Load-Flexible Power Generation," *Applied Energy* 2021, *In Press*.
4. **Gainey, B.**, Lawler B. "Lean Flammability Limit of High-Dilution Spark Ignition with Ethanol, Propanol, and Butanol," *Int J Engine Research* 2021 *In Review*.
5. M. Rahimi Boldaji, **B. Gainey**, B. Lawler "Thermally stratified compression ignition enabled by wet ethanol with a split injection strategy: A CFD simulation study," *Appl Energy* 235:813-826, 2019, <https://doi.org/10.1016/j.apenergy.2018.11.009>.
6. Zhou, Y., Sofianopoulos, A., **Gainey, B.**, Lawler, B., Mamalis, S. "A system-level numerical study of a homogeneous charge compression ignition spring-assisted free piston linear alternator with various piston motion profiles," *Applied Energy* 239, 820-835, 2018, <https://doi.org/10.1016/j.apenergy.2019.01.240>.
7. Zhou, Y., **Gainey, B.**, Hariharan, D., Lawler, B., Mamalis, S. "Understanding HCCI Combustion in a Free Piston Engine with a Multi-Zone, Control-Mass Model with Thermal Stratification and Chemical Kinetics," *SAE Technical Paper 2019-01-0958*, 2019, <https://doi.org/10.4271/2019-01-0958>.
8. Hariharan, D., Yang, R., Zhou, Y., **Gainey, B.**, et al. "Catalytic partial oxidation reformation of diesel, gasoline, and natural gas for use in low temperature combustion engines," *Fuel* 246:295-307, 2019, <https://doi.org/10.1016/j.fuel.2019.02.003>.
9. Hariharan, D., **Gainey, B.**, Yan, Z., Mamalis, S., Lawler, B. "Experimental study of the effect of start of injection and blend ratio on single fuel reformate RCCI," *J. Eng. Gas Turbines Power*, 142(8):081010, 2020, <https://doi.org/10.1115/1.4047814>.
10. Yan, Z., **Gainey, B.**, Hariharan, D., Lawler, B. "Investigation into Reactivity Separation Between Direct Injected and Premixed Fuels in RCCI Combustion Mode," *ASME ICEF 2019-7130* 2019, <https://doi.org/10.1115/ICEF2019-7130>.
11. Yan, Z., **Gainey, B.**, Hariharan, D., Lawler, B. "Improving the controllability of partial fuel stratification at low boost levels by applying a double late injection strategy," *Int. J. Eng. Res.* 2020, <https://doi.org/10.1177/1468087419896511>

12. Rahimi-Boldaji, M., **Gainey, B.**, O'Donnell, P., Lawler, B. "Investigating the Effect of Spray Included Angle on Thermally Stratified Compression Ignition with Wet Ethanol Using Computational Fluid Dynamics," *Applied Thermal Engineering* 170:114964, 2020, <https://doi.org/10.1016/j.applthermaleng.2020.114964>.
13. O'Donnell, P., Boldaji, M., **Gainey, B.**, Lawler, B. "Varying Intake Stroke Injection Timing of Wet Ethanol in LTC," *SAE Technical Paper* 2020-01-0237, 2020, <https://doi.org/10.4271/2020-01-0237>.
14. Yan, Z, **Gainey, B.**, Gohn, J., et al., "The Effects of Thick Thermal Barrier Coatings on Low-Temperature Combustion," *SAE Int. J. Adv. & Curr. Prac. in Mobility* 2(4):1786-1799, 2020, <https://doi.org/10.4271/2020-01-0275>.
15. Gohn, J., **Gainey, B.**, Zainul, S., Lawler, B. "Wet ethanol in LTC: How water fraction and DTBP affect combustion and intake temperature at naturally aspirated and boosted conditions," *Fuel* 267:117094, 2020, <https://doi.org/10.1016/j.fuel.2020.117094>.
16. Zhou, Y., **Gainey, B.**, Lawler, B. "An ultrafast multi-zone HCCI model with Autoignition, Global reaction and Interpolation (AGI) for achieving comparable accuracy to detailed chemical kinetics models," *Combustion and Flame* 221:487-501, 2020, <https://doi.org/10.1016/j.combustflame.2020.08.016>.

## References

1. Najt P., Foster D. "Compression-ignited homogeneous charge combustion," SAE technical paper 830264, 1983, <http://dx.doi.org/10.4271/830264>.
2. Dec, J., Hwang, W., "Characterizing the Development of Thermal Stratification in an HCCI Engine Using Planar-Imaging Thermometry," SAE Int. J. Engines 2(1):421-438, 2009, <https://doi.org/10.4271/2009-01-0650>.
3. Snyder, J., Dronniou, N., Dec, J., Hanson, R. "PLIF measurements of thermal stratification in an HCCI engine under fired operation." SAE Int J Engines 4(1):1669–88, 2011, <http://dx.doi.org/10.4271/2011-01-1291>.
4. Lawler, B., Hoffman, M., Filipi, Z., Güralp, O., Najt, P. "Development of a postprocessing methodology for studying thermal stratification in an HCCI engine". J Eng Gas Turb Power 134:102801, 2012, <https://doi.org/10.1115/1.4007010>.
5. Lawler, B., Lacey, J., Dronniou, N., Dernotte, J., Dec, J., Güralp, O. "Refinement and Validation of the thermal stratification analysis: a post-processing methodology for determining temperature distributions in an experimental HCCI engine," SAE Technical Paper 2014-01-1276, 2014, <https://doi.org/10.4271/2014-01-1276>.
6. Lawler, B., Joshi, S., Lacey, J., Güralp, O., Najt, P., Filipi, Z. "Understanding the effect of wall conditions and engine geometry on thermal stratification and HCCI combustion," *Proceedings of the ASME 2014 Internal Combustion Engine Division Fall Technical Conference. Volume 1: Large Bore Engines; Fuels; Advanced Combustion; Emissions Control Systems*. Columbus, Indiana, USA. October 19–22, 2014. V001T03A020. ASME. <https://doi.org/10.1115/ICEF2014-5687>.
7. Lawler, B., Mamalis, S., Joshi, S., Lacey, J., Guralp, O., Najt, P. "Understanding the effect of operating conditions on thermal stratification and heat release in a homogeneous charge compression ignition engine," Applied Thermal Engineering 112:392-402, 2017, <https://doi.org/10.1016/j.applthermaleng.2016.10.056>.

8. Noehre, C., Andersson, M., Johansson, B., and Hultqvist, A. "Characterization of Partially Premixed Combustion," SAE Technical Paper 2006-01-3412, 2006, <https://doi.org/10.4271/2006-01-3412>.
9. Kolodziej, C., Kodavasal, J., Ciatti, S., Som, S., Shidore, N., Delhom, J. "Achieving Stable Engine Operation of Gasoline Compression Ignition Using 87 AKI Gasoline Down to Idle," SAE Technical Paper 2015-01-0832, 2015, <https://doi.org/10.4271/2015-01-0832>.
10. Sjoberg, M., Dec, J. "Smoothing HCCI heat-release rates using partial fuel stratification with two-stage ignition fuels. SAE technical paper," SAE Technical Paper 2006-01-0629, 2006, <https://doi.org/10.4271/2006-01-0629>.
11. Kokjohn, S., Hanson, R., Splitter, D., Reitz, R. "Fuel reactivity controlled compression ignition (RCCI): a pathway to controlled high-efficiency clean combustion," *Int J Engine Res.* 12: 209– 226, 2011, <https://doi.org/10.1177/1468087411401548>.
12. Lawler, B., Splitter, D., Szybist, J., Kaul, B. "Thermally Stratified Compression Ignition: A new advanced low temperature combustion mode with load flexibility," *Applied Energy* 189:122-132, 2017, <https://doi.org/10.1016/j.apenergy.2016.11.034>.
13. Gainey, B., Hariharan, D., Yan, Z., Lawler, B. "A Split Injection of Wet Ethanol to Enable Thermally Stratified Compression Ignition," *International Journal of Engine Research* 21(8):1441-1453, 2018, <https://doi.org/10.1177/1468087418810587>.
14. Lopez-Pintor, D., Dec, J., Gentz, G. " $\Phi$ -Sensitivity for LTGC Engines: Understanding the Fundamentals and Tailoring Fuel Blends to Maximize This Property," SAE Technical Paper 2019-01-0961, 2019, <https://doi.org/10.4271/2019-01-0961>.
15. Messerly, R., Rahimi, M., St. John, R. "Towards quantitative prediction of ignition-delay-time sensitivity on fuel-to-air equivalence ratio," *Combustion and Flame* 214:103-115, 2020, <https://doi.org/10.1016/j.combustflame.2019.12.019>.
16. Rathmann, R., Szklo, A., Schaeffer, R. "Land use competition for production of food and liquid biofuels: An analysis of the arguments in the current debate," *Renewable Energy* 35(1):14-22, 2010 <https://doi.org/10.1016/j.renene.2009.02.025>.

17. Zabed, H., Sahu, J., Suely, A., Boyce, A., Faruq, G. "Fuel ethanol production from lignocellulosic biomass: An overview on feedstocks and technological approaches," *Renewable and Sustainable Energy Reviews* 66:751-774, 2016, <https://doi.org/10.1016/j.rser.2016.08.038>.
18. Gírio, F., Fonseca, C., Carvalheiro, .F., Duarte, L., Marques, S., Bogel-Lukasik, R. "Hemicelluloses for fuel ethanol: a review," *Bioresour Technol* 101:4775–800, 2010 <https://doi.org/10.1016/j.rser.2016.08.038>.
19. Lee, Y., Iyer, P., Torget, J. "Dilute-acid hydrolysis of lignocellulosic biomass," *Adv.Biochem. Eng./Biotechnol*, 65:93–115, 1999, <https://doi.org/10.1533/9781845699611.2.143>.
20. Shahbazi, A., Zhang, B., Edited by: Waldon, K. "Bioalcohol production: biochemical conversion of lignocellulosic biomass – Chapter 5 - Dilute and concentrated acid hydrolysis of lignocellulosic biomass," (Woodhead Publishing Ltd, 2010), 143-158, <https://doi.org/10.1533/9781845699611.2.143>.
21. Koppram, R., Tomas-Pejo, E., Xiros, C., Olsson, L. "Lignocellulosic ethanol production at high-gravity: challenges and perspectives," *Trends in Biotechnology* 32(1):46-53, 2014, <https://doi.org/10.1016/j.tibtech.2013.10.003>.
22. Galazka, J., Tian, C., Beeson, W. "Cellodextrin Transport in Yeast for Improved Biofuel Production," *Science*, 330(6000):84-86, 2010, <https://doi.org/10.1126/science.1192838>.
23. Boulton, R., Singleton, V., Bisson, L., Kunkee, R. "Principles and Practices of Winemaking: Yeast and biochemistry of ethanol fermentation," (Boston, Springer, 1999), 102–92, [https://doi.org/10.1007/978-1-4757-6255-6\\_4](https://doi.org/10.1007/978-1-4757-6255-6_4).
24. Hahn-Hagerdal, B., Karhumaa, K., Fonseca, C., Spencer-Martins I., Gorwa-Grauslund, M. "Towards industrial pentose-fermenting yeast strains," *Applied Microbiology and Biotechnology* 74:937-953, 2007, <https://doi.org/10.1007/s00253-006-0827-2>.
25. Kropke, M., Mihalcea, C., Bromley, J., Simpson, S. "Fermentative production of ethanol from carbon monoxide," *Current Opinion in Biotechnology* 22(3): 320-325, 2011, <https://doi.org/10.1016/j.copbio.2011.01.005>.

26. Liew, F., Martin, M., Tappel, R., et al. "Gas Fermentation – A Flexible Platform for Commercial Scale Production of Low-Carbon-Fuels and Chemicals from Waste and Renewable Feedstocks," *Frontiers in Microbiology* 7(694), 2016, <https://doi.org/10.3389/fmicb.2016.00694>.
27. Kim, S., Dale, B. "Global potential bioethanol production from wasted crops and crop residues," *Biomass and Bioenergy* 26(4):361-375, 2004, <https://doi.org/10.1016/j.biombioe.2003.08.002>.
28. Wilhelm, W., Johnson, J., Karlen, D., Lightle, D. "Corn Stover to Sustain Soil Organic Carbon Constrains," *Biomass Supple. Agronomy Journal* 99:1665-1667, 2007, <https://doi.org/10.2134/agronj2007.0150>.
29. Zabed, H., Sahu, J., Suely, A., Boyce, A., Faruq, G. "Bioethanol production from renewable sources: Current perspectives and technological progress," *Renewable and Sustainable Energy Reviews* 71:475-501, 2017, <https://doi.org/10.1016/j.rser.2016.12.076>.
30. Perlack, R., et al. "Biomass as feedstock for a bioenergy and bioproducts Industry: the technical feasibility of a billion-ton annual supply," Oak Ridge National Laboratory Report ORNL/TM-2005/66, US Dept. of Energy, April 2005.
31. Perlack, R., et al. "US billion-ton update: biomass supply for a bioenergy and bioproducts industry," Oak Ridge National Laboratory Report ORNL/TM-2005/66, US Dept. of Energy, August 2011.
32. Renewable Fuels Association, "2019 Ethanol Industry Outlook," Renewable Fuels Association, 2019.
33. Verhelst, S., Turner, J., Sileghem, L., Vancoillie, J. "Methanol as a fuel for internal combustion engines," *Progress in Energy and Combustion Science* 70:43-88, 2019, <https://doi.org/10.1016/j.pecs.2018.10.001>.
34. Pearson, R., Eisaman, M., Turner, J. "Energy storage via carbon-neutral fuels made from CO<sub>2</sub>, water, and renewable energy," *Proceedings of the IEEE* 100(2):440-460, Feb. 2012, <https://doi.org/10.1109/JPROC.2011.2168369>.
35. Klabunde, J., Bischoff, C., Papa, A. "Ullmann's Encyclopedia of Industrial Chemistry – Propanols," (Wiley, 2018), 1-14, [https://doi.org/10.1002/14356007.a22\\_173](https://doi.org/10.1002/14356007.a22_173).

36. Ouyang, J., Kong, F., Su, G., Hu, Y., Song, Q. "Catalytic Conversion of Bio-ethanol to Ethylene over La-Modified HZSM-5 Catalysts in a Bioreactor," *Catalysis Letters* 132:64-74, 2009, <https://doi.org/10.1007/s10562-009-0047-3>.
37. Haro, P., Ollero, P., Trippe, F. "Technoeconomic assessment of potential processes for bio-ethylene production," *Fuel Processing Technology* 114:35-48, 2013, <https://doi.org/10.1016/j.fuproc.2013.03.024>.
38. Liu, K., Atiyeh, H., Stevenson, B., Tanner, R., Wilkins, M., Huhnke, R. "Continuous syngas fermentation for the production of ethanol, n-propanol, and n-butanol," *Bioresource Technology* 151:69-77, 2014, <https://doi.org/10.1016/j.biortech.2013.10.059>
39. Ammar, E., Wang, Z., Yang, S. "Metabolic engineering of *Propionibacterium freudenreichii* for n-propanol production," *Applied Microbiology and Biotechnology* 97:4677-4690, 2013 <https://doi.org/10.1007/s00253-013-4861-6>.
40. Shen, C., Liao, R. "Metabolic engineering of *Escherichia coli* for 1-butanol and 1-proanol production via the keto-acid pathways," *Metabolic Engineering* 10(6):312-320, 2007, <https://doi.org/10.1016/j.ymben.2008.08.001>.
41. Inokuma, K., Liao, J., Okamoto, M., Hanai, T. "Improvement of isopropanol production by metabolically engineering *Escherichia coli* using gas stripping," *Journal of Bioscience and Bioengineering* 110(6):696-701, 2010 <https://doi.org/10.1016/j.jbiosc.2010.07.010>.
42. Jang, Y., Malaviya, A., Lee, J., Im, J., Lee, S., Lee, J., Eom, M., Cho, J., Seung, D. "Metabolic Engineering of *Clostridium acetobutylicum* for the Enhanced production of isopropanol-butanol-ethanol fuel mixture," *AIChE* 29(4):1083-1088, 2013, <https://doi.org/10.1002/btpr.1733>.
43. Kumar, M., Gayen, K. "Developments in biobutanol production: New insights," *Applied Energy* 88:1999-2012, 2011, <https://doi.org/10.1016/j.apenergy.2010.12.055>.
44. Atsumi, S., Hanai, T., Liao, J. "Non-fermentative pathways for synthesis of branched-chain higher alcohols as fuels," *Nature* 451(7174):86-89, 2008 <https://doi.org/10.1038/nature06450>.

45. Peralta-Yahya, P., Kasling, J. "Advanced biofuel production in microbes," *Biotechnology Journal* 5:147-162, 2010, <https://doi.org/10.1002/biot.200900220>.
46. Weber, C., Farwick, A., Benisch, F., Brat, D., Dietz, H., Subtil, T., Boles, E. "Trends and Challenges in the microbial production of lignocellulosic bioalcohol fuels," *Applied Microbiology and Biotechnology* 87:1303-1315, 2010, <https://doi.org/10.1007/s00253-010-2707-z>
47. Cardose Generoso, W., Schadeweg, V., Oreb, M., Boles, E. "Metabolic engineering of *Saccharomyces cerevisiae* for production of butanol isomers," *Current Opinion in Biotechnology* 33:1-7, 2015, <https://doi.org/10.1016/j.copbio.2014.09.004>.
48. Wess, J., Brinek, M., Boles, E. "Improving isobutanol production with the yeast *Saccharomyces cerevisiae* by successively blocking competing metabolic pathways as well as ethanol and glycerol formation," *Biotechnology for Biofuels* 12:173, 2019, <https://doi.org/10.1186/s13068-019-1486-8>.
49. Swidah, R., Ogunlabi, O., Grant, C., Ashe, M. "n-Butanol production in *S. cerevisiae*: co-ordinate use of endogenous and exogenous pathways," *Applied Microbiology and Biotechnology* 102:9857-9866, 2018, <https://doi.org/10.1007/s00253-018-9305-x>.
50. Zhang, Y., Lane, S., Chen, J., Hammer, S., Luttiner, J., Yang, L., Jin, Y., Avalos, J. "Xylose utilization stimulates mitochondrial production of isobutanol and 2-methyl-1-butanol in *Saccharomyces cerevisiae*," *Biotechnology for Biofuels* 12:223, 2019, [10.1186/s13068-019-1560-2](https://doi.org/10.1186/s13068-019-1560-2).
51. Promdonkoy, P., Siripong, W., Downes, J., Tanapongpipat, S., Runguphan, W. "Systematic improvement of isobutanol production from D-xylose in engineered *Saccharomyces cerevisiae*," *AMB Express* 9:160, 2019 <https://doi.org/10.1186/s13568-019-0885-3>.
52. Ghiaci, P., Norbeck, J., Larsson, C. "2-Butanol and butanone production in *Saccharomyces cerevisiae* through combination of a B12 dependent dehydratase and a secondary alcohol dehydrogenase using a TEV-based expression system," *PLoS ONE* 9(7):102774, 2014, <https://doi.org/10.1371/journal.pone.0102774>.



53. Ehrlich, F. "Über die Bedingungen der Fuselölbildung und über ihren Zusammenhang mit dem Eiweissaufbau der Hefe. Ber. Dtsch," Chem. Ges. 40:1027-1047, 1907, <https://doi.org/10.1002/cber.190704001156>.
54. Hazelwood, L., Daran, J., van Maris, A., Pronk, J., Dickinson, J. "The Ehrlich pathway for fusel alcohol production: a century of research on *Saccharomyces cerevisiae* metabolism," *Appl Environ Microbiol.* 74:3920, 2008, <https://doi.org/10.1128/AEM.02625-07>.
55. Zhang, K., Sawaya, M., Eisenberg, D., Liao, J. "Expanding metabolism for biosynthesis of nonnatural alcohols," *Proc Natl Acad Sci* 105(52):20653–8, 2008, <https://doi.org/10.1073/pnas.0807157106>.
56. Cann, A., Liao, J. "Pentanol isomer synthesis in engineered microorganisms," *Appl Microbiol Biotechnol* 85(4):893–899, 2009, <https://doi.org/10.1007/s00253-009-2262-7>.
57. Hammer, S., Zhang, Y., Avalos, J. "Mitochondrial Compartmentalization Confers Specificity to the 2-Ketoacid Recursive Pathway: Increasing Isopentanol Production in *Saccharomyces cerevisiae*," *ACS Synth. Biol.* 9(3):546-555, 2020, <https://doi.org/10.1021/acssynbio.9b00420>.
58. Marcheschi, R., Li, H., Zhang, K., Noey, E., Kim, S., Chaubey, A., Huok, K., Liao, J.. "A synthetic recursive '+1' pathway for carbon chain elongation," *ACS Chem. Biol.* 7(4):689-697, 2012, <https://doi.org/10.1021/cb200313e>.
59. Westbrook, C., Curran, H. "Mathematical Modelling of Gas-Phase Complex Reaction Systems: Pyrolysis and Combustion: Chapter 7 Detailed kinetics of fossil and renewable fuel combustion," (Elsevier, 2019) ISBN: 9780128195796.
60. Mack, J., Schuler, D., Butt, R., Dibble, R. "Experimental investigation of butanol isomer combustion in Homogeneous Charge Compression Ignition (HCCI) engines," *Applied Energy* 165:612-626, 2016, <https://doi.org/10.1016/j.apenergy.2015.12.105>.
61. Weber, B., Kumar, K., Zhang, Y., Sung, C. "Autoignition of n-butanol at elevated pressure and low-to-intermediate temperature," *Combustion and Flame* 158:809-819, 2011, <https://doi.org/10.1016/j.combustflame.2011.02.005>.

62. Zador, J., Fernandes, Y., Georgievskii, G., Meloni, G., Taatjes, C., Miller, J. "The reaction of hydroxyethyl radicals with O<sub>2</sub>: a theoretical analysis and experimental product study," *Proceedings of the Combustion Institute* 32:271-277, 2009, <https://doi.org/10.1016/j.proci.2008.05.020>.
63. Da Silva, G., Bozzelli, J., Liang, L., Farrell, J. "Ethanol oxidation: kinetics of the a-hydroxyethyl radical + O<sub>2</sub> reaction," *J. Physical Chemistry A* 113:8923-8933, 2009, <https://doi.org/10.1021/jp903210a>.
64. Shirazi, S., Abdollahipoor, B., Windom, B., Reardon, K., Foust, T. "Effects of blending C3-C4 alcohols on motor gasoline properties and performance of spark ignition engines: A review" *Fuel Processing Technology* 197:106194, 2020, <https://doi.org/10.1016/j.fuproc.2019.106194>.
65. Maurya, R., Agarwal, A. "Experimental Investigations of Performance, Combustion and Emission Characteristics of Ethanol and Methanol Fueled HCCI Engine," *Fuel Processing Technology* 126:30-48, 2014, <https://doi.org/10.1016/j.fuproc.2014.03.031>.
66. Sjoberg, M., Dec, J. "Ethanol autoignition characteristics and HCCI performance for wide ranges of engine speed, load and boost," *SAE Int. J. Engines* 3(1):84-106, 2010, <https://doi.org/10.4271/2010-01-0338>
67. Svensson, E., Verhelst, S., "Simulation Based Investigation of Achieving Low Temperature Combustion with Methanol in a Direct Injected Compression Ignition Engine," *SAE Technical Paper* 2019-01-1152, 2019, <https://doi.org/10.4271/2019-01-1152>.
68. Svensson, E., Tuner, M., and Verhelst, S., "Influence of Injection Strategies on Engine Efficiency for a Methanol PPC Engine," *SAE Int. J. Adv. & Curr. Prac. in Mobility* 2(2):653-671, 2020, <https://doi.org/10.4271/2019-24-0116>.
69. Sjoberg, M., Dec, J. "Smoothing HCCI heat-release rates using partial fuel stratification with two-stage ignition fuels," *SAE Technical Paper* 2006-01-0629, 2006, <https://doi.org/10.4271/2006-01-0629>.
70. Saffy, H., Northrop, W., Kittelson, W., Boies, W. "Energy, carbon dioxide and water use implications of hydrous ethanol production" *Energy Conversion and Management* 105:900-907, 2015, <https://doi.org/10.1016/j.enconman.2015.08.039>.

71. Togbé C, Dagaut P, Mzè-Ahmed A, Diévar P, Halter F, Foucher F. "Experimental and detailed kinetic modeling study of 1-hexanol oxidation in a pressurized jet-stirred reactor and a combustion bomb," *Energy Fuels* 24(11):5859-5875, 2010, <https://doi.org/10.1021/ef101255w>.
72. Heufer, K., Bugler, J., Curran., S. "A comparison of longer alkane and alcohol ignition including new experimental results for n-pentanol and n-hexanol," *Proceedings of the Combustion Institute* 34:511-518, 2014, <https://doi.org/10.1016/j.proci.2012.05.103>.
73. Yang, Y., Dec, J., Dronniou, N., Simmons, B. "Characteristics of Isopentanol as a Fuel for HCCI Engines," *SAE Int. J. Fuels Lubr.* 3(2):725-741, 2010, <https://doi.org/10.4271/2010-01-2164>.
74. Gainey, B., Yan, Z., Gohn, J., Rahimi Boldaji, M., Lawer, B. "TSCI with Wet Ethanol: an Investigation of the Effects of Injection Strategy on a Diesel Engine Architecture," *SAE Technical Paper* 2019-01-1146, 2019, <https://doi.org/10.4271/2019-01-1146>.
75. Kalghatgi, G., "Fuel Anti-Knock Quality - Part I. Engine Studies," *SAE Technical Paper* 2001-01-3584, 2001, doi:10.4271/2001-01-3584.
76. Risberg, P., Kalghatgi, G., and Ångström, H., "Auto-ignition Quality of Gasoline-Like Fuels in HCCI Engines", *SAE Technical Paper* 2003-01-3215, 2003, doi:10.4271/2003-01-3215.
77. Liu, H., Yao, M., Zhang, B., Zheng, Z. "Influence of Fuel and Operating Conditions on Combustion Characteristics of a Homogenous Charge Compression Ignition Engine", *Energy & Fuels* 23:1422-1430, 2009, <https://doi.org/10.1021/ef800950c>.
78. Shibata, G., Urushihara, T. "Auto-Ignition Characteristics of Hydrocarbons and Development of HCCI Fuel Index", *SAE Technical Paper* 2007-01-0220, 2007, <https://doi.org/10.4271/2007-01-0220>.
79. Truedsson, I., Cannella, W., Johansson, B., Tuner, M., "Development of New Test Method for Evaluating HCCI Fuel Performance," *SAE Technical Paper* 2014-01-2667, 2014, <https://doi.org/10.4271/2014-01-2667>.
80. Rochstroh, T., Kolodziej, C., Goldsborough, S., Wallner, T., Jspersen, M. "Insights into Engine Knock: Comparison of Knock Metrics across Ranges of Intake Temperature and Pressure in the CFR Engine," *SAE Int. J. Fuels Lubr.* 11(4):545-561, 2018, <https://doi.org/10.4271/2018-01-0210>.

81. Waqas, M. "Effect of Intake Temperature and Engine Speed on the Auto-ignition Reactivity of the Fuels for HCCI Fuel Rating" SAE Technical Paper 2020, *In Review*.
82. Wallner, T. "Correlation Between Speciated Hydrocarbon Emissions and Flame Ionization Detector Response for Gasoline/Alcohol Blends," J. Eng. Gas Turbines Power 133(8):082801, 2011, <https://doi.org/10.1115/1.4002893>
83. Hohenberg, G. "Advanced Approaches for Heat Transfer Calculations," SAE Technical Paper 790825, 1979, <https://doi.org/10.4271/790825>.
84. Heywood, J. B. "Internal Combustion Engine Fundamentals," (New York, McGraw-Hill, 1988), ISBN0-07-100499-8.
85. ISO/IEC/OIML/BIPM, "Guide to the Expression of Uncertainty in Measurement," JCGM 100:2008
86. JCGM "Joint Committee for Guides in Metrology Evaluation of measurement data – Supplement 1 to the 'Guide to the expression of measurement' – Propagation of distributions using Monte Carlo method," 2008;101.
87. Cox, M., Harris, P., Siebert, B. "Evaluation of measurement uncertainty based on the propagation of distributions using Monte Carlo simulation," Meas Tech. 46:824–33, 2003, <https://doi.org/10.1023/B:METE.0000008439.82231.ad>.
88. Chew, G., Walczyk, T. "A Monte Carlo approach for estimating measurement uncertainty using standard spreadsheet software," Anal Bioanal Chem. 402:2463–9, 2012, <https://doi.org/10.1007/s00216-011-5698-4>.
89. Longtin, J. "The uncertainty tree: Reducing the uncertainty of uncertainty analysis," Review of Scientific Instruments 73:3698, 2002, <https://doi.org/10.1063/1.1505654>.
90. McBride, B., Zehe, M., Gordon, S., "NASA Glenn Coefficients for Calculating Thermodynamic Properties of Individual Species," NASA/TP—2002-211556, 2002.
91. J. Chang, O. Guralp, Z. Filipi, D. Assanis, "New Heat Transfer Correlation for An HCCI Engine Derived From Measurements of Instantaneous Surface Heat Flux," SAE Technical Paper 2004-01-2996, 2004, <https://doi.org/10.4271/2004-01-2996>.

92. Graham, L., Belisle, Sheri., Baas, C.L. "Emissions from light duty gasoline vehicles operating on low blend ethanol gasoline and E85," Atmospheric Environment 42(19):4498-4516, 2008, <https://doi.org/10.1016/j.atmosenv.2008.01.061>.
93. Dec, J., Sjoberg, M., Hwang, W. "The Effects of EGR and its Constituents on the Autoignition of Single- and Two-Stage Fuels," SAE Technical Paper 2007-01-0207, 2007, <https://doi.org/10.4271/2007-01-0207>.
94. Da Silva, G., Bozzelli, J., Liang, L., Farrell, J. "Ethanol Oxidation : Kinetics of the  $\alpha$ -Hydroxyethyl Radical + O<sub>2</sub> Reaction" J. Phys Chem. A 113(31):8923-8933, 2009, <https://doi.org/10.1021/jp903210a>.
95. Dec, J., Yang, Y., "Boosted HCCI for High Power without Engine Knock and with Ultra-Low NOx Emissions - using Conventional Gasoline," SAE Int. J. Engines 3(1):750-767, 2010, <https://doi.org/10.4271/2010-01-1086>.
96. Eng J. "Characterization of pressure waves in HCCI combustion," SAE Technical Paper 2002-01-2859, 2002, <https://doi.org/10.4271/2002-01-2859>.
97. Makkapati, S., Curtis, E. "Boosted HCCI - Experimental Observations in a Single Cylinder Engine," SAE Technical Paper 2014-01-1277, 2014, <https://doi.org/10.4271/2014-01-1277>.
98. Rahimi-Boldaji, M., Gainey, B., O'Donnell, P., Lawler, B. "Investigating the Effect of Spray Included Angle on Thermally Stratified Compression Ignition with Wet Ethanol Using Computational Fluid Dynamics," Applied Thermal Engineering 170:114964, <https://doi.org/10.1016/j.applthermaleng.2020.114964>.
99. Moon, S., Kim, G., Chu, S., Kang, J., Min, K., Choi, H., Ha, T. "Numerical Analysis on the Effect of Piston Bowl Geometry in Gasoline-Diesel Dual-Fuel Combustion," SAE Technical Paper 2019-01-1164, 2019, <https://doi.org/10.4271/2019-01-1164>.
100. Splitter, D., Wissink, M., Kokjohn, S., Reitz, R. "Effect of compression ratio and piston geometry on RCCI load limits and efficiency," SAE Technical Paper 2012-01-0383, 2012, <https://doi.org/10.4271/2012-01-0383>.

101. Dempsey, A. B., Walker, N. R., & Reitz, R. "Effect of piston bowl geometry on dual fuel reactivity controlled compression ignition (RCCI) in a light-duty engine operated with gasoline/diesel and methanol/diesel," SAE International Journal of Engines 6(1):78-100, 2013, <https://doi.org/10.4271/2013-01-0264>.
102. Lacey, J., Filipi, Z., Sathasivam, S., Cannella, W., Fuentes-Afflick, P. "HCCI Operability Limits: The Impact of Refinery Stream Gasoline Property Variation" J. Eng. Gas Turbines Power 135(8):081505, 2013, <https://doi.org/10.1115/1.4024260>.
103. Dadsetan, M., Chitsaz, I., Amani, E. "A study of swirl ratio effects on the NO<sub>x</sub> formation and mixture stratification in an RCCI engine," Energy 182:1100-1114, 2019, <https://doi.org/10.1016/j.energy.2019.06.109>.
104. Loeper, P., Ra, Y., Foster, D., and Ghandhi, J., "Experimental and Computational Assessment of Inlet Swirl Effects on a Gasoline Compression Ignition (GCI) Light-Duty Diesel Engine," SAE Technical Paper 2014-01-1299, 2014, <https://doi.org/10.4271/2014-01-1299>.
105. Petersen E. et al. "Discrepancies between shock tube and rapid compression machine ignition at low temperatures and high pressures," Shock Waves 1:739-744, 2008, [https://doi.org/10.1007/978-3-540-85168-4\\_119](https://doi.org/10.1007/978-3-540-85168-4_119)
106. Zhang, C., Wu, H. "Combustion characteristics and performance of a methanol fueled homogeneous charge compression ignition engine," Journal of the Energy Institute 89(3):346-353, 2016, <https://doi.org/10.1016/j.joei.2015.03.005>.
107. He, B., Yuan, J., Lie, M., Zhao, H. "Combustion and emission characteristics of a n-butanol HCCI engine," Fuel, 115:758-764, 2014, <https://doi.org/10.1016/j.fuel.2013.07.089>.
108. Xie, H., Wei, Z., He, B., Zhao, H. "Comparison of HCCI Combustion Respectively Fueled with Gasoline, Ethanol and Methanol through the Trapped Residual Gas Strategy," SAE Technical Paper 2006-01-0635, 2006, <https://doi.org/10.4271/2006-01-0635>.

109. Maurya R., Agarwal, A. "Experimental investigations of performance, combustion and emission characteristics of ethanol and methanol fueled HCCI engine," *Fuel Processing Technology* 126:30-48, 2014, <https://doi.org/10.1016/j.fuproc.2014.03.031>.
110. Brassat, A., Thewes, M. "Analysis of the effects of certain alcohol and furan-based biofuels on controlled auto ignition," SAE Technical Paper 2012-01-1135, 2012, <https://doi.org/10.4271/2012-01-1135>.
111. Ortiz-Soto, E., Vavra, J., Babajimopoulos, A. "Assessment of residual mass estimation methods for cylinder pressure heat release analysis of HCCI engines with negative valve overlap," Proceedings of the ASME 2011 Internal Combustion Engine Division Fall Technical Conference. ASME 2011 Internal Combustion Engine Division Fall Technical Conference. October 2-5, 2011. pp. 481-490. ASME. <https://doi.org/10.1115/ICEF2011-60167>.
112. Sarathy, S., Oswald, P., Hansen, N., Kohse-Hoinghaus, K. "Alcohol Combustion Chemistry," *Progress in Energy and Combustion Science* 44:40-102, 2014, <https://doi.org/10.1016/j.pecs.2014.04.003>.
113. Weber BW, Sung C-J. "Comparative autoignition trends in butanol isomers at elevated pressure," *Energy Fuels* 27(3):1688-1698, 2013, <https://doi.org/10.1021/ef302195c>.
114. Vranckx, S., Heufer, K., Lee, C., Olivier, H., Schill, L., Kopp, W., Leonhard, K., Taatjes, C., Fernandes, R. "Role of peroxy chemistry in the high-pressure ignition of n-butanol – Experiments and detailed kinetic modelling," *Combustion and Flame* 158(8):1444-1455, 2011, <https://doi.org/10.1016/j.combustflame.2010.12.028>.
115. Man, X., Tang, C., Zhang, J., Zhang, Y., Pan, L., Huang, Z., Law, C. "An experimental and kinetic modeling study of n-propanol and i-propanol ignition at high temperatures," *Combustion and Flame* 161(3):644-656, 2014, <https://doi.org/10.1016/j.combustflame.2013.08.003>.
116. Sjöberg, M., Dec, J., "Combined Effects of Fuel-Type and Engine Speed on Intake Temperature Requirements and Completeness of Bulk-Gas Reactions for HCCI Combustion," SAE Technical Paper 2003-01-3173, 2003, <https://doi.org/10.4271/2003-01-3173>.
117. Gohn J, Gainey B, Zainul S, Lawler B. "Wet ethanol in LTC: how water fraction and DTBP affect combustion and intake temperature at naturally aspirated and boosted conditions," *Fuel* 267:117094, 2020, <https://doi.org/10.1016/j.fuel.2020.117094>.

118. Yanowitz, J., Ratcliff, M., McCormick, R., Taylor, J., Murphy, M. "Compendium of Experimental Cetane Numbers," NREL/TP-5400-61693, 2017.
119. Foong, T., Morganti, K., Brear, M., da Silva, G., "The Effect of Charge Cooling on the RON of Ethanol/Gasoline Blends," SAE Int. J. Fuels Lubr. 6(1):34-43, 2013, <https://doi.org/10.4271/2013-01-0886>
120. Sluder, C., Szybist, J., McCormick, R., Ratcliff, M., Zigler, B. "Exploring the relationship between octane sensitivity and heat-of-vaporization," SAE Int. J. Fuels Lubr. 9(1):80-90, 2016, <https://doi.org/10.4271/2016-01-0836>.
121. Kumar, K., Sung, C. "Autoignition of Methanol: Experiments and Computations," Int J of Chemical Kinetics 43(4), 2011, <https://doi.org/10.1002/kin.20546>.
122. Mittal, G., Burke, S., Davies, V., Parajuli, B., Metcalfe, W. "Autoignition of ethanol in a rapid compression machine," Combustion and Flame 161:1164-1171, 2014, <https://doi.org/10.1016/j.combustflame.2013.11.005>.
123. Noorani, K., Akih-Kumgeh, A., Bergthorson, J. "Comparative high temperature shock tube ignition of C1-C4 Primary alcohols," Energy Fuels 24:5834-5843, 2010, <https://doi.org/10.1021/ef1009692>.
124. Heufer, K., Bugler, J., Curran, S. "A comparison of longer alkane and alcohol ignition including new experimental results for n-pentanol and n-hexanol," Proceedings of the Combustion Institute 34:511-518, 2013, <https://doi.org/10.1016/j.proci.2012.05.103>.
125. Johnson, M., Goldsborough, S. "A shock tube study of n- and iso-propanol ignition," Energy Fuels 23(12):5886-5898, 2009, <https://doi.org/10.1021/ef900726j>.